

UNCLASSIFIED

AD NUMBER: AD0902023

LIMITATION CHANGES

TO:

Approved for public release; distribution is unlimited.

FROM:

Distribution authorized to U.S. Gov't. agencies only;
Administrative/Operational Use; 30 Jun 1970. Other requests shall be
referred to the Office of Naval Research, Washington, DC 20360.

AUTHORITY

ONR LTR, 25 FEB 1974

THIS PAGE IS UNCLASSIFIED

AD-902023

①

Westinghouse

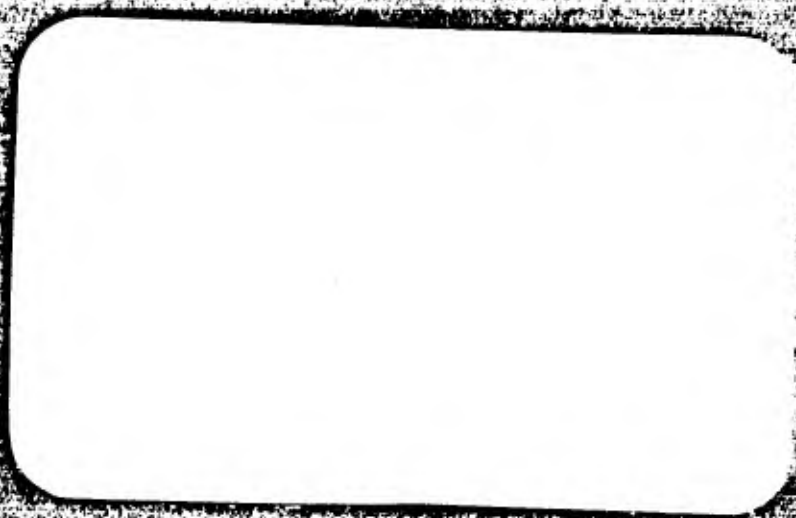


AD-902023

AD

501-52

DDC
RECEIVED
FEB 25 1974
ILLUSTRATED



Reproduction in whole or in part is permitted
for any purpose of the United States Government.

Submitted to: Office of Naval Research
Department of the Navy
Washington, D.C. 20360
Under Contract N00014-69-C-0150
NRL Reqn 00173-9-005189/11-25-68

30 June 1970

E. L. Maxwell
D. L. Stone
R. D. Croghan
L. Ball
A. D. Watt

Details of illustrations in
this document may be better
studied on microfiche.

This document has been approved
for public release and sale; its
distribution is unlimited.

DDC
RECEIVED
FEB 25 1974
C

DEVELOPMENT OF A
VLF ATMOSPHERIC NOISE
PREDICTION MODEL

APPROVED FOR
[Signature]

Westinghouse Georesearch Laboratory, 8401 Baseline, Boulder, Colo. 80303

ABSTRACT

This report describes the development of a digital computer model for predicting the characteristics of VLF atmospheric noise. The model provides for the calculation of 1) mean values of vertical electric field intensity, 2) the standard deviation from the mean values, 3) mean values for voltage deviation, V_d , and 4) the direction of arrival of the noise energy. The model calculates values for any location on the earth at any frequency from 10 to 30 kHz.

Five algorithms which form the basis for the model are described in the report. They are: (I) An algorithm for computing electromagnetic power radiated from every region of the earth. Improved thunderstorm day maps and lightning discharge data provide the input to the computations. (II) An algorithm for computing the standard deviation of power radiated for every region of the earth. Statistics of thunderstorm and lightning occurrence provide the data input to these computations. (III) An algorithm for the propagation of energy within the earth-ionosphere waveguide. This algorithm, or model, includes the effects of ground conductivity, direction of propagation, latitude, sun zenith angle and day or night path conditions. The three most significant modes of propagation are used. (IV) An algorithm which uses the results of I, II and III to compute noise field intensities (E_v), standard deviations (σ_N), V_d 's and direction of arrival values for any location on the earth's surface, for any hour, any month and at any frequency from 10 to 30 kHz. (V) An algorithm to take the output of IV and prepare contour plots, polar plots, diurnal plots, frequency interpolation plots and data inputs to computer programs for communications system analysis.

The prediction model was used to compute E_v , σ_N and V_d at 20 kHz, in a 1 kHz bandwidth, for every 10° longitude and every 10° latitude (from 80°S to 80°N). These were computed for each hour and month and were used in the preparation of contours for noise prediction maps. Frequency

interpolation plots, for interpolating values from the 20 kHz prediction maps to any frequency from 10 to 30 kHz were prepared. Plots were mad for each season, every fourth hour, to represent each of 34 regions of the earth. The bulk of the calculations, contour plots, etc. were used in the preparation of a VLF atmospheric noise prediction manual to be published by the United States Government.

Calculated values from the prediction model were compared with measured data from ten of the world-wide ESSA noise stations. Calculated and measured values of E_v generally agree within ± 3 dB; σ_N within ± 1 dB; and V_d within ± 2 dB. Examples of the comparisons are given in this report as evidence of the value of this realistic and comprehensive noise prediction model.

TABLE OF CONTENTS

		<u>Page</u>
1.0	INTRODUCTION	1-1
2.0	THUNDERSTORM DAY MAPS	2-1
2.1	<u>The Thunderstorm</u>	2-1
2.2	<u>World Meteorological Organization (WMO) Maps</u>	2-5
2.3	<u>Preparation of New Maps</u>	2-6
2.3.1	Data Obtained	2-6
2.3.2	Methods Used to Prepare New Maps	2-9
2.4	<u>Using the New Maps</u>	2-14
3.0	ELECTROMAGNETIC ENERGY RADIATED PER SQUARE KILOMETER	3-1
3.1	<u>Converting Thunderstorm Days to Lightning Discharges Per Square Kilometer</u>	3-1
3.1.1	Lightning Counters	3-2
3.1.2	Lightning Counter Data	3-3
3.2	<u>Energy Radiated Per Discharge</u>	2-12
3.2.1	Cloud-to-Ground Discharges	3-12
3.2.2	Intra-Cloud Discharges	3-25
3.2.3	Radiated EM spectra of Typical Discharges	3-35
3.3	<u>An Algorithm For Computing Power Radiated From Any Region On the Earth's Surface</u>	3-38
4.0	PROPAGATION	4-1
5.0	STATISTICS OF THUNDERSTORMS AND LIGHTNING	5-1
5.1	<u>Description of Data Obtained</u>	5-1
5.2	<u>The Diurnal Variation of Thunderstorms and Lightning Charges</u>	5-10
5.3	<u>Statistics of Thunderstorm Days</u>	5-25

	<u>Page</u>
5.3.1 Cumulative Distributions	5-25
5.3.2 Standard Deviation vs. Number of Thunderstorm Days	5-35
5.3.3 Correlation With Distance	5-35
5.3.4 Correlation With Sunspot Cycles	5-41
5.4 <u>Statistics of Lightning Discharges</u>	5-41
6.0 CALCULATION OF FIELD INTENSITIES	6-1
6.1 <u>Description of the Algorithm</u>	6-1
6.2 <u>Description of the Computer Program</u>	6-16
6.3 <u>Comparison of Calculated and Measured Values</u>	6-16
6.4 <u>Computation of Frequency Modifiers</u>	6-32
7.0 CALCULATION OF STANDARD DEVIATION	7-1
7.1 <u>Development of the Algorithm</u>	7-3
7.2 <u>Description of the Algorithm</u>	7-18
7.3 <u>Comparison of Calculated and Measured Values</u>	7-21
7.4 <u>Variation With Frequency</u>	7-26
8.0 CALCULATION OF VOLTAGE DEVIATION (V_d)	8-1
8.1 <u>The Algorithm for Estimating V_d</u>	8-2
8.2 <u>Comparison of Calculated and Measured Values</u>	8-4
8.3 <u>Variation of V_d With Frequency</u>	8-4
8.4 <u>The Output</u>	8-5
9.0 CALCULATION OF THE DIRECTION OF ARRIVAL OF ATMOSPHERIC NOISE	9-1
10.0 SUMMARY	10-1
ACKNOWLEDGEMENTS	10-4
11.0 REFERENCES	11-1
APPENDIX A Tables of Comparisons Between Measured and Predicted Noise Values	A-1
APPENDIX B Fourier Transforms and Spectral Analysis	B-1

ILLUSTRATIONS

	<u>Page</u>
Figure 2-0 Distribution of Electric Charge Within a Thunderstorm.	2-4
Figure 2-1 Copy of WMO Map - January	2-15
Figure 2-2 Copy of WMO Map - July	2-16
Figure 2-3 Thunderstorm Day Map - January	2-17
Figure 2-4 Thunderstorm Day Map - April	2-18
Figure 2-5 Thunderstorm Day Map - July	2-19
Figure 2-6 Thunderstorm Day Map - October	2-20
Figure 3-1 Location of Lightning Counters	3-5
Figure 3-2 Relationship Between Thunderstorm Days and Lightning Discharges	3-7
Figure 3-3 Proportion of Lightning Discharges which are Cloud-to-Ground	3-10
Figure 3-4 Freezing Level vs Latitude During Dec-Jan-Feb	3-11
Figure 3-5 Phases of a Typical Cloud-to-Ground Discharge Process	3-13
Figure 3-6 Current Wave Form vs Time For a Series of Return Strokes	3-16
Figure 3-7 Probability Distribution of the Number of Return Strokes per Discharge	3-17
Figure 3-8 Apparent Height vs Stroke Order for Strokes in Discrete and Hybrid Flashes; from Brook, Kitigawa, and Workman [1962]	3-20
Figure 3-9 Current-Moment vs Time For Return Strokes	3-21

Figure 3-10	Current Moments Associated With the Leader and Junction Phases of the Lightning Discharge	3-23
Figure 3-11	Intra-Cloud Flash - Illustrating Structure of Noise as a Function of Frequency	3-27
Figure 3-12	Peak Electric Field Variations From a Vertical Discharge to Ground. From Watt [1967]	3-32
Figure 3-13	Cumulative Distribution of Peak Electric Fields Radiated From Lightning Discharges	3-33
Figure 3-14	Frequency Spectra of a Typical Cloud-to-Ground Discharge	3-39
Figure 3-15	Frequency Spectra of a Typical Intra-Cloud Discharge	3-40
Figure 4-1	Conductivity Area Designations	4-19
Figure 5-1	Diurnal Curve of Percentage of Thunderstorm Occurrences For Colo., Wyo., Mont.	5-12
Figure 5-2	Diurnal Curve of Percentage of Thunderstorm Occurrences For Minn., Iowa, Mo., Ark., La., Miss., Ill., Wis.	5-13
Figure 5-3	Diurnal Curve of Percentage of Thunderstorm Occurrences For Minn., Iowa, Mo., Ark., La., Miss., Ill., Wis.	5-14
Figure 5-4	Diurnal Curve of Percentage of Thunderstorm Occurrences For Bangkok, Thailand	5-15
Figure 5-5	Diurnal Curve of Percentage of Thunderstorm Occurrences For All Pacific Islands	5-16
Figure 5-6	Diurnal Curve of Percentage of Thunderstorm Occurrences For All Oceans - October	5-17
Figure 5-7	Diurnal Curve of Lightning Counts - Boulder, Colo.	5-19
Figure 5-8	Diurnal Curve of Lightning Counts - Slough, England	5-20

Figure 5-9	Diurnal Variation of Thunderstorms Across the United States - July	5-22
Figure 5-10	Diurnal Variation of Thunderstorms Around the World - July	5-23
Figure 5-11	Diurnal Variation of Thunderstorms During the Year - Ariz., N.Mex., Utah	5-24
Figure 5-12	Cumulative Distribution of Thunderstorm Days San Juan, Puerto Rico	5-26
Figure 5-13	Cumulative Distribution of Thunderstorm Days Squared - San Juan, Puerto Rico	5-27
Figure 5-14	Cumulative Distribution of Thunderstorm Days San Juan, Puerto Rico	5-28
Figure 5-15	Cumulative Distribution of Thunderstorm Days Squared - San Juan, Puerto Rico	5-29
Figure 5-16	Cumulative Distribution of Thunderstorm Days Tampa, Florida	5-31
Figure 5-17	Cumulative Distribution of Thunderstorm Days to the 1.5 Power - Tampa, Florida	5-32
Figure 5-18	Cumulative Distribution of Thunderstorm Days Squared - Tampa, Florida	5-33
Figure 5-19	Cumulative Distribution of Thunderstorm Days Nebraska Group	5-34
Figure 5-20	Standard Deviation vs Mean Value For Thunderstorm Days	5-36
Figure 5-21	Correlation of Thunderstorm Activity as a Function of Distance Between Stations - Nebraska	5-38
Figure 5-22	Correlation of Thunderstorm Activity as a Function of Distance Between Stations - Nebraska	5-39
Figure 5-23	Correlation of Thunderstorm Activity as a Function of Distance Between Stations - Southeast Group	5-40

Figure 5-24	Average Thunderstorm Days per Month and Year for the Nebraska Group of Stations and Yearly Mean Sunspot Number (Sunspot Data From Watt - 1967)	5-43
Figure 5-25	Cumulative Distribution of Lightning Counts Boulder, Colorado	5-44
Figure 5-26	Cumulative Distribution of Lightning Counts Singapore	5-45
Figure 5-27	Cumulative Distribution of Lightning Counts Singapore	5-46
Figure 5-28	Standard Deviation of Lightning Counts per Day per Time Block	5-47
Figure 6-1	Major Transmitter Map	6-3
Figure 6-2	Diurnal Modifier Map, Dec-Jan-Feb	6-6
Figure 6-3	Diurnal Modifier Map, Mar-Apr-May	6-7
Figure 6-4	Diurnal Modifier Map, June-July-Aug	6-8
Figure 6-5	Diurnal Modifier Map, Sept-Oct-Nov	6-9
Figure 6-6	VLF Atmospheric Noise Prediction Flow Chart	6-17
Figure 6-7	Final Comparison of Predicted and Measured Field Intensities, Boulder, Colo., Dec-Jan-Feb	6-19
Figure 6-8	Final Comparison of Predicted and Measured Field Intensities, Enkoping, Sweden, Dec-Jan-Feb	6-20
Figure 6-9	Final Comparison of Predicted and Measured Field Intensities, Pretoria, S.Afr., Dec-Jan-Feb	6-21
Figure 6-10	Final Comparison of Predicted and Measured Field Intensities, Singapore, Malaya, Dec-Jan-Feb	6-22
Figure 6-11	Final Comparison of Predicted and Measured Field Intensities, Boulder, Colo., June-July-Aug	6-23

Figure 6-12	Final Comparison of Predicted and Measured Field Intensities, Enköping, Sweden, June-July-Aug	6-24
Figure 6-13	Final Comparison of Predicted and Measured Field Intensities, Pretoria, S.Afr., June-July-Aug	6-25
Figure 6-14	Final Comparison of Predicted and Measured Field Intensities, Singapore, Malaya, June-July-Aug	6-26
Figure 6-15	Diurnal Variation of Vertical Electric Field Intensity, Boulder, Colo., Dec-Jan-Feb	6-28
Figure 6-16	Diurnal Variation of Vertical Electric Field Intensity, Pretoria, S.Afr., Dec-Jan-Feb	6-29
Figure 6-17	Diurnal Variation of Vertical Electric Field Intensity, Boulder, Colo., June-July-Aug	6-30
Figure 6-18	Diurnal Variation of Vertical Electric Field Intensity, Pretoria, S.Afr., June-July-Aug	6-31
Figure 6-19	Locations for Computation of Frequency Interpolations	6-33
Figure 6-20	Frequency Interpolation of Vertical Electric Field Intensity, Dec-Jan-Feb	6-34
Figure 6-21	Frequency Interpolation of Vertical Electric Field Intensity, Dec-Jan-Feb	6-35
Figure 6-22	Frequency Interpolation of Vertical Electric Field Intensity, Dec-Jan-Feb	6-36
Figure 6-23	Frequency Interpolation of Vertical Electric Field Intensity, Dec-Jan-Feb	6-37
Figure 7-1	Scatter Plot of the Standard Deviation of (Thunderstorm Days) ^{1.5} vs Thunderstorm Days.	7-6
Figure 7-2	Variance Modifier Map, Dec-Jan-Feb	7-14
Figure 7-3	Variance Modifier Map, Mar-Apr-May	7-15

Figure 7-4	Variance Modifier Map, June-July-Aug	7-16
Figure 7-5	Variance Modifier Map, Sept-Oct-Nov	7-17
Figure 7-6	Final Comparison of Predicted and Measured Standard Deviation, Balboa, Canal Zone, Sept-Oct-Nov	7-22
Figure 7-7	Estimated Standard Deviation of Atmospheric Noise at 13 kHz, Balboa, Canal Zone, Sept-Oct-Nov	7-23
Figure 7-8	Final Comparison of Predicted and Measured Standard Deviation, Enkoping, Sweden June-July-Aug	7-24
Figure 7-9	Estimated Standard Deviation of Atmospheric Noise at 13 kHz, Enkoping, Sweden, June-July-Aug	7-25
Figure 8-1	Final Comparison of Predicted and Measured Voltage Deviation, Boulder, Colo., Dec-Jan-Feb	8-6
Figure 8-2	Estimated Values of Voltage Deviation for VLF Atmospheric Noise - Bandwidth is 1 kHz, Boulder, Colo., Dec-Jan-Feb	8-7
Figure 8-3	Final Comparison of Predicted and Measured Voltage Deviation, Enkoping, Sweden, Dec-Jan-Feb	8-8
Figure 8-4	Estimated Values of Voltage Deviation for VLF Atmospheric Noise - Bandwidth is 1 kHz, Enkoping, Sweden, Dec-Jan-Feb	8-9
Figure 9-1	Expected Directional Variation of Atmospheric Noise Effective Field Intensity for 10° Sectors in dB to 1μv/m in a 1 kHz bw	9-3
Figure 9-2	Expected Directional Variation of Atmospheric Noise Effective Field Intensity for 10° Sectors in dB rel to 1μv/m in a 1 kHz bw	9-4
Figure 9-3	Expected Directional Variation of Atmospheric Noise Effective Field Intensity for 10° Sectors in dB rel to 1μv/m in a 1 kHz bw	9-5

Figure 9-4	Expected Directional Variation of Atmospheric Noise Effective Field Intensity for 10° Sectors in dB rel to 1μv/m in a 1 kHz bw	9-6
Figure 9-5	Expected Directional Variation of Atmospheric Noise Effective Field Intensity for 10° Sectors in dB rel to 1μv/m in a 1 kHz bw	9-7
Figure 9-6	Expected Directional Variation of Atmospheric Noise Effective Field Intensity for 10° Sectors in dB rel to 1μv/m in a 1 kHz bw	9-8
Figure 9-7	Average Rates of Occurrence of Atmospherics Over 4-Hour Intervals Against Their Directions of Arrival	9-9

1.0 INTRODUCTION

This is a "brief" report summarizing the work done to develop an improved VLF atmospheric noise prediction model. To report on the work in full detail would result in a large book and would have taken more time than was available. The interested reader can obtain more information, however, from the references.

The first attempt at the development of an essentially non-empirical model for the prediction or calculation of VLF atmospheric noise field intensities was undertaken during 1965 and 1966 under Contract Nobsr-93159. The results of this first effort were reported by Maxwell and Stone [1966]. Meteorological data and the physics of lightning discharges were used for the first time to determine the energy radiated from every section of the earth's surface. The earth ionosphere waveguide model was then used to compute the total field intensity at any given location resulting from the energy radiated at all locations. This basic concept has been refined and expanded in the work reported here. In particular, we have sought to make the following improvements in the noise prediction model:

- 1) Improve the accuracy and resolution of thunderstorm day maps,
- 2) Improve the computation of radiated power for each section of the earth's surface,
- 3) Improve the propagation model to effect a more accurate computation of field intensities,
- 4) Improve the efficiency of the computer program,
- 5) Develop a more comprehensive overall model for computation of field intensities,
- 6) Develop a subroutine to the major computer program for the calculation of direction-of-arrival plots,
- 7) Develop a model for the computation of the standard deviation of the mean noise field intensities,

- 8) Develop a model for the computation of voltage deviation (V_d),
- 9) Improve the method for accomplishing interpolation of the basic 20 kHz predictions to any other frequency between 10 and 30 kHz.

This report will describe the efforts made to accomplish the improvements listed above, and present comparisons between predicted values and measured values obtained by the Environmental Science Services Administration (ESSA) from their world-wide network of noise measuring sites. The 20 kHz predictions of field intensity, standard deviation and V_d are presented in a VLF Atmospheric Noise Prediction Manual prepared under this contract for publication by the United States Government. The manual also contains frequency interpolation curves and examples of direction-of-arrival plots. Copies of this manual can be obtained from the Naval Research Laboratory, Washington, D.C.

2.0 THUNDERSTORM DAY MAPS

2.1 The Thunderstorm

The major source of atmospheric noise in the ELF through HF bands is that generated by lightning in thunderstorms. Under certain conditions precipitation static, manmade noise, or electromagnetic energy from solar disturbances can become dominant over the ever present noise from lightning. The purpose of this project, however, was to develop a model for predicting atmospheric noise from lightning. We will begin with a description of the source of lightning - the thunderstorm.

The development of a thunderstorm requires a high degree of instability in the atmosphere. Whenever the atmosphere is made unstable by the appropriate addition or subtraction of thermal energy, a convective overturning takes place in the process of restoring stability. This begins with the development of a cumulous cloud. With the addition of energy in the form of warm, moist air, the updrafts tend to become violent and a thunderstorm is created. The major violent updrafts and the associated phenomena occur as convection units, usually separate from one another, so that thunderstorms can be considered as a number of "cells" separated by comparatively quiet, though often cloud-filled air.

There are three primary types of thunderstorms, associated with the mechanism leading to the development of atmospheric instability.

These three types are:

- 1) Convection or heat,
- 2) Frontal,
- 3) Orographic.

The instability for the heat-generated storm is caused by excessive heating of the ground and the lower atmospheric layers producing strong updrafts. The development of a frontal storm is generated by the

uplifting of warm air by the invasion of cold air at ground level along a front. The orographic storm is generated by the mechanical uplifting of moist air as it moves up the slopes of mountains. A minimum relative humidity of about 75 percent is thought to be necessary for the generation of a thunderstorm. Although the generation of frontal and orographic storms are assisted by the atmospheric processes described, the heating of the atmosphere by the sun is almost always involved as evidenced by a preference for all types of thunderstorms to occur during afternoon or maximum temperature rise hours.

There is one important exception to the statement that all types of thunderstorms occur more often in afternoon hours. The generation of thunderstorms over the oceans represents a fourth type of thunderstorm generation process whereby the instability develops not from the heating of the lower atmosphere but from the cooling of the upper atmosphere. Over the oceans the temperature of the bottom layers of the clouds tends to remain relatively constant whereas the top of the clouds will heat up during the day and cool off during the night. If the top of the clouds becomes appreciably cooler than the bottom layers an unstable condition will exist. This hypothesis is not discussed in any literature of which we are aware, but was developed through discussions with D. J. Sartor at the National Center for Atmospheric Research. The hypothesis is most strongly supported as will be shown in Section 5.2, by the preferential occurrence of thunderstorms over the oceans during late evening and early morning hours. For very thorough discussions of thunderstorms, see Byers [1953] and Byers and Braham [1949].

Without the separation of electric charge within a thunderstorm they would simply be the most common of the violent storms which the atmosphere produces. The fact that charge separation occurs produces lightning. Studies of the mechanisms of charge separation have produced dozens of reports describing as many theories. Discussions of possible

mechanisms include those by Moore et al. [1958], Chalmers [1958], Vonnegut [1963], and Sartor [1967]. Sartor proposes that "the growth of electric fields in clouds resulting from charge rearrangement due to particle interaction and translation is calculated under the assumption that the initial electrification is provided by the fair weather charge distribution of the atmosphere or by some other basic charge separating process. The results demonstrate that particle interaction must be taken into account in the electrification process during the precipitation formation period. In fact, they show that, starting with the normal fair weather field, it is possible to explain qualitatively and quantitatively many of the presently known observations of the electrical growth and field recovery behavior of thunderstorms." To date, Sartor's work seems to offer the most acceptable theory of the charge generation process.

Whatever the cause, the ultimate result is a general distribution of electric charge within the thunderstorm as shown in Figure 2-0. The first strokes of lightning in a thundercloud usually take place between two differently charged layers within the cloud itself. The lowering of charge within the cloud and therefore the development of cloud ground discharges appears to be associated with precipitation. It has been reported by many that lightning discharges to ground appear to be most frequent in the region of precipitation. Byers [1949] reports that the maximum frequency of lightning generated precedes the time of maximum five-minute rainfall.

For our purposes, a description of thunderstorms and the lightning generated thereby must be supplemented by a knowledge of the distribution of thunderstorms around the world. The circulation of heat and moisture in the atmosphere is such as to create preferred areas for thunderstorm activity. The seasonal changes in the circulation are quite pronounced, resulting in thunderstorms as far north as the Arctic Circle in summer and the

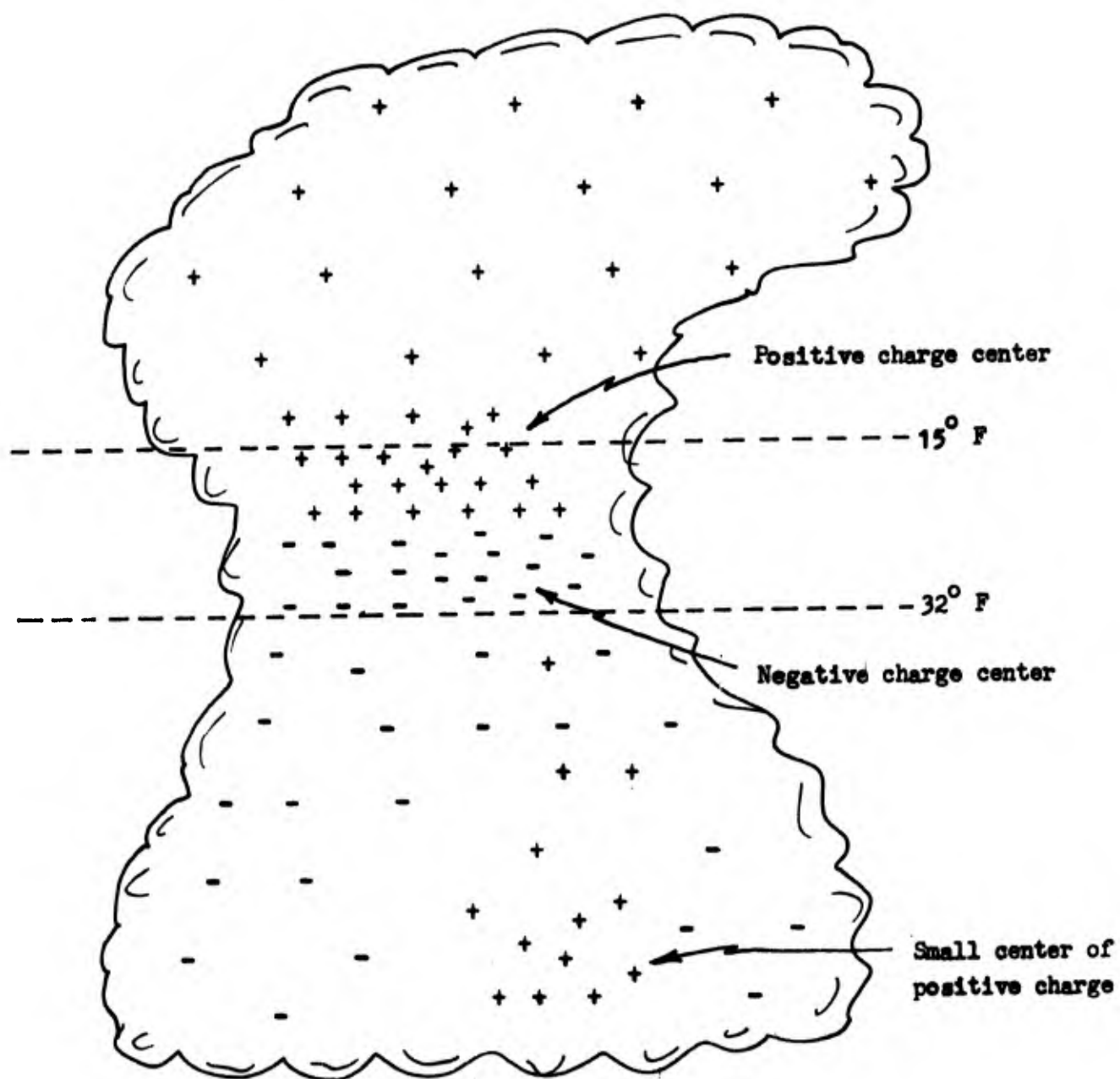


Figure 2-0 Distribution of electric charge within a thunderstorm.

displacement of activity to the southern hemisphere during northern winter. The world distribution of thunderstorms is the subject of the following section.

2.2 World Meteorological Organization (WMO) Maps

In 1955, the World Meteorological Organization published the first maps showing world distribution of thunderstorm days. These maps were based upon data received from national meteorological services of most of the countries in the world. The Wetterdienst of the Federal Republic of Germany and the Meteorological Office of the United Kingdom supplied WMO with approximately six million marine observations of thunder and thunder plus lightning. These data formed the basis for their estimates of thunderstorm distribution at sea. Part I of their publication, WMO/OMN-21.pp.21, contains tables showing thunderstorm data over the land areas of the world. Part II of that publication contains tables for ocean areas and a series of maps showing monthly, seasonal, and annual distribution of thunderstorm days over the world. It was the seasonal maps from this publication that were used for the first noise calculations reported by Maxwell and Stone [1966].

The effort to develop an improved model for atmospheric noise predictions required better maps than those prepared by the WMO. Figure 2-1 is a copy of the original WMO map for January. It will be noted that there are several shaded areas, marked greater than some value, on this map. These represent areas, primarily maritime locations, where the data was so limited, and often conflicting, that accurate determination of thunderstorm days was very difficult. Acknowledging the shortcomings of the data, it was, nevertheless, considered imperative that some attempt at establishing contours for these areas was necessary for this effort. In addition to the shaded area problem, it was evident upon examining the monthly maps, that there was insufficient resolution of thunderstorm activity to accurately determine the energy radiated from all sections of the earth. For monthly

maps, increments of two thunderstorm days would be much better than the five thunderstorm day increments used by WMO. Preparation of improved thunderstorm lay maps is described in the following subsection.

2.3 Preparation of New Maps

2.3.1 Data Obtained

Our ultimate goal was to obtain all of the data possible with the time and funds available. This is perhaps an appropriate point to discuss the reason for using thunderstorm day data. Obviously it would be much better to have data on the occurrence of thunderstorms, i.e., we would prefer to know the number of thunderstorms occurring at a given location during a given month rather than the number of days on which one or more thunderstorms were observed. Or better yet, world-wide observations of lightning discharges would directly provide the information required for determining energy radiated from a given section of the earth. Thunderstorm day data is used because it is the only data which has been obtained for a long period of time at thousands of stations all over the world. Most meteorological observers record the observance of thunder and/or lightning. These observations may take place once an hour, once every three hours, once every six hours, or even at some locations, only once or twice a day, when the station is occupied for some specific reason. Most stations today take data once an hour, or at least once every three or four hours. They do not indicate how many thunderstorms have occurred during the period from one observation to the next. For the most part, they record whether thunder was heard within fifteen minutes or one hour prior to the specified observation time. Thus, it is impossible from this data to determine the number of thunderstorms. Furthermore, many countries do not publish the hourly or three-hour observations, but only monthly summaries, which usually indicate the number of days on which thunder was heard. This being the only data available globally, one has no choice but to use it and

learn how to relate it to lightning discharges and energy radiated. Inadequate as the data may seem, it has served admirably well, as will become evident later in this report.

The tables in the WMO report, Parts I and II, provided one of the major sources of thunderstorm data. A recently published supplement to the WMO report provided data for the Soviet Union which had not been available at the time of the original publications. The total data obtained from WMO publications came from approximately four-thousand meteorological stations and marine locations.

In addition to the WMO data we found more recent thunderstorm day data at the National Weather Records Center (NWRC) at Asheville, North Carolina. In particular, the U. S. Naval Weather Service World-Wide Air-field Summaries, Volumes I through X, contain data for approximately three thousand stations around the world. Table 2-1 is a copy for one station from Vol. IX, Part 2. The thunderstorm day data, underlined, was supplied for all stations, on computer tape, by the Naval Weather Service. The data was taken directly from the master tapes containing all of the data in the summaries. A small amount of data was obtained from copies of foreign publications, on file at NWRC. Additional marine data was obtained from documents compiled by the Naval Weather Service Command under NWRC job number 75001, October 26, 1967, under which data from ships at sea had been summarized for each 10° by 10° region of the world's oceans. All of the data obtained from NWRC was similar in kind and quality to that originally collected by WMO. The two sets of data are quite complementary since the WMO data was obtained prior to 1950, and most of the NWRC data represents observations made during and after World War II. The manner in which this data, from some seven thousand locations, was used in the preparation of new thunderstorm day maps will be described in the next subsection.

Table 2-1 Page from World-Wide Airfield Summaries. Volume IX

STA NO. 65201 (IN AREA NUMBER 02)		LAGOS API-KEJA. FEDERAL REPUBLIC OF NIGERIA												ELEVATION(FT) 00132		
		LATITUDE 0635N						LONGITUDE 00320E								
PARAMETER DESCRIPTION		JAN	FEB	MAR	APR	MAY	JUN	JUL	AUG	SEP	OCT	NOV	DEC	AMN	POR (YRS)	NO.
ABS MAX TMP (F)		95	96	99	99	104	93	93	96	94	96	99	99	104	32	-20
MEAN MAX TMP (F)		88	89	89	89	87	85	83	82	83	85	88	88	86	32	-28
MEAN MIN TMP (F)		74	77	78	77	76	74	74	73	74	74	75	75	75	32	-28
ABS MIN TMP (F)		63	66	60	69	62	69	68	66	68	69	69	66	60	32	-528
MEAN NO DYS TMP = OR GTR 90(F)		13.2	13.0	14.5	14.0	11.9	9.0	7.0	5.9	6.7	9.4	12.7	13.2	130.5	32	-29
MEAN NO DYS TMP = OR LES 32(F)		0.0	0.0	0.0	0.0	0.0	0.0	0.0	0.0	0.0	0.0	0.0	0.0	0.0	32	-29
MEAN NO DYS TMP = OR LES 0(F)		0.0	0.0	0.0	0.0	0.0	0.0	0.0	0.0	0.0	0.0	0.0	0.0	0.0	32	-29
MEAN DEW PT TMP (F)		75	74	77	75	75	75	73	72	73	74	76	76	75	0	-50
MEAN REL HUM (PCT)		83	81	80	81	85	88	88	86	88	88	85	83	85	10	-32
MEAN PRESS ALT (FT)		17	18	-20	-63	-63	-41	-46	-21	4	11	9	16	-14	0	-50
MEAN PRECIP (IN)		1.10	1.80	3.90	5.70	10.90	17.70	10.50	2.60	5.60	8.20	2.70	1.00	71.7	65	-6
MEAN SNOW FALL (IN)		0.0	0.0	0.0	0.0	0.0	0.0	0.0	0.0	0.0	0.0	0.0	0.0	0.0	32	-29
MEAN NO DYS PRCP = OR GTR 0.1 IN		2.5	4.0	7.2	8.8	10.4	16.3	13.5	4.9	9.1	12.1	4.9	2.3	96.0	65	-29
MEAN NO DYS SNFL = OR GTR 1.5 IN		0.0	0.0	0.0	0.0	0.0	0.0	0.0	0.0	0.0	0.0	0.0	0.0	0.0	32	-29
MEAN NO DYS W/OCUR VSBY LES 1/2 MI		2.0	9.0	13.0	16.0	18.0	16.0	6.0	2.0	9.0	19.0	15.0	4.0	129.0	5	-24
MEAN NO DYS TSFMS		0.1	0.1	0.0	0.3	1.1	0.5	0.8	0.7	0.3	0.3	0.0	0.0	0.4	2	12474
P FREQ WND SPD = OR GTR 17 KTS		0.1	0.0	0.0	0.0	0.5	0.0	0.1	0.0	0.0	0.1	0.0	0.0	0.1	2	12474
P FREQ WND SPD = OR GTR 28 KTS		48.1	46.3	22.4	16.1	25.4	43.6	46.7	38.2	44.0	30.3	22.1	21.7	33.7	2	12495
P FREQ LES 5000 FT A/D LES 5 MI																
P FREQ LES 1500 FT A/D LES 3 MI																
FOR 00-02 LST		12.9	24.1	8.6	3.4	3.3	16.0	11.9	7.0	8.4	10.9	5.6	2.2	9.5	2	1557
03-05 LST		26.9	35.6	6.5	0.0	2.2	21.8	11.8	15.2	13.9	16.7	11.9	8.6	14.3	2	1563
06-08 LST		60.2	65.5	11.8	2.3	8.6	26.1	21.1	30.6	38.0	28.6	23.8	35.5	29.3	2	1560
09-11 LST		53.8	48.3	8.6	8.0	3.2	23.7	26.9	27.6	30.0	45.7	31.7	43.0	29.2	2	1565
12-14 LST		40.7	20.7	6.5	0.0	2.2	19.2	21.0	12.9	18.9	17.2	11.1	20.9	15.9	2	1562
15-17 LST		26.9	13.8	4.3	2.3	3.3	13.5	15.7	7.0	18.0	11.4	4.0	1.1	10.1	2	1561
18-20 LST		23.7	14.9	3.2	1.1	1.1	12.2	12.9	4.3	11.1	8.6	10.3	0.0	8.6	2	1566
21-23 LST		9.7	23.0	6.5	6.9	4.3	3.8	6.5	3.8	7.8	7.0	7.1	2.2	7.4	2	1561
P FREQ LES 300 FT A/D LES 1 MI																
FOR 00-02 LST		3.2	3.4	0.0	0.0	0.0	0.0	0.0	0.0	0.0	0.0	0.0	0.0	0.6	2	1557
03-05 LST		3.2	10.3	1.1	0.0	1.1	0.0	0.5	2.7	1.1	0.0	0.0	1.1	1.8	2	1563
06-08 LST		4.3	27.6	2.2	0.0	2.2	0.7	1.6	3.2	1.1	0.5	0.8	14.0	4.9	2	1560
09-11 LST		0.0	9.2	1.1	0.0	0.0	3.2	1.1	0.0	0.0	1.6	0.0	0.0	1.4	2	1565
12-14 LST		1.1	4.6	0.0	0.0	0.0	1.3	0.0	0.5	0.0	0.5	0.0	3.3	0.9	2	1562
15-17 LST		0.0	5.7	0.0	0.0	0.0	0.0	0.0	0.0	0.0	0.0	0.0	0.0	0.5	2	1561
18-20 LST		0.0	4.6	0.0	0.0	0.0	1.9	0.5	0.0	0.0	0.0	1.6	0.0	0.7	2	1566
21-23 LST		0.0	4.6	0.0	1.1	1.1	0.0	0.5	0.0	0.0	0.5	0.0	0.0	0.7	2	1561

2.3.2 Methods Used to Prepare New Maps

The data obtained from world-wide airfield summaries, being on magnetic tape, was ready for use as it was received. All of the WMO data, however, was available only in printed form. The World Meteorological Organization had retained no copies of the data in any other format. This data was therefore manually punched onto computer cards. The accuracy of the card punching operation was checked by comparing annual values with summations of the monthly values. In this manner, we not only discovered our own errors in card punching, but discovered some errors in the original data. The new marine data obtained from NWRC required the most work to make it ready for use in the preparation of new maps. This data had been combined into records of the frequency of occurrence of thunderstorms during six hour time blocks, from which we computed the number of thunderstorm days based on statistical methods developed by Brooks and Carruthers [1953]. Data from 81 Russian-Chinese stations, obtained from microfilm records at NWRC (originally tabulated by the U.S. Air Force Air Weather Service), was also presented as frequency of occurrence of thunderstorms, not as thunderstorm days. See Table 5-1, Section 5.1, for a sample of this data. Conversion of the marine and Russian-Chinese data was accomplished as follows.

From Brooks and Carruthers [1953], two equations for conversion of frequency of occurrence data to thunderstorm day data are developed.

$$N_{TD} = 30 - 30 q \left(1 - \frac{PI}{D} \right)^{[(24/I)-1]} \quad (2-1)$$

and

$$N_{TD} = 30 - 30 [q_1(q_2 + a_1 p_1)(q_3 + a_2 p_2) \dots (q_n + a_{n-1} p_{n-1})] \quad (2-2)$$

where

- N_{TD} is the number of thunderstorm days/month,
 I is the interval between observations in hours,
 D is the duration of the thunderstorms in hours,
 p is the probability of occurrence, and
 q is the probability of non-occurrence.

Equation (2-1) is valid for data not having a diurnal variation. This equation was erroneously used by WMO in their analysis of marine data, on the assumption that storms at sea are equally probable any hour of the day. This is a widely held misconception which will be disproved later in this report. Fortunately, there were seven Russian stations for which thunderstorm day data was available from a separate publication, in addition to the frequency of occurrence data being analyzed. Trial computations were run using both equations for these seven Russian observations.

Data on the duration of thunderstorms, based on the period of time that thunder could be heard or lightning seen, was obtained from Aiya and Sonde [1963]. They report a mean duration during which thunder can be heard of 78 minutes and a mean duration during which lightning can be seen of 207 minutes. Since land stations report thunder heard, values between 1 and 2 were used for D . The computations for the seven Russian stations showed the best agreement with measured values of N_{TD} , with $I = 6$ and $D = 1.25$. $I = 6$ was consistent with the reported six-hour observations.

We were also able to obtain comparisons between reported thunderstorm days and calculations of N_{TD} for the marine data. This was done by using marine frequency of occurrence data from the Great Lakes and

comparing calculated N_{TD} values with reported N_{TD} values from land stations around the lakes. Procedures aboard ships normally call for meteorological observations on three- to six-hour intervals. Calculations were made, therefore, using values of 3 and 6 for I. Since marine observations include, and the data did not discriminate between, thunder heard and lightning seen, values from 1 to 3 were used for D. The results indicated I = 6 and D values from 1.5 to 2 are best for marine data.

Equation (2-2) generally produced smaller differences between N_{TD} values computed from frequency of occurrence data and N_{TD} values obtained directly from observations. For the final analysis of the NWRC marine data, equation (2-2) was used with I = 6 and D = 2. The Russian-Chinese data was analyzed using the same equation with I = 6 and D = 1.25.

In the final analysis, a good deal of effort was required to make effective use of the marine data and the Russian-Chinese data. The effort was worthwhile, however, since adequate marine data was very limited and the Russian data obtained from WMO did not include the far eastern reaches of Russia, Manchuria, Mongolia, and China. The importance of this data became very evident when the new thunderstorm day maps were finally prepared, and it was determined that considerably more thunderstorm activity occurs in China, Mongolia, and Manchuria than was indicated on the WMO maps. The additional marine data undoubtedly resulted in more accurate estimates of thunderstorm activities at sea, although no comparison is available.

On the completion of this analysis we had data from some seven thousand locations ready for computer analysis. The distribution of this data over the surface of the earth was of course highly irregular. As many as sixty-five meteorological stations are located within a 2° Longitude by 2° Latitude square in Europe. This is in contrast with some regions in South America and Asia where there may be no stations in a 5° square region.

Except for the oceans, the region with the least meteorological data is South America.

The analysis of this data was accomplished at the IBM Data Processing Division in Denver, using their 1130 Numerical Surface Techniques and Contour Map Plotting Program. The characteristics of this program are described by Batcha and Reese [1964]. This program takes irregularly distributed data and computes values at the mesh points of a regularly spaced grid. After a mesh point determination has been carried out, smooth contours are computed and drawn. The data are smoothed by several processes described in the above-referenced paper. This was particularly valuable on this task, since the quality of some of the data included was questionable.

Because of the poor quality of some of the data, particularly ocean data, and the lack of data in certain regions, such as South America, the output of the computer contouring program was not directly usable. The computer contour maps were placed underneath a world map upon which the contours from the WMO maps had been lightly drawn. These two sets of contours, plus continuous reference to many sources of climatological data and some papers containing thunderstorm day contours for specific countries, were used in the manual preparation of the final maps. In North America, Europe, and Africa, where data in greater quantity and of better quality existed, the computer drawn contours were followed exactly with no manual modification. For most of the other regions of the world a certain amount of modification and interpretation of the computer drawn contours was required.

2.3.3 The New Maps

Only monthly maps were prepared under this contract since the use of seasonal maps for the computation of expected values is relatively inaccurate. Contour intervals of two thunderstorm days were used to obtain improved accuracy for calculating noise field intensities. The contours were drawn on an 18 x 24 inch cylindrical projection of the world.

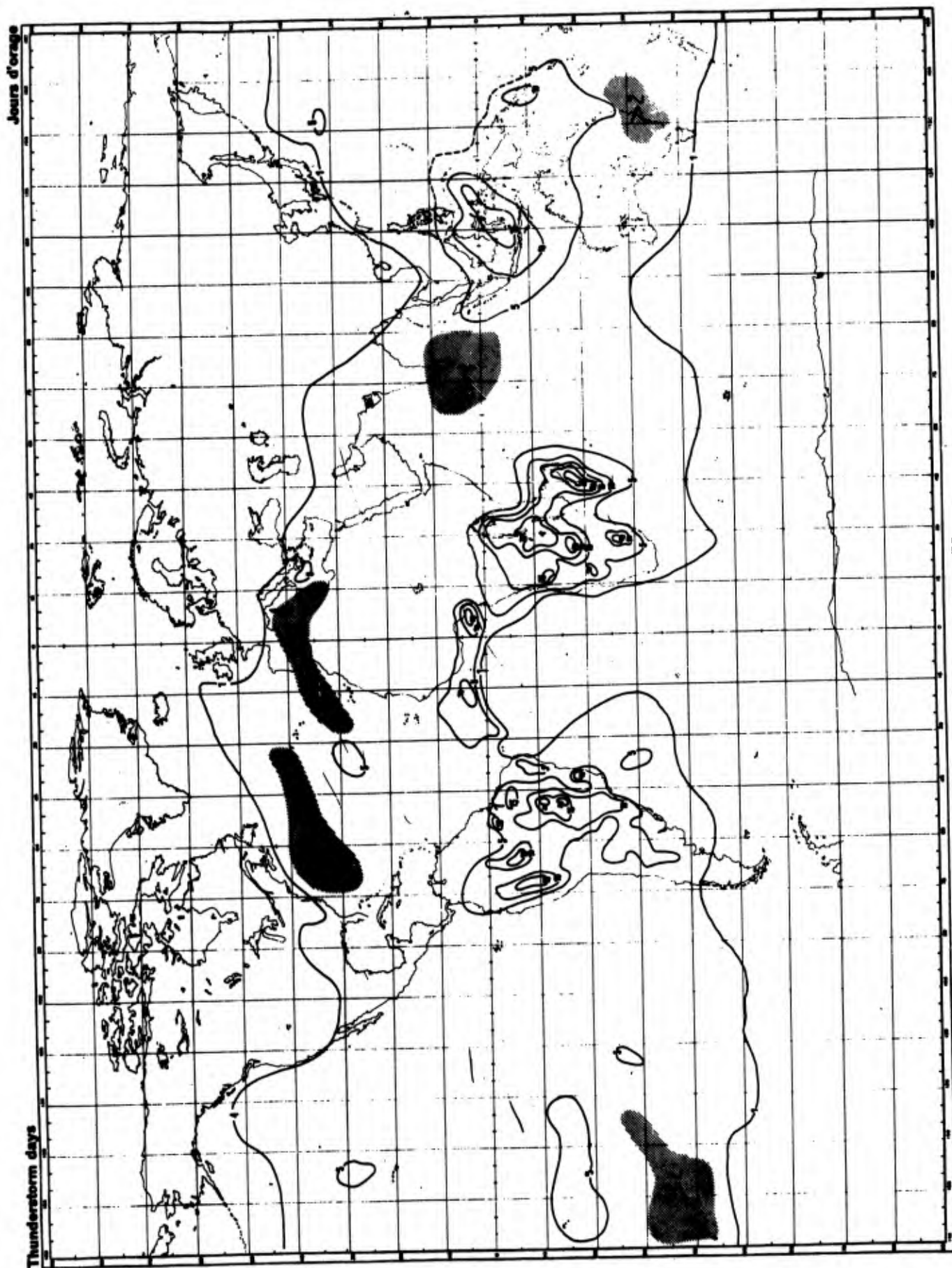
Figures 2-1 and 2-2 are reproductions of the WMO thunderstorm day maps for January and July. Figures 2-3 through 2-6 are reproductions of the maps prepared under this contract for January, April, July, and October. These are the middle months of the three seasons and adequately represent the change in thunderstorm activity from one season to the next. We will refer to the maps prepared under this contract as the WGL (Westinghouse Georesearch Laboratory) maps.

A comparison of the WMO and WGL maps for January and July shows generally good agreement, particularly in the United States and Europe. For South America and Asia, many significant differences will be noted. In particular for the month of July, quite high thunderstorm activity is indicated for China, Manchuria, and Mongolia. This is, of course, supported by the new data obtained under this contract, and is further supported by climatological information which shows monsoon type winds moving into those areas during the month of July. The validity of these maps is also supported in the final analysis by the comparison of predicted and measured field intensities at Ohira, Japan, as is further discussed in Section 6.4. It can be seen that the WGL contours for ocean areas are in general agreement with the WMO shaded areas. The accuracy in computing energy radiated is greatly enhanced by the use of contours on the WGL maps. The reliability of these contours in the ocean areas is of course much less than the contours drawn over land regions where continuous meteorological records have been obtained for many decades. The greater resolution of the WGL maps is evident and was also important.

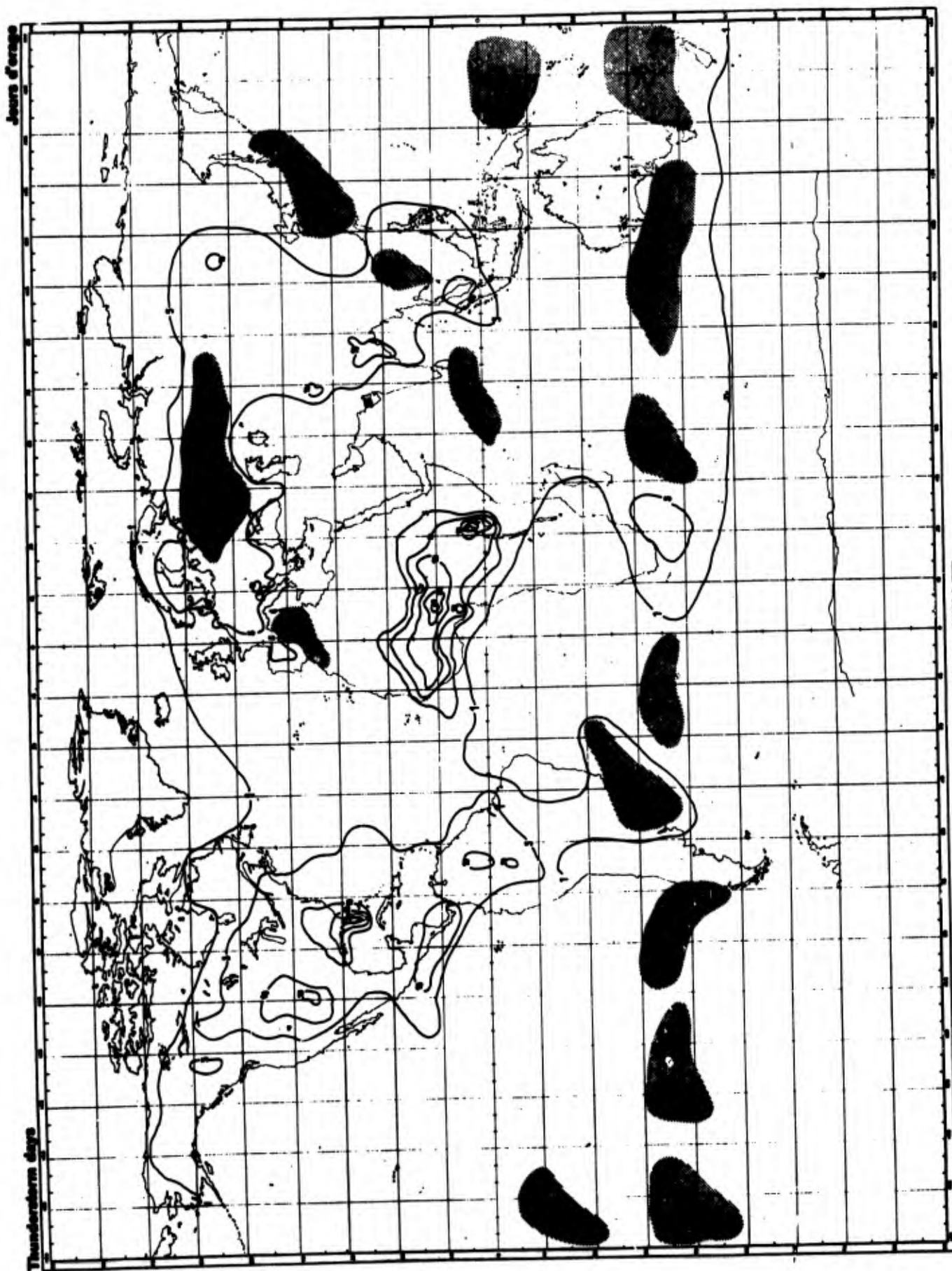
If time and funds had permitted, we would like to have shown copies of the many climatological charts which were used on this job, as well as copies of the thunderstorm day maps obtained from individual countries. The references for this report contain a list of the more significant material used on this project.

2.4 Using the New Maps

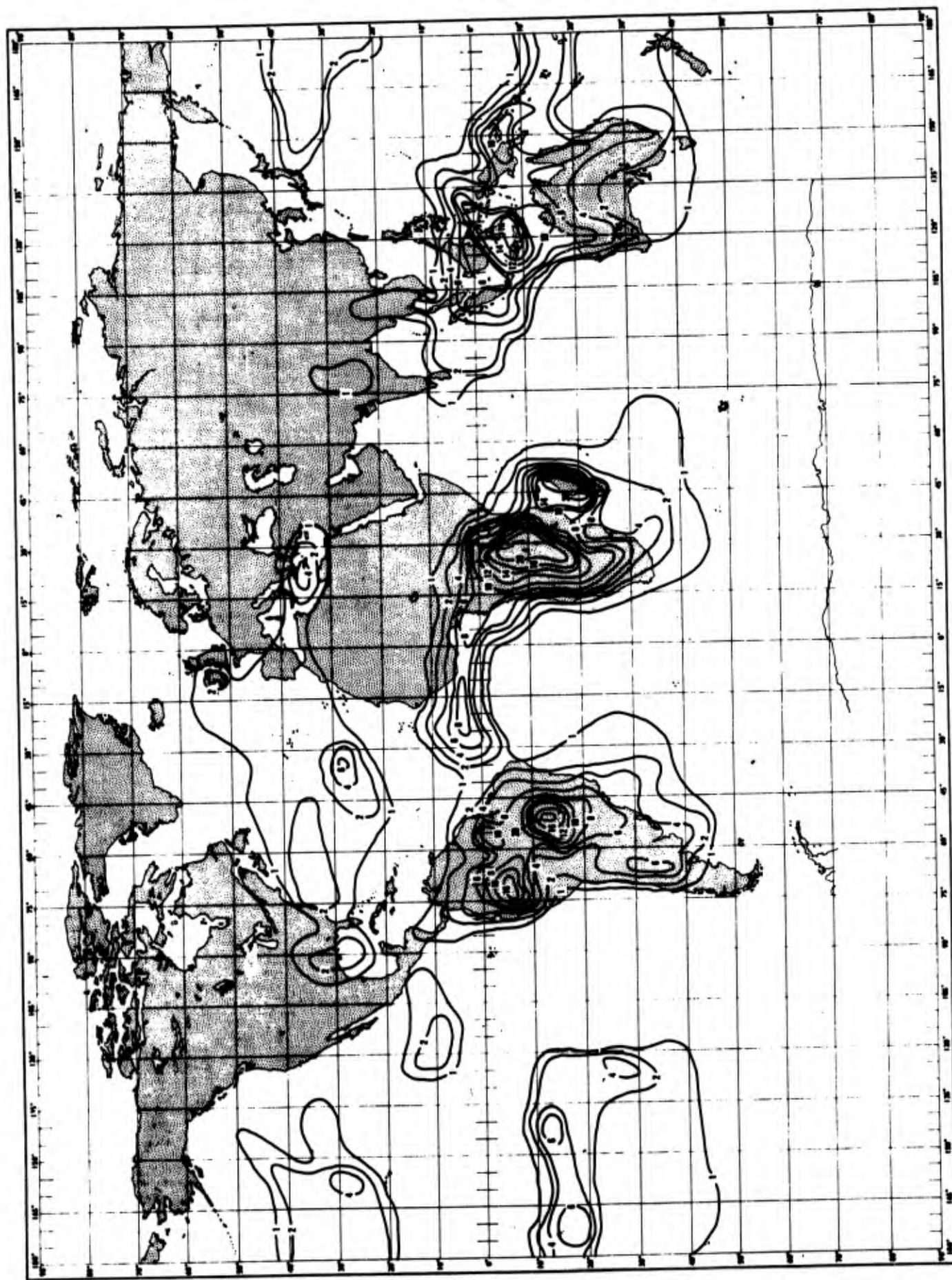
First, the new maps, i.e., the contours, were digitized. The digitized contours were then fed into a computer program (THUNCON) which is described by Stone [1970]. THUNCON computed for each 5° by 5° section of the earth's surface, the area and the centroid of the area enclosed by each contour. The output of the THUNCON was in turn fed into another computer program called SUMAN which performed the first steps in converting the digitized thunderstorm day maps into electromagnetic energy radiated per square kilometer. More details on these procedures are included in the next section.



JANUARY / JANVIER
Figure 2-1 Copy of WMO Map



JULY / JUILLET
Figure 2-2 Copy of WMO Map



January

(Prepared by Westinghouse Georesearch Laboratory)

Thunderstorm Days

Figure 2-3

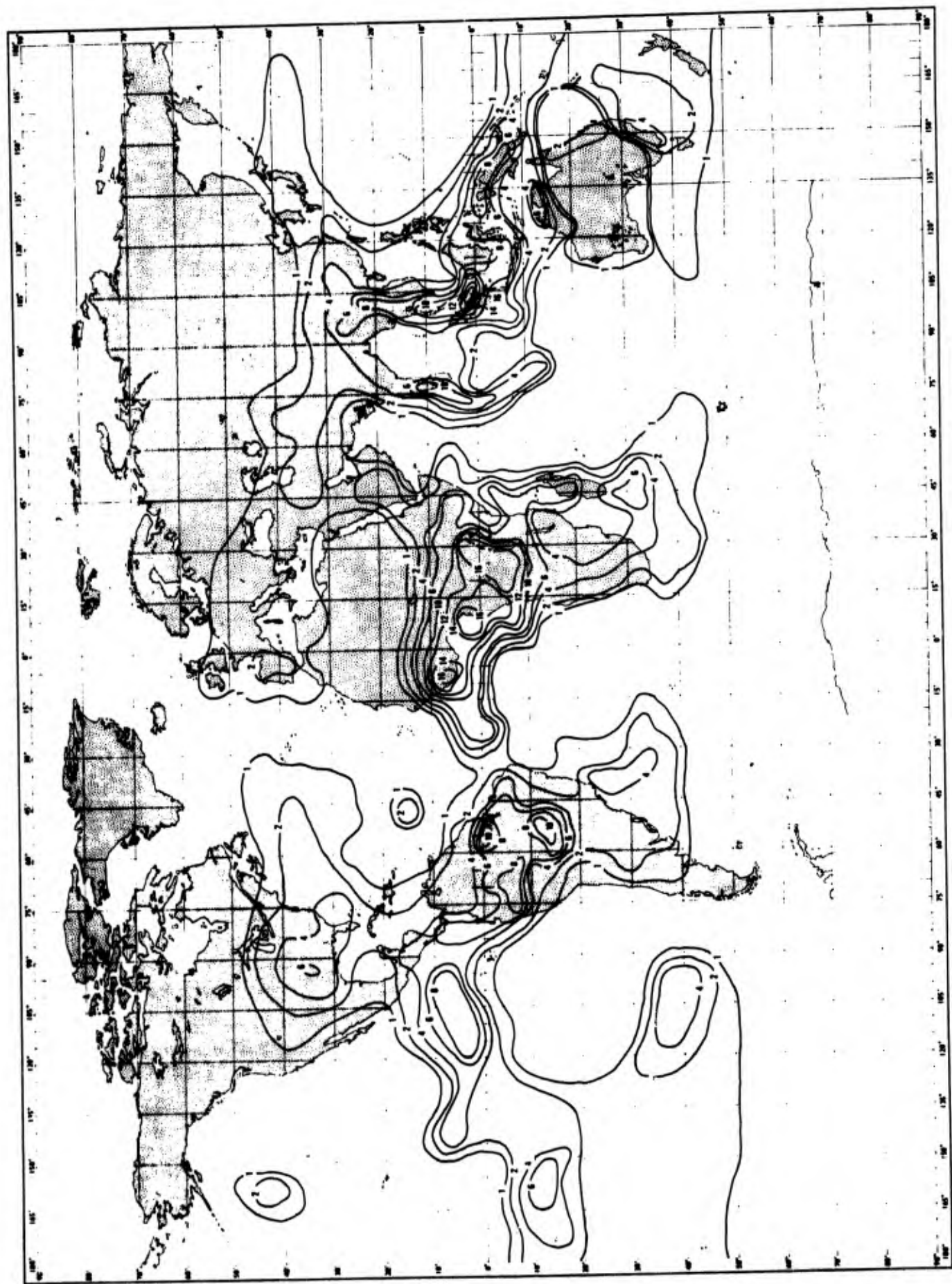
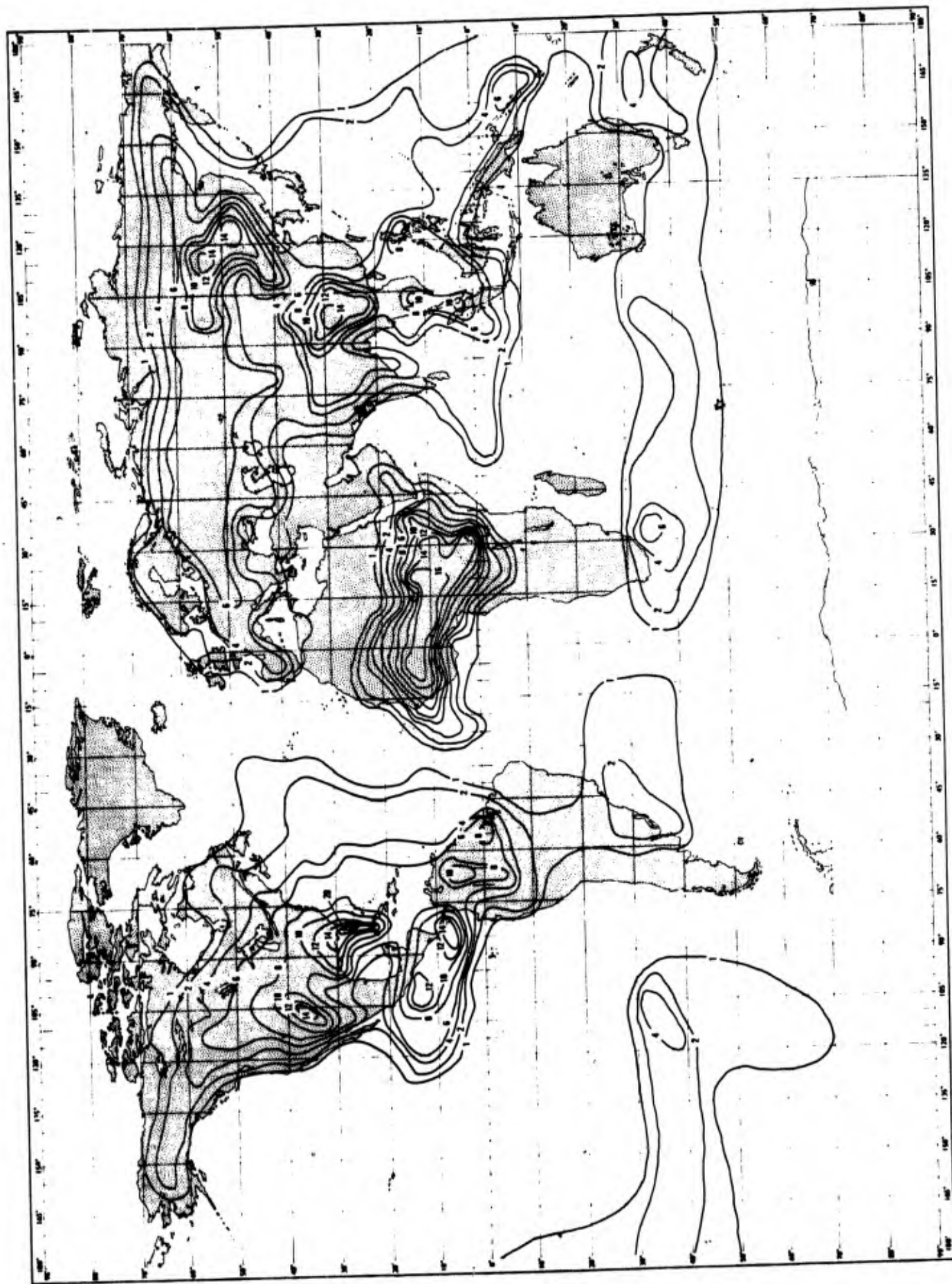


Figure 2-4 Thunderstorm Days (Prepared by Westinghouse Georesearch Laboratory) April



July

Figure 2-5 Thunderstorm Days (Prepared by Westinghouse Georesearch Laboratory)

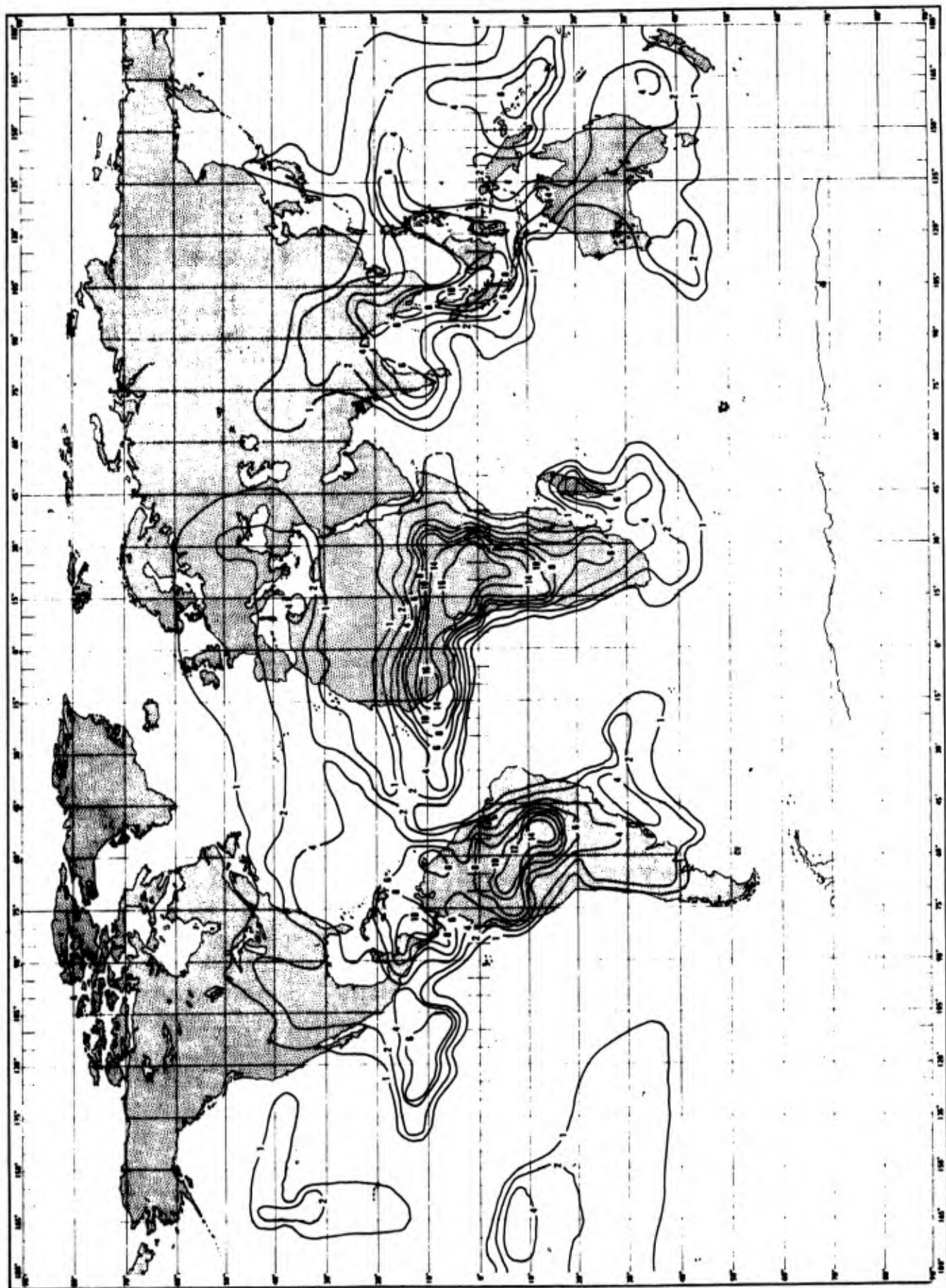


Figure 2-6 Thunderstorm Days (Prepared by Westinghouse Georesearch Laboratory) October

3.0 ELECTROMAGNETIC ENERGY RADIATED PER SQUARE KILOMETER

The transformation of thunderstorm day data to thunderstorm density or number of lightning discharges is not a simple matter. For instance, no differentiation is made between a day on which thunder is heard once and a day on which thunder is heard continuously. Also the severity of thunderstorms can be quite variable from one location to another and from one season to another. The characteristics of the lightning discharges produced by the thunderstorms are also variable and add a third complexity to the problem. This section describes the development of an algorithm for computing power radiated per square kilometer from thunderstorm and lightning data.

3.1 Converting Thunderstorm Days to Lightning Discharges Per Square Kilometer

There are three main types of lightning discharges. The cloud-to-ground discharge results when the potential between the electric charges in the cloud and the earth become sufficient to cause a breakdown or ionization of the air between the cloud and the earth. This normally occurs between the lower negative charge center and the ground. The intra-cloud discharge is a discharge or transfer of charge between the positive and negative charge centers of a single thunderstorm cell. Intra-cloud discharges are by far the most frequent of all. Cloud-to-cloud discharges are relatively rare and could be defined as the transfer of charge between different thunderstorm cells of a complex storm system or the transfer of charge between thunderstorm cells of distinctly separate clouds. Because of the very different characteristics of the individual events which make up an entire lightning discharge the energy radiated by the three discharge types are different in amplitude, detailed structure, and total energy radiated. In addition to determining the total number of lightning discharges per

square kilometer at any location it is important that we know the percentage of the total which are cloud-to-ground, intra-cloud, and cloud-to-cloud. these will be determined in the following subsections.

3.1.1 Lightning Counters

Only during the past decade has there been accurate data collected relative to the frequency of occurrence of lightning discharges. This data has been obtained from lightning counters. A lightning counter is basically a device which is triggered when the electric field, due to a lightning discharge, exceeds a preset threshold. Each time the counter is triggered it actuates some sort of totalizing device. There are many kinds of lightning flash counters, but two in most common usage are the CCIR and ERA. The CCIR counter was developed by the Consultative Committee for International Radio (CCIR) from an original design by Sullivan and Wells [1957]. The CCIR counter is a wideband device covering almost the entire VLF frequency range.

The ERA counter was originally developed commercially by the British Electrical Research Association (ERA). The frequency coverage of this device is about 200 Hz to 2 kHz. This counter is intended to trigger more readily from cloud-to-ground discharges. The discrimination against intra-cloud discharges occurs primarily because of its frequency pass band. The electric fields produced by cloud-to-ground discharges have large components in the 200 to 2 kHz range whereas intra-cloud discharges produce very little energy in this frequency range. The CCIR counter is not nearly so effective in discriminating against intra-cloud discharges. One of the best and most comprehensive discussions of lightning flash counters is given by E. T. Pierce [1968]. Pierce has summarized the results of many workers in this field and much of the following information was obtained from his report (ibid).

3.1.2 Lightning Counter Data

There are two primary difficulties associated with the use of lightning counter data. They are: (1) Uncertainty relative to the effective range over which the counter records lightning flashes, and (2) Uncertainty relative to the percentage of the counts which are cloud-to-ground discharges and the percentage which are intra-cloud discharges. The effective range of the ERA counter can be estimated relatively accurately because of its low frequency pass band. At its center frequency of 600 Hz the electric fields within its range are effectively electrostatic fields, which fall off in amplitude inversely with distance cubed. Even with the uncertainties associated with the calculations of the field intensity of lightning discharges in this frequency range, most estimates of the effective range of an ERA counter operating with a threshold of 5 volts per meter fall within 10 to 40 kilometers. After reviewing all of the information available, we selected an effective range of 20 kilometers for the ERA counter.

Because of the higher frequency response of the CCIR counter, the fields within its range of operation are radiation fields whose amplitudes will decrease inversely with distance. The wide pass band of the CCIR counter further complicates any attempt to estimate its range since the fields produced by lightning discharges over its 1.5 to 40 kHz 6 dB pass band are extremely variable. With the CCIR counter set with a threshold of 3 volts, estimates of range vary from 16 to 110 kilometers, Pierce [1968]. We have selected an effective range of 40 kilometers for the work reported herein.

For the effective ranges selected, the number of counts recorded should be equivalent to the total number of discharges, of all three types, which occur within these distances, from the counters. Considering the wide range of estimates from the workers in this field, uncertainties relative to the actual operational conditions for some of the data, and considering the problems associated with any attempt at a theoretical analysis

of the operation of the counters, we can justify the ranges which we selected primarily by the consistent results we have obtained from our analysis of a wide variety of lightning counter data.

The data which we obtained for use on this project came from the locations indicated on Figure 3-1. Most of the data was unpublished and was supplied through the courtesy of many people whose assistance is recognized in the Acknowledgment Section of this report. ERA and CCIR counters are about equally represented among these locations. Some of the data was available only as monthly total counts, much of it was available on the basis of hourly counts and we obtained data from Darwin, Australia from readings taken every five minutes. Most of the data had been obtained over three to ten year periods.

Assuming the 20 and 40 kilometer ranges mentioned above, the data was normalized to obtain lightning counts per square kilometer per month. The normalized data was plotted relative to thunderstorm days per month as shown in Figure 3-2. The thunderstorm day data for Uganda, Kenya, Singapore, and Australia were obtained from individual records for the specific months during which the lightning counters were in operation. The thunderstorm day data for Boulder, Colorado, Slough, England, Denmark, and Singapore are mean values obtained from tables and maps for these regions.

A careful examination of Figure 3-2 shows no tendency for CCIR or ERA data to be consistently higher or lower than the other. This would tend to indicate that the ranges selected for these two instruments are reasonable.

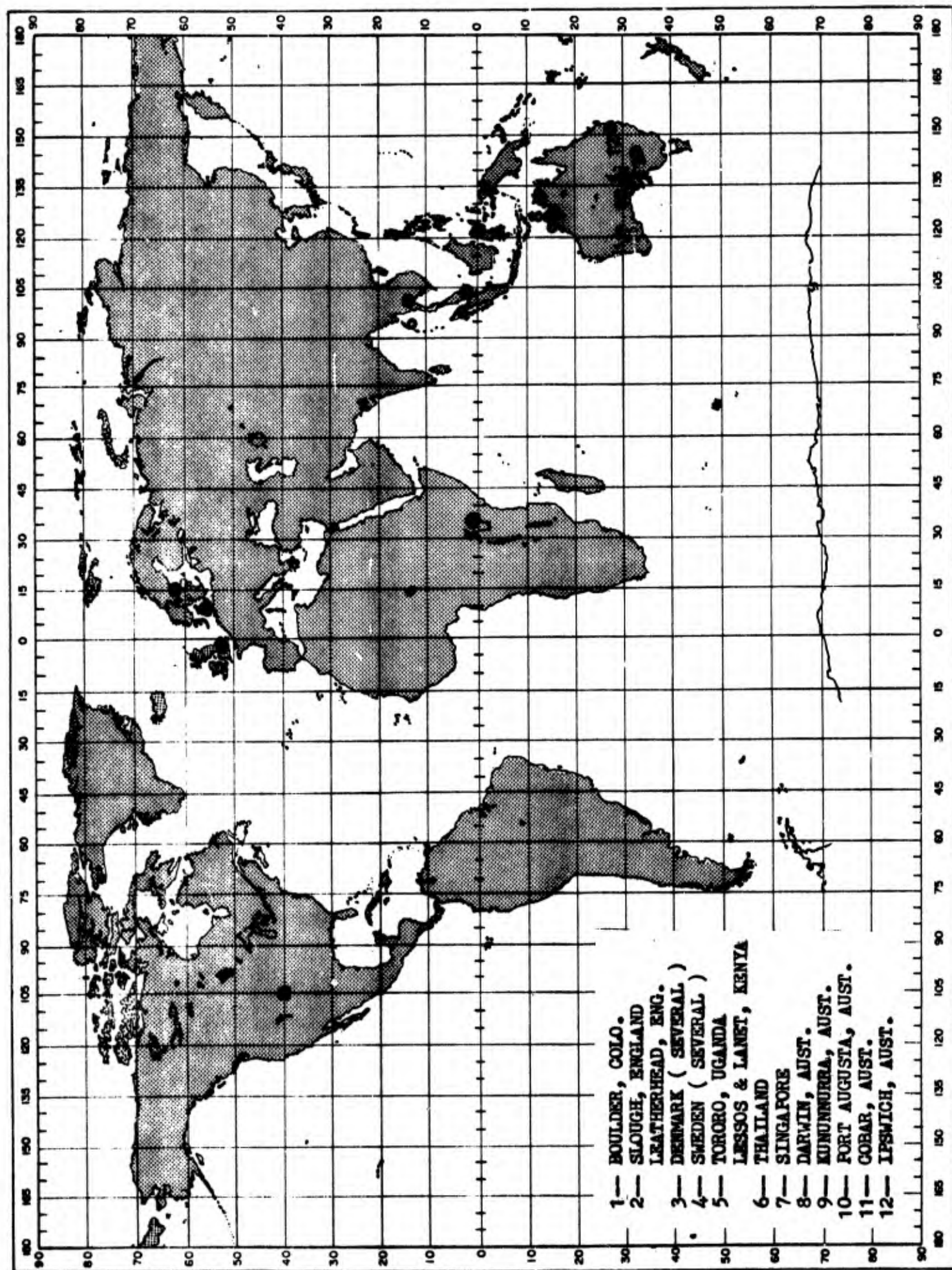


Figure 3-1 Location of Lightning Counters

A number of researchers have attempted to establish a relationship between lightning discharges per unit area and thunderstorm days. Muller-Hillebrand [1963] reported that data obtained in Sweden and Switzerland indicated the number of cloud-to-ground discharges, per unit area increased as the square of thunderstorm days. Horner [1967] analyzed data from Slough, England and Singapore. His results showed a linear relationship for England and a square relationship for Singapore. Similar results were obtained by Pierce [1968] who showed that data for Bangkok may be roughly expressed by two straight lines which have the equations

$$D_m = 2 N_{TD} \quad \text{for } N_{TD} \leq 3 \quad (3-1)$$

$$D_m = (2/3) N_{TD}^2 \quad \text{for } N_{TD} > 3 \quad (3-2)$$

Where: D_m is mean daily count per month for a CCIR counter and

N_{TD} is thunderstorm days per month.

It would not be difficult, however, to fit Pierce's data to a single line having an intermediate slope. Prentice and Robson [1968] present the work of other researchers whose results vary from a linear to a square law relationship. An average of the results presented by Prentice and Robson agrees well with the results shown on Figure 3-2. Most researchers reporting on this relationship have had data obtained over just a few years from only one or two locations. The disagreement among their results is therefore not surprising.

The equations for both of the lines shown on Figure 3-2 were used in the initial experimental noise calculations. Ultimately the equation

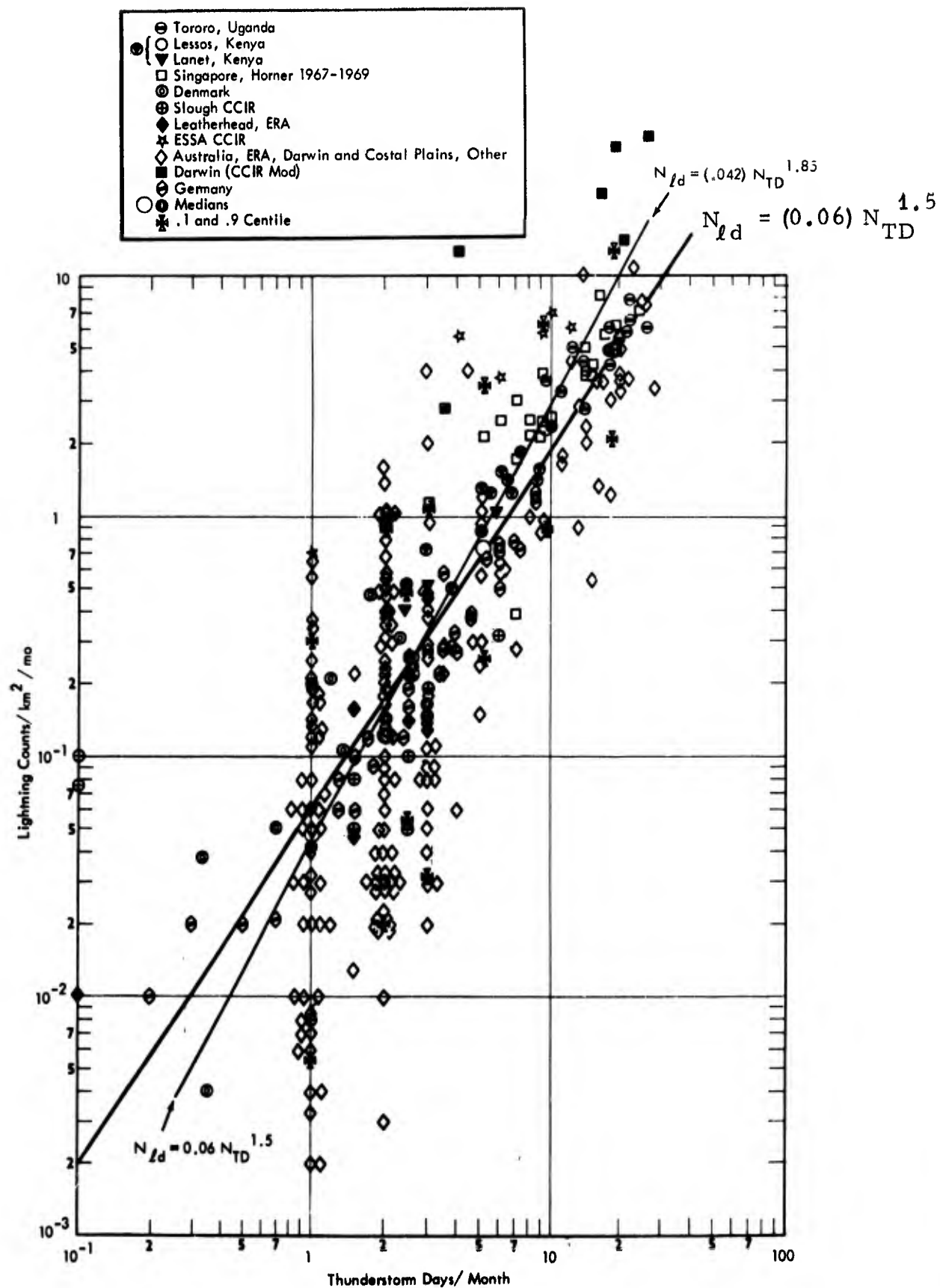


Figure 3-2 Relationship Between Thunderstorm Days and Lightning Discharges

$$N_{ld} = 0.06 N_{TD}^{1.5} \quad (3-3)$$

where N_{ld} = lightning discharges/km²/month

N_{TD} = thunderstorm days/month

yielded the most accurate calculations of atmospheric noise.

We next needed to determine the percentage of these discharges which were cloud-to-ground discharges.

3.1.3 Ratio of Cloud-to-Ground and Intra-Cloud Discharges

Cloud-to-cloud discharges are so infrequent that they are unimportant in a determination of total energy radiated per square kilometer. We will, therefore, concern ourselves only with cloud-to-ground and intra-cloud discharges in the following discussion. The percentage of all discharges which are cloud-to-ground have been estimated by a number of researchers from visual observations. There are no accurate measurements available. Pierce [1968] reports on the results of several estimates at different latitudes and suggests the equation

$$P = 0.1 \left[1 + \left(\frac{\phi}{30} \right)^2 \right] \quad (3-4)$$

where P is the proportion of flashes to ground and
 ϕ is latitude in degrees.

This agrees well with the general relationship reported by many that the percentage of ground discharges increases with increasing latitude. It is recognized, however, that the percentage of flashes to ground is dependent on factors other than latitude.

For instance, cloud-to-ground flashes are more common over mountainous areas than the low lands. It has also been noted that

very severe storms, particularly hail storms and tornados, produce relatively few flashes to ground. Those regions on the earth where terrain would have a marked effect upon the percentage of flashes to ground are relatively few and therefore, no attempt was made to include the terrain effect in our calculations. The effect of storm severity can be included, however, since the more severe storms tend to occur most frequently at locations having high number of thunderstorm days per month. Figure 3-3 presents visual estimates for several locations grouped according to those stations that lie between 0 and 20° latitude, 20° to 40° latitude, and 40° to 60° latitude. The plotting of the data points relative to thunderstorm days per month is an estimate in itself based upon thunderstorm day maps since most of the sources of information did not report actual thunderstorm days per month for the time that they made their estimate of the percentages of ground and cloud flashes. We cannot, therefore, make a strong argument about any agreement between the data and the empirical equation which we derived,

$$P = 0.05 + \frac{\sin \phi + 0.05}{(N_{TD} + 3)^{1/2}} \quad (3-5)$$

There is, however, reasonable justification for expecting the proportion of cloud-to-ground discharges to be related to both latitude and the number of thunderstorm days.

Figure 3-4 shows the average worldwide median height of the 0°C isotherm, as a function of latitude, during December, January and February. Since the charge separation in a thunderstorm occurs around the freezing level the height of the charge centers will be a function of freezing level and therefore, latitude. The higher the charge centers, the lower is the probability that a discharge to ground will occur. Similarly, it is well known that the more severe storms reach to greater altitudes, also indicating higher

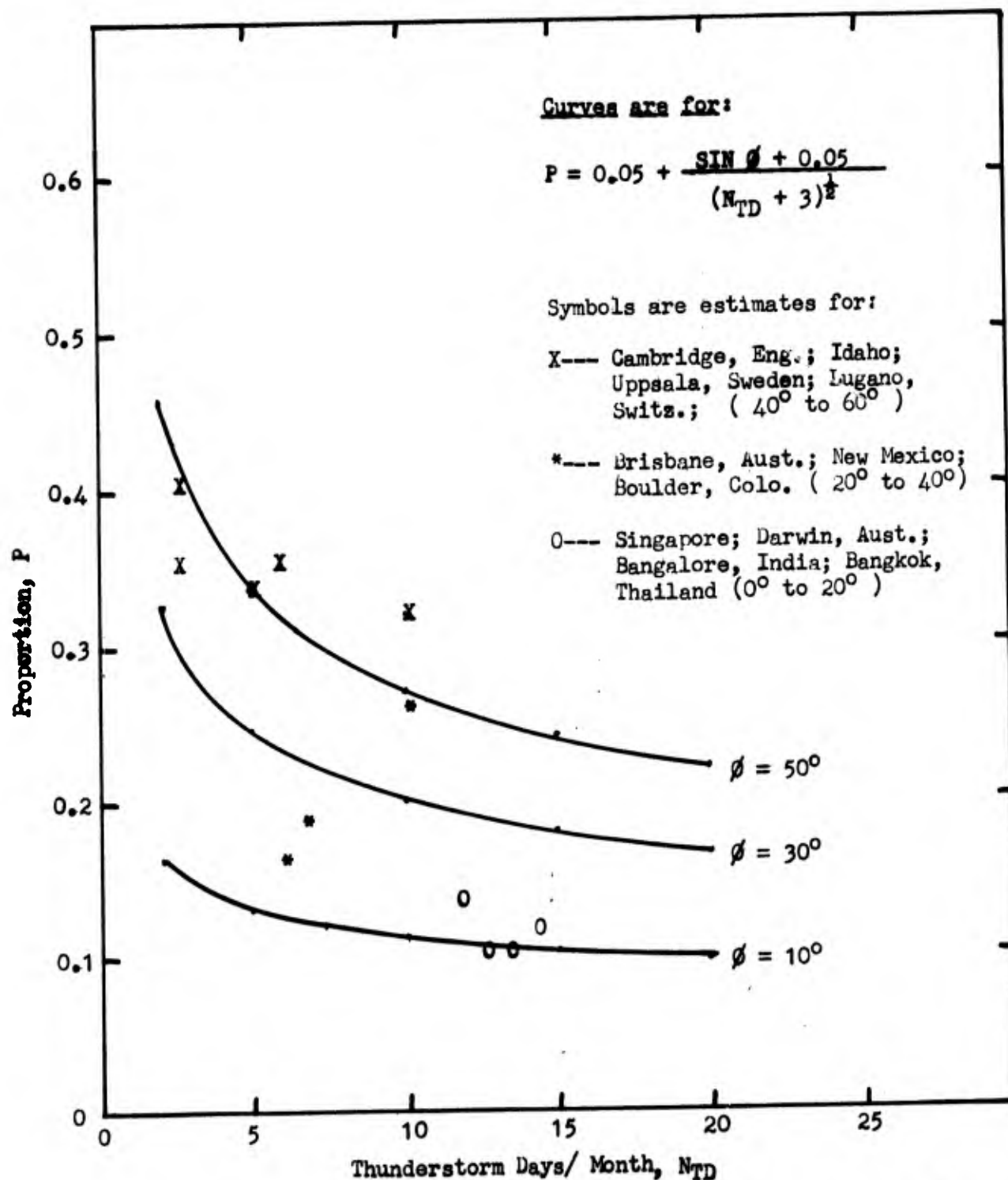


Figure 3-3 Proportion of Lightning Discharges which are Cloud-to-Ground

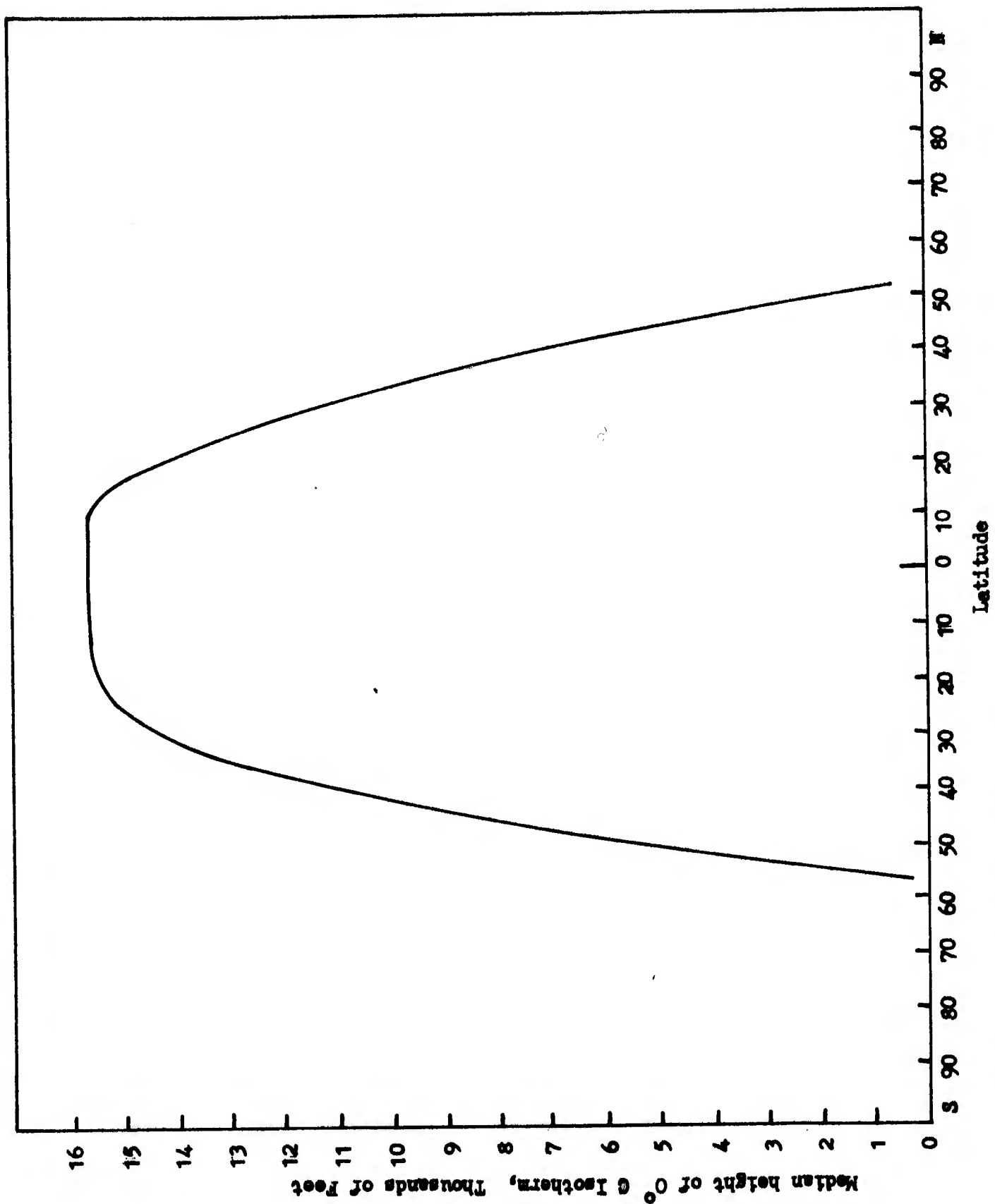


Figure 3-4 Freezing level vs Latitude during Dec-Jan-Feb

charge centers and lower probability of cloud-to-ground discharges. Byers [1953] notes that thunderstorms without ground strokes have negative and positive charge centers in close proximity. This distribution of charge centers is reported as being typical for hail storms. Byers also notes that a number of workers have reported almost continuous lightning in hail storms with virtually none of it reaching the ground.

Although equation (3-5) is simply an attempt to empirically fit poor data, we believe it is important to recognize the need for a model whereby the proportion of cloud-to-ground discharges is varied as a function of latitude and storm characteristics. This equation was used in the final noise calculation program.

The principle sources of information on the proportion of cloud-to-ground discharges are: Muller-Hillebrand [1963 b], Mackerras [1963], Prentice and Robson [1968], Lang [1963], Fuquay [1962], Aiya and Sonde [1963], Brook and Kitagawa [1960], and Pierce [1968].

3.2 Energy Radiated Per Discharge

Having established relationships between thunderstorm days and the number of cloud-to-ground and intra-cloud discharges per square kilometer, we must now examine these discharges in sufficient detail to establish the electromagnetic energy radiated therefrom. We will begin with a detailed description of the lightning discharges.

3.2.1 Cloud-to-Ground Discharges

Breakdown Phase

A typical cloud-to-ground discharge can be considered as having at least six different phases, with several repetitions of the last three phases. In Figure 3-5 the initial breakdown phase (a) is caused when the potential exceeds the breakdown threshold of air, which is in the order of 10^6 volts per meter for air with moisture droplets. Small streamers start the



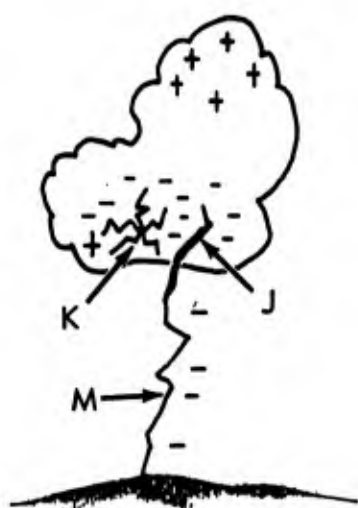
(a) Initial Break Down



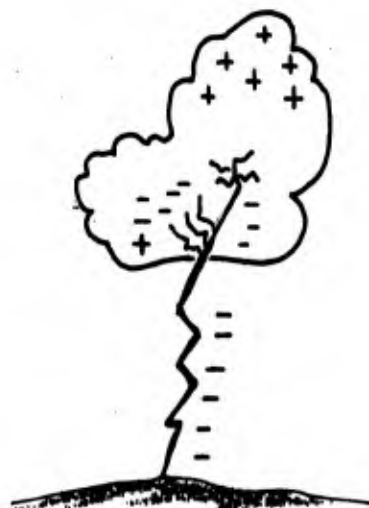
(b) Stepped Leader



(c) Main Return Stroke



(d) Streamer and Junction J, K, and M Changes



(e) Dart Leader



(c₂) Second Return Stroke

Figure 3-5 Phases of a Typical Cloud to Ground Discharge Process .

charge transfer process within the cloud; this usually occurs between the main negative charge center and a low lying positive charge center. The first part of this initial breakdown phase occurs in 2 to 10 milliseconds and results in an effective lowering of negative charge to neutralize the small positive charge center. Clarence and Malan [1957] show that the breakdown phase usually consists of two stages where the initial charge neutralization stage is followed by an intermediate "I" stage lasting from 0 to 400 milliseconds, during which small rapid electric field changes are observed near the storm cloud.

Observations of the breakdown phase usually show a number of small rapid pulses [Malan, 1963]. The fields are produced by an equivalent upward flow of current from the small positive charge center near the base of the cloud to the main negative charge center. The length involved is in the order of 1 to 3 km. In order to correspond to the total charge transfer indicated by electrostatic field changes as well as to the radiated fields observed by Taylor, the currents involved must be in the order of 1000 amperes during the peak flow of current and dropping down to the order of 100 amperes. The peak moment shown is 1.5×10^6 ampere-meters and the peak moment differential is in the order of 1.5×10^{11} ampere meters per second. This corresponds to a radiated electric field normalized to 1 km of 30 volts per meter*. When the moment decay curve is appreciably longer than the build up time, the differential results in appreciably greater positive amplitudes than negative amplitudes. Not many details are available relative to the velocity of propagation of streamer or leaders within the cloud. It is believed, however, that velocities within the cloud may be in the order of 5×10^7 meters per second. If this is the case, we would expect a rise time of 20 μ sec for a path length of 1 kilometer. This appears to be in agreement with the waveforms of radiated fields observed by Taylor.

* See Appendix A.

Stepped Leader Phase

The stepped leader phase shown in Figure 3-5(b) is estimated to have currents reaching values as high as several kiloamps and having a low continuing value in the order of several hundred amperes. It is important to note that observations by Norinder [1954] as well as others, indicate that the current moment pulses last for periods in the order of 20 microseconds. It is believed to have a weakly ionized, slowly moving, pilot streamer which advances away from the charge center in spurts 10 to 100 meters long with spurt velocities of about 5×10^5 meters per second. This process repeats until the leader reaches the ground. If we assume the currents as being near 2000 amperes and an effective length of 200 meters, the current moment reaches levels of 4×10^5 ampere-meters. The moment differential reaches a value in the order of 2×10^{11} amp-meters/sec. This corresponds to a peak radiated electric field of 40 V/m when normalized to 1 km.

Main Return Stroke Phase

Once the step leader reaches the ground, a very large amplitude current starts to flow and the main return stroke is initiated which travels upward with an initial velocity in the order of 8×10^7 meters/second. Current wave form versus time is shown in Figure 3-6 for a series of return strokes. Several important facts can be observed. (1) The peak currents are in the order of tens of thousands of amperes and they are separated by intervals in the order of 40 milliseconds. Between the current peaks, there is a continuous flow of current amounting to several hundreds of amperes. This type of discharge which has been called the "long" discharge contains several multiple current peaks, i.e. strokes, each lasting about 100 μ sec. The peak current tends to decrease with the increasing number of strokes. Some discharges called "short" discharges have only a single stroke and the current flow may stop after a few

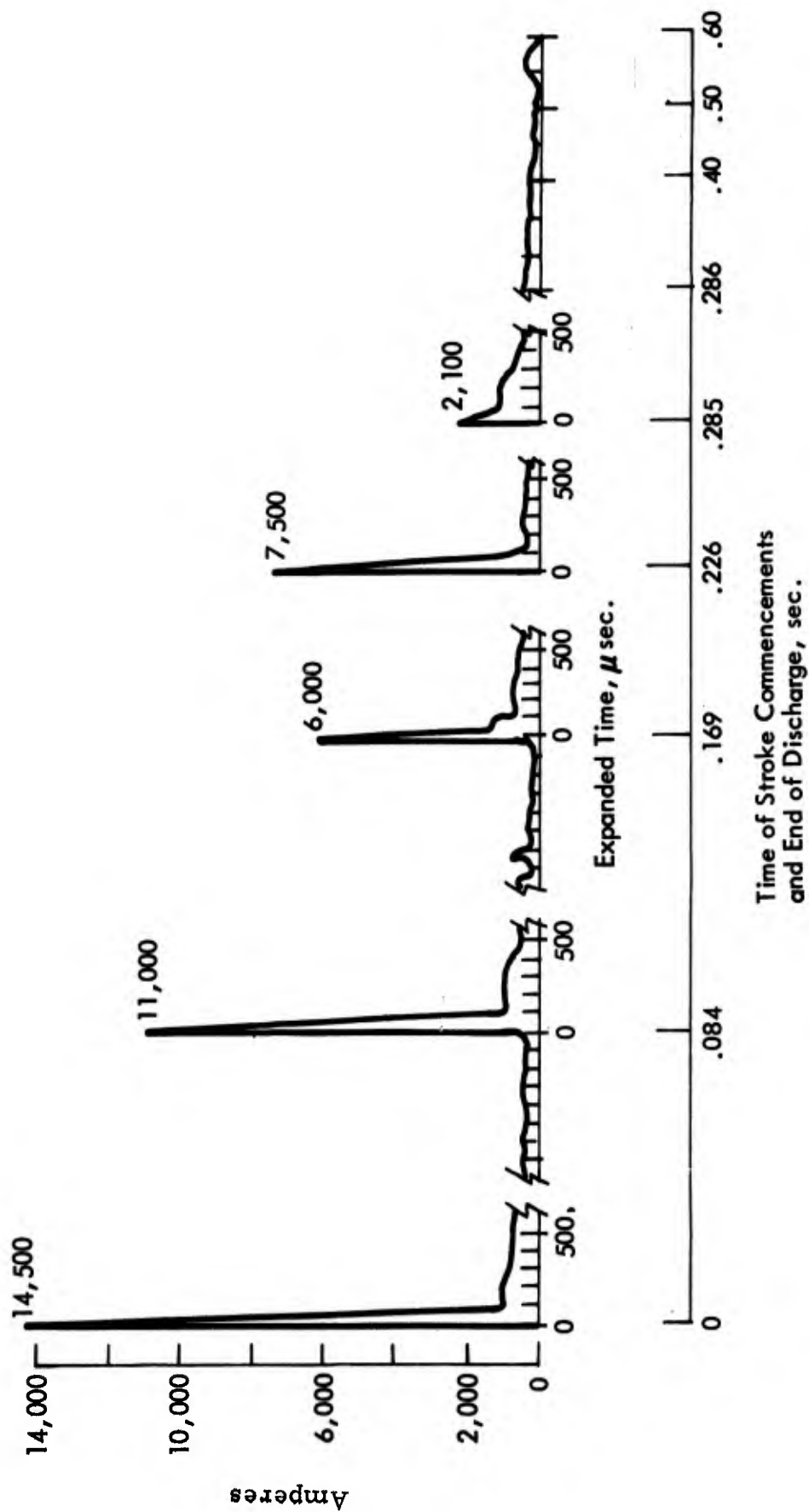
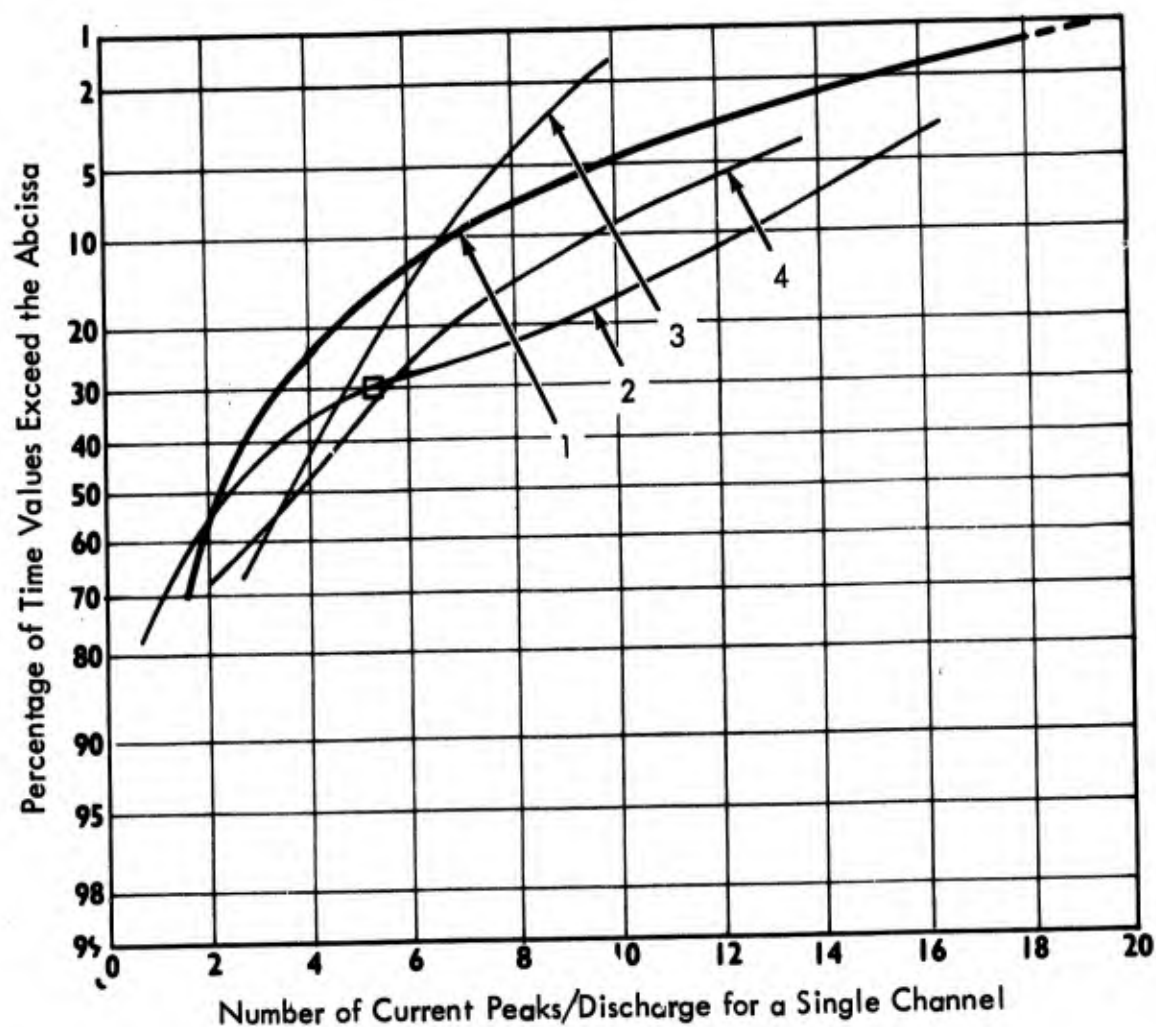


Figure 3-6 Current Wave Form vs. Time For a Series of Return Strokes



1. Hagenguth [1947]
2. Kitagawa, Brook, and Workman* [1962],
New Mexico ~1.5 to 2km, □, Average = 5.5
3. Norinder [1950], Scandinavia
4. Schonland [1956], South Africa

* Data Adjusted to Indicate Strokes
Per Path in a Discharge

Figure 3-7

Probability Distribution of the Number
of Return Strokes per Discharge

milliseconds. Short strokes usually lower only a few coulombs to ground. Long strokes lower in the order of 10 to 30 coulombs per discharge. Studies of the number of return strokes in lightning discharges have been carried out by several individuals and the results are summarized in Figure 3-7. The median value lies somewhere in the order of 3 strokes while the average value is 4 to 5. The time interval between successive strokes of the multiple discharge has been analyzed by Hagenguth [1947] and the results show the median time between strokes appears to be in the order of 40 milliseconds with average values running from 50 to 60 milliseconds.

It is important to note that as the stroke order increases, higher charge centers within the cloud are being discharged. This is borne out by observations of Brook, Kitagawa, and Workman [1962]. Their results are shown in Figure 3-8 where it is seen that the height of stroke one is about 3 kilometers. The height increases to something in the order of 10 kilometers for strokes of order 10 to 12. Another interesting feature is that the charge lowered per stroke decreases as the stroke order increases. The average charge lowered per stroke drops from about 6.5 coulombs for the first stroke to something in the order of 1 coulomb per stroke for the high order strokes. The cumulative average value is 2.5 coulombs per stroke. The decrease in charge is associated with a decrease in peak current magnitude as was shown in Figure 3-6. It is important to note that the 2.5 coulombs lowered per stroke times an assumed average of 5 strokes yields a value in the order of 12.5 coulombs as being lowered by the peak current phases (return strokes) of the discharge. Measurements of the total field indicate that on the average 25 coulombs is lowered per discharge or approximately twice that lowered during the individual strokes.

Observations by Berger reported by Pierce [1962] indicate that the initial phase of the current vs. time observed at the ground has an increasing

slope with time so that it is not a simple exponential as it has often been represented. This effect however, (due to the importance of finite channel velocities) is of rather small importance in determining the radiating characteristics of a lightning discharge over the major portion of the radiation frequency spectrum. McCann [1944] shows the median rise time to be about $2\frac{1}{2}$ microseconds, while subsequent strokes have rise times in the order of 1 microsecond. Pierce, et al reach the conclusion that an average value of rise time should be in the order of 3 or 4 microseconds which is in good agreement with the results of McCann. The average decay time (defined as the time required for the current to decay to one half the maximum amplitude) based on data from McCann, is found to be about 45 microseconds.

Summarizing the results obtained thus far we arrive at representative current pulses having a rise time of 2.5 microseconds and a decay time of around 45 microseconds with a peak current of 20 kiloamperes. This appears to agree well with the most probable form for return stroke currents as shown by Pierce, Arnold, and Dennis.

Figure 3-9 shows anticipated current at the ground versus time, reaching a peak value in the order of 30 kiloamperes. This value is probably somewhat below the average for low altitude strokes, and in fact the peak field variations produced from this idealized stroke are somewhat lower than the average values observed. The center figure (6) on Figure 3-9(c) where it appears that the maximum moment occurs at 50 microseconds and has a value of 3.5×10^7 ampere meters. The moment decays back to some low value in about 140 microseconds. Also shown on this figure are the integral of the moment and the moment differential. These results will be used in Subsection 3.2.3 in determining the radiated EM spectra.

Streamer and Junction Phase

The streamer and junction phase lasts for the interval between return

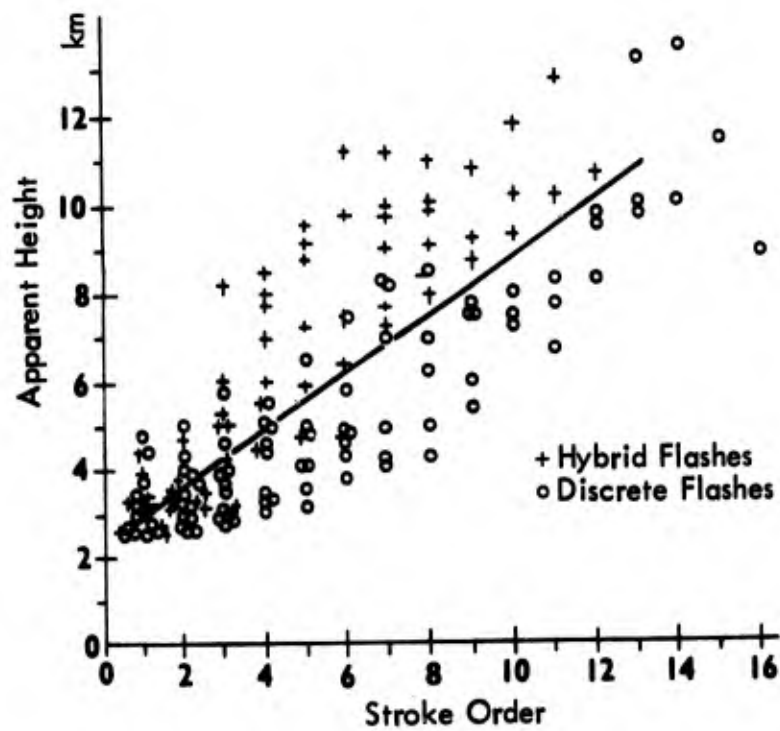


Figure 3-8 Apparent Height vs. Stroke Order for Strokes in Discrete and Hybrid Flashes; from Brook, Kitigawa, and Workman [1962]

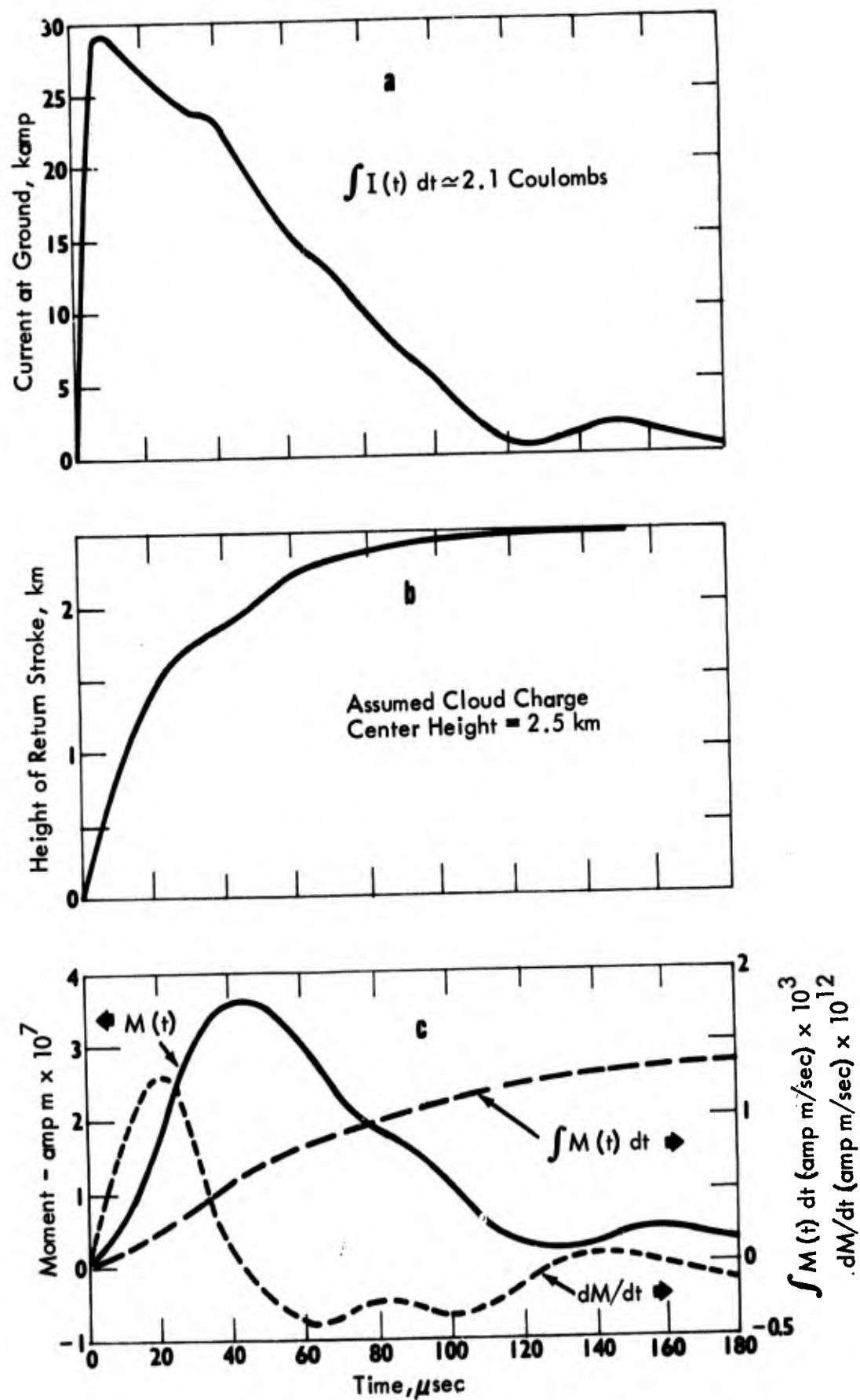


Figure 3-9 Current-Moment vs Time For Return Strokes

strokes which averages 50 to 60 milliseconds. Malan and Schonland [1953] show that there are slow variations in the electrostatic field which may be either positive or negative slopes, or a combination depending on observing distance. During this junction phase, there are small rapid moment changes associated with streamers apparently extending from the top of the discharge channel to tap fresh charge centers in the cloud. These are called K field changes. It is believed that the slow electric field variation, J change, during this phase is actually the integral of the K changes plus other small interconnecting discharges of short length and duration.

Details of the processes involved in producing the K field changes are not well known and considerable difference of opinion exists in the literature relative to size and nature of K process characteristics.

Observation of radiated fields indicate K pulse amplitudes of 0.05 to 0.2 that of the main return pulse for frequencies near 100 kHz. The spacing between K pulses is quite variable. Kitagawa and Brook [1960] give distributions indicating intervals between K pulses of 6 to 10 milliseconds which appear to include even the very small pulses. Observations of radiated fields - vs. - time by Malan [1958] and Horner [1964] show two to four large K (ℓ K) pulses between each return stroke. This would be about 20 milliseconds spacing for the larger K pulses. Also shown on the records is evidence of many short, low amplitude pulses.

It is our opinion that the short low amplitude pulses (sK) are associated with short inter-connecting "coronal type discharges" and that the ℓ K pulses are the result of follow up streamers connecting charge centers which may be separated by lengths in the order of 1 kilometer. The peak currents involved for ℓ K pulses are believed to be near 3 kiloamperes and if velocities of 5×10^7 meters/second are used, the moment vs. time resulting is shown at the top of Figure 3-10. The peak moment of 1.5×10^6

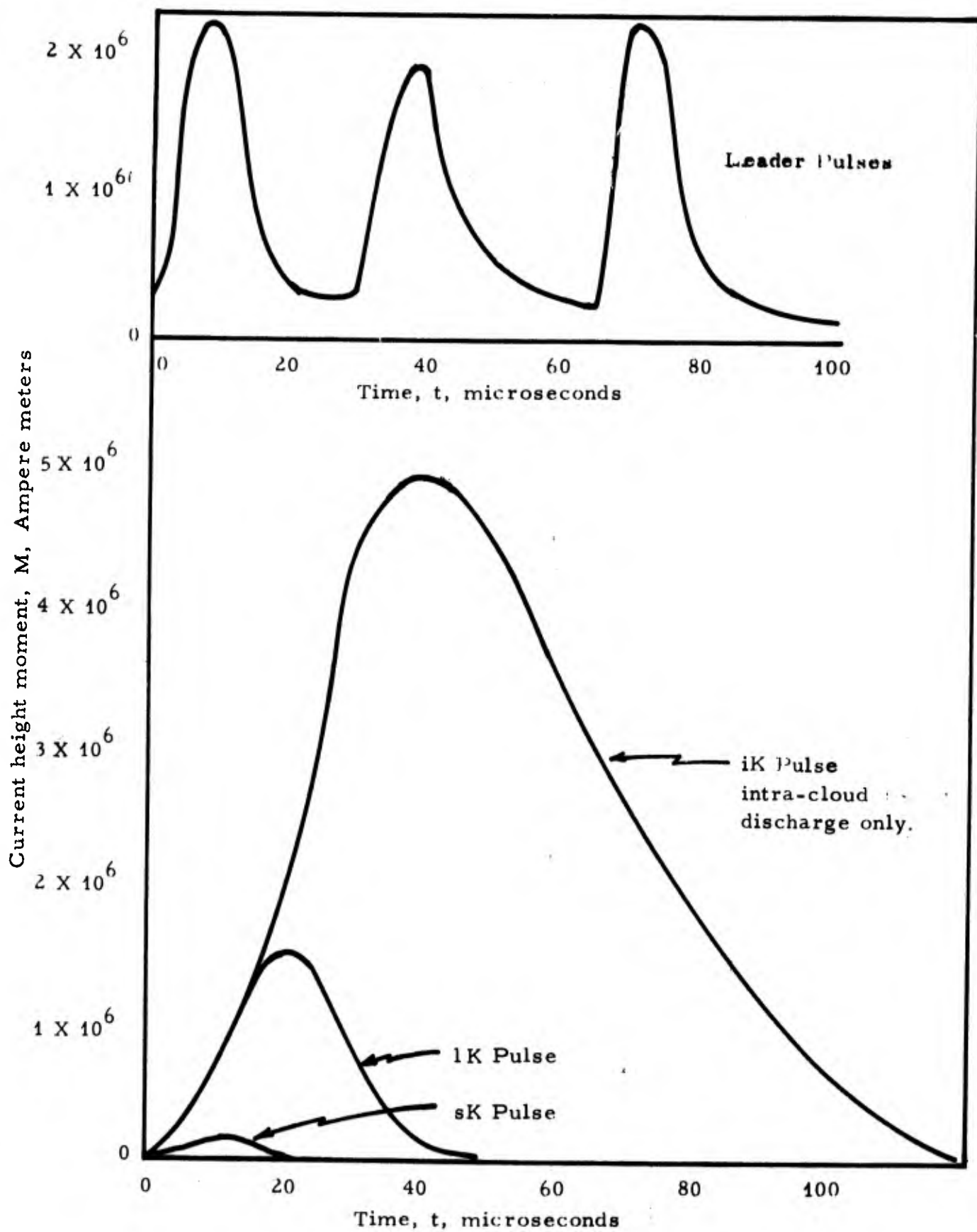


Figure 3-10 Current moments associated with the leader and junction phases of the lightning discharge.

ampere-meters is close to that proposed by Arnold and Pierce [1964] although the currents and channel lengths assumed are different.

The short pulses (sK) shown at the bottom of Figure 3-10 are for assumed lengths of 10 and 100 meters, currents of 10^3 amperes and velocities of 5×10^7 meters/second. The pulse rise time of 2 and 0.2 microseconds are of the range seen by some observers. These pulses are much closer spaced than the lK pulses. They radiate most of their energy in the HF region.

The M process involves the whole return stroke channel with lengths in the order of 3 kilometers. The channel is still fairly well ionized so that a velocity of 5×10^7 meters/second is assumed and a current of 10^3 amperes. A possible moment vs. time is shown in the middle of Figure 3-10.

Dart Leader Phase

The dart leader has a velocity of about 10^7 meters/second and if the length is 3 kilometers, the moment rise time will be in the order of 300 microseconds. Assuming a current of 5 kiloamperes yields a peak moment of about 1.5×10^7 ampere-meters or about 0.2 that of the average main return stroke. The rate of rise is much less, however, so that the peak radiated field will be less than one tenth that of the main return stroke. It is interesting to note that the moment is not likely to decrease to a low value before the next return stroke. At the end of the dart leader travel the current begins to rise rapidly in the next return stroke.

Final Phase

After the last main return stroke, there is a final phase which may last for several tenths of a second. During this phase an appreciable amount of charge can be lowered, and fluctuations in the current moment can radiate energy similar to that occurring in the intermediate stages.

3.2.2 Intra-Cloud Discharges

Compared to the cloud-to-ground discharge, there is relatively little information about intra-cloud discharges. They are a great deal different from cloud-to-ground discharges. Whereas a cloud-to-ground discharge normally begins with an initial breakdown and stepped leader phases which carry negative charge to the ground, Takagi [1961] and Ogawa and Brook [1964] indicate that 75 percent of intra-cloud discharges are initiated by downward positive charge streamers. Since the positive charge consists of heavy ions, this streamer process is much slower than the stepped leader of the cloud-to-ground discharge. Pierce [1969] reports the effective vertical speed of the intra-cloud streamer to be 10^4 meters/second compared to the velocity of 5×10^7 meters/second for the stepped leader of the cloud-to-ground discharge. This slow moving positive streamer of the intra-cloud discharge produces very little energy in the VLF band. It could be a significant contributor to ELF radiation. As might be expected, the duration of the initial breakdown and stepped leader phases of the cloud-to-ground discharge are much shorter (10 to 150 milliseconds) than is the duration of the initial portion of cloud discharges (50 to 300 milliseconds); see Kitagawa and Brook [1960]. Kitagawa and Brook have also compared the intervals between pulses of ground and cloud discharges and finds the mean interval for ground discharges to be 80 microseconds whereas the mean interval between pulses for cloud discharges is 640 microseconds.

Figure 3-11 from Pierce [1969] serves to illustrate the character of an intra-cloud discharge. The initial (positive streamer) portion of the intra-cloud discharge is followed by the very active portion which consists of very small and irregular pulses and some pulses which appear to be similar to K pulses. The final portion of an intra-cloud discharge is the J type portion which is very similar to the junction and streamer portion of a cloud-to-ground discharge. It appears to consist of small and large K

type pulses. There are, of course, no return strokes in an intra-cloud discharge since the discharge does not touch earth. The earth is a low impedance sink for charge thereby enabling the current in the ionized channel to rise to a high value (in the order of 5 to 30 kiloamperes) in a few microseconds. In a cloud flash, the ionized channel does not make contact with such a low impedance source or sink for current. Mackerras [1968] et al; have noted unusually large pulses occurring as part of intra-cloud discharges, however, and we have therefore included an extra large K change (iK) as part of our intra-cloud discharge model.

We propose that a reasonable model at VLF for an intra-cloud discharge might consist of sK, lK, and extra large (iK) pulses. The physical significance of these pulses are not well understood, but it is assumed that the sK and lK pulses are similar in nature to the same events observed in cloud-to-ground discharges. Since both types of discharges apparently consist of streamers which collect charge from small charge centers within the cloud, this is not an unreasonable assumption. The justification for an iK event comes mostly from the consideration that intra-cloud discharges are longer than the streamer events between return strokes of the ground discharge. This offers the opportunity for extra large charge centers to discharge through a major part of the entire length of the intra-cloud discharge. We assume that the shape of the iK pulses should be similar to the lK changes as shown on Figure 3-10, with a somewhat larger amplitude and longer time period.

Summary of Typical Discharge Characteristics

The characteristics of typical discharges are summarized in Tables 3-1, 3-2 and 3-3. We hesitate to claim that these are characteristics of an average discharge. It is doubtful that sufficient data exists to define average characteristics. The occurrence of discharges similar to the typical ones described here, however, is quite probable.

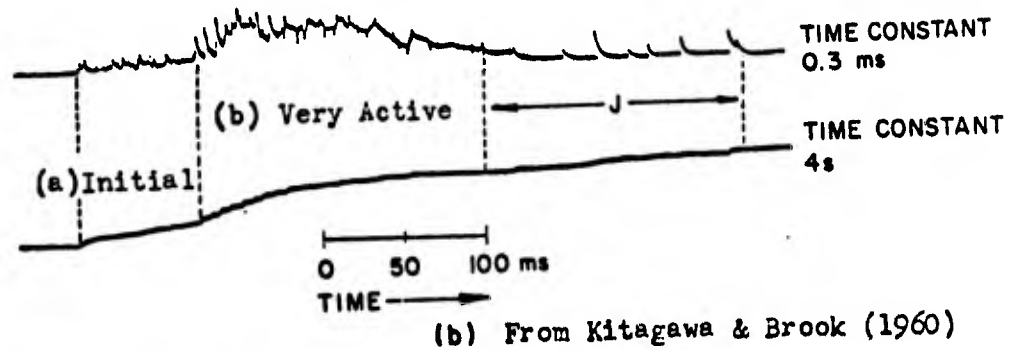
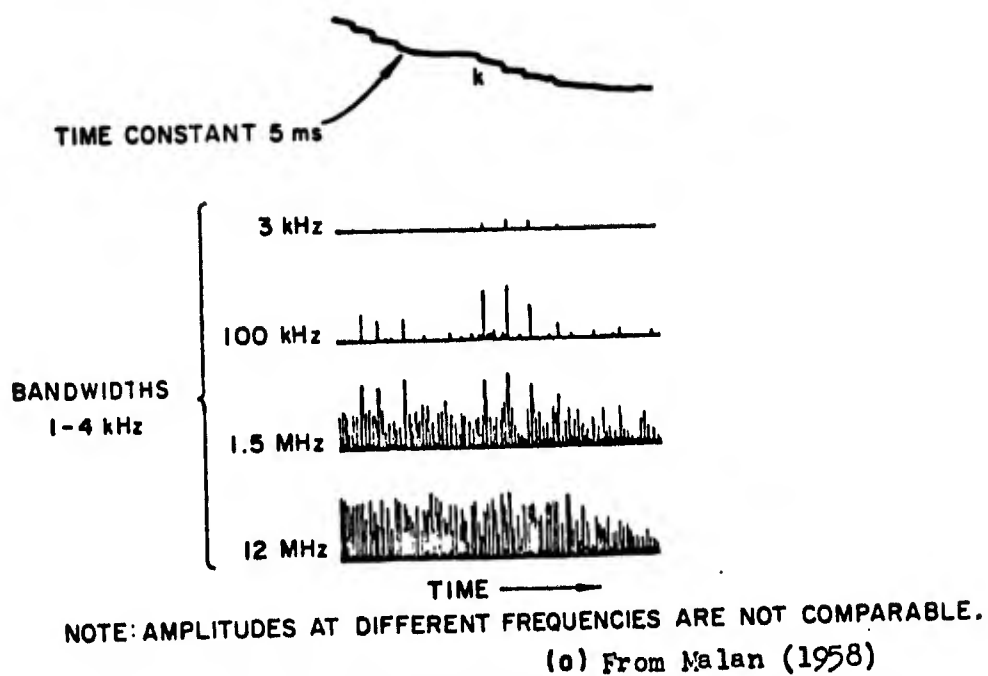


Figure 3-11 INTRACLOUD FLASH—ILLUSTRATING STRUCTURE OF NOISE AS A FUNCTION OF FREQUENCY

Reference to Figures 3-5, 3-9 and 3-10 may help in assimilating the information in the tables.

The reasonableness of the characteristics selected for a typical cloud-to ground return stroke can be checked by comparing fields measured near discharges with values calculated for typical stroke of Figure 3-9 and Tables 3-1 and 3-3.

When observed peak electric field variations are plotted vs. distance from the source, the results shown in Figure 3-12, Watt [1967], are obtained. The slow decrease in the 1 km range is due to finite height of the source, i. e. 2 to 3 km. Out to this distance, the field decreases as a log function, i. e.

$$E_z \simeq \frac{\mu \omega I}{\pi} \ell_n \left(\frac{2\pi d}{\lambda} \right) \quad (3-6)$$

as described by Wait [1959] and Watt [1967], p. 463. In the 10 kilometer range, the field is decreasing as $1/d^3$. Beyond 50 kilometers, the radiation term dominates and the fields decrease as $1/d$. Projecting back to 1 kilometer yields a value of 300 volts/meter. The synthesized ground return stroke of Figure 3-9 has a peak value near 250 volts/meter; see Watt [1960].

Observations of the distribution of peak fields produced from a large number of discharges are given on Figure 3-13. Data was obtained from Taylor and Jean [1959] and Taylor [1963]. The larger values are seen to be associated with low altitude storms. Median values are about 350 volts/meter while average values are near 450 volts/meter. The rms value of the distributions will be even higher.

The model for the typical return stroke seems reasonable.

TABLE 3-1
Length of Phases and Number of Pulses in Typical Cloud-to-Ground Discharge

Phase*	Length/Phase Milliseconds	Number of pulses/phase					
		R	L	1 K	s K	D	M
(a) Initial Breakdown	90	-	-	2	10		
(b) Stepped Leader	4	-	100	-	-		
(c) Return Stroke (n = 5)**	0.1	1	-	-	-		
(d) Streamer & Junction (n - 1 = 4)**	50	-	-	3	15		
(e) Dart Leader	0.3	-	-	-	-	1	
(f) Final	100	-	-	6	30	-	
Total For Discharge	~ 400	5	100	20	100	1	0.1

* See Figures 3-5 and 3-6

**This "typical" cloud-to-ground discharge has 5 return strokes and therefore, 4 streamer and junction phases.

TABLE 3-2

Length of Phases and Number of Pulses in a Typical Intracloud Discharge

Phase	Length Milliseconds	Number of Pulses/Phase		
		<u>l k</u>	<u>s K</u>	<u>i K</u>
<u>Name</u>				
(a) Initial	~ 100	-	30	-
(b) Very Active	~ 150	10	50	5
(c) Junction & Streamer	~ 150	10	20	5
Total for Discharge	~ 400	20	100	10

TABLE 3-3

Electrical Moment Characteristics of Typical Pulses

Pulse Type	Likely Channel		Vertical Moment		Pulse Shape shown in Figure
	Length Meters	Peak current amperes	M_p ampere-meters	$\frac{1}{2}$ length, δ seconds	
R	3.5×10^3	3×10^4	5×10^7	5×10^{-5}	3-9 *
L	$200 + 10^3$	2×10^3	4×10^5	10^{-5}	
l K		4×10^3	2×10^6	2×10^{-5}	3-10
s K	200	10^3	1.5×10^5	10^{-5}	3-10
i K	2×10^3	5×10^3	5×10^6	4×10^{-5}	3-10

* Channel length and amplitude increased over that shown in this figure.

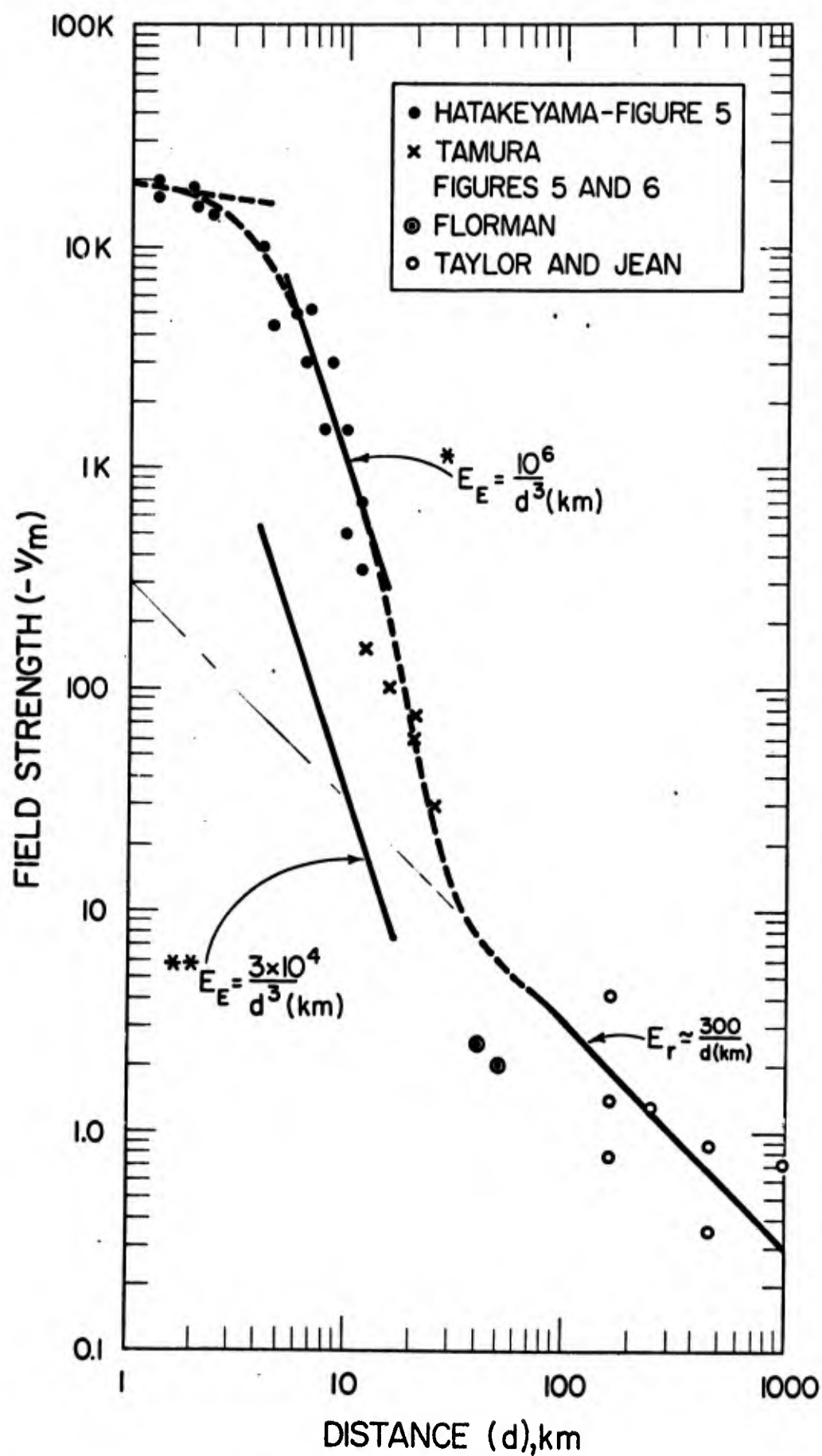


Figure 3-12 Peak Electric Field Variations from a Vertical Discharge to Ground. From Watt (1967)

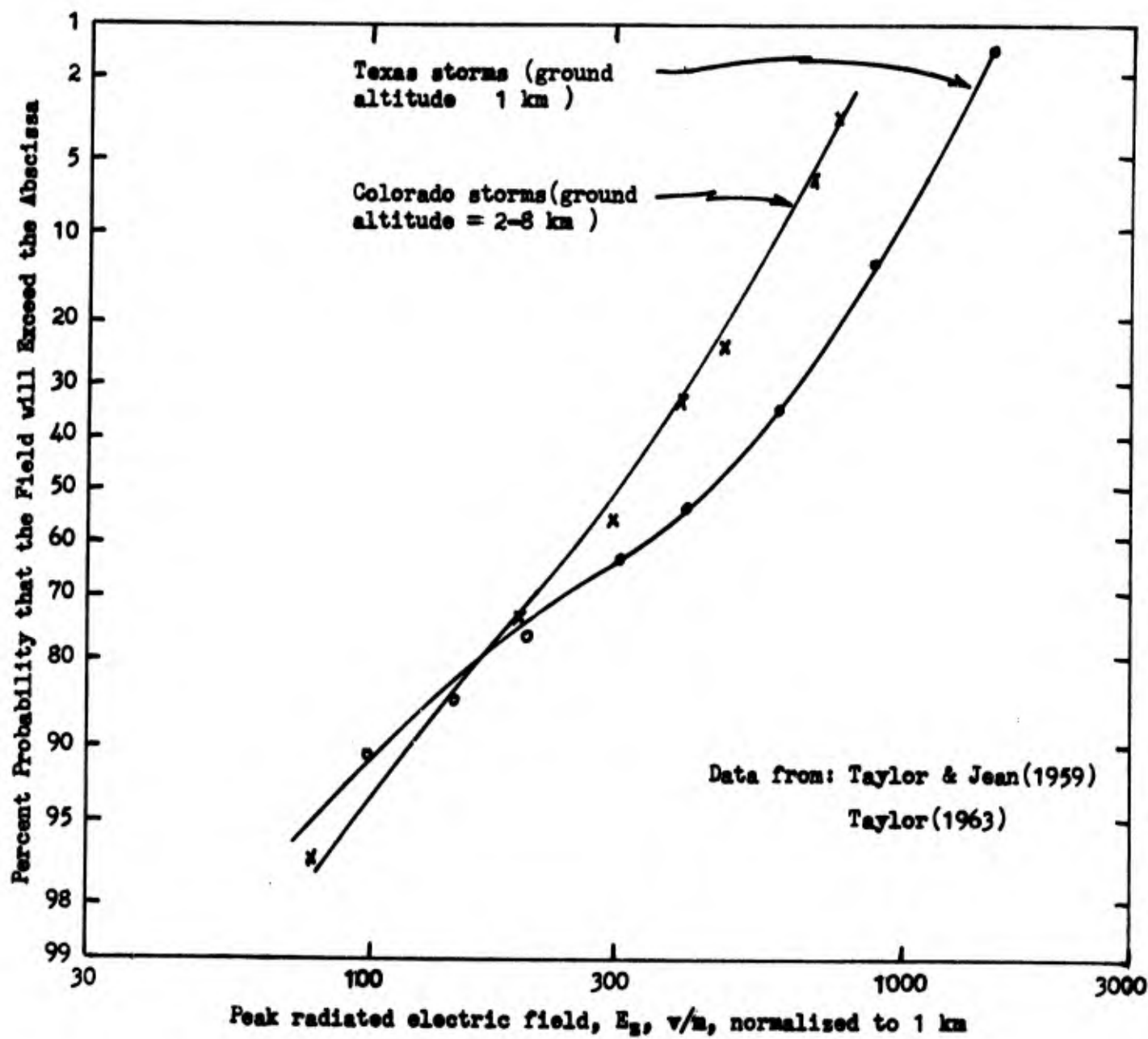


Figure 3-13 Cumulative distribution of peak electric fields radiated from lightning discharges.

3.2.3 Radiated EM Spectra of Typical Discharges

The electrical moments, $M(t)$, for most of the lightning processes are seen in Figures 3-9 and 3-10 to have a basic triangular shape with rounded corners. A triangular waveform has a Fourier transform of $\sin^2 x/x^2$ as is shown in Appendix B. Rounding of the corners has little effect on the spectrum for frequencies below the reciprocal of the rounding interval. For frequencies above this point, the rounding usually produces a faster decrease in amplitude with frequency. In the case of the triangular pulse where at high frequencies the frequency function $g(f)$ approaches kf^{-2} , rounding will usually change to kf^{-3} .

Spectrum Derivation

From Watt [1960, p. 429], it can be shown that the radiated field frequency spectrum $g(\omega)_r$ is related to the induction field spectrum $g(\omega)_i$ by the relation

$$g(\omega)_r = \frac{2\pi f d g(\omega)_i}{3 \times 10^8} \quad (3-7)$$

Since

$$g(\omega)_i = \frac{-60}{d^2} \int_{-\infty}^{\infty} M(t) e^{-i \omega t} dt, \quad (3-8)$$

we obtain

$$g(\omega)_r = \frac{4\pi \times 10^{-7} f}{d} \int_{-\infty}^{\infty} M(t) e^{-i \omega t} dt. \quad (3-9)$$

From Appendix B, we see that for triangular pulses

$$\int_{-\infty}^{\infty} M(t) e^{-i \omega t} dt = M_p \delta \frac{\sin^2(\pi f \delta)}{(\pi f \delta)^2} \quad (3-10)$$

where M_p is the peak of the moment waveform in ampere-meters, δ is the $1/2$ pulse length in seconds, and f is the frequency in Hertz. When the radiated spectrum is desired for a normalized distance of 1 km from the source, the preceding relations yield

$$g(\omega)_r = 4\pi \times 10^{-10} M_p \delta f \frac{\sin^2 \pi f \delta}{(\pi f \delta)^2} \quad (3-11)$$

1 km

which is for a + and - frequency spectrum. From Appendix B, it is seen that the peak voltage (positive frequency only) spectrum is twice the above values and that the rms spectra is $\sqrt{2}$ times $g(\omega)_r$. This yields

$$E_z(f)_r \approx 1.8 \times 10^{-9} M_p \delta f \frac{\sin^2 \pi f \delta}{(\pi f \delta)^2} \quad (3-12)$$

rms, 1 km

Energy Radiated per Pulse or Discharge

The power radiated by a vertical current-moment is related to the electric field by the relation

$$P_r = \frac{E_z^2 d^2}{90} \quad (3-13)$$

If the radiated rms field at 1 km (E_{z1km}) from the source is known, the power is related to it

$$P_r = 1.11 \times 10^4 E_{z1km}^2 \quad (3-14)$$

The spectrum $g(f)_r$ derived for the current-moment is in volt-seconds and when a unity bandwidth is employed, i.e. one Hertz, the square of $E_{z1km}(f)_r$ yields watt-seconds, i.e. energy when placed in equation (3-14). As a result,

$$U(f)_r = 1.11 \times 10^4 |E_{z1km}(f)_r|^2 \quad (3-15)$$

This means if $E_{z1km}(f)_r$ is in dB rel (1 V/m)-second, $U(f)_r$ is obtained by adding 40.5 dB. If $E_{z1km}(f)_r$ is in dB rel (1 μ V/m)-second, $-120 + 40.5 = -79.5$ must be

added to the voltage-time spectrum to obtain the energy density spectrum.

Spectra of Typical Discharges

Using the models outlined in Sections 3.2.1 and 3.2.2 for a "typical" discharge we will calculate a "typical" discharge spectrum.

The electrical moment model for a cloud-to-ground discharge goes through the basic phases shown in Figure 3-5. The duration of each phase and typical numbers of the various pulse types occurring within each phase are given in Table 3-1. The average number "n" of each type of pulse expected during a given phase is also shown. The model for an intra-cloud discharge is given in Table 3-2.

Characteristics of the basic pulse types are shown in Table 3-3 where the moment peaks, M_p , are chosen with amplitude values believed to be close to the rms value of the pulse amplitude distribution for each type of pulse. The overall radiated spectrum expected is obtained from the individual spectrum for each pulse multiplied by the \sqrt{n} . This assumes a linear increase in power with the number of pulses. The M pulse occurring occasionally between the return pulses, and the D pulse associated with the dart leader are not expected to contribute materially to the over-all spectrum. Numerous shorter pulses with lengths in the order of a microsecond are also present but are not considered here because of their negligible contribution at VLF.

The frequency spectrum produced by the important individual pulses in the VLF to LF frequency region are obtained with the aid of equation (3-12) modified slightly according to the spectral shape in Figure B-1 which shows that skewing of the pulse reduces the null depth at $f\delta = 1$ and rounding the corners reduces the amplitude for $f\delta > 1$. Three different

spectral shapes are employed: One for R pulses, one for L and sK pulses, and one for lK and iK pulses.

The frequency spectrum for an individual pulse is now obtained as:

$$E_{z1km}(f)_r \approx 1.8 \times 10^{-9} M_p \delta f G(\omega)_{\text{normalized}} \quad (3-16)$$

where: M_p is the maximum current-length moment of the pulse (See Table 3-3),

δ is the $1/2$ pulse length for the pulse involved (see Figure B-1, and Table 3-3),

f is the frequency in Hz,

$G(\omega)_{\text{normalized}}$ is the normalized frequency spectrum shown in

Figure B-2, and

$E_{z1km}(f)_r$ is the frequency spectrum of the radiation component of the rms vertical electric field.

It is important to note that this function is for frequencies from 0 to ∞ and that the amplitudes are $\sqrt{2}$ times, i. e. 3 dB greater than the $g(\omega)$ Fourier transform which has been shown by most authors. The energy per event spectrum can readily be obtained by combining equations (3-15) and (3-16) to obtain

$$U(f)_r \approx 3.56 \times 10^{-14} M_p^2 \delta^2 f^2 G(\omega)_{\text{normalized}}^2 \quad (3-17)$$

where $U(f)_r$ is the energy density spectrum in watt-seconds per event.

Typical pulse peak moments, M_P , and one-half lengths, δ , are given in Table 3-3. Employing the total number of pulses of each type listed in Table 3-1, the spectra for a cloud-to-ground discharge is shown in Figure 3-14. Note the $E_{zn} = \sqrt{n} E_{z1}$ while $U(f)_n = n U(f)_1$. The dashed curve is the composite spectrum of the whole discharge. The spectra for an intra-cloud discharge is shown in Figure 3-15.

All the spectra shown thus far are based on models believed to represent a "typical" discharge. This term is used since enough data is not available to choose true average or median, discharges. Long discharges, produced by long cloud-to-ground distances, are known to radiate more energy than short discharges which occur when the cloud base is close to the ground.

The final algorithm developed for computing power radiated per square kilometer uses a variable discharge similar to the typical discharge described above. The characteristics of the discharges are computed for each 5° by 5° area of the earth's surface and are dependent upon the number of thunderstorm days. The pulses used and their characteristics are identical with those used in the typical discharges described above with the exception of the return stroke. The basis for changing the characteristics of the return strokes for different regions is discussed in the following section.

3.3 An Algorithm For Computing Power Radiated From Any Region On The Earth's Surface

Thunderstorm day data in the form of thunderstorm day maps is the only worldwide data which may be related to electromagnetic energy radiated by lightning discharges. The algorithm which begins with this data and computes the electromagnetic energy radiated for any region on the earth's surface is presented below.

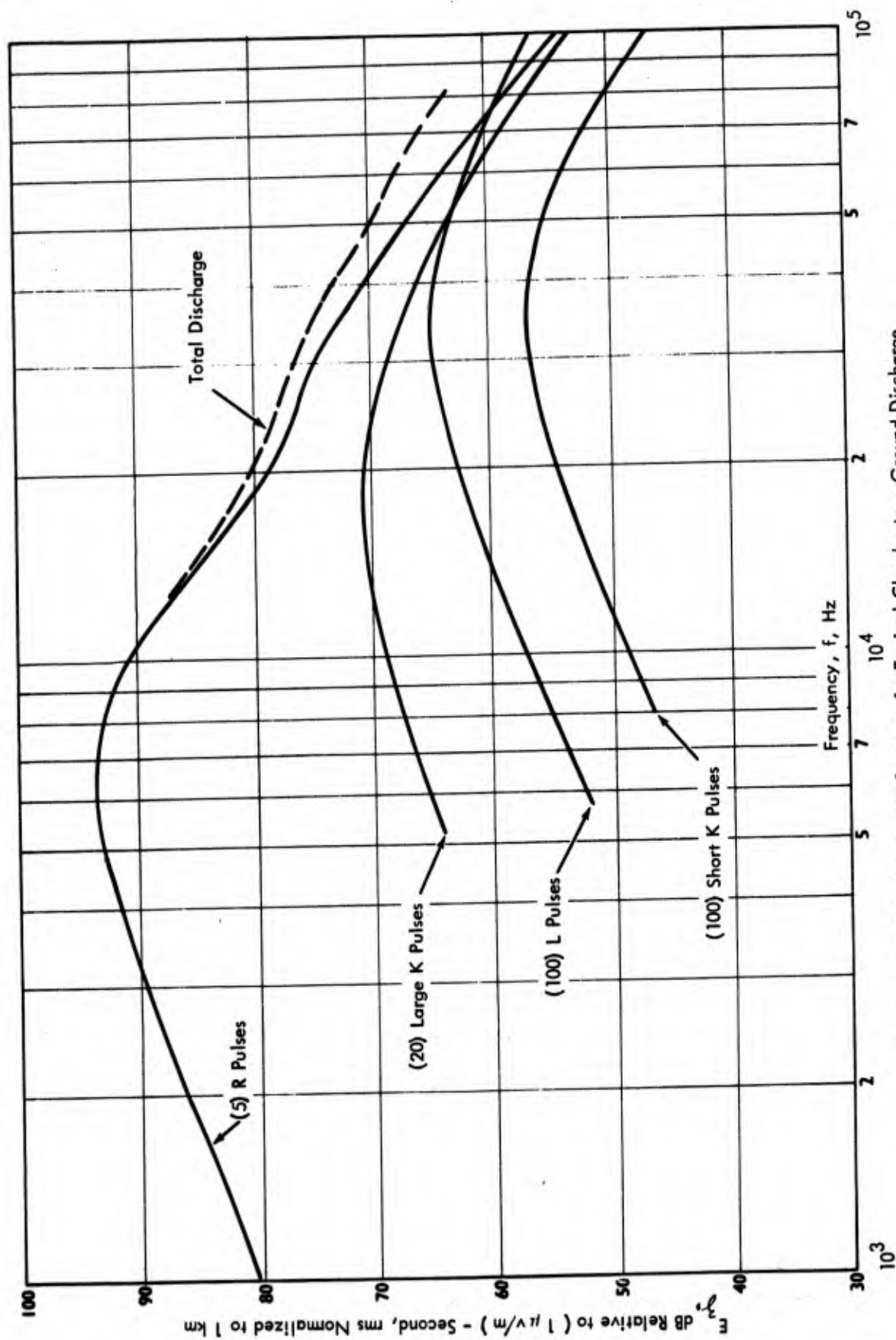


Figure 3-14 Frequency Spectra of a Typical Cloud - to - Ground Discharge

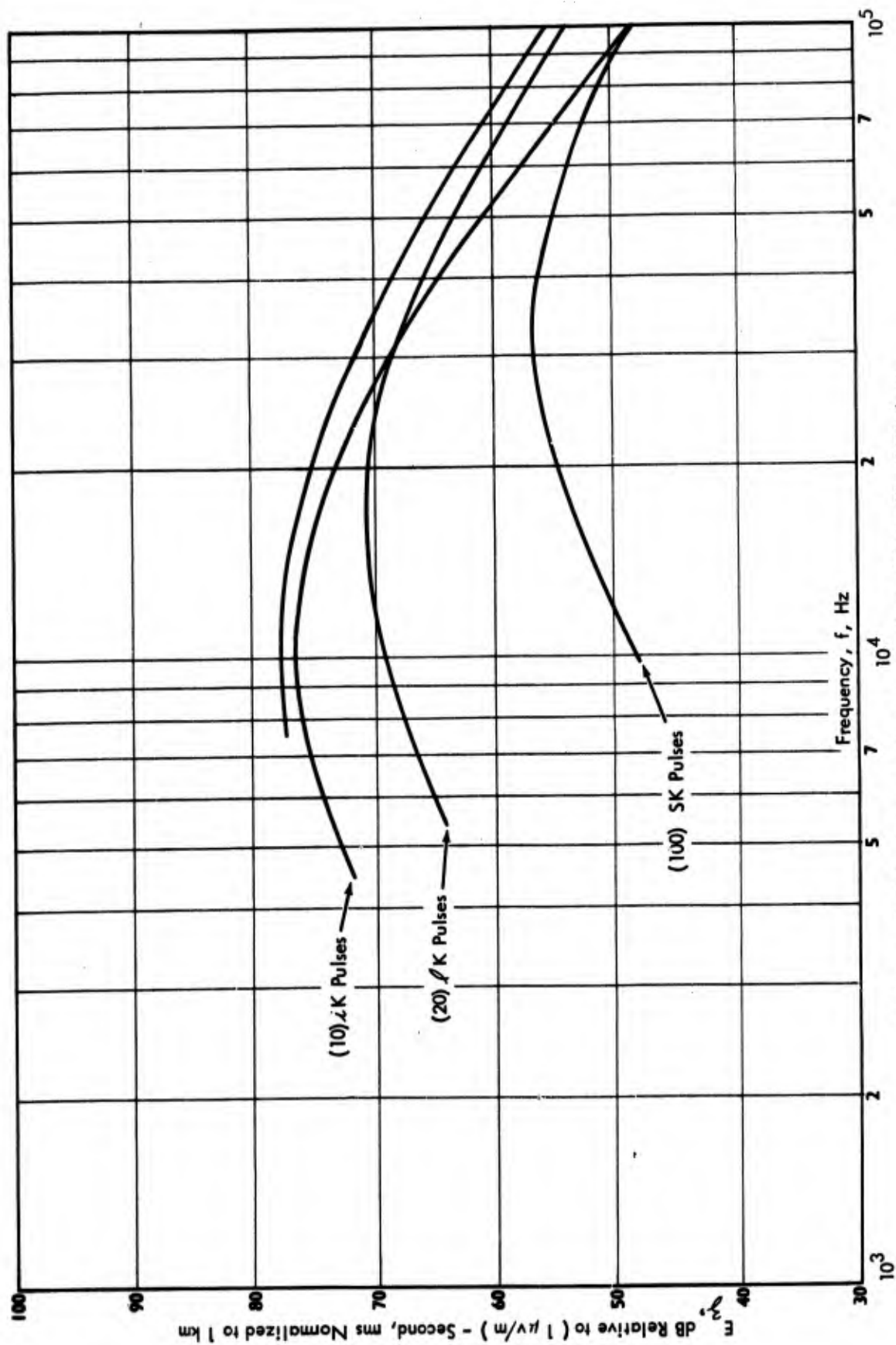
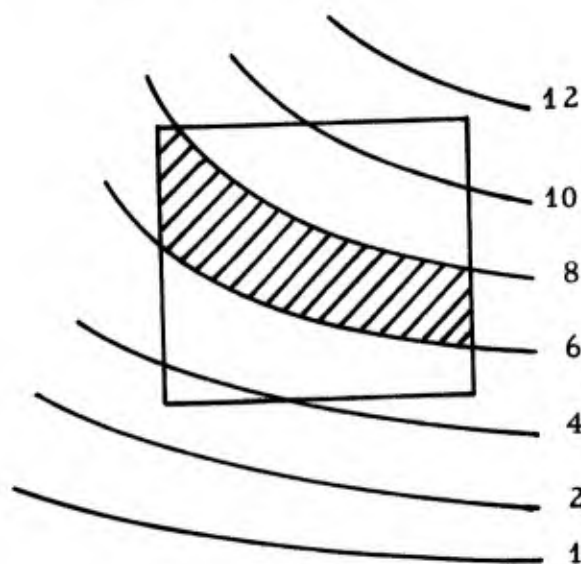


Figure 3-15 Frequency Spectra of a Typical Intra-Cloud Discharge

THE ALGORITHM FOR COMPUTING POWER RADIATED

STEP 1

The world is divided into 5° longitude by 5° latitude regions. We then determine which thunderstorm day (TD) contours encircle or cross each region and the area, in km^2 , enclosed by each contour crossing the region. We then compute the delta areas (ΔA) between contours and assign a TD value to this area equal to the mean of the two contours (ΔA_{TDm}). For instance, for the region shown below



we obtain delta areas:

$$\Delta A_{1.5} = A_1 - A_2 = 0$$

$$\Delta A_3 = A_2 - A_4$$

$$\Delta A_5 = A_4 - A_6$$

$$\Delta A_7 = A_6 - A_8 \text{ (crosshatched)}$$

$$\Delta A_9 = A_8 - A_{10}$$

$$\Delta A_{10} = A_{10} - 0$$

Note that the area enclosed by the highest contour is assigned a TD value equal to that contour value.

The delta areas are the output of STEP 2. This step is carried out by the computer program THUNCON, Stone [1970].

STEP 2

Using equation (3-3) and the output of Step 1 we compute the number of lightning discharges per month (N_{ld}) for a given transmitter,

$$N_{ld} = 0.06 \sum_{i=1}^n \Delta A_{TD_{m_i}} N_{TD_{m_i}}^{1.5} \quad (3-18)$$

where $N_{TD_{m_i}}$ is the mean number of thunderstorm days for the i^{th} delta area. The effective center of lightning activity within the region is computed using a centroid concept. The effective number of thunderstorm days for the region (N_{TD_e}) is that value which would result in the same N_{ld} for the total area of the region.

The output of STEP 2 is the number of lightning discharges per month for each 5° by 5° region, its centroidal location and N_{TD_e} .

This is part of the computer program SUMAN, Stone [1970].

STEP 3

We now determine the number of cloud-to-ground discharges (N_{gd}) and intracloud discharges (N_{cd}) for each region. Using equation (3-5),

$$N_{gd} = N_{ld} \left[0.05 + \frac{\sin \phi + 0.05}{(N_{TD_e} + 3)^{1/2}} \right] \quad (3-19)$$

$$N_{cd} = N_{ld} - N_{gd} \quad (3-20)$$

N_{gd} and N_{cd} are the output of STEP 3. This step is part of SUMAN, Stone [1970].

STEP 4

We will now determine the following characteristics of each ground and cloud discharge:

- N_R --- The number of return strokes per discharge.
- L_R --- The average return stroke length in km.
- I_R --- Return stroke peak current in kiloamps.
- D_R --- Half return stroke pulse width (δ) in seconds.
- M_R --- Moment of return stroke in ampere-meters.
- N_{sK} --- Number of small K pulses per ground discharge.
- N_{lK} --- Number of large K pulses per discharge.
- N_{iK} --- Number of cloud K pulses per discharge.
- N_L --- Number of leader pulses per discharge.
- N_{sKc} --- Number of small K pulses per cloud discharge.

From Figures 3-6, 3-7, and 3-8 we know that the number of return strokes, their height and current are interrelated. These, in turn, are related to storm severity, cloud height, freezing level and other little known factors. Vonnegut [1963] reports that total storm energy increases with the 5th power of storm diameter.

Noting that storm size, severity, height and freezing level are all related to the number of thunderstorm days, it was decided that increasing N_R with N_{TD} should be a reasonable way to provide for an additional increase in radiated energy from large storms. This is in general agreement with reports on the number of return strokes per discharge from various researchers.

The variables listed are related to N_{TD_e} as follows:

$$N_R = N_{TD_e}^{1/2} + 1 \quad (3-21)$$

$$L_R = 2.5 N_R^{1/2} \text{ (see Fig. 3-9)} \quad (3-22)$$

$$I_R = 45 N_R^{-0.34} \quad (3-23)$$

$$D_R = (3.1 N_R^{1.08} + 1) / N_R^{1/2} \times 10^{-5} \quad (3-24)$$

$$M_R = \left[(I_R) (L_R) \times 10^6 \right] / 2 \quad (3-25)$$

$$N_{sK} = 20 N_R \quad (3-26)$$

$$N_{lK} = 4 N_R \quad (3-27)$$

$$N_{iK} = 5 N_{TD_e}^{1/2} \quad (3-28)$$

$$N_L = 30 L_R \quad (3-29)$$

$$N_{sKc} = 5 N_{iK} \quad (3-30)$$

The above equations are empirical, based on data from several papers by Kitagawa, Brook, Workman, Pierce, Mackerras and others. Common sense indicates of course that if an average of 4 ℓ K events occur between return strokes and follow the last, then

$$N_{\ell K} = 4 N_R$$

Similar relations will be noted in the other equations.

The output of this step provides values for each of the variables listed.

This step is part of PWRCOM, Stone [1970].

STEP 5

This is the final step which takes the outputs of previous steps and computes power radiated from each 5° by 5° region.

From equation (3-17) we obtain

$$U = 3.56 \times 10^{-14} (N) (fMDG)^2 \quad (3-31)$$

where: f is frequency in Hertz

N is the number of pulses/discharge

M is the moment of the pulse

D is the $\frac{1}{2}$ width of the pulse

G is the normalized frequency spectrum from a log-log plot of Figure B-2.

U is energy in watt seconds

Using data from STEP 4 we compute

$$U_R, U_{\ell K}, U_L, U_{sK}, U_{iK}, U_{sKc}.$$

Next, the total energy for each cloud-to-ground and intra-cloud discharge is computed from,

$$U_{CG} = U_R + U_L + U_{lK} + U_{sK} \quad (3-32)$$

$$U_{CC} = U_{iK} + U_{lK} + U_{sKC} \quad (3-33)$$

Finally the power for each 5° by 5° region is computed from,

$$P_{CG} = (U_{CG}) (N_{gd}) / 2.59 \times 10^6 \quad (3-34)$$

$$P_{CC} = (U_{CC}) (N_{cd}) / 2.59 \times 10^6 \quad (3-35)$$

$$\underline{\underline{P_{Total} = P_{CG} + P_{CC}}} \quad (3-36)$$

Note: 2.59×10^6 is the number of seconds in a month.

THIS COMPLETES THE ALGORITHM.

Obviously this algorithm is not rigorous, nor is all the data input exact. It is an algorithm which reasonably approximates the real world, uses most of the available data and can be expanded and improved as our knowledge of thunderstorms and lightning improve. Of most importance, it works. Powers computed using this algorithm were used with little change for the computation of noise field intensities.

4.0 PROPAGATION

Having established the noise energy radiated from each 5° by 5° region of the earth's surface (these are also combined later into 15° by 15° regions) we must now determine how this energy propagates to other regions of the earth. For ease of terminology, we will refer to each 5° by 5° or 15° by 15° source of energy as a noise transmitter or equivalent noise transmitter.

The propagation path characteristics are defined by the electric properties of the earth and ionosphere along a great circle route between the noise transmitter and the receiving location. The properties of the earth-ionosphere waveguide are changing continuously along this great circle route. For the earth, the variable is the conductivity of the sea water and the ground along the path, which remain constant with time. The conductivity of the ionosphere is much more complicated because of the random nature of the plasma and the factors affecting the ionization and recombination rates. The earth's magnetic field has a strong effect on the ionospheric effective conductivity; making it anisotropic in nature. Parameters which must be considered and which are independent variables are listed as follows.

1. Time: This accounts for the effect of the sun's radiation upon the ionosphere (sun zenith angle).
2. Latitude: This accounts for the effect of cosmic ray particles incident upon the ionosphere. These charged particles tend to be guided along the earth's magnetic field lines; thus, the effect is greater with increasing latitude.

3. Sun Spot Number: The particle influx from the sun, which changes with sun spot number, varies the steady state effect of high energy galactic particles.
4. Season: Although season weather patterns may affect the conductivity of the ionosphere at the lower heights, it is assumed that the seasonal effect is mainly related to changes in sun zenith angle.
5. Directional Effect: This effect is determined by the direction of the earth's magnetic field with respect to the direction of the propagating energy. The effective conductivity can be greater than or less than the conductivity that would exist assuming the same ion concentration but without the magnetic field.

The use of the above variables in computing the field will be discussed when the parameters in the field strength equations are defined.

The total field at a receiving site is the rms value of the composite field from all noise transmitters. The phase relationship between noise transmitters is random so their powers are added directly. The composite field from each noise transmitter is the total field from all modes propagating to the receiver site. In the case of a single man-made coherent signal, this would be the vector sum of the field of each mode, when it is assumed that the duration of the transmitted pulses is large with respect to propagation delay time between the modes. In the case of a lightning stroke, the duration of the pulse can be small with respect to the delay time. In addition, the equivalent noise transmitter represents the effect of all lightning strokes within a large area. This area is large enough to result

in a complete range of phase differences between two modes from in phase, to 180° out of phase (this assumes pulse duration long with respect to time delay). The composite field from each noise transmitter is assumed then to be the sum of the equivalent power in each mode, or the rms value of all propagating modes. In the noise calculations performed, the composite field is assumed to be made up of three significant modes excited at the transmitter. Mode conversion at sunrise/sunset boundaries was neglected.

The general equation for computing the total vertical electric field for each mode is given below.

$$\begin{aligned}
 20 \log |E_{nm}| \approx & 104.3 + 10 \log P_r - 10 \log f - 10 \log h_t - 10 \log h_r + 30 \log \cos \psi_m \\
 & - 10 \log (a \sin d/a) + 10 \log |\Lambda_{m,t}| + 10 \log |\Lambda_{n,r}| \\
 & + 20 \log |G_{m,t}| + 20 \log |G_{n,r}| + 20 \log |S_{nm}^{rt}| - a_{nm} d / 10^6
 \end{aligned}
 \tag{4-1}$$

where:

$20 \log |E_{nm}|$

is the vertical electric field for the n^{th} mode at the receiver produced by the m^{th} mode excited by the transmitter in dB relative to 1 v/m. It was assumed that $m=n$ and $n=1, 2, 3$.

P_r

is the power radiated into the half space above the earth in watts,

f

is the frequency in Hertz.

h_t and h_r

are the effective ionospheric heights at the transmitter and receiver locations respectively, i.e., 7×10^4 meters for daytime and 9×10^4 meters for nighttime.

$\cos \psi_m$

is the cosine of the angle of "take off" from the earth's surface at mode resonance. Normally $\psi_m \sim 0$ for low order modes so that $30 \log \cos \psi_m \sim 0$.

$|\Lambda_{m,t}|$ and

$|\Lambda_{n,r}|$

are the magnitudes of mode excitation factor at the transmitter and receiver respectively,

a

is the earth's radius $\sim 6.4 \times 10^6$ meters,

d

is the path distance: $(a \sin d/a)$ accounts for the energy spreading in the spherical guide structure,

$|G_{m,t}|$ and

$|G_{n,r}|$

are the height gain factors relative to the field at the surface at the transmitter and receiver respectively,

S_{nm}^{rt}

is the scattering coefficient which accounts for losses at discontinuities along the path, such as abrupt changes in surface conductivity, or in guide height which can occur for a sunrise-sunset boundary,

a_{nm}

is the effective or apparent attenuation rate in dB/1000 km which is normally different for each mode number and section of a propagation path.

The general equation may be simplified for this application as follows. The height gain functions, $G_{m,t}$ and $G_{n,r}$, are assumed equal to unity. This assumes that the vertical electric field calculated is for a receiving antenna located on the ground, and that the height gain of the lightning source is accounted for in the equivalent radiated power. The scattering coefficient, S_{nm}^{rt} is also assumed equal to unity. This is a valid approximation at the lower frequency, e.g. $f < \sim 10$ kHz. As frequency increases the energy scattered out of a mode increases, and at $f = 30$ kHz this loss could be as great as 4 dB during a sunrise transition. For the majority of the propagation paths at $f = 30$ kHz the loss is less than this because the loss decreases as the propagation path becomes less perpendicular to the sunrise boundary, i.e., more parallel to the boundary; also the loss at sunset is much less than sunrise. Modes converted from one to another at a boundary were neglected in the field strength calculation. The loss in any one mode owing to scattering does not represent a total loss; rather it represents a conversion of energy from one mode to another, and this newly generated mode continues to propagate to the receiver and add to the total noise power. This tends to be a cancelling effect; thus, scattering losses were not included in this noise analysis.

With these approximations, the field strength equation can be written as:

$$\begin{aligned} 20 \log |E_{nm}| \approx & 104.3 + 10 \log P_r - 10 \log f - 10 \log h_t - 10 \log h_r \\ & - 10 \log (a \sin d/a) + 10 \log |\Lambda_{m,t}| + 10 \log |\Lambda_{n,r}| \\ & - a_{nm} d / 10^6 \end{aligned} \quad (4-2)$$

In the above equation, the term $10 \log f$ is uniquely defined for each choice of frequency. Each month of the year defines a set of noise transmitters and their location; thus, each month defines a matrix of transmitter and receiver distances which define the term $10 \log (a \sin d/a)$. The monthly values of the radiated power of each noise transmitter, P_r , is modified for each hour of the day. These powers and their modifiers are defined in section 6.1 of this report. The terms h_t and h_r are determined by the location of the transmitter and receiver and the GMT hour used. If the transmitter and receiver are in daytime, then the total path is daytime and $h_t = h_r = 7 \times 10^4$ meters. If they are both found to be nighttime, then the path is all nighttime and $h_t = h_r = 9 \times 10^4$. If both these conditions fail, then the path is transitional and one height is set equal to 7×10^4 meters and the other is set to 9×10^4 .

The terms of main concern here are $\Lambda_{m,t}$, $\Lambda_{n,r}$, and a_{nm} . The excitation factor is a function of the height of reflection, the conductivity gradient of the ionosphere, the ground conductivity, and the direction of propagation. Of these variables, the effect of the latter one is the least well known. Because of this, the excitation factor is assumed to be independent of direction of propagation. Table 4-1 shows the excitation factor as a function of height and conductivity gradient, i.e., daytime or nighttime, and ground conductivity. It should be noted that the values are $20 \log \Lambda$ rather than $10 \log \Lambda$. The input to the program requires $20 \log \Lambda$. The computer program determines the conductivity area (Figure 4-1) of the transmitter and receiver, and whether they are in daytime or nighttime conditions. These computer results are used to define the excitation factors, $10 \log |\Lambda_{m,t}|$ and $10 \log |\Lambda_{n,r}|$ for the appropriate path and time.

The attenuation term, a_{nm} , is the more difficult term to evaluate since it is changing continually along the path. To simplify this procedure, the attenuation term was divided into the following terms:

$$a_{nm} d/10^6 = M \left(a_{a,n} d/10^6 + \sum_{l=1}^L \Delta a_{I,l} \Delta d_l / 10^6 \right) + \sum_{k=1}^K \Delta a_{G,k} \Delta d_k / 10^6 \quad (4-3)$$

where:

$a_{a,n}$

is the average north-south attenuation rate for the sun directly overhead and at the equator for sea water and for the n^{th} order mode. Values of $a_{a,n}$, for $n = 1, 2, 3$; $h = 70$ km and 90 km; and for $10, 13, 20, 25, 30$ kHz are shown in Table 4-2.

M

is the modification of the total ionospheric attenuation rate with direction of propagation.

$\Delta a_{I,l}$

is the change in $a_{a,n}$ for conditions other than the ionospheric conditions used to specify $a_{a,n}$. It is computed for each incremental distance, Δd_l , along the path according to equation (4-4) which follows.

Δd_l

is this incremental distance. It was assumed that $\Delta \alpha_{I,l}$ remains constant over a 4000 km path length with the receiver located at the center of one of these distances; thus, Δd_1 is 2000 km unless the path length is less. The next value, Δd_2 , is 4000 km with the properties of ionosphere defined at the center of this path. Again, if the total length is less than $\Delta d_1 + \Delta d_2$, then Δd_2 is adjusted to give the correct total. This process is continued until the total path is transversed.

$\Delta \alpha_{G,k}$

is the change due to finite ground conductivity. These values are shown in Table 4-1 (ALPD1 denotes $\Delta \alpha_G$ for daytime mode 1, etc.); k denotes the total number of conductivity areas the path transverses. (See the conductivity map of the world, Figure 4-1 and Table 4-4.)

Δd_k

is the total distance the great circle path is within a given conductivity area.

The directional factor, M, is determined from

$$M = 1 - k \sin \phi_a$$

where:

ϕ_a is the direction of propagation with respect to North. Note that true North was used instead of magnetic North. The small error in not using a shifted coordinate system can be neglected.

k is a modifier defined by

$$k = \left(\frac{10^4}{f} \right)^{1/2} K_{10 \text{ kHz}} e^{-\beta |\theta - 90|}$$

where:

θ is the co-latitude in degrees, and
 f is the frequency Hz. The remaining factors are defined by Table 4-3. The values shown in Table 4-3 are expected to be mode dependent; however, because of lack of data, they were assumed to be applicable to the three modes used.

The value $\Delta a_{I,l}$ was assumed equal to the following empirical equation:

$$\Delta a_{I,l} = A f [\sin (90 - 2\theta) + 1] + B f (\sin |z|) \sin^2 \theta \quad (4-4)$$

where:

θ is the co-latitude in degrees,
 z is the sun zenith angle where $z = 0$ when the sun is overhead. When $\sin |z|$ is negative, it is set equal to zero.

f is the frequency in Hz
 A is set equal to 2.2×10^{-5}
 B is set equal to 2.8×10^{-5} .

The values of A and B are expected to be mode dependent; however, for the calculation performed, they were assumed independent. New values of $\Delta\alpha_{I,l}$ were computed at the center of each Δd_l along the path.

When the path is transitional, the average attenuation term is computed by

$$\alpha_{a,n} d/10^6 = \left(\alpha_{a,n}^D d_D + \alpha_{a,n}^N d_N \right) / 10^6$$

where d_D and d_N are respectively the path distance that is day and the path distance that is night. Relative to $\Delta\alpha_{I,l}$ only, no attempt was made to subdivide an incremental distance Δd_l into portions of day or night; however, when the path did change its diurnal characteristics, the appropriate value of $\Delta\alpha_{I,l}$ for the next Δd_l and all remaining values were computed. The value $\Delta\alpha_{G,k} \Delta d_k / 10^6$, however, was split into component daytime and nighttime parts if the transitional zone occurred within the conductivity area.

The conductivity values assigned to the areas shown on Figure 4-1 (see Table 4-4) were based on the maps prepared by Morgan [1968]. Estimates of average effective conductivity were made for areas containing several conductivity values. In order to account for spreading, the spatially distributed nature of our energy sources and the tendency for fields to "recover" on the far side of a low conductivity region, small regions were not weighted heavily when estimating effective conductivity.

Frequency = 10 kHz

TABLE 4-1(A)
DELTA ATTENUATION VALUES AND EXCITATION FACTORS
FOR PROPAGATION MODES 1, 2 & 3, DAY AND NIGHT

ALPD1	ALPN1	ALPD2	ALPN2	ALPD3	ALPN3	EXD1	EXN1	EXD2	EXN2	EXD3	EXN3
0	0	0	0	0	0	+0.8	-1.0	1.3	1.2	0.7	0.9
0.3	0.2	0.4	0.2	~0.5	0.4	0.8	- .8	1.4	1.2	0.7	0.9
0.7	0.5	0.8	0.5	~1.0	0.9	0.9	- .6	1.5	1.3	0.7	0.9
1.2	0.9	1.5	1.1	~1.6	~1.3	1.1	- .3	1.6	1.4	0.7	0.9
2.2	1.4	2.4	1.8	~3.1	~2.6	1.4	0.0	1.7	1.5	0.7	0.9
4.5	2.5	6.1	3.6	~7.9	~6.1	2.0	+0.5	1.8	1.7	0.7	0.9
8.5	6.2	10.5	6.5	~12.3	~10.5	3.0	+1.0	2.0	1.9	0.7	0.9
19	14	22	9.1	~23.5	~14.0	4.0	+1.5	2.1	2.2	0.7	0.9
36	~28	27	12.2	~30.0	~20.0	5.0	+2.0	2.3	2.5	0.7	0.9

CONDUCTIVITY

4
3 x 10⁻²
10⁻²
3 x 10⁻³
10⁻³
3 x 10⁻⁴
10⁻⁴
3 x 10⁻⁵
10⁻⁵

TABLE 4B1(B)
DELTA ATTENUATION VALUES AND EXCITATION FACTORS
FOR PROPAGATION MODES 1, 2 & 3, DAY AND NIGHT

ALPD1	ALPN1	ALPD2	ALPN2	ALPD3	ALPN3	EXD1	EXN1	EXD2	EXN2	EXD3	EXN3
0	0	0	0	0	0	0	-200	1.2	1.3	0.7	1.0
0.35	0.25	0.4	0.3	0.6	0.4	0.2	-1.9	1.2	1.3	0.7	1.0
0.7	0.4	0.9	0.7	1.22	1.0	0.3	-1.7	1.2	1.4	0.7	1.0
1.0	0.6	1.2	0.9	1.4	1.2	0.5	-1.5	1.3	1.5	0.7	1.0
1.3	0.8	1.6	1.3	1.8	1.5	0.7	-1.4	1.4	1.6	0.7	1.0
2.3	1.4	2.7	2.3	3.5	3.0	1.0	-1.0	1.5	1.7	0.7	1.0
5.0	3.0	7.0	5.0	9.0	7.0	2.0	-0.8	1.6	1.9	0.7	1.0
10.5	6.7	12.0	9.7	14.0	12.0	3.5	-0.6	1.8	2.2	0.7	1.0
18.0	9.0	20.0	12.0	21.0	14.0	4.2	-0.4	2.2	2.5	0.7	1.0
23.0	10.0	25.0	14.0	27.0	16.0	5.0	-0.2	2.5	2.8	0.7	1.0
28.0	11.0	31.0	20.0	34.0	23.0	6.0	0	2.8	3.2	0.7	1.0

CONDUCTIVITY

4
 3×10^{-2}
 1×10^{-2}
 5×10^{-3}
 3×10^{-3}
 1×10^{-3}
 3×10^{-4}
 1×10^{-4}
 5×10^{-5}
 3×10^{-5}
 1×10^{-5}

Frequency = 20 kHz

TABLE 4-1(C)
DELTA ATTENUATION VALUES AND EXCITATION FACTORS
FOR PROPAGATION MODES 1, 2 & 3, DAY AND NIGHT

ALPD1	ALPN1	ALPD2	ALPN2	ALPD3	ALPN3	EXD1	EXN1	EXD2	EXN2	EXD3	EXN3
0	0	0	0	0	0	-1.7	-10	1.7	2.2	1.0	1.7
0.35	0.1	0.5	0.4	0.85	0.57	-1.2	-9.5	1.8	2.4	1.0	1.7
0.7	0.2	1.1	1	1.7	1.4	-1.0	-8.9	+1.9	2.5	1.0	1.7
1.5	0.5	2.3	2	2.5	2.1	-0.2	-8	2.2	2.8	1.0	1.7
2.6	1.0	3.8	3.5	5.0	4.2	0.5	-6.6	2.5	3.2	1.0	1.7
6	2.6	7.6	7.7	13	10	2.1	-4	2.7	3.6	1.0	1.7
13.5	5.2	15.2	16	20	17	4.0	-2	-3	4	1.0	1.7
16	3.7	28	20	38	23	5	-7	3.8	5	1.0	1.7
9.5	1.5	36	28	48	32	4.0	-13	4.0	4.0	1.0	1.7

CONDUCTIVITY

4
 3×10^{-2}
 10^{-2}
 3×10^{-3}
 10^{-3}
 3×10^{-4}
 10^{-4}
 3×10^{-5}
 10^{-5}

Frequency = 25 kHz

TABLE 4D1(D)
DELTA ATTENUATION VALUES AND EXCITATION FACTORS
FOR PROPAGATION MODES 1, 2 & 3, DAY AND NIGHT

ALPD1	ALPN1	ALPD2	ALPN2	ALPD3	ALPN3	EXD1	EXN1	EXD2	EXN2	EXD3	EXN3
0	0	0	0	0	0	-3.8	-19	233	2.5	1.3	2.3
0.3	0	0.6	0.4	0.9	.6	-3.5	-18.5	226	2.8	1.3	2.3
0.5	0.1	1.5	1.1	~1.9	1.6	-2.6	-17.7	229	3.1	1.3	2.3
1.3	0.2	2.7	2.2	~2.8	~2.4	-1.7	-16.5	322	3.6	1.3	2.3
2.5	0.3	4.8	4.0	~5.6	~4.7	-0.8	-15	336	4.4	1.3	2.3
6.7	1.5	10	~8.44	~14.5	~11.2	2.0	~2.13	339	3.730	4.730	2.3
12.8	3.0	~19.5	~12	~22	~29	2.30	~2.12	420	~4000	1.3	2.3
8.0	~2.5	~31.0	~12	~40	~26	~25	~21	~2.0	~0	1.3	2.3
6.4	~0.5	~31.0	~11	~46	~36	~6.0	~227	~0.0	~9	1.3	2.3

CONDUCTIVITY

4
3 x 10⁻²
10⁻²
3 x 10⁻³
10⁻³
3 x 10⁻⁴
10⁻⁴
3 x 10⁻⁵
10⁻⁵

Frequency = 30 kHz

TABLE 4-1(E)

DELTA ATTENUATION VALUES AND EXCITATION FACTORS
FOR PROPAGATION MODES 1, 2 & 3, DAY AND NIGHT

ALPD1	ALPN1	ALPD2	ALPN2	ALPD3	ALPN3	EXD1	EXN1	EXD2	EXN2	EXD3	EXN3
0	0	0	0	0	0	-6.5	-34	2.6	1.9	1.7	3.0
0.2	0	0.7	0.3	1.0	.7	-6.0	-29.5	2.9	2.4	1.7	3.0
0.4	0	1.6	1.0	2.1	1.7	-4.8	-28.5	3.3	3.0	1.7	3.0
1.0	0	3.5	2.0	3.1	2.6	-3.6	-27.3	3.8	3.8	1.7	3.0
2.0	0.1	6.0	3.9	6.1	~5.2	-2.3	-26.6	4.7	4.9	1.7	3.0
5.5	0.4	~13	8.5	16.0	~12.3	+0.2	~24	~3.0	8.0	1.7	3.0
7.4	0.5	~22.5	10.8	~25.0	~21.0	-7.0	~26	~1.5	12.0	1.7	3.0
5.0	0.4	~32	~6	~35	~12	~-16.0	~-39	~0.0	-9.0	1.7	3.0
4.2	0	~20	~0	~23	~5	~-26	~-45	~-4.0	-14.0	1.7	3.0

CONDUCTIVITY

4
3 × 10⁻²
10⁻²
3 × 10⁻³
10⁻³
3 × 10⁻⁴
10⁻⁴
3 × 10⁻⁵
10⁻⁵

TABLE 4-2

Average North-South Attenuation at the Equator
With the Sun Directly Overhead

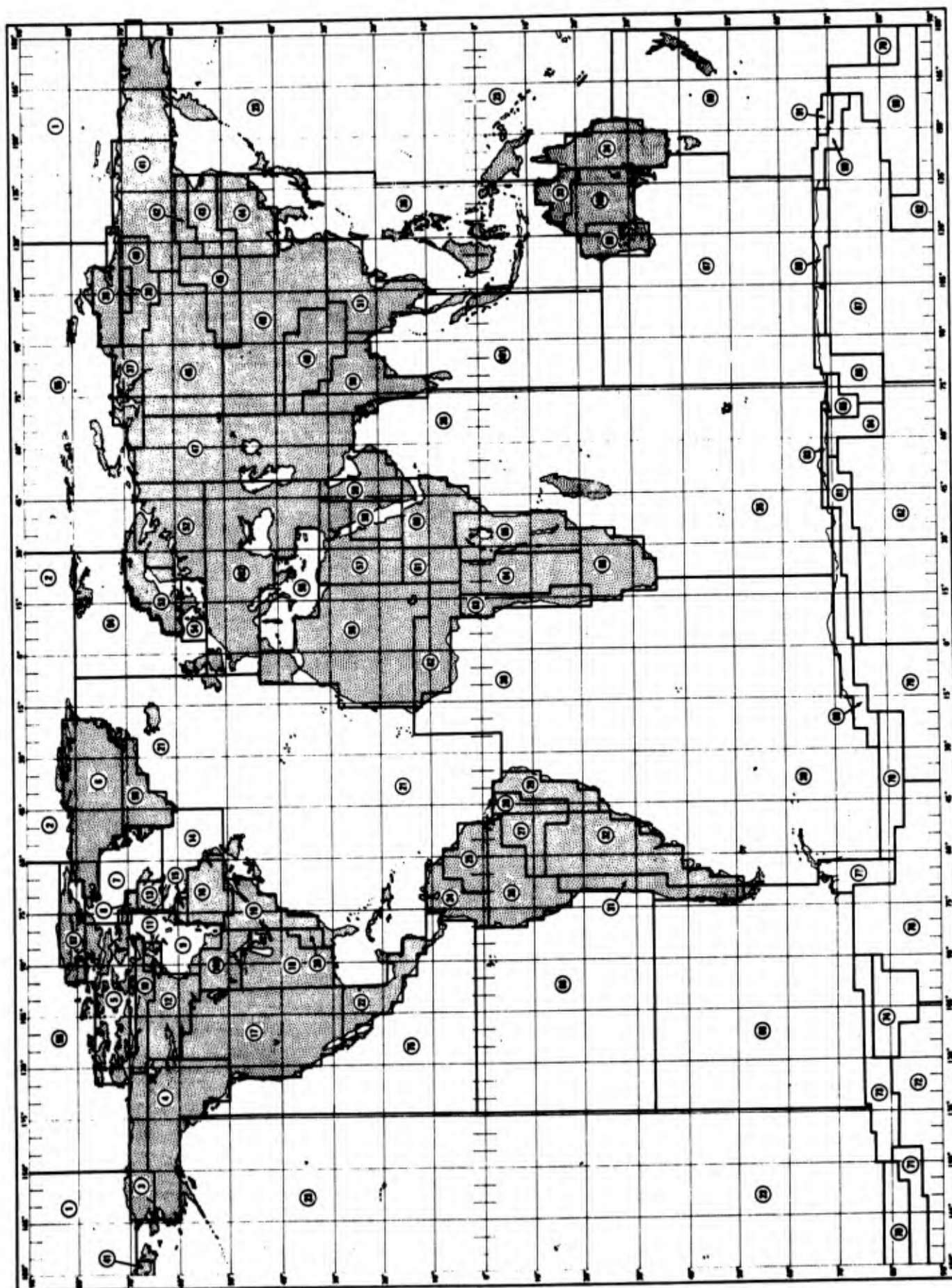
Frequency <u>kHz</u>	<u>a_{1D}</u>	<u>a_{2D}</u>	<u>a_{3D}</u>	<u>a_{1N}</u>	<u>a_{2N}</u>	<u>a_{3N}</u>
10	2.5	23	32	1.0	5.3	21
13	2.1	15	20	0.9	5.5	13
20	1.75	8.3	14.5	0.85	1.8	8.5
25	2.1	6.2	11.5	1.1	1.3	5.0
30	2.65	5.0	10.5	1.65	1.0	5.0

TABLE 4-3

<u>Condition</u>		<u>K_{10 kHz}</u>	<u>β</u>
<u>Direction</u>	<u>Diurnal</u>		
W → E	Day	0.68	.04
W → E	Night	0.7	.03
E → W	Day	1.1	.04
E → W	Night	2.0	.03

TABLE 4-4 EFFECTIVE CONDUCTIVITY FOR AREAS GIVEN ON FIGURE 4-1

AREA	σ	AREA	σ	AREA	σ	AREA	σ	AREA	σ
1	4	28	1×10^{-2}	55	4	82	1×10^{-5}		
2	4	29	3×10^{-3}	56	1×10^{-2}	83	1×10^{-4}		
3	1×10^{-3}	30	4	57	1×10^{-2}	84	3×10^{-5}		
4	5×10^{-3}	31	3×10^{-3}	58	1×10^{-2}	85	1×10^{-4}		
5	1×10^{-2}	32	1×10^{-2}	59	1×10^{-2}	86	3×10^{-5}		
6	1×10^{-5}	33	1×10^{-2}	60	5×10^{-3}	87	1×10^{-5}		
7	4	34	1×10^{-2}	61	1×10^{-3}	88	4		
8	5×10^{-5}	35	4	62	3×10^{-3}	89	3×10^{-5}		
9	4	36	4	63	3×10^{-3}	90	3×10^{-5}		
10	1×10^{-4}	37	3×10^{-3}	64	5×10^{-3}	91	1×10^{-4}		
11	3×10^{-3}	38	1×10^{-3}	65	3×10^{-3}	92	3×10^{-5}		
12	3×10^{-4}	39	3×10^{-4}	66	1×10^{-2}	93	1×10^{-4}		
13	1×10^{-3}	40	3×10^{-4}	67	4	94	4		
14	4	41	1×10^{-3}	68	4	95	4		
15	1×10^{-4}	42	1×10^{-4}	69	4	96	4		
16	1×10^{-3}	43	3×10^{-4}	70	5×10^{-3}	97	1×10^{-3}		
17	1×10^{-2}	44	1×10^{-2}	71	3×10^{-4}	98	1×10^{-5}		
18	3×10^{-2}	45	1×10^{-3}	72	3×10^{-5}	99	1×10^{-2}		
19	3×10^{-3}	46	1×10^{-2}	73	3×10^{-5}	100	1×10^{-2}		
20	1×10^{-3}	47	1×10^{-2}	74	1×10^{-5}	101	4		
21	4	48	1×10^{-2}	75	4	102	1×10^{-2}		
22	1×10^{-2}	49	3×10^{-3}	76	3×10^{-5}	103	3×10^{-3}		
23	4	50	5×10^{-3}	77	1×10^{-4}				
24	1×10^{-2}	51	5×10^{-3}	78	1×10^{-4}				
25	1×10^{-3}	52	1×10^{-2}	79	3×10^{-5}				
26	1×10^{-2}	53	3×10^{-3}	80	1×10^{-4}				
27	3×10^{-3}	54	4	81	3×10^{-5}				



Conductivity Area Designations (See Table 4-4 For Conductivity Values)

Figure 4-1

5.0 STATISTICS OF THUNDERSTORMS AND LIGHTNING

In addition to the distribution of thunderstorms and lightning discharges geographically, our noise prediction model must include their distribution diurnally. Furthermore, since this project called for the prediction of the standard deviation of atmospheric noise as well as the prediction of mean values, it was important to determine the statistical distribution of thunderstorms and lightning from day-to-day, month-to-month, and year-to-year. Only very fragmentary results for limited regions and limited time periods were available in the literature for any of the statistical distributions. We therefore sought and obtained data adequate to compute the statistics required.

5.1 Description of Data Obtained

All of the thunderstorm data useful for statistical analysis was obtained from the National Weather Records Center courtesy of the Naval Weather Service.

The Russian-Chinese data referred to in Section 2.2.1 which was obtained from NWRC tabulation CL-6817 provided data on the diurnal variation of thunderstorms for these regions of the world. The data for Szemao, China are shown in Table 5-1. Since this data was taken only every three hours, it is not the best data for determining diurnal distributions, but it is the only data for that part of the world and provided useful information. The original United States Air Force A and B summaries of surface meteorological data provided all other diurnal distribution data outside of the United States. These original, or "old" A and B summaries contained records of hourly observations which are ideal for this application. The new A and B summaries which are presently under preparation and will replace the original summaries contain only three hour data. Table 5-2 is a list of the stations for which A and B summary data was obtained.

Table 5-1

Data from Tabulation CL 6817 - National Weather Records Center

PERCENTAGE FREQUENCY OF THUNDERSTORM OCCURRENCE												
56964 SZEMAO CHINA												
HR/GCT	JAN	FEB	MAR	APR	MAY	JUN	JUL	AUG	SEP	OCT	NOV	DEC
00	22 33 N 101 02 E											
PCT			1.3				1.7	1.2	.9	1.9		
OBS	81	74	80	76	73	48	60	83	112	105	82	82
03												
PCT												
OBS	51	66	89	77	76	64	70	80	104	102	51	53
06												
PCT				1.3	5.6	14.8	1.5	11.8	10.1	1.8		
OBS	74	72	85	77	71	54	66	93	109	114	82	78
09												
PCT			8.7	9.3	9.2	13.9	21.6	13.2	13.6	7.6		
OBS	43	37	69	75	76	79	74	91	103	105	45	41
12												
PCT	3.8		7.4	3.7	6.5	9.9	12.8	9.9	6.5	4.4		
OBS	80	76	81	81	77	81	86	91	108	114	76	79
15												
PCT	1.8	2.1	1.8	5.9	3.5	3.9	4.2		1.3			
OBS	55	47	56	51	57	51	48	84	77	80	51	53
18												
PCT			4.8	1.2	1.2	1.3	2.6	5.4		1.8		
OBS	75	71	84	81	84	80	77	92	97	114	72	77
21												
PCT			2.7	5.4			1.4	6.5	3.7			
OBS	50	50	75	74	80	78	74	93	109	111	53	55

PCT Percentage of observations when thunderstorms were observed.

OBS Total number of observations.

TABLE 5-2

List of Stations from Old Air Force A & B Summaries

<u>WBAN No.</u>	<u>NAME</u>	<u>No. of Years of Data</u>
33308	Adana, Turkey	8
11603	Aguadilla, Puerto Rico	23
15033	Alconbury, England	7
26401	Anchorage, Alaska	22
41207	Angeles, Luzon	17
14508	Argentia, Newfoundland	8
43306	Ashiya Kyushu, Japan	9
34187	Aviano, Italy	7
94795	Bagotville, Que	9
10701	Balboa, Canal Zone	17
48455	Bangkok, Thailand	9
27401	Barter Island, Alaska	16
13023	Ben Guerir, Morocco	10
35104	Berlin, Germany	10
13602	Bermuda	10
34049	Bitburg, Germany	10
60703	Canton Island	20
34052	Chaumont, France	10
26407	Fairbanks, Alaska	18
46763	Falingkong, Formosa	6
15605	Fort Chimo, Quebec	8
35032	Frankfurt, Germany	10
44402	Furumaki, Japan	10
10502	Georgetown, Br. Guiana	8
15607	Goose, Newfoundland	12
12714	Grand Turk Island	8
41414	Guam	15
11706	Guantanamo Bay, Cuba	10
21504	Hilo, Hawaii	14
42401	Iwo Jima	11
17220	Izmir, Turkey	10
21603	Johnston Island	18
43223	Kangnung, Korea	7
16201	Keflauik, Iceland	15
11704	Kingston, Jamaica	8
40309	Koror Island	12
43219	Kunsan, Korea	10

TABLE 5-2 (cont.)

WBAN No.	NAME	No. of Years of Data
40604	Kwajalein Atoll	18
22536	Lihue, Kauai, Hawaii	13
14011	Madrid, Spain	6
22701	Midway Island	10
13019	Nouasseur, Morocco	9
42206	Okinawa	6
43242	Osan-ni, Korea	10
20604	Palmyra Island	25
40504	Ponape Caroline Island	12
03135	Prestwick, Scotland	17
13025		5
50801	Salinas, Ecuador	5
13601	St. George Bermuda	11
43307	Tokyo, Japan	10
43307	Tokyo, Japan	9
11610	Trinidad	8
40505	Truk Caroline Island	15
41606	Wake Island	10
35050	Wethers Field, England	10
35010	Wiesbaden, Germany	10
14010	Zaragoza, Spain	6

Table 5-3 is a copy of data similar to that obtained from the A and B summaries. This data for Atlanta, Georgia was obtained from the United States Air Force Air Weather Service tabulation number CL-8307. This tabulation contains data for 117 stations throughout the United States. These tabulations give the total number of observations made and the total number of thunderstorms which were observed. As is evident from the total number of observations, the data for Atlanta, Georgia represents 14 years of data collection. All of the data in this tabulation are for a minimum of 10 years. Table 5-3 shows only the first six months for Atlanta, but all 12 months were presented for all stations. In total, then, we had diurnal distribution data from 257 stations around the world.

We obtained data on the statistical distribution, i.e. the variation of thunderstorm days per month from year-to-year, from climatological record books obtained from the National Weather Records Center. These climatological records contained records of the number of thunderstorm days for each month of each year for 50 to 80 years. Table 5-4 is a copy of the first page of the record for Toledo, Ohio. Records from 130 stations representing all 50 states and Puerto Rico were obtained. Similar records were obtained from foreign publications, on file at NWRC, for the locations listed on Table 5-5. From 4 to 36 years of data were available from these locations. Table 5-6 presents the 11 years of data available for Tororo, Uganda. The data from these foreign locations, although very limited, were for the most part from regions of very high thunderstorm activity and were important in determining the variability of thunderstorm activity for such regions.

Since most of the lightning counter data discussed in Section 3.1.2 provided hourly or monthly totals for specific days and months, this data was quite suitable for calculating the statistics of the frequency of lightning discharges. The data was also used to plot diurnal distributions of

Table 5-3

Number of Thunderstorms Observed at Atlanta, Georgia
Over a 14 Year Period.

STA	HOUR, LST	JAN	FEB	MAR	APR	MAY	JUN
13874	00		1	3	3	9	5
	OBS	432	395	434	420	434	420
	01		3	1	8	7	4
	OBS	433	395	434	420	434	420
	02	2	5		6	2	1
	OBS	433	395	434	420	434	419
	03	1	3	3	4	5	2
	OBS	433	395	434	420	434	420
	04		2	5	3		1
	OBS	433	395	434	420	434	420
	05	1	2	4	2	1	2
	OBS	432	395	434	420	434	420
	06	2	1	2	2	2	
	OBS	434	395	434	420	434	419
	07			3	2	1	
	OBS	434	395	434	420	434	420
	08			2	3	2	1
	OBS	433	395	434	420	434	420
	09			2	3	2	1
	OBS	434	394	433	420	434	420
	10	1		2	2	3	
	OBS	434	395	434	420	433	420
	11	1		1	2	2	6
	OBS	434	393	434	420	433	420
	12			1	3	6	9
	OBS	434	395	434	420	434	420
	13		1	1	6	5	13
	OBS	434	395	434	420	434	420
	14	1	2		1	8	12
	OBS	434	395	434	420	434	420
	15		1	1	4	8	16
	OBS	434	395	434	420	434	420
	16	1		2	6	13	22
	OBS	434	395	434	420	434	419
	17	4		6	4	8	19
	OBS	434	395	434	420	434	420
	18	2	1	6	4	16	17
	OBS	434	395	434	419	434	420
	19		1	6	7	12	22
	OBS	434	395	434	420	434	420
	20	1	1	6	11	12	20
	OBS	434	394	434	420	434	419
	21	2		3	8	7	12
	OBS	434	395	434	420	434	419
	22	1		1	7	7	3
	OBS	434	395	434	420	434	417
	23		1		2	9	6
	OBS	434	395	434	420	434	420
	ALL HRS	20	25	61	103	147	194
	TOTAL OBS	10407	9476	10415	10079	10414	10072

OBS Total observations made.

iii

WEATHER—NUMBER OF DAYS WITH FOG, HAIL, THUNDERSTORMS, TOLEDO, OHIO

YEAR.	JANUARY.	FEBRUARY.	MARCH.	APRIL.	MAY.	JUNE.	JULY.	AUGUST.	SEPTEMBER.	OCTOBER.	NOVEMBER.	DECEMBER.	ANNUAL.
1871	0	0	0	2	1	3	5	9	2	0	1	1	2
1872	0	7	0	0	1	2	5	5	5	1	1	0	1
1873	0	0	0	1	3	3	5	3	2	1	0	0	0
1874	0	0	0	0	0	3	4	2	3	1	0	2	0
1875	0	0	0	1	1	2	3	1	0	4	0	1	0
1876	0	0	0	0	1	2	1	0	0	0	1	0	0
1877	0	0	0	1	3	2	2	3	0	0	2	0	1
1878	0	0	0	1	0	3	2	0	0	0	0	0	0
1879	0	0	0	2	0	3	4	6	3	0	1	0	0
1880	0	0	0	1	6	5	3	10	4	0	1	0	0
1881	0	0	0	1	0	2	8	5	0	0	2	0	0
1882	0	0	0	1	1	2	12	2	10	5	2	0	0
1883	0	0	0	1	3	5	5	7	0	4	2	0	1
1884	1	0	0	2	0	3	14	6	1	2	2	0	0
1885	0	0	0	0	0	3	6	8	6	1	1	0	0
1886	0	1	0	0	1	9	4	2	4	0	0	0	1
1887	0	0	2	0	0	4	5	6	1	3	0	0	0
1888	0	0	0	0	2	3	4	3	0	1	0	0	0
1889	0	0	0	0	3	4	6	3	0	1	0	0	0
1890	0	0	0	2	3	4	5	4	0	1	0	0	0
Sums,	16	18	52	163	310	691	1031	896	595	3511	199	514	370
MEANS,	1	1	4	1	2	3	5	4	3	2	1	1	4

REMARKS: No data previous to 1890.

TABLE 5-5

A tabulation of "Days with Thunderstorms" for the following locations were obtained from Foreign Publications

Nairobi, Kenya
Tororo, Uganda
Entebbe Airport, Uganda
Tabora Airport, Tanzania
Pretoria, South Africa
Gaberones, South Africa
Maseru, Lesotho
Harrismith, South Africa
Johannesburg, South Africa
Abidjan-Aero, Ivory Coast
Lome-Aero, Togo
Huancayo, Peru
Puno, Peru
Cobija, Bolivia
Riberalta, Bolivia
Trinidad, Bolivia
Analalava, Madagascar
Tananarive, Madagascar
Penang Aerodrome, Malaysia
Sitiawan, Malaysia
Subang Apt., Kuala Lumpur, Malaysia
Mersing, Malaysia

Table 5-6

WB Form 920-11A
(Formerly 1078-A)

U. S. DEPARTMENT OF COMMERCE, WEATHER BUREAU

Station, Tororo County, _____ State, Uganda

Latitude, 00° 41' N Longitude, 34° 10' E Elevation, 3842 feet.

Data, Days with Thunderstorms[illegible]

REMARKS

SOURCE: East African Meteorological Department, The Weather of East Africa.

National Weather Records Center
Environmental Science Services Administration
Federal Building, Asheville, N. C. 28801

Commerce-Weather Bureau, Washington, D. C.

lightning occurrence. From 1 to 10 years of data were obtained from the locations listed Section 3.1.2. The tabulations from which this data were obtained were not suitable for reproduction, so no examples are presented for the lightning data in this report.

The statistical analysis of the data described and the results therefrom are discussed in the following sections.

5.2 The Diurnal Variation of Thunderstorms and Lightning Charges

It would have been impossible and useless to plot the diurnal distribution of thunderstorms at each of the 257 stations for all 12 months of the year. Since the noise sources, or transmitters, are computed for 5° by 5° and 15° by 15° regions (see Section 3.3), it was decided that whenever possible, diurnal distributions should be plotted for a combination of the data obtained from regions approximating these sizes. The data were actually plotted for each individual station on a single figure for all stations within selected regions. Plots for some 50 groups, or regions, around the world were made for January, April, July, and October. This represents, we are sure, the most complete compilation ever made on the diurnal distribution of thunderstorms.

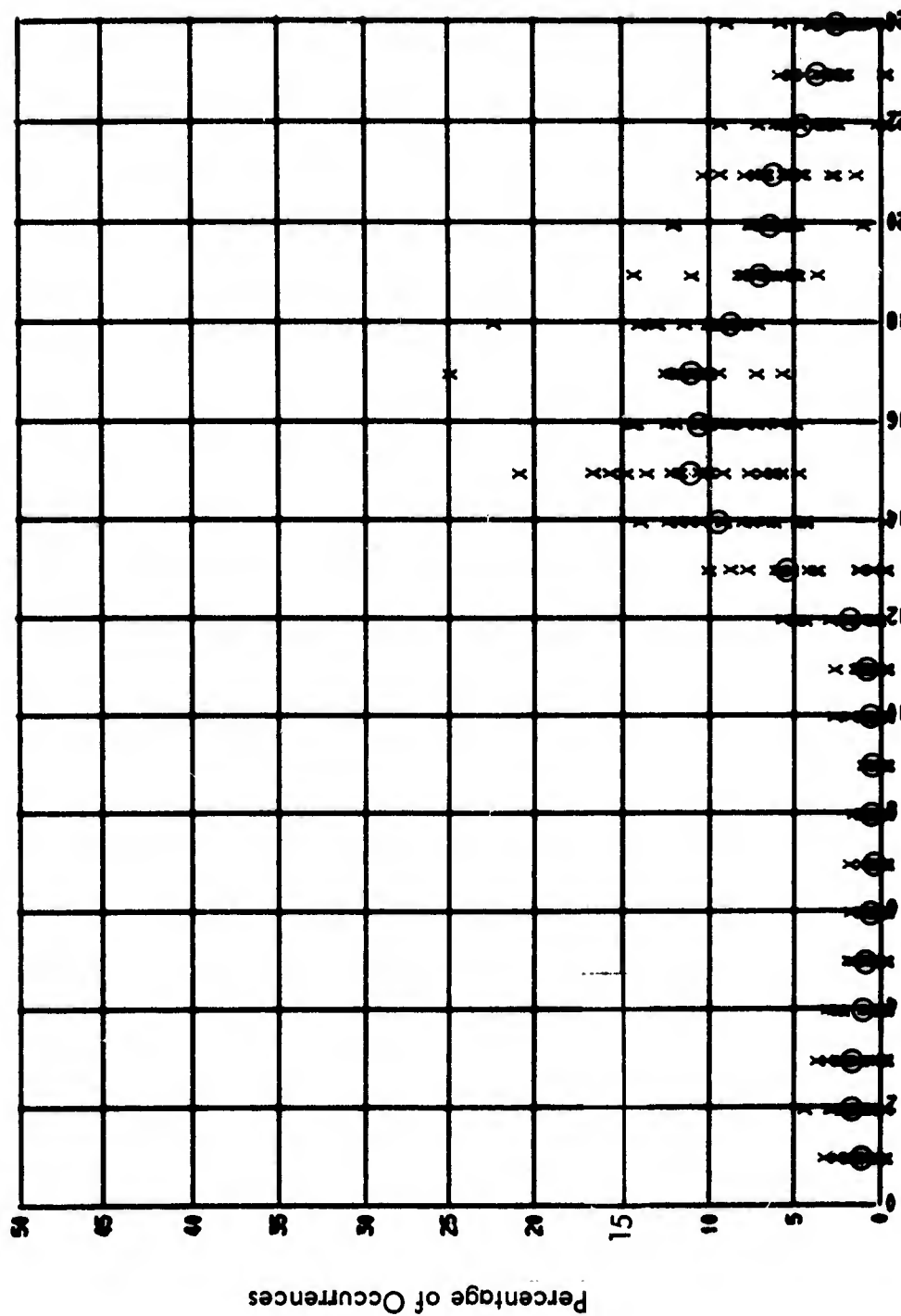
The compilation of the percentage of thunderstorm occurrences for each hour and the plotting of each computed value was accomplished entirely by computer. Copies of the actual plots for a representative sample are shown in Figures 5-1 through 5-6. Figure 5-1 shows a good deal of consistency in the diurnal pattern of thunderstorm occurrence for the states represented. It is obvious from Figure 5-2 and 5-3 that some of the locations in these states have appreciably different diurnal patterns. Figure 5-4, which is data plotted for a single station, illustrates the relatively simple and well behaved plots which would probably be obtained for any single station. For the noise prediction model being developed it would, of course,

have been impossible to use the individual diurnal patterns to represent the localized differences, since this would have required using thousands of noise transmitters for each calculation of expected noise instead of the 100 or less actually used. The value of doing so would have been very questionable anyway, since the localized effects will certainly be averaged out in the final analysis.

Figures 5-2 and 5-3 also serve to illustrate the change in diurnal patterns from one season to the next. This occurs for virtually all regions of the world, although it is less pronounced for tropical areas.

We have mentioned earlier in this report that there is a widely held misconception that the occurrence of storms over oceans have a flat diurnal pattern, i.e. the storms have been reported to show no preference for any hour of the day. The reason for this misconception is clearly evident upon examining Figure 5-5. This data, for all Pacific islands, certainly would lead one to prescribe a flat diurnal pattern for the oceans. It is our contention that data from islands show virtually no recognizable diurnal pattern because such stations observe a mixture of storms which are generated over the oceans, caused by a cooling of the upper layers of the clouds, and storms generated over the island itself caused by a heating of the land and the lower atmosphere. That ocean storms do have a very pronounced diurnal pattern is evident from Figure 5-6. This data shows high percentages of occurrence because the computations were erroneously made for hourly data, whereas the data used were the six hour data obtained from the National Weather Records Center (see Section 2.2.1). This plot represents the data from virtually all of the 10° ocean sectors wherein appreciable thunderstorm activity occurs. The data from each 10° by 10° region has been plotted relative to its local standard time. These results are in good agreement with the hypothesis proposed by Doyne J. Sartor of the National Center For Atmospheric Research. In other words, if

DIURNAL CURVE OF PERCENTAGE OF THUNDERSTORM OCCURRENCES for Colo. - Wyo. - Mont.



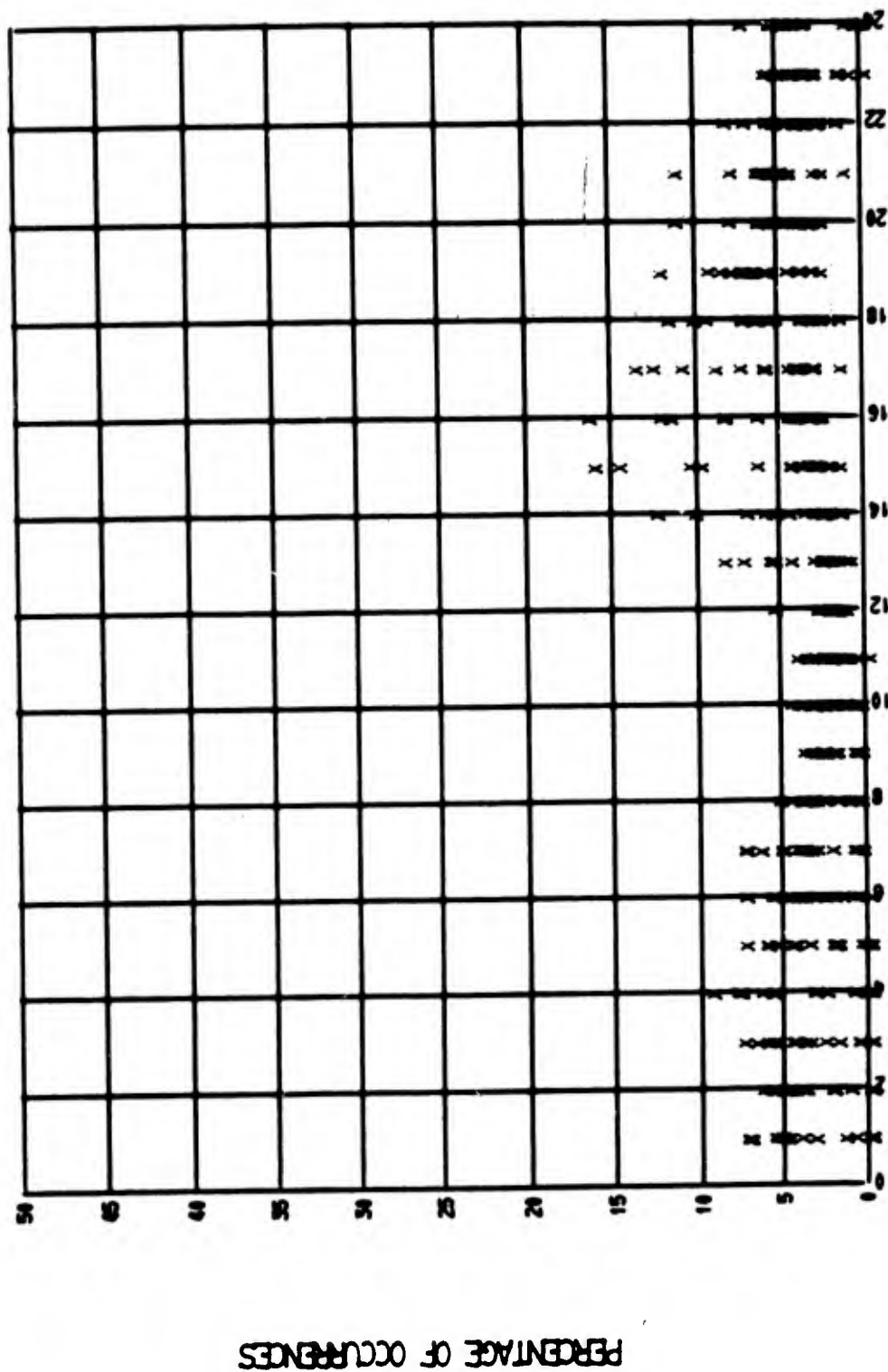
TIME

MONTH 7

Figure 5-1

DIURNAL CURVE OF PERCENTAGE OF THUNDERSTORM OCCURRENCES

FOR MINN. - IOWA, - MO. - ARK. - LA. - MISS. - ILL. - WIS

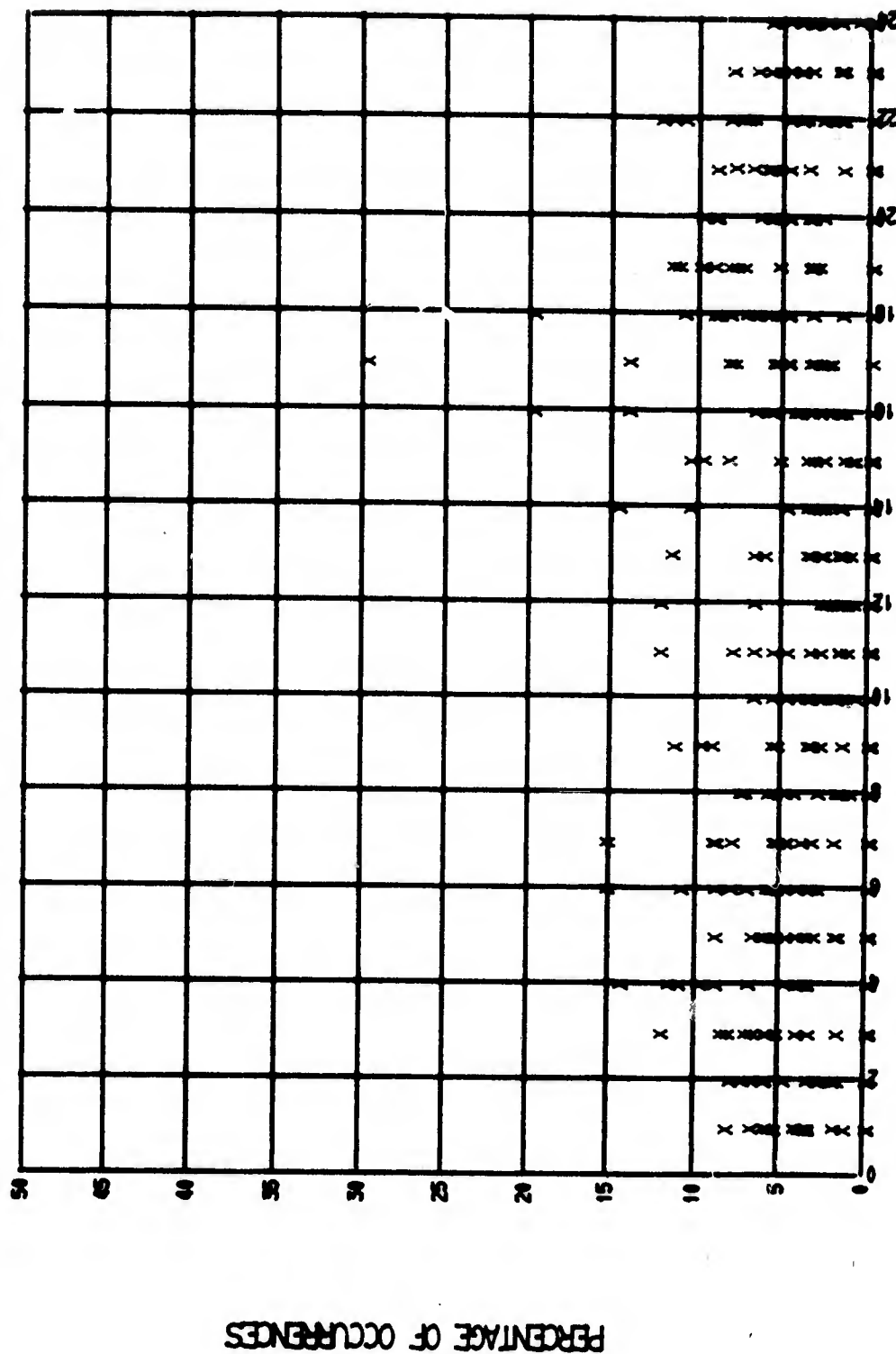


TIME

FIGURE 5-2

DIURNAL CURVE OF PERCENTAGE OF THUNDERSTORM OCCURRENCES

FOR MINN. - IOWA - MO. - ARK. - LA. - MISS. - ILL. - WIS.



TIME

FIGURE 5-3

DIURNAL CURVE OF PERCENTAGE OF THUNDERSTORM OCCURRENCES

FOR BANGKOK, THAILAND

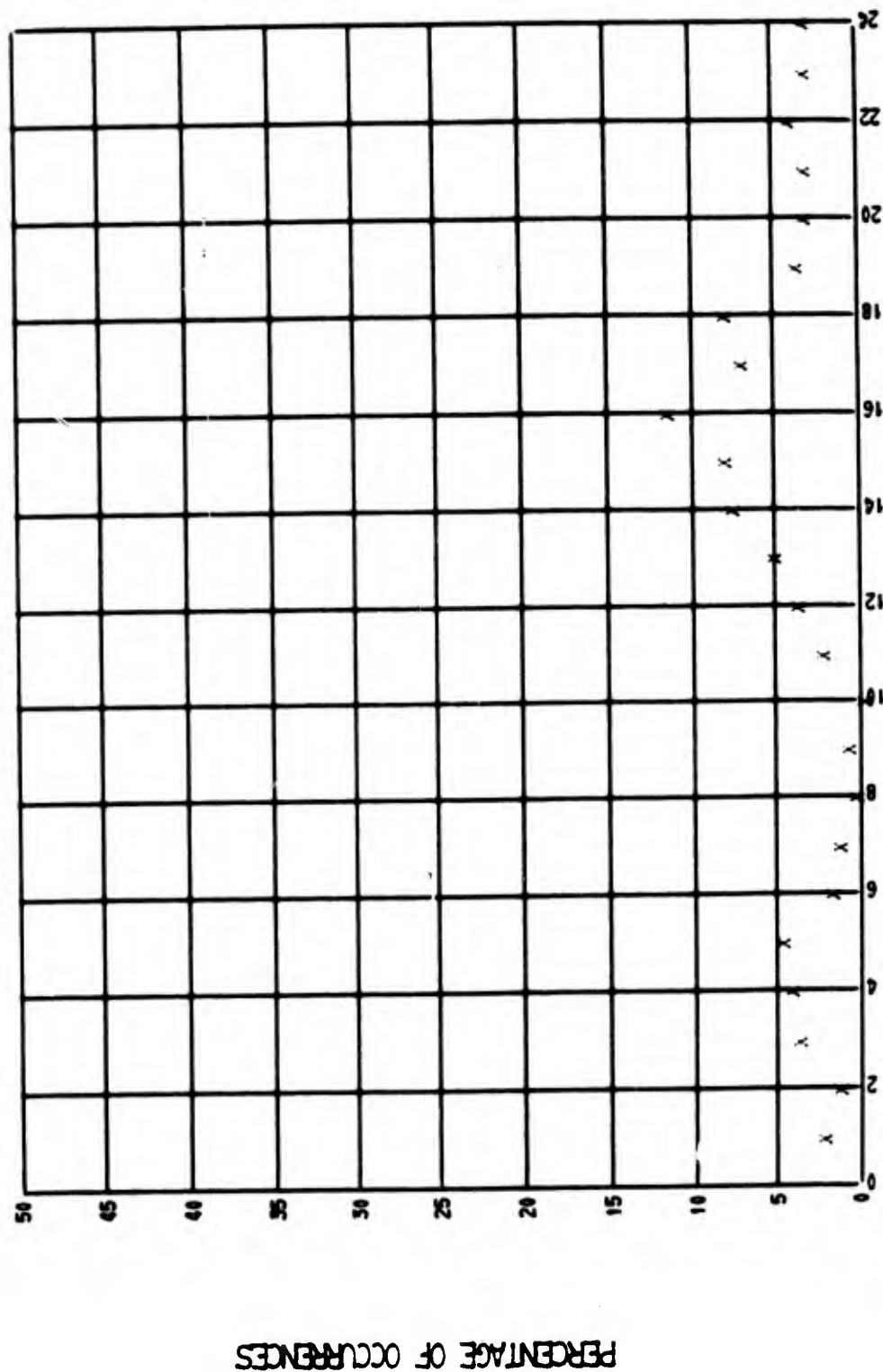
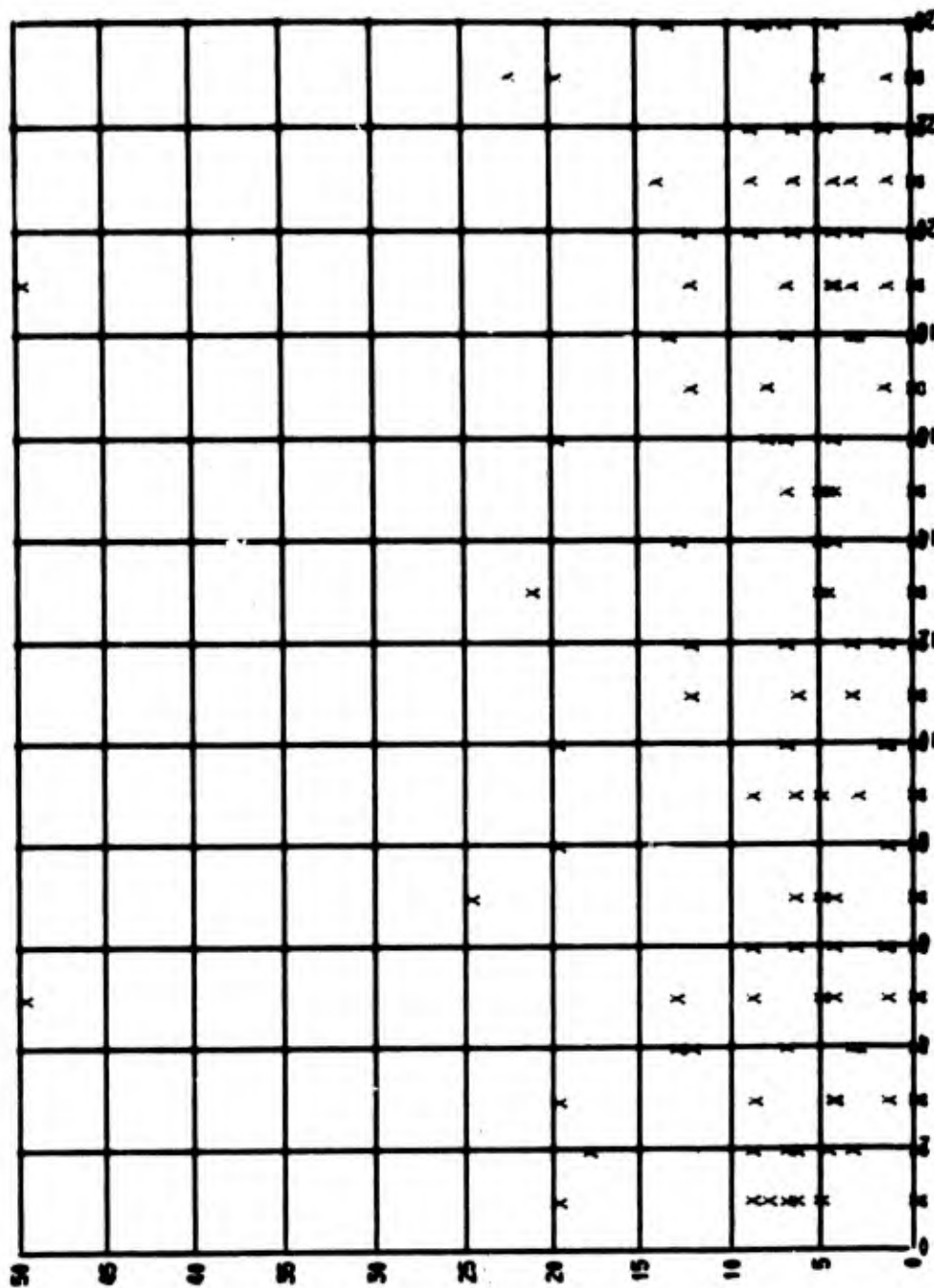


FIGURE 5-4

DIURNAL CURVE OF PERCENTAGE OF THUNDERSTORM OCCURRENCES

FOR ALL PACIFIC ISLAND



TIME

FIGURE 5-5

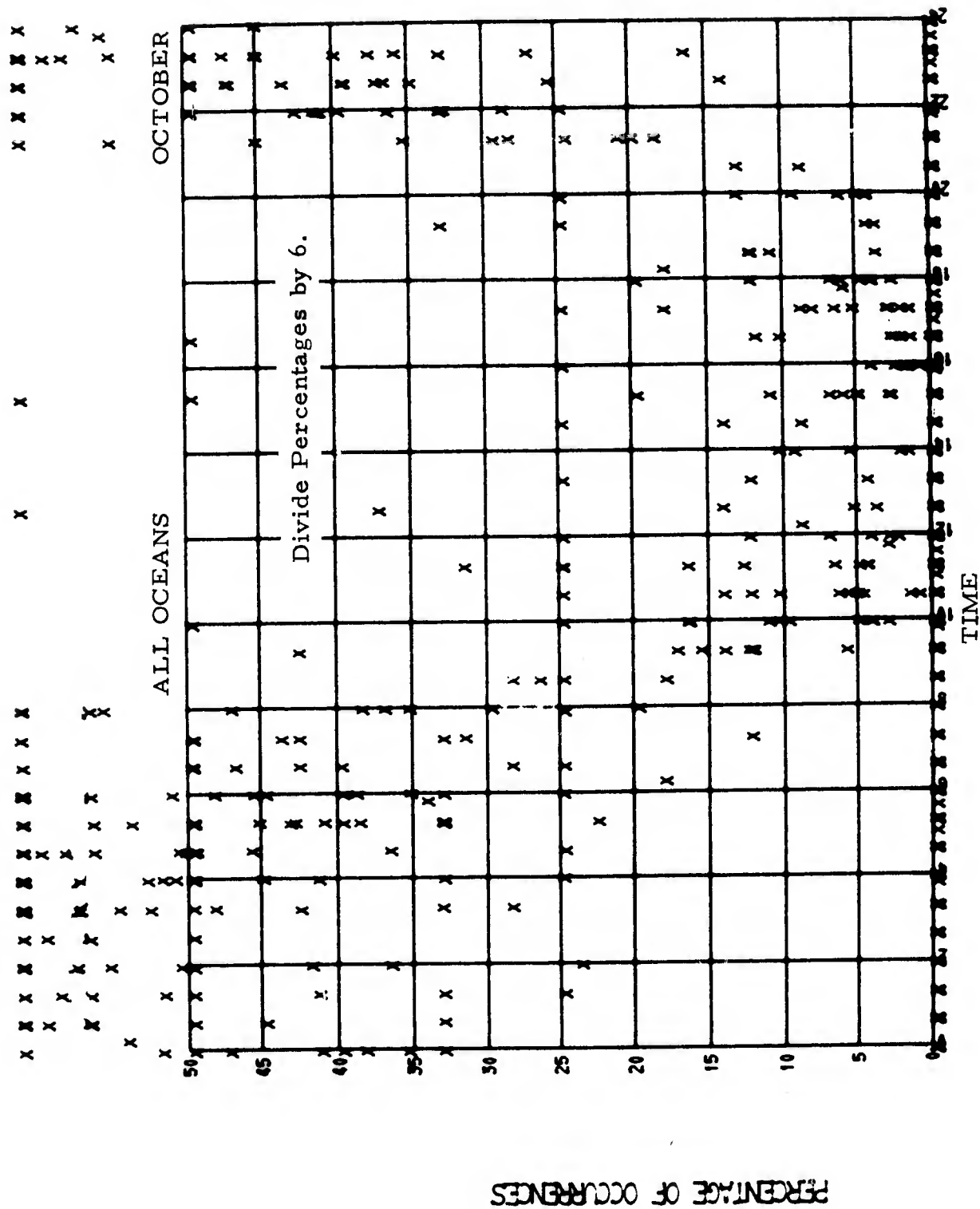


FIGURE 5-6 DIURNAL CURVE OF PERCENTAGE OF THUNDERSTORM OCCURRENCES

storms generated over the ocean are caused by instabilities set up by the cooling of the upper reaches of the clouds and the constant temperatures of the lower level maintained by the ocean temperature, then one would expect the maximum occurrence of ocean thunderstorms to be during the early morning hours and the minimum occurrence to occur during middle afternoon hours. Such a pattern is clearly evident from Figure 5-6.

As would be expected from the preceding discussions, results from land stations near a region wherein storms are actively generated over the ocean tend to show a double peak in thunderstorm activity during the day. This is evident to a certain extent on Figure 5-4 for Bangkok. It was even more evident in the month of July for Bangkok and can be noted in the records for several other locations, such as Puerto Rico, Cuba, Formosa, etc. A great deal of care and a certain amount of guesswork was therefore involved in the selection of diurnal patterns for the 15° by 15° regions containing a mixture of land and sea areas. This was particularly difficult for such areas as Indonesia, the Philippines, Japan, the Mediterranean, Central America, etc. The thunderstorm day maps were examined to determine if the thunderstorm activity seemed to be centered primarily over land or water before a diurnal pattern was assigned.

Examples of diurnal plots of the occurrence of lightning discharges as determined from lightning counter data at ESSA, Boulder, Colorado and Slough, England are shown on Figures 5-7 and 5-8. Comparing Figures 5-1 and 5-7, a good agreement is noted between the diurnal distribution of thunderstorms and the diurnal distribution of lightning discharges. This was not unexpected.

Figure 5-9 illustrates the change in the diurnal distribution of thunderstorms for different regions within the United States. The very low activity during the hours just before noon, followed a very high peak in

BOULDER, COLORADO LONG -105 LAT 40 MONTH /

x x

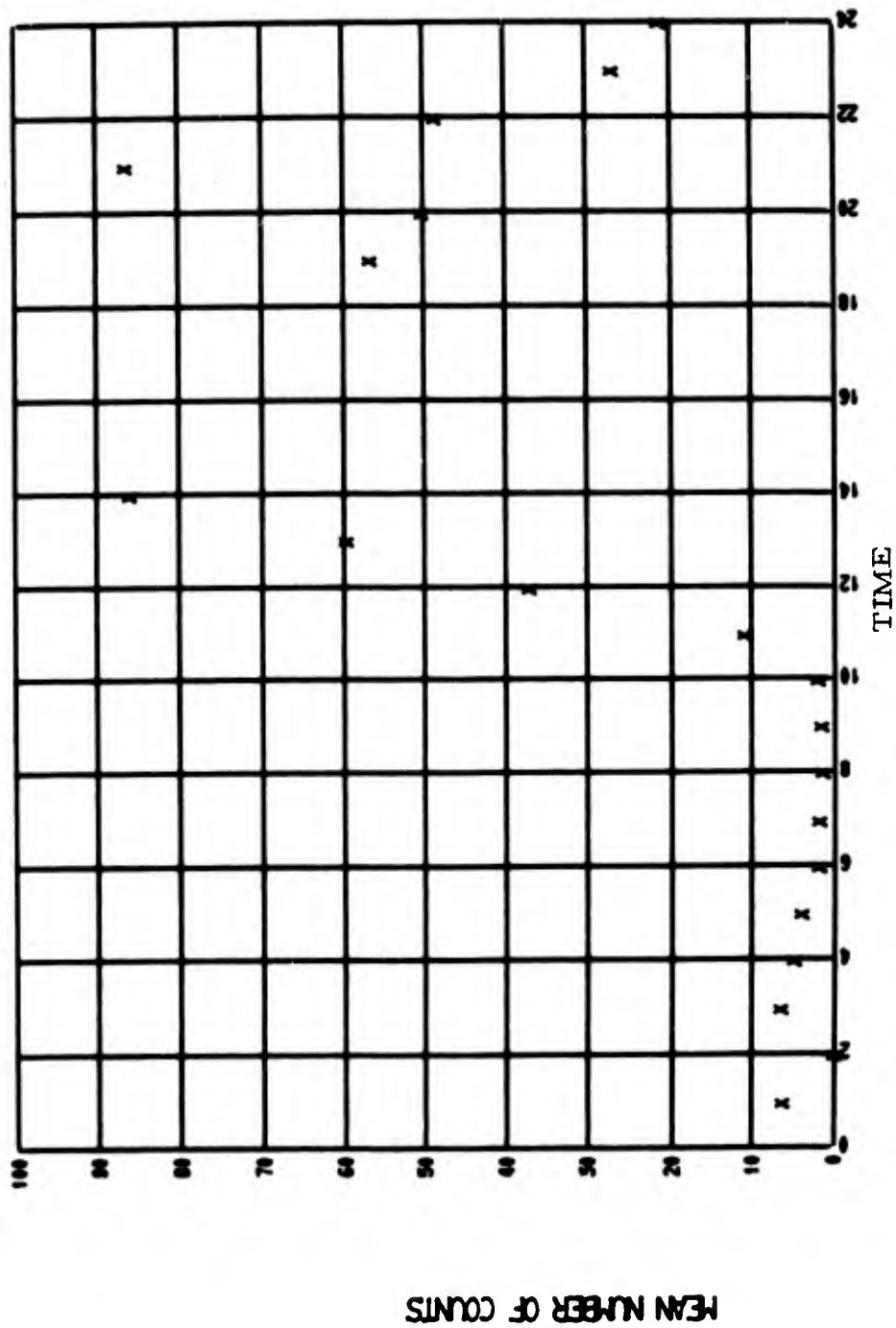


FIGURE 5-7 DIURNAL CURVE OF LIGHTNING COUNTS

SLOUGH, ENGLAND LONG 0 LAT 51 MONTH 10

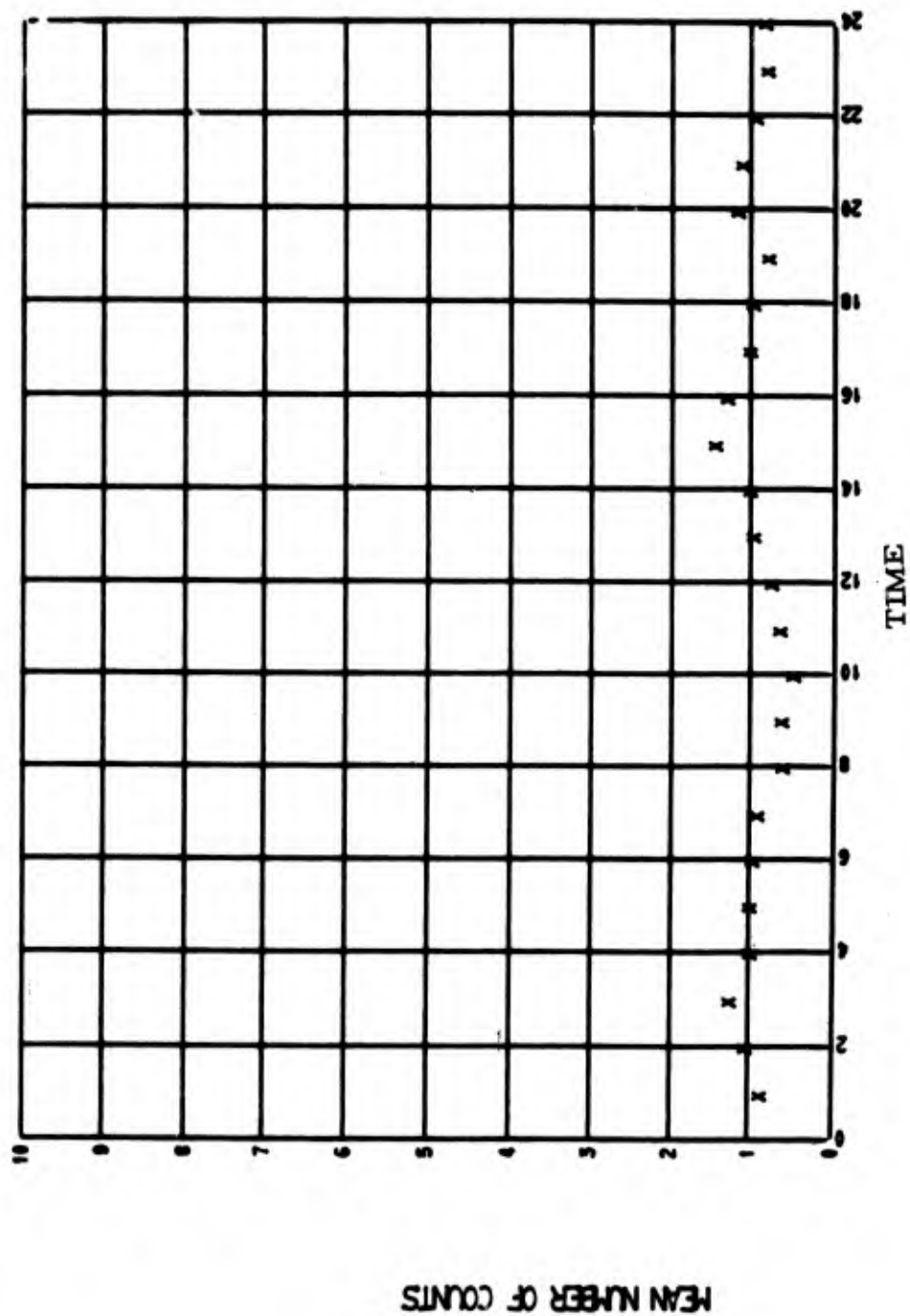


FIGURE 5-8 DIURNAL CURVE OF LIGHTNING COUNTS

activity in the early afternoon (groups 2 and 3) appear to be representative of regions where thunderstorms are generated primarily from thermal convection and/or orographic effects. Locations where frontal activity tends to play an important part in thunderstorm generation tend to have less extremes in their diurnal patterns.

Figure 5-10 presents representative curves for a variety of locations around the world. The double maximum noted for Japan and Korea is another example of the effect of having a mixture of land and sea storms. Why the data from the Philippines does not show this effect is not known. The data from Helsinki, Finland is particularly interesting in that a peaking in activity occurs very shortly after noon. It is probable that this is due to the very long days and short nights enjoyed by Finland during the month of July.

Figure 5-11 illustrates the change in diurnal patterns from one season to the next for the same location. A change in the thunderstorm generation processes is clearly evident from these results.

The fallacy in the use of two or three diurnal patterns for the entire world for all months is clearly evident. It should be noted that there were outstanding regions where no diurnal distribution data was available. This included South America and much of Africa. Climatological similarities between these regions and other locations was used to select a diurnal pattern for use in the noise computation. These were modified as appropriate based on the comparison of predicted and measured values for these locations. The diurnal pattern for the middle month of each season was used for all three months of the season since changes from one month to the next are relatively small for most locations. If in the future more and better data is obtained for more locations, the model can be made even more exact.

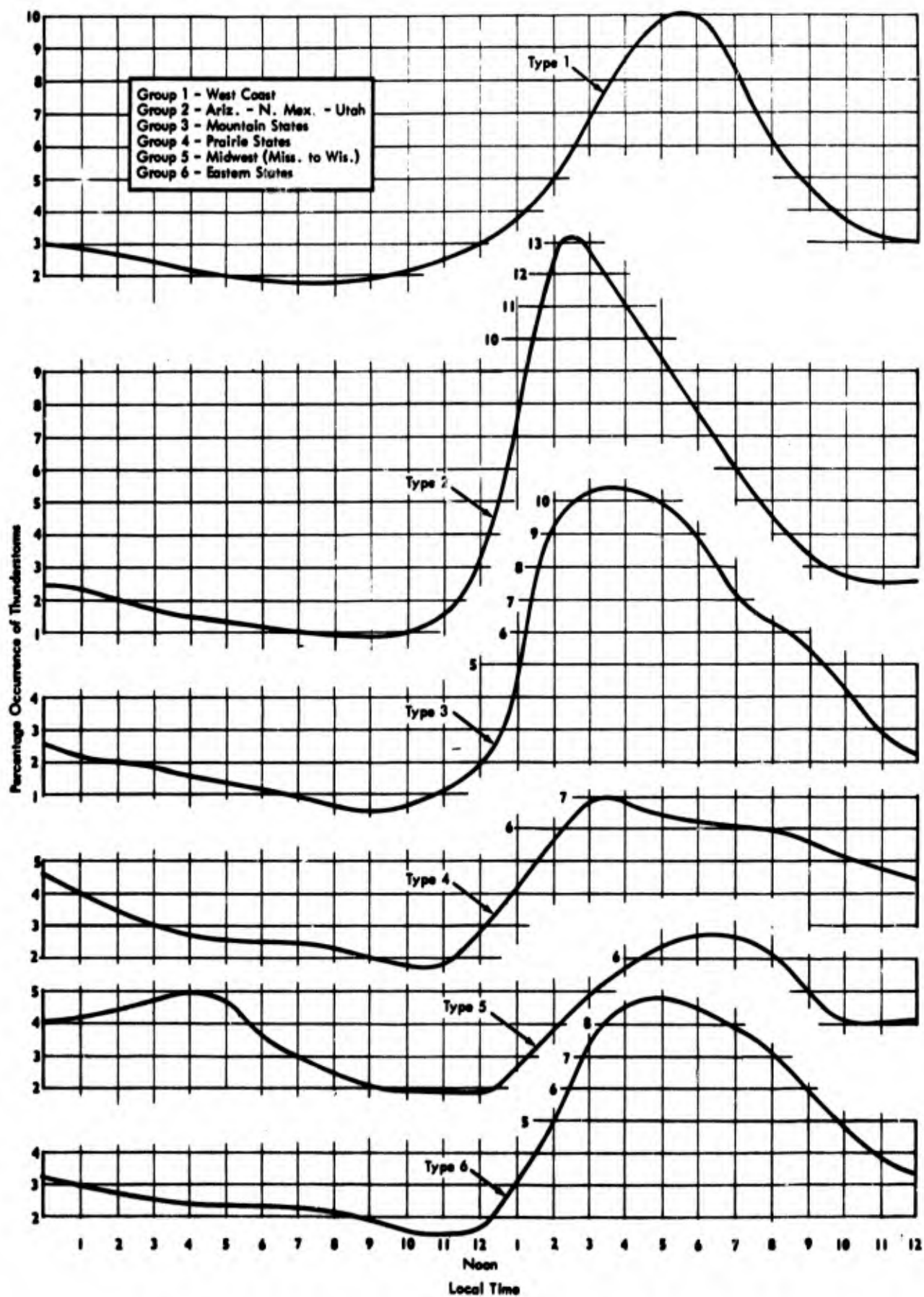


Figure 5-9 Diurnal Variation of Thunderstorms Across the United States - July

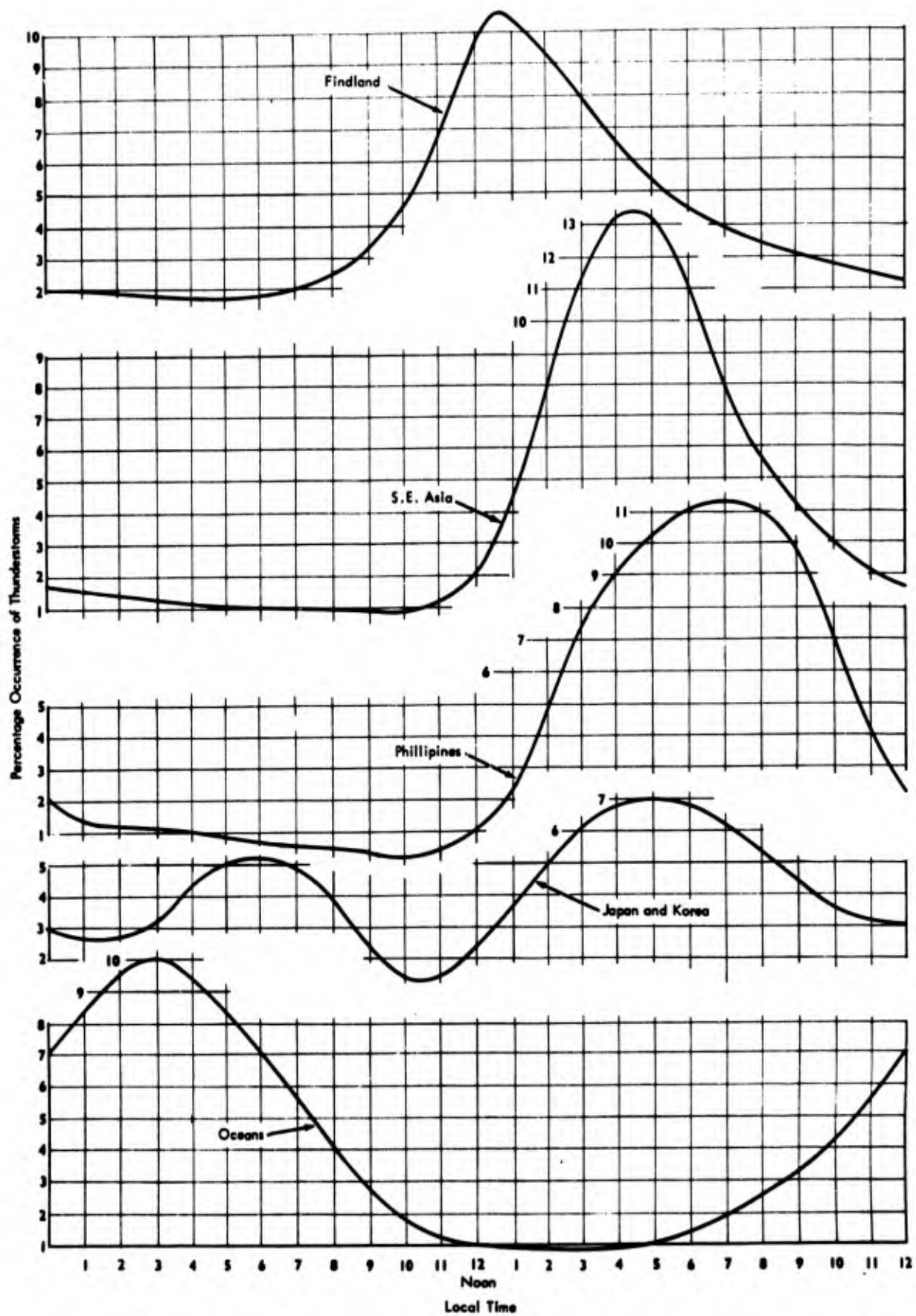


Figure 5-10 Diurnal Variation of Thunderstorms Around the World - July

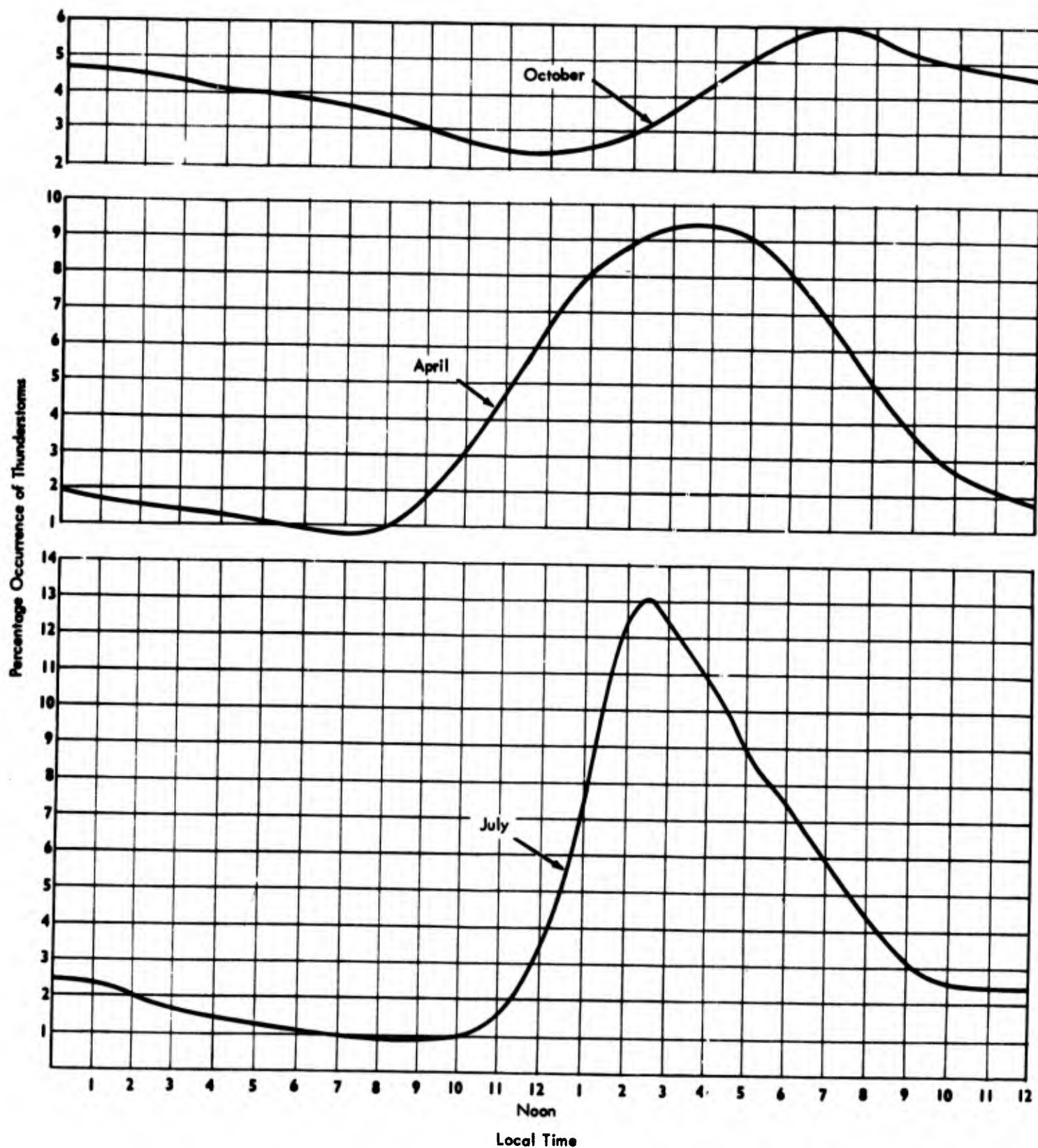


Figure 5-11 Diurnal Variation of Thunderstorms During the Year - Ariz.-N. Mex.-Utah

The final diurnal modifiers assigned to the 15° by 15° regions for each three-month seasonal period are presented in tabular form in Section 6.3.3. For the most part the diurnal patterns used are very close to those plotted from the measured data. Modifications of the measured data were required for those locations where the 15° by 15° region included areas having different diurnal patterns, such as the land and sea areas previously discussed.

5.3 Statistics of Thunderstorm Days

In order to estimate the standard deviation of atmospheric noise it was necessary to gain an understanding of the statistics of the sources of atmospheric noise. This was accomplished by analyzing the thunderstorm day and lightning discharge data. In this section we will present the results of the analyses and in Section 7.0 we will discuss how they were used in the calculation of standard deviation of atmospheric noise.

The data used for the statistical analyses were the climatological records and the foreign publication data described in Section 5.1.

5.3.1 Cumulative Distributions

Figure 5-12 presents the cumulative distribution of thunderstorm days for the month of July at San Juan, Puerto Rico. Although the distribution is somewhat skewed at low values of thunderstorm days, it closely approximates a normal distribution for the higher values. Because of the relationship between thunderstorm days and lightning discharges, as discussed in Section 3.1, we were interested in the distribution of thunderstorm days squared. Figure 5-13 presents the cumulative distribution of thunderstorm days squared for the month of July at San Juan, Puerto Rico. The curve now more nearly approximates a normal distribution for all values of thunderstorm days squared. Figures 5-14 and 5-15 presents similar figures for San Juan for the month of October. Neither distribution

LONG-066 LAT+18 MO 7 MEAN 7.02000 SIGMA 6.96958

SAN JUAN, PUERTO RICO

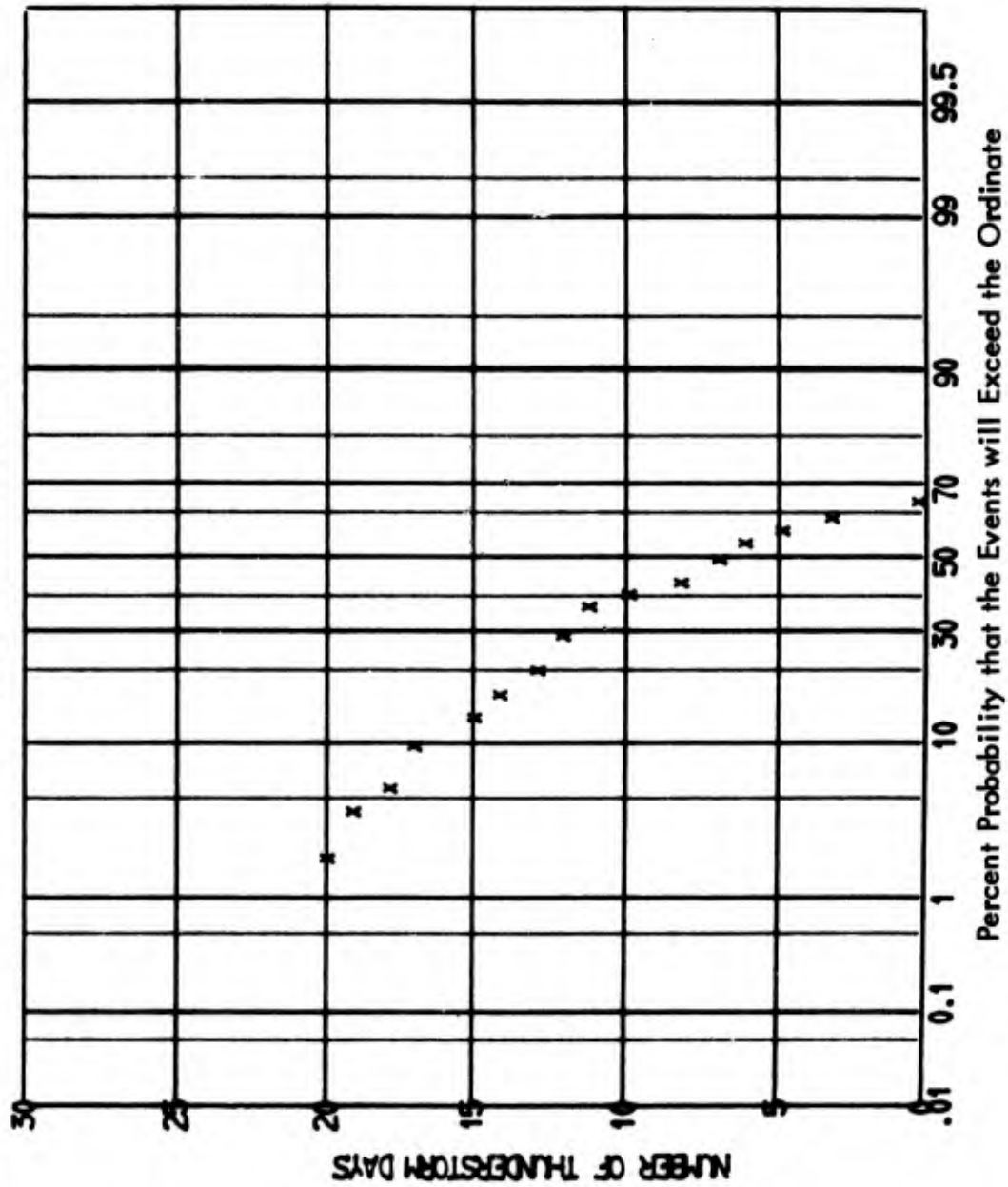


Figure 5-12 CUMULATIVE DISTRIBUTION OF THUNDERSTORM DAYS

SIGMA 123.39874

LONG-066 LAT+18 MO 7

SAN JUAN, PUERTO RICO

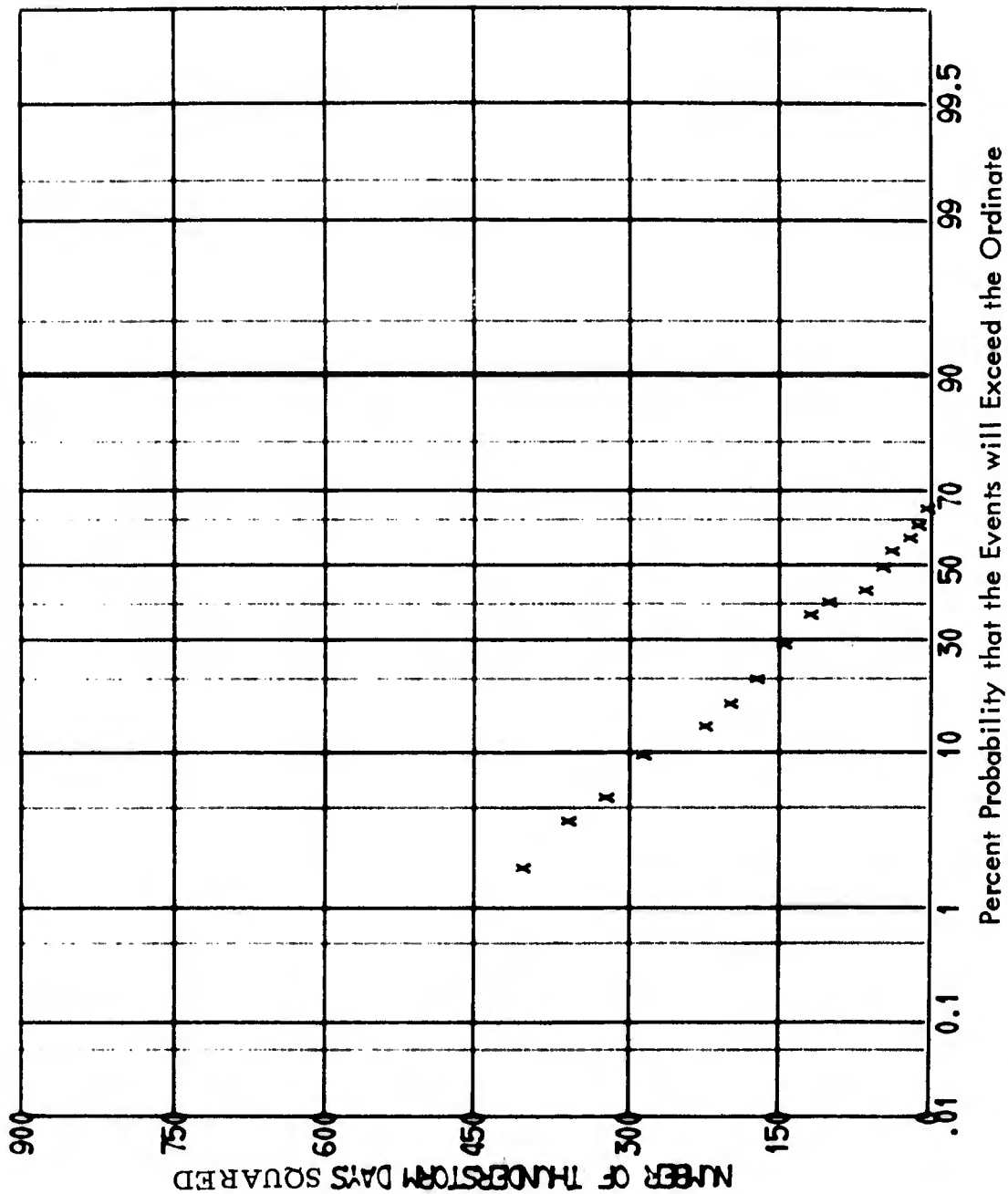


Figure 5-13 CUMULATIVE DISTRIBUTION OF THUNDERSTORM DAYS SQUARED

LONG-066 LAT+18 MO10 MEAN 1.34000 SIGMA 1.91247

SAN JUAN, PUERTO RICO

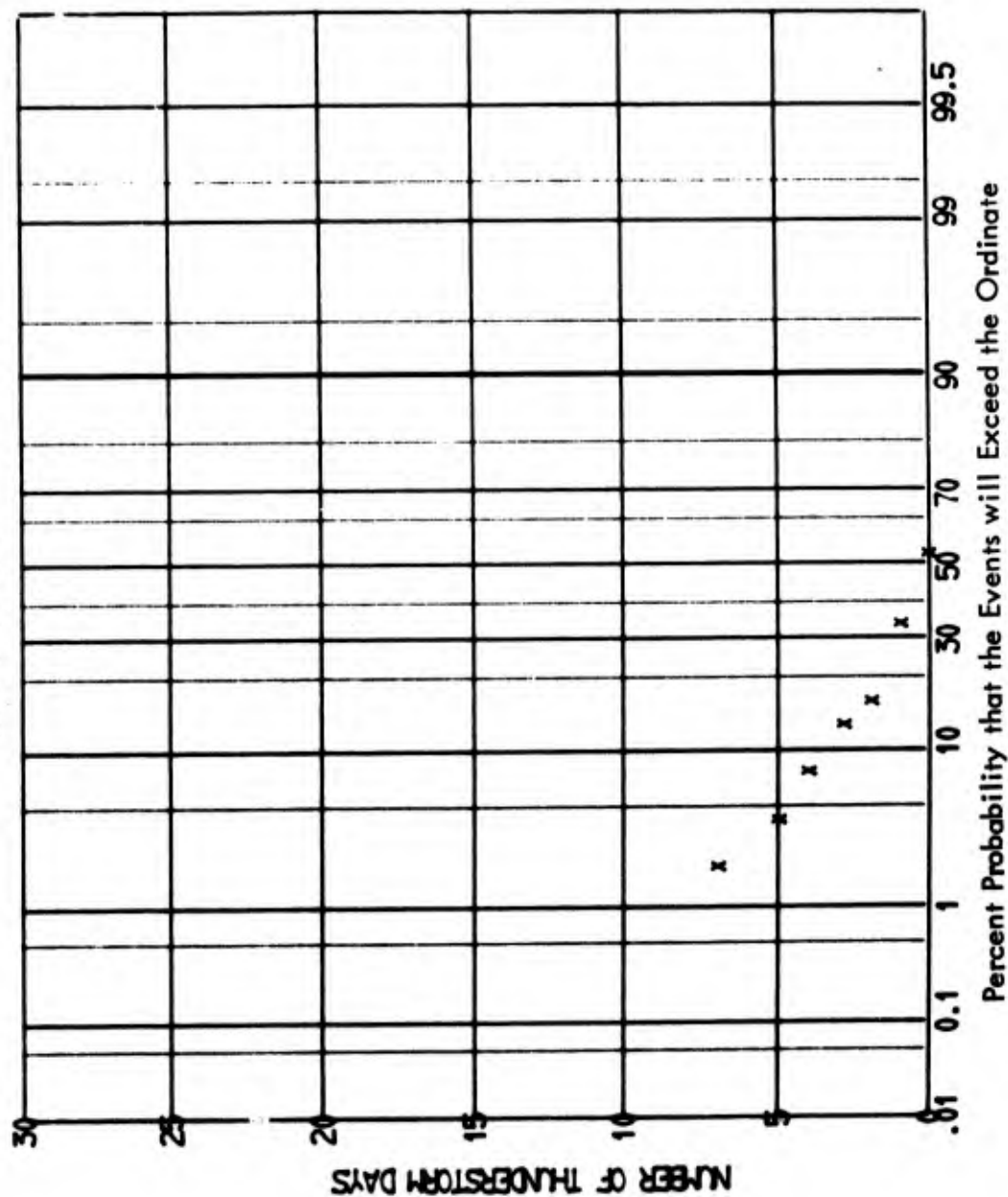


Figure 5-14 CUMULATIVE DISTRIBUTION OF THUNDERSTORM DAYS

LONG-066 LAT+18 MO10 MEAN 5.38000 SIGMA 12.26059

SAN JUAN, PUERTO RICO

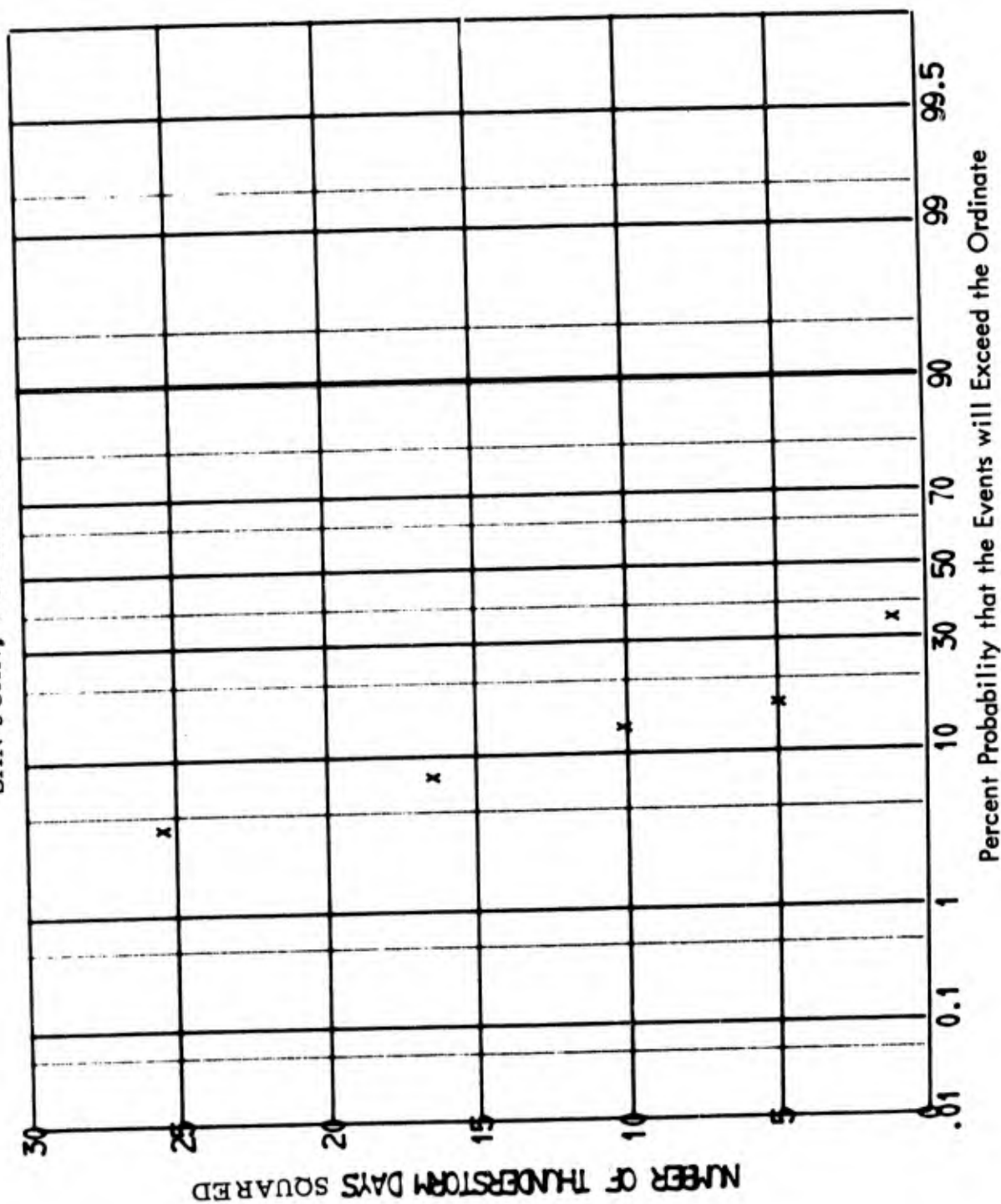


Figure 5-15 CUMULATIVE DISTRIBUTION OF THUNDERSTORM DAYS SQUARED

resembles a normal distribution when the number of thunderstorm days is very low. Similar results were obtained for many other locations and months. This is consistent with the results of Kendall [1962] who found that the frequency of thunderstorm days in Canada closely approximates a Poisson distribution. In Canada the mean number of thunderstorm days does not exceed 8 for any location or any month. For most locations the average number of thunderstorm days lies between 1 and 6 for the month of July. It appears then, that for locations having a very high thunderstorm activity that the distribution of thunderstorm days closely approximates a normal distribution, whereas for locations having a very low level of activity that the frequency of thunderstorm days approximates a Poisson distribution. This is further supported by the results shown in Figure 5-16. for data from Tampa, Florida during the month of July. This data shows a very close approximation to a normal distribution. Figures 5-17 and 5-18 show distributions for Tampa, Florida for the months of June and July for thunderstorm days to the 1.5 power and thunderstorm days squared. Both show a close approximation to a normal distribution.

As will be discussed in considerable detail in Section 7.0 the nature of the thunderstorm day data and our ultimate use thereof required that we treat the statistical analysis of the data for an entire region as if we were summing the lightning discharges reported for each location within the area to obtain the total number of lightning discharges within the region. Based on the law of large numbers we would expect the distribution of the sum of the data from a large number of climatological stations, or lightning counter stations, to approach a normal distribution, even if the distribution of the original data was not normal. This is discussed in more detail in Section 7.2. Figure 5-19 is a plot of the distribution of the mean number of thunderstorm days for the Nebraska group, a group of stations in Kansas, Nebraska, and the Dakotas. This combined data more nearly

LONG- 82 LAT+27 NO 7 MEAN18.48000 SIGMA 3.18952

TAMPA, FLORIDA

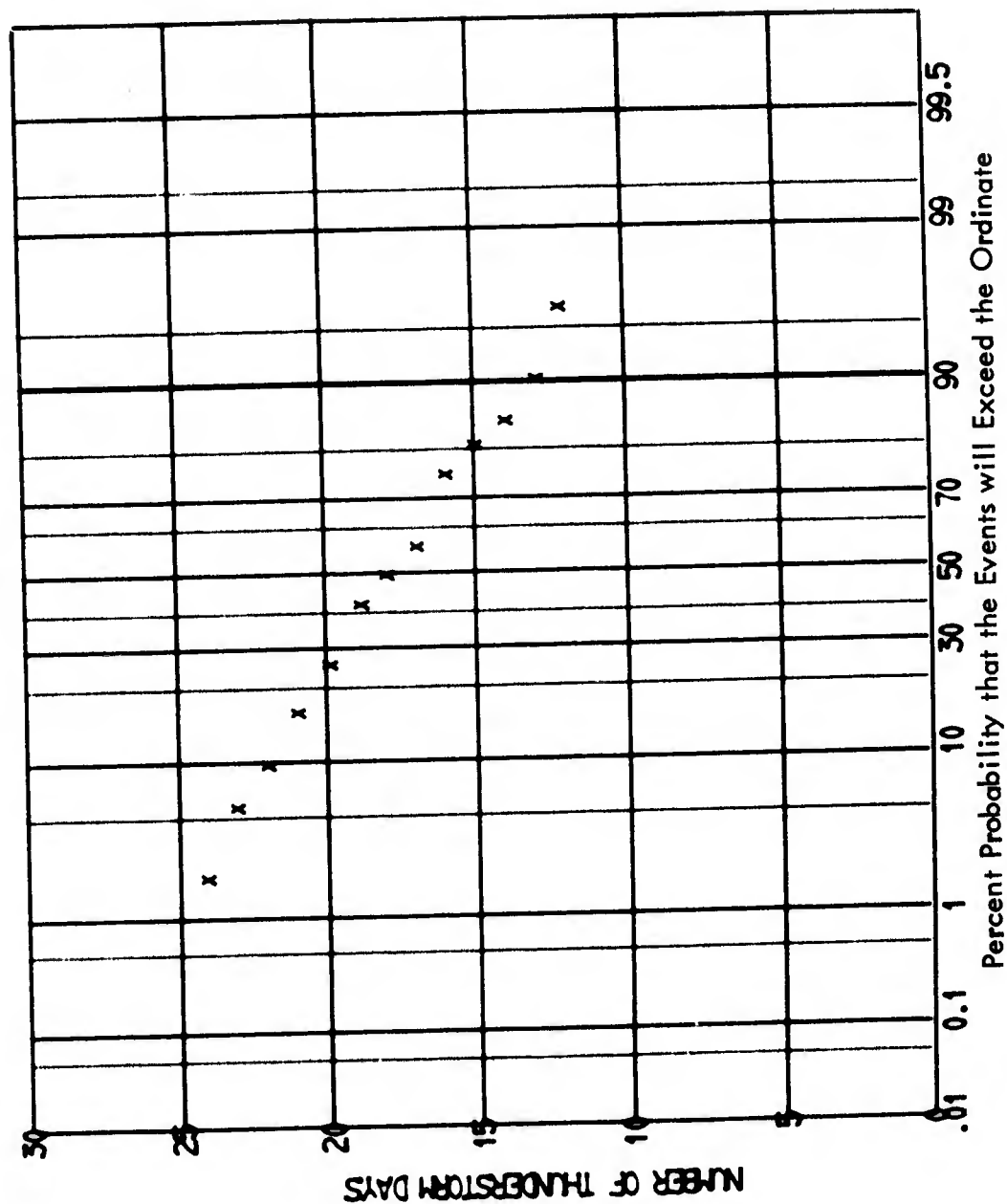


Figure 5-16 CUMULATIVE DISTRIBUTION OF THUNDERSTORM DAYS

LONG- 82 LAT+27 MO 6 MEAN 65.188 SIGMA 22.205

TAMPA, FLORIDA

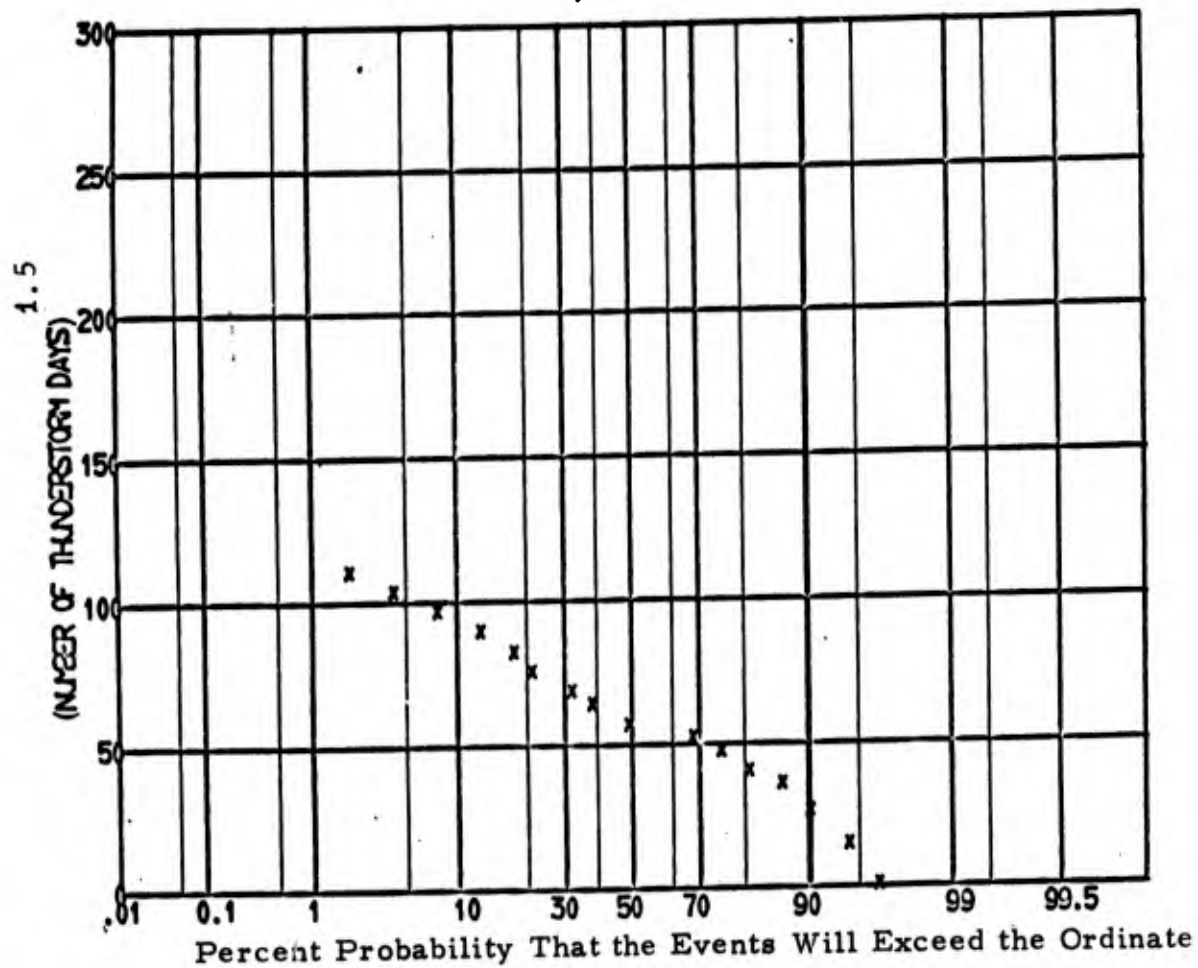


Figure 5-17 CUMULATIVE DISTRIBUTION OF THUNDERSTORM DAYS TO THE 1.5 POWER

LONG- 82 LAT+27 MO 7 MEAN*1.48000 SIGMA 117.69734

TAMPA, FLORIDA

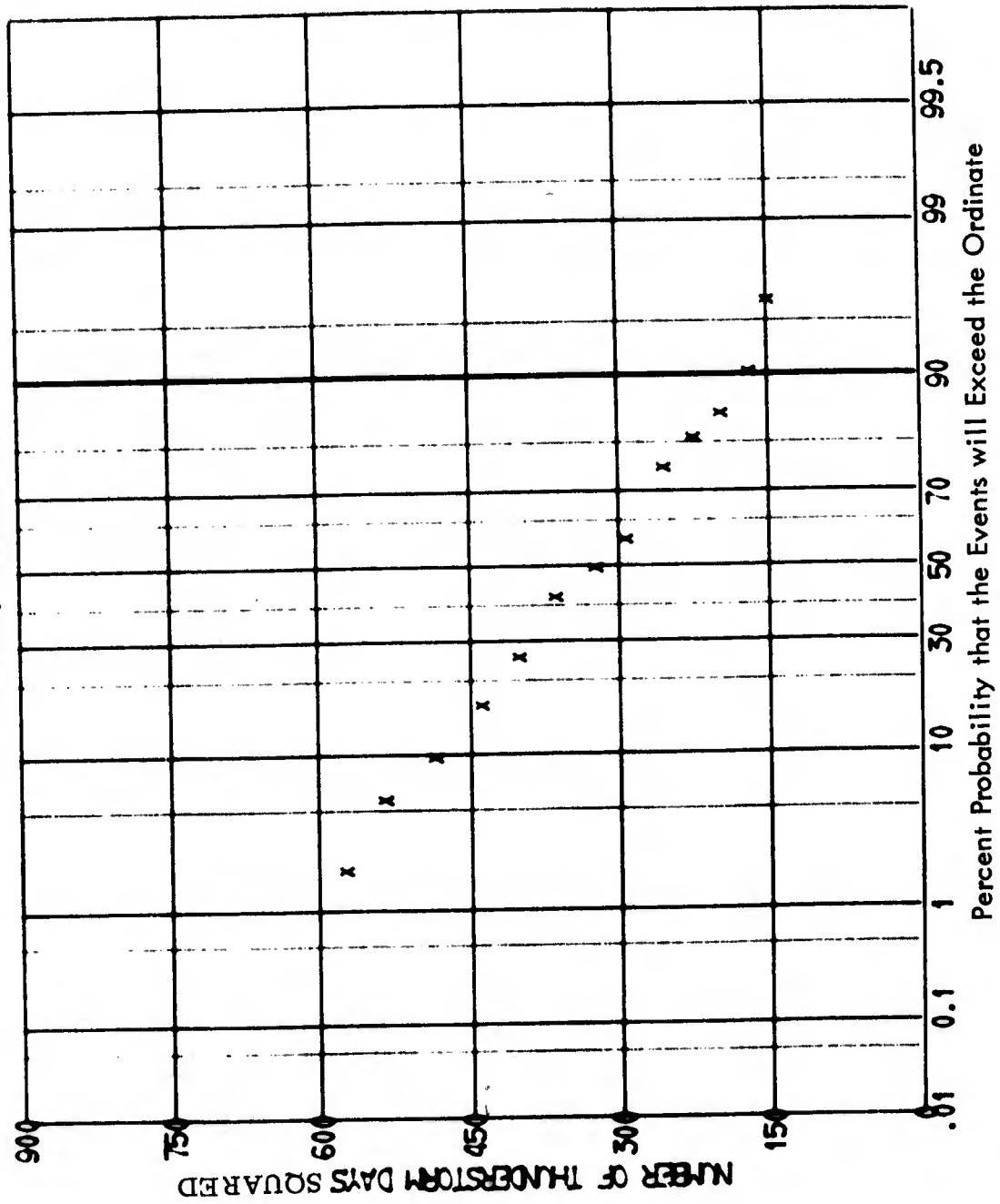


Figure 5-18 CUMULATIVE DISTRIBUTION OF THUNDERSTORM DAYS SQUARED

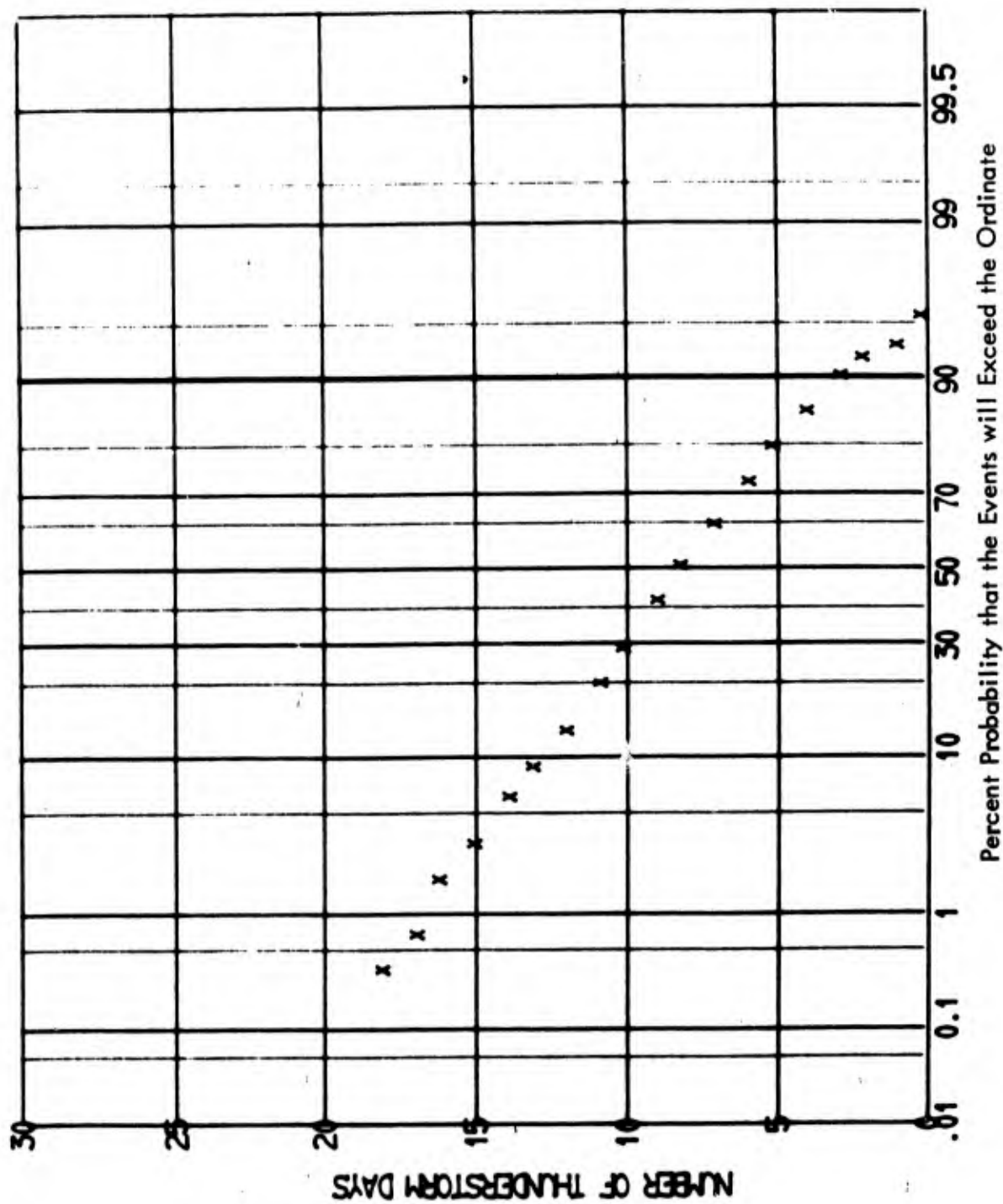


Figure 5-19 CUMULATIVE DISTRIBUTION OF THUNDERSTORM DAYS

approximates a normal distribution than the data for any single station itself.

5.3.2. Standard Deviation vs. Number of Thunderstorm Days

The number of locations where we had sufficient data to compute the standard deviation of thunderstorm days was very limited. It was desired, therefore, to establish a relationship between thunderstorm days and the standard deviation of thunderstorm days. Figure 5-20 is a scatter plot of mean thunderstorm days per month vs. standard deviation of thunderstorm days per month for a representative sample of climatological data in the United States and the few foreign locations for which data was available. A dashed line, fitted by eye to the points, has been drawn to emphasize the correlation between the mean value for 50 years of data and the standard deviation of individual yearly values around the mean. The solid line was taken from Atkinson [1967] who studied thunderstorms in Southeast Asia. The reasonably good agreement between his analysis and our results for the United States, Uganda and Singapore tends to indicate that the relationship between mean thunderstorm days and the standard deviation of thunderstorm days is much the same for every part of the world. This is, of course, a very limited sampling but a significant departure from the relationships found to be valid for the United States and Southeast Asia is not anticipated. We should note that Atkinson (ibid) found the occurrence of thunderstorm days in Southeast Asia to closely approximate a normal distribution.

5.3.3. Correlation With Distance

The standard deviation of the total thunderstorm activity over a large region such as our 5° by 5° and 15° by 15° equivalent noise transmitter, can be determined from the standard deviation of thunderstorm occurrence for small areas within the region, provided the correlation between thunderstorm activity at any two locations is known. Climatological

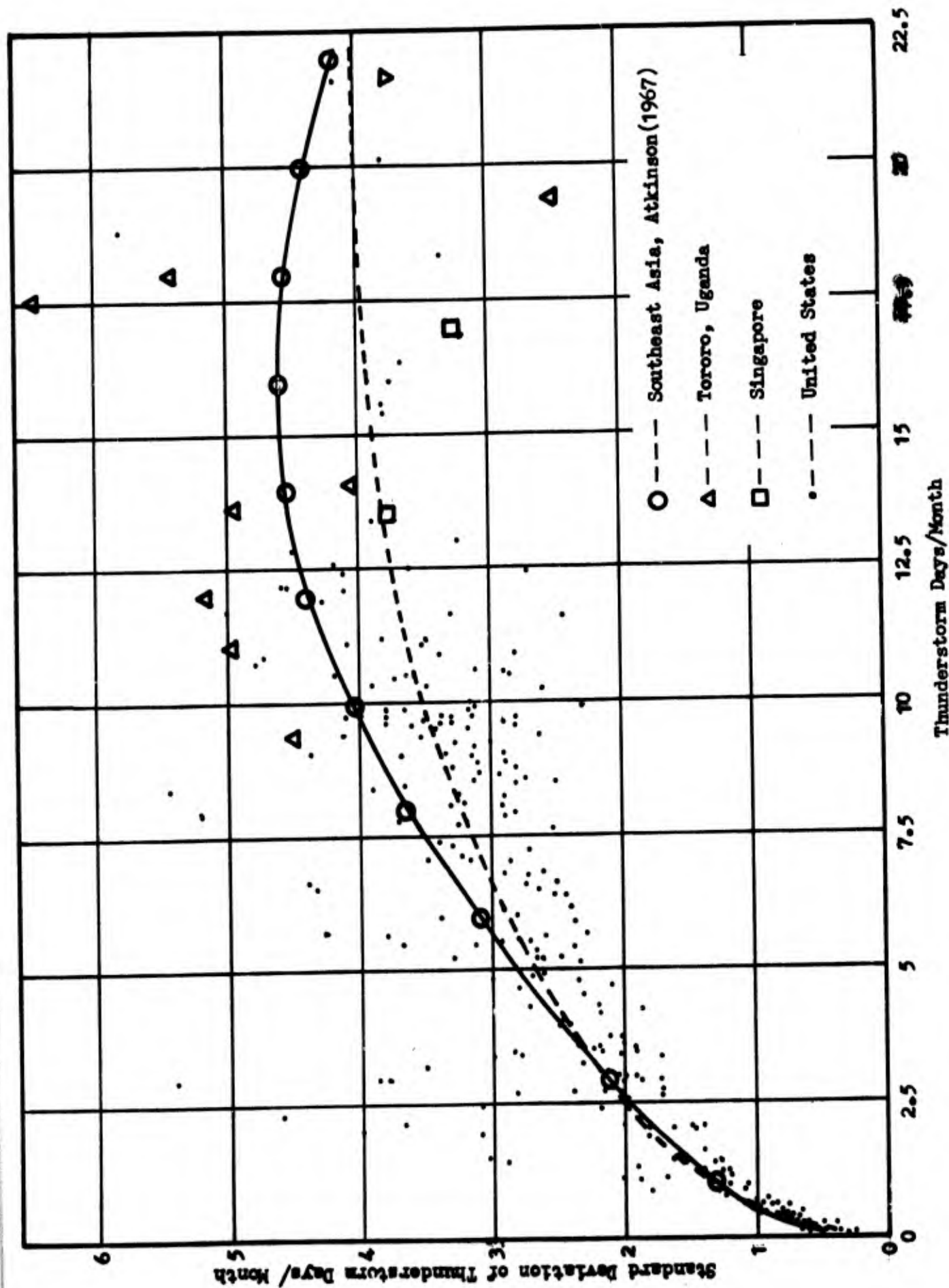


Figure 5-20 Standard Deviation vs Mean Value For Thunderstorm Days

data for stations having a continuous record from 1901 to 1950 were analyzed for two station groups. A group of 12 stations in Kansas, Nebraska, and the Dakotas, called the Nebraska Group, was analyzed first. The mean value of thunderstorm days was computed for each station for the 50 year record. The correlation coefficient between each pair of stations was computed according to the equation.

$$r = \frac{\sum (X - \bar{X}) (Y - \bar{Y})}{(n - 1) \sigma_x \sigma_y} \quad (5-2)$$

where:

\bar{X} and \bar{Y} are the mean values for each station of a pair
and X and Y represent values for a single year for each
station of a pair.

σ_x and σ_y are the standard deviations of the values
for each station.

The computed correlation coefficients were plotted as a function of distance in degrees between each pair of stations. Figure 5-21 and 5-22 present the results for May and January for the Nebraska Group. The correlations approach 1 at 0 distance and 0 at large distances, as would be expected. Similar data is shown on Figure 5-23 for the Southeast Group which consisted of thirteen stations in the states of Florida, Georgia, the Carolinas, Alabama, Kentucky and Tennessee. These results and the results for other months from the same group indicated an increase in correlation coefficient for locations and months of high thunderstorm activity. This information was very important in the development of a model for the computation of the standard deviation of atmospheric noise as presented in Section 7.0.

STATION SET Nebraska MONTH 1 YEAR 1901 TO YEAR 1950

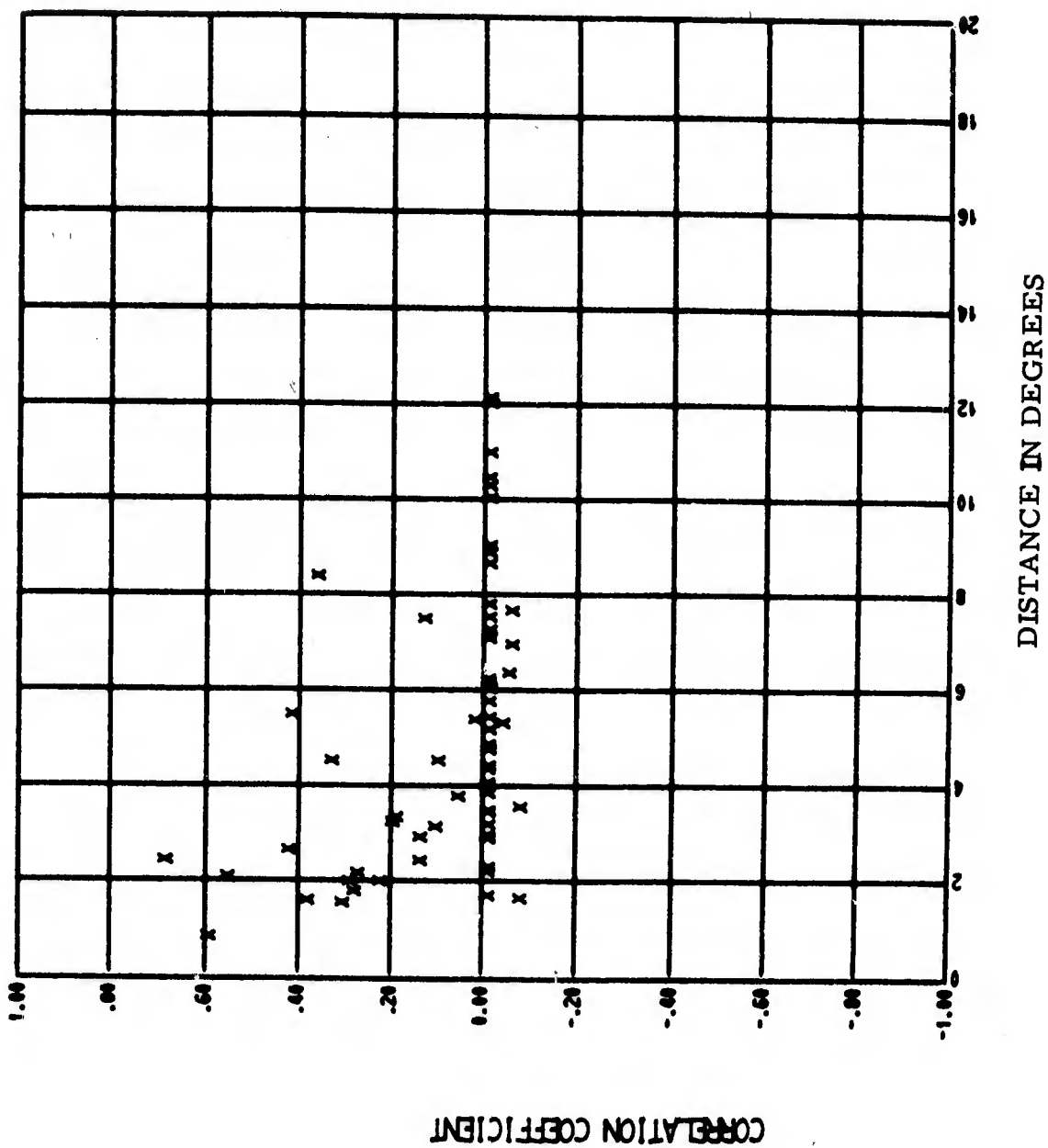


Figure 5-21 Correlation of Thunderstorm Activity as a Function of Distance Between Stations.

STATION SET Nebraska MONTH 5 YEAR 1901 TO YEAR 1950

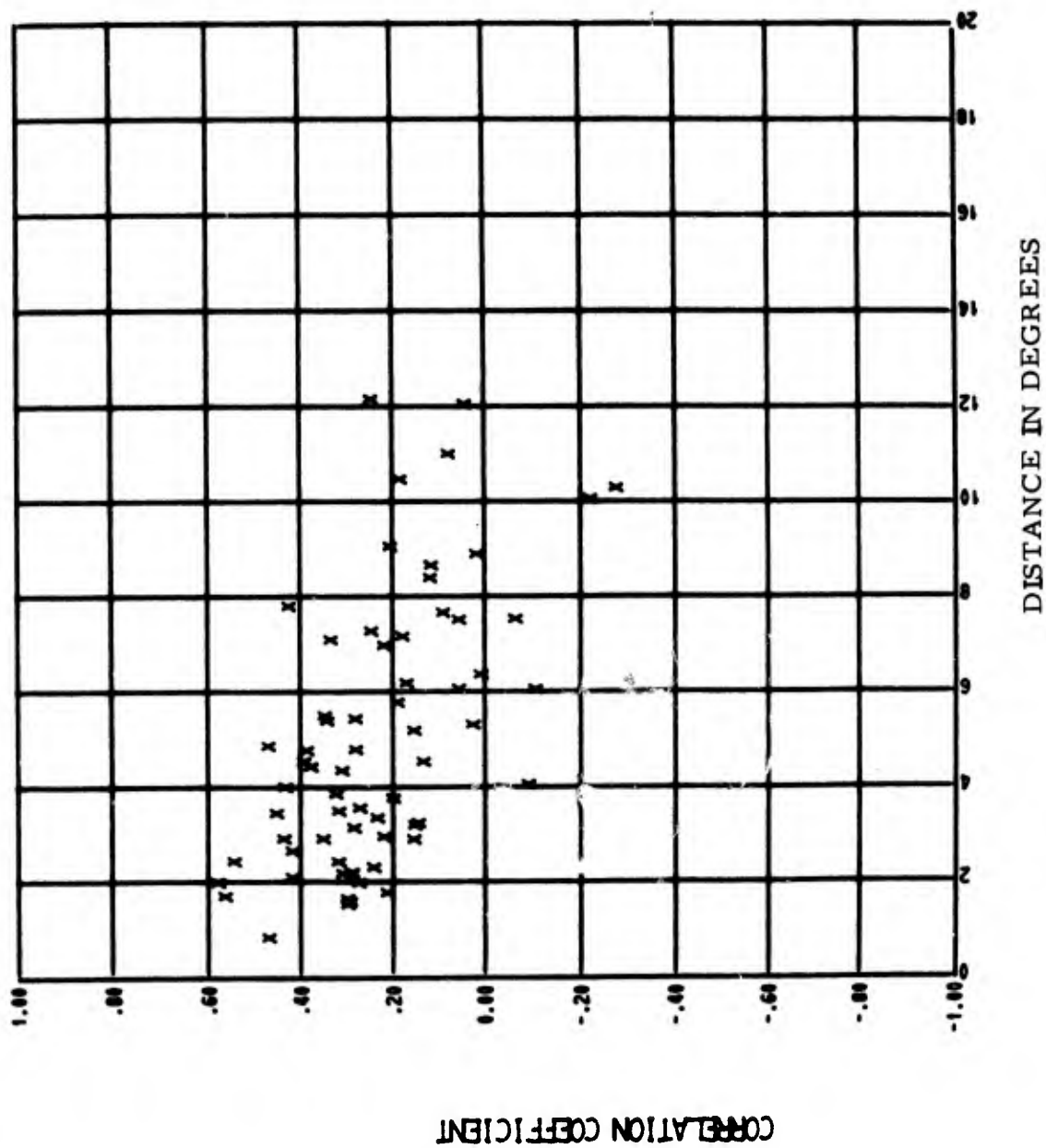


Figure 5-22 Correlation of Thunderstorm Activity as a Function of Distance Between Stations.

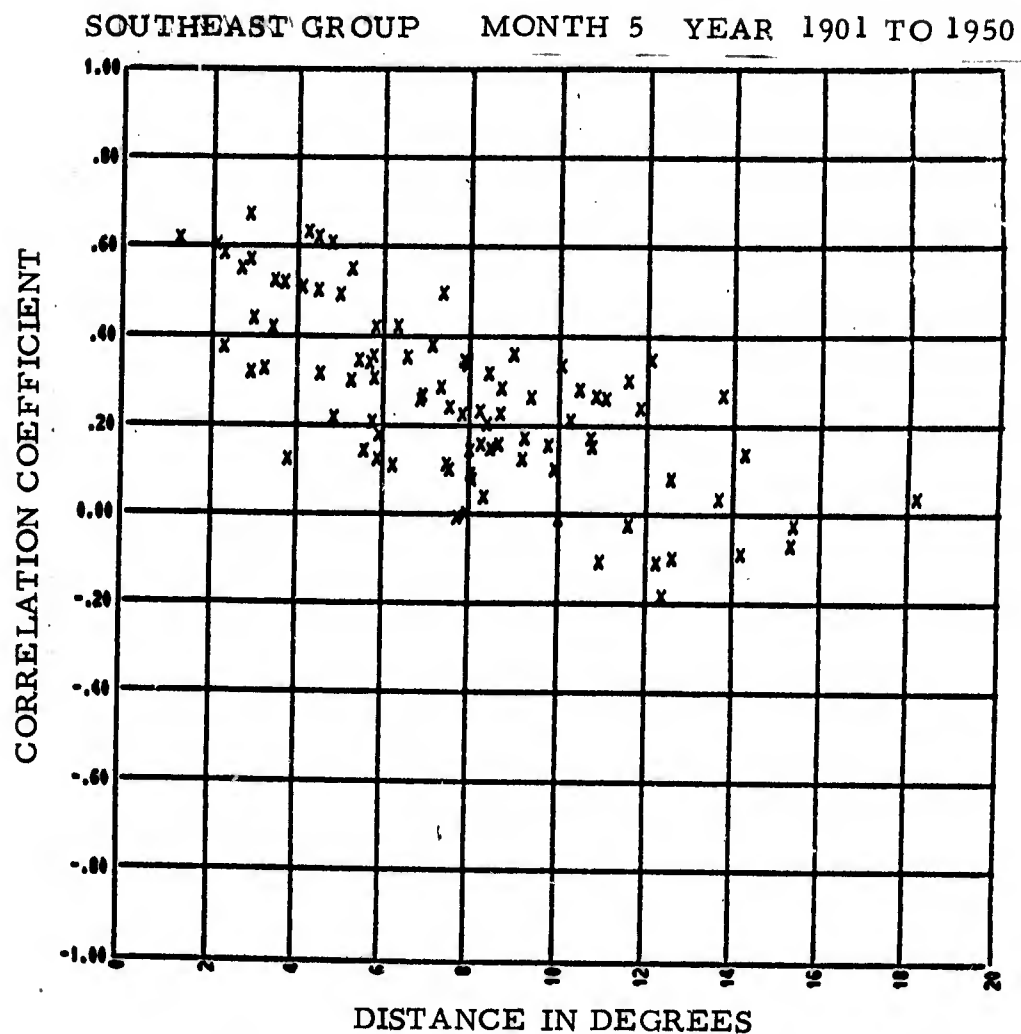


Figure 5-23 Correlation of Thunderstorm Activity as a Function of Distance Between Stations.

5.3.4. Correlation With Sunspot Cycles.

The user of any atmospheric noise predictions and users of the model developed under this program should be aware of long term weather cycles which are not specifically provided for in most models including this one. Most of the meteorological data used in developing this noise prediction model was obtained after 1900. It is apparent from Figure 5-24 that thunderstorm activity was relatively constant from 1900 to 1950 and presumably also for the past twenty years. Prior to 1900, however, there was a period of thirty years when thunderstorm activity was appreciably lower than it has been for the past seventy years. That there is some correlation between these long term fluctuations of thunderstorm activity and sunspot number is apparent from the data obtained from Watt 1967. The very low number of sunspots in the 1870's and 1880's apparently resulted in a reduction in the number of thunderstorm days. Both data extend back just far enough in time to show apparent higher sunspot number prior to 1875 with a resultant higher thunderstorm activity.

Apparently a significant decrease in sunspot activity in future decades could result in significantly lower noise values than will be predicted using meteorological data from the first half of this century.

5.4 Statistics of Lightning Discharges

The distribution of thunderstorm days represents primarily the variation in thunderstorm activity and therefore the variation in atmospheric noise levels from year to year. The distribution of lightning counts from hour-to-hour and day-to-day is indicative of the variation of atmospheric noise from hour-to-hour and day-to-day. It was important therefore to analyze the distribution of lightning counts from the hourly data obtained from lightning counters. Figure 5-25 presents the cumulative distribution of lightning counts recorded during the hour from 8:00 am to 9:00 am during the month of July. This data was obtained from a lightning counter at

Boulder, Colorado which was operated for about three years. Figure 5-26 is a similar plot of data for Singapore for the same hour during the month of April. Figure 5-27 shows the cumulative distribution of lightning counts recorded during the hour 6:00 pm to 7:00 pm at Singapore. No effort was made to determine what type of distribution this data most closely resembles but it is obvious that it is not a normal distribution. It would appear that it might approximate a Poisson distribution.

Since we again had relatively few measurements of the standard deviation of lightning discharges, we needed to establish a relationship between lightning counts and their standard deviation. Figure 5-28 shows a scatter plot of the mean number of lightning counts per day or time block and the standard deviation of these counts. There was not a sufficient sample of data for any given hour to permit the accurate calculation of standard deviation for many locations. Daily counts for several stations and data within four hour time blocks were used and plotted together. The equation for the line, which was fit by eye to the data, is indicated on the figure. The use of this equation in the prediction model is described in Section 7.0.

Although more data in kind and in number would have been very desirable and would certainly have resulted in the development of a better prediction model, the data obtained is the best available at this date and was adequate to establish the desired results.

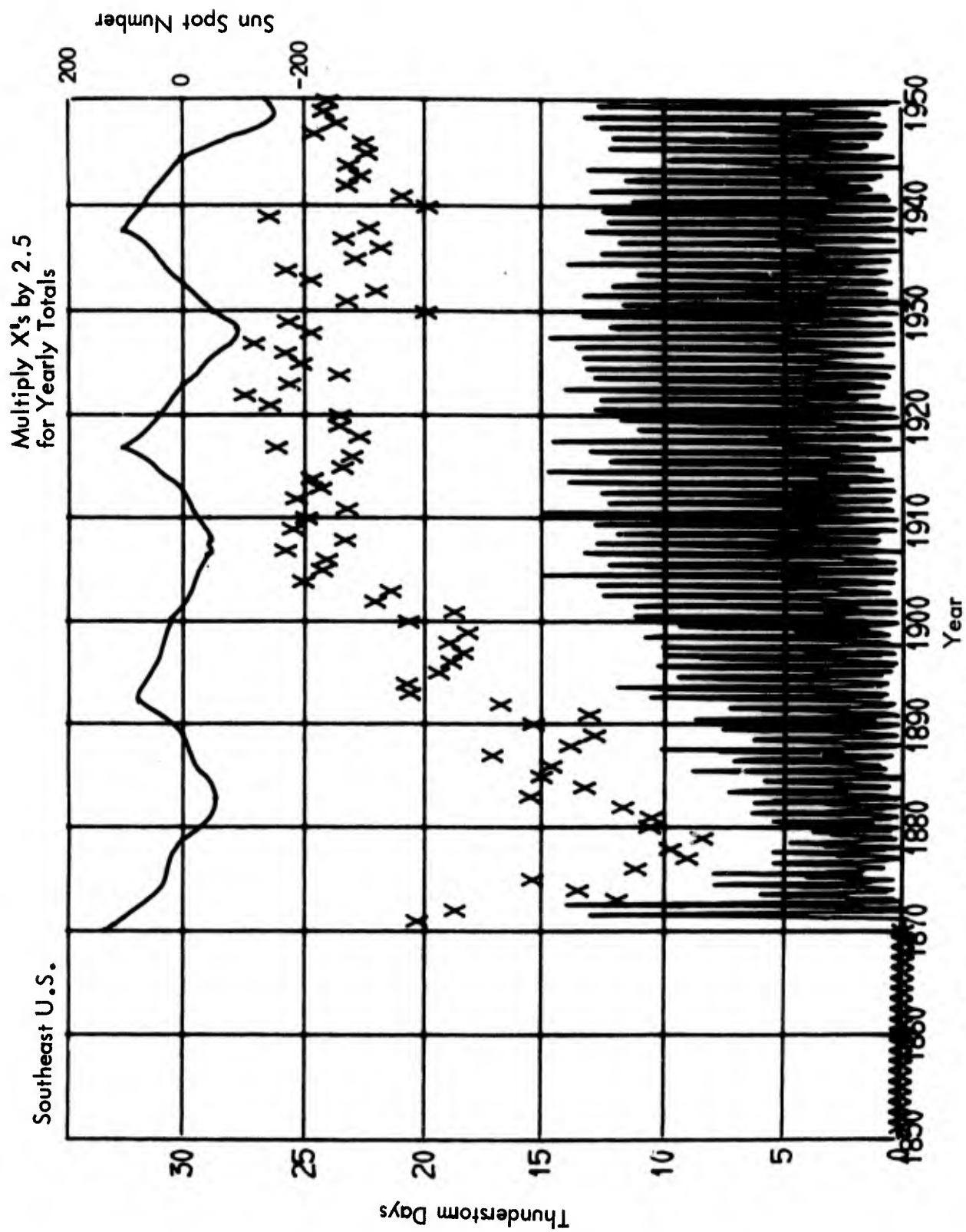


Figure 5-24
Average Thunderstorm Days per Month and Year
for the Nebraska Group of Stations and Yearly Mean
Sunspot Number (Sun Spot Data from Watt - 1967)

LONG-105 LAT+40 MO 7 HOUR 8 SIGMA 8.54208

BOULDER, COLORADO

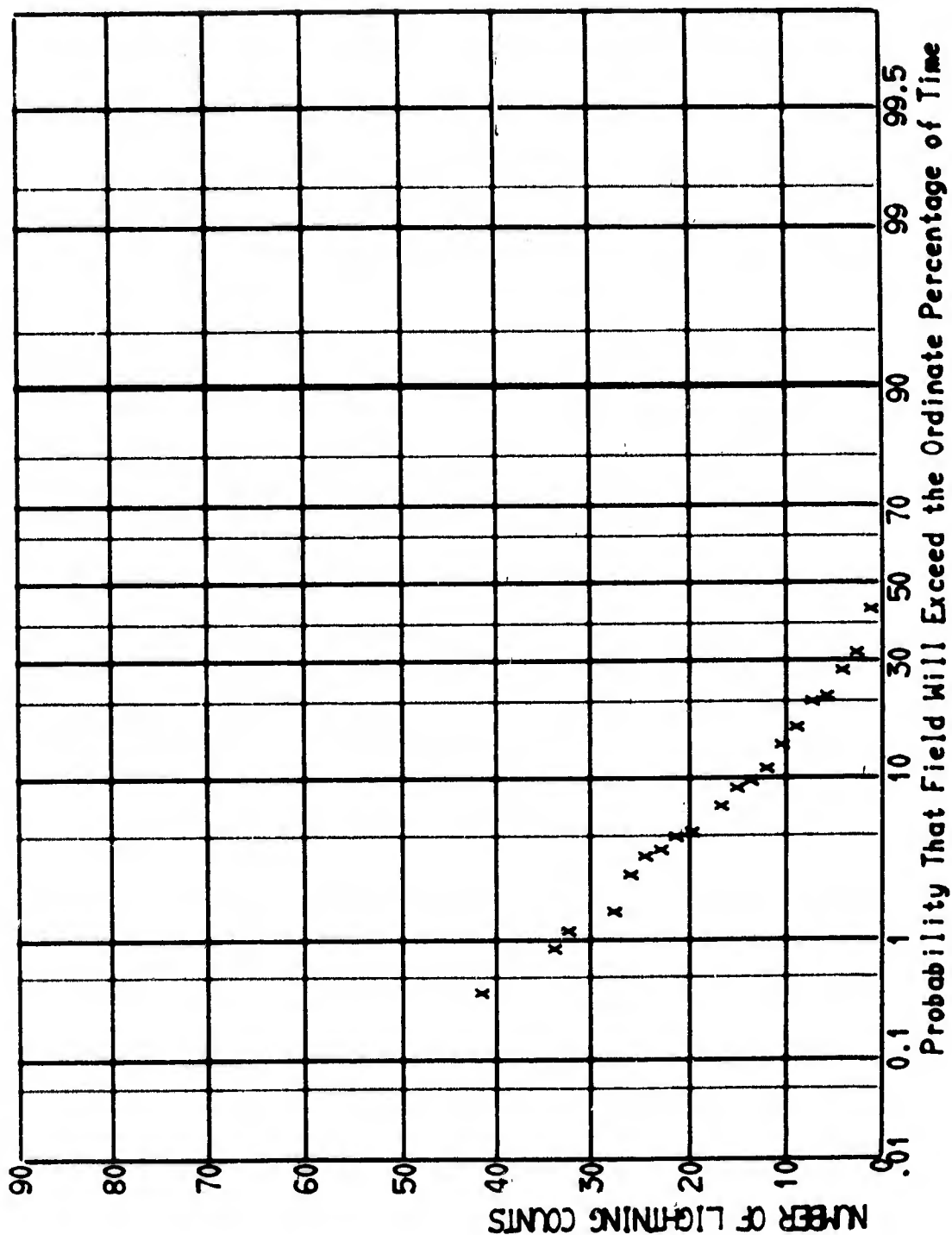


Figure 5-25 CUMULATIVE DISTRIBUTION OF LIGHTNING COUNTS

Singapore LONG+104 LAT+01 NO 4 HOUR 8 SIGMA 35.09118

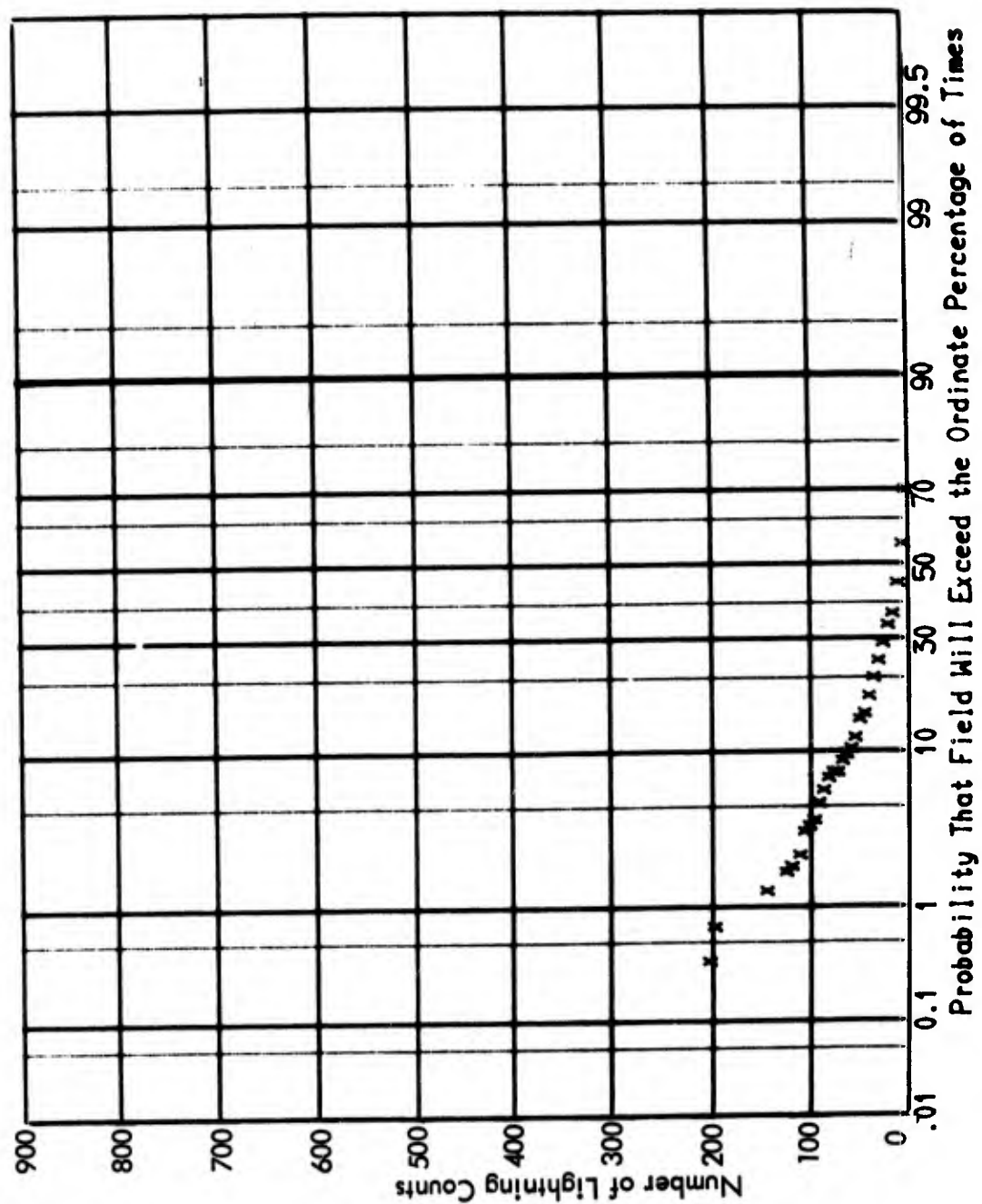


Figure 5-26 CUMULATIVE DISTRIBUTION OF LIGHTNING COUNTS

Singapore xLONG+104 LAT+01 MO 4 HOUR18 SIGMA 253.25433

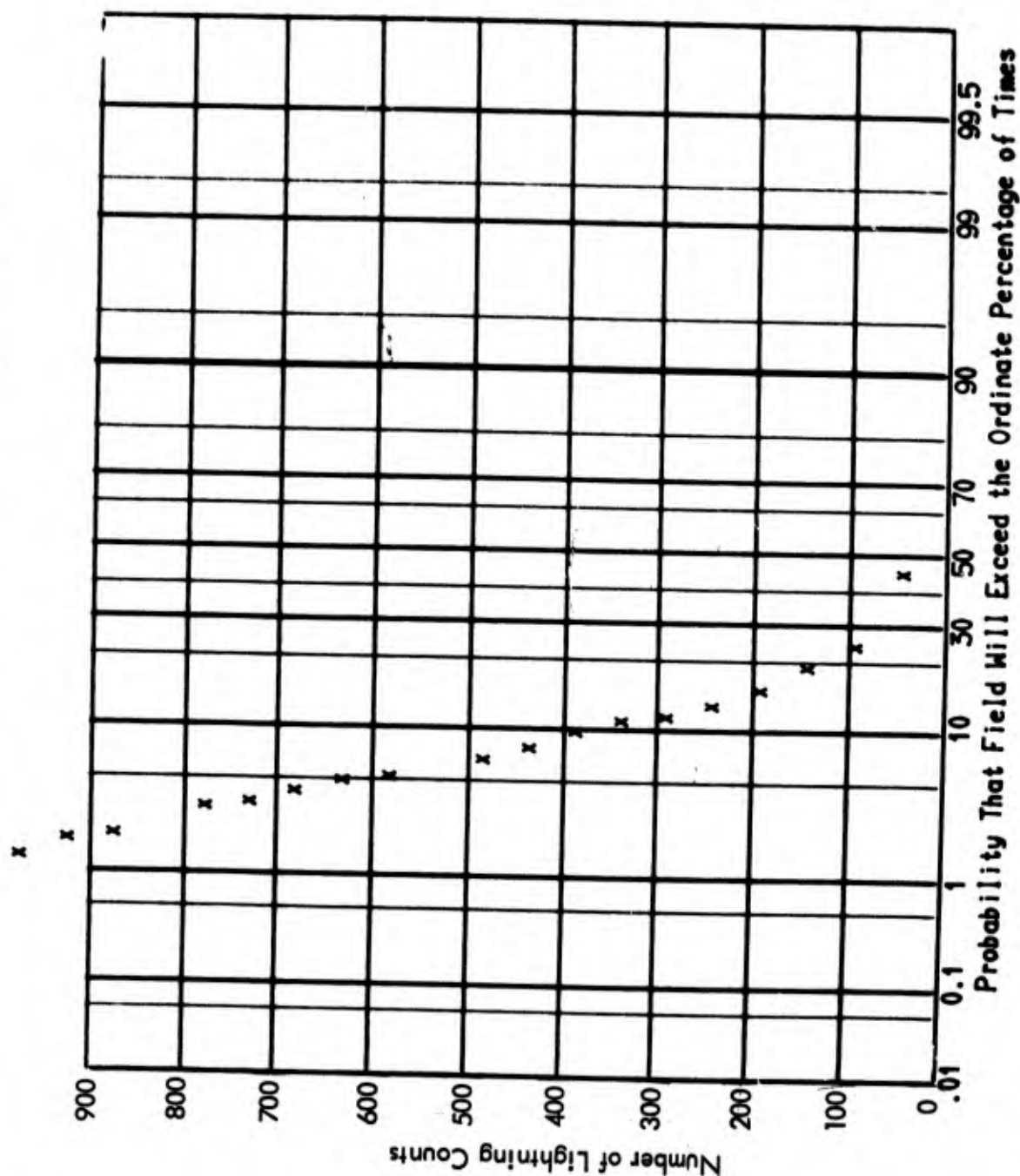


Figure 5-27 CUMULATIVE DISTRIBUTION OF LIGHTNING COUNTS

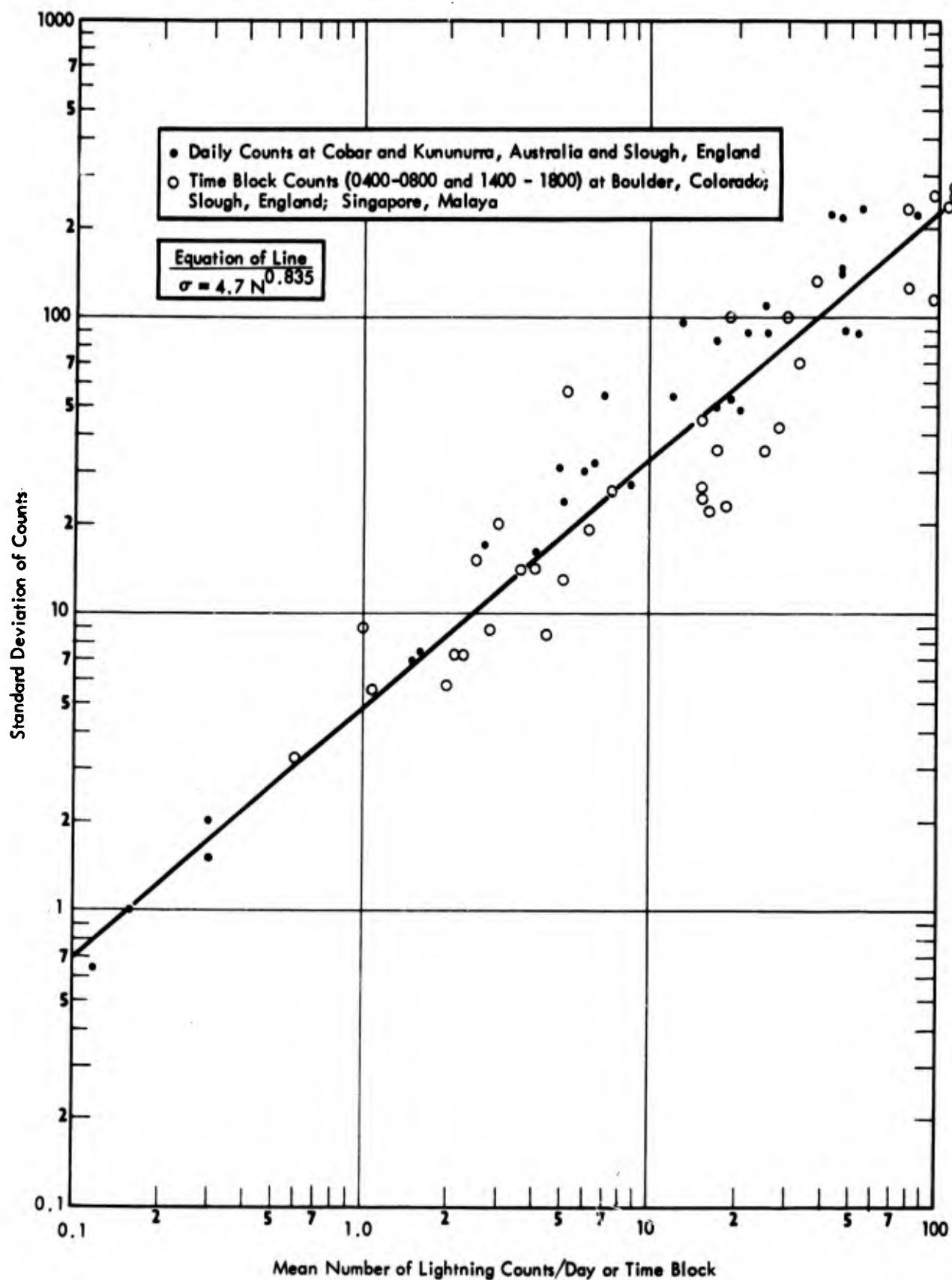


Figure 5-28 Standard Deviation of Lightning Counts per Day or per Time Block

6.0 CALCULATION OF FIELD INTENSITIES

This section and the following three sections describe the final model for the prediction of VLF atmospheric noise. This section will discuss the computation of field intensities. Previous sections have provided the technical basis for the algorithm or model developed, and that information will not be repeated here. Rather the step by step procedures used will be described.

6.1 Description of the Algorithm

STEP I

The algorithm, described in Section 3.3, for computing power radiated by the 5° by 5° regions on the earth's surface will be considered Step I in the computation of field intensities.

STEP II

The 5° by 5° regions (we will hereafter refer to these as minor noise transmitters) are combined into 15° by 15° regions (we will hereafter refer to these as major noise transmitters). The power of the major noise transmitters is the sum of the power of the minor transmitters; the location of the major transmitter is the effective location or centroid of the minor transmitters. The location and number designation of the major noise transmitters is given in Figure 6-1. The nine minor transmitters that make up a major are illustrated for major transmitter number 1 (Figure 6-1).

This step is part of the computer program COMPWR, Stone [1970].

STEP III

The conductivity area (see Figure 4-1) within which each minor and major transmitter is located is identified and added to the transmitter data.

This step is part of program SUMAN, Stone [1970].

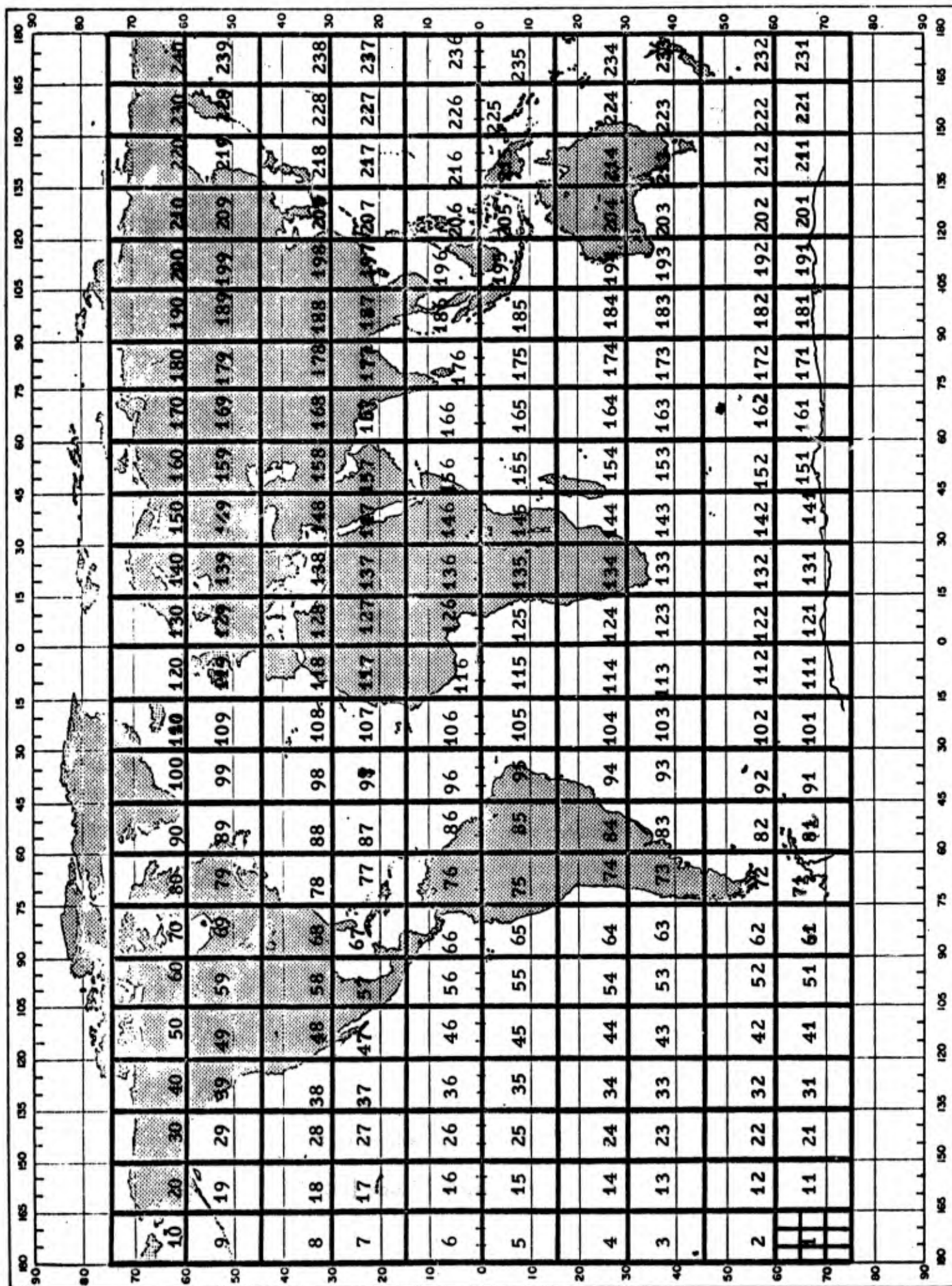


Figure 6-1 MAJOR TRANSMITTER MAP

STEP IV

Tables of diurnal modifiers (see Table 6-1) based on the diurnal distribution of thunderstorm and lightning are read into the computer program. The proper diurnal modifier for each minor and major transmitter is identified for the month for which computations are being made (see Figures 6-2 through 6-5).

This step is accomplished in the computer program MODVAR, Stone [1970]. The output of MODVAR contains all of the specifications, power, location, etc. for all transmitters as an input to the major prediction program NOISLAN.

STEP V

The output of MODVAR and all other input data required for the computation of noise field intensities is read into the computer. This includes:

- o ground conductivity data,
- o propagation data (attenuation coefficients, excitation factors, etc.),
- o transmitter data (from MODVAR),
- o diurnal modifier tables,
- o receiver locations (the location at which fields are to be computed), and
- o frequency, month and hour data which specify the computations which are to be made.

This is part of the main computer program NOISLAN, Stone [1970].

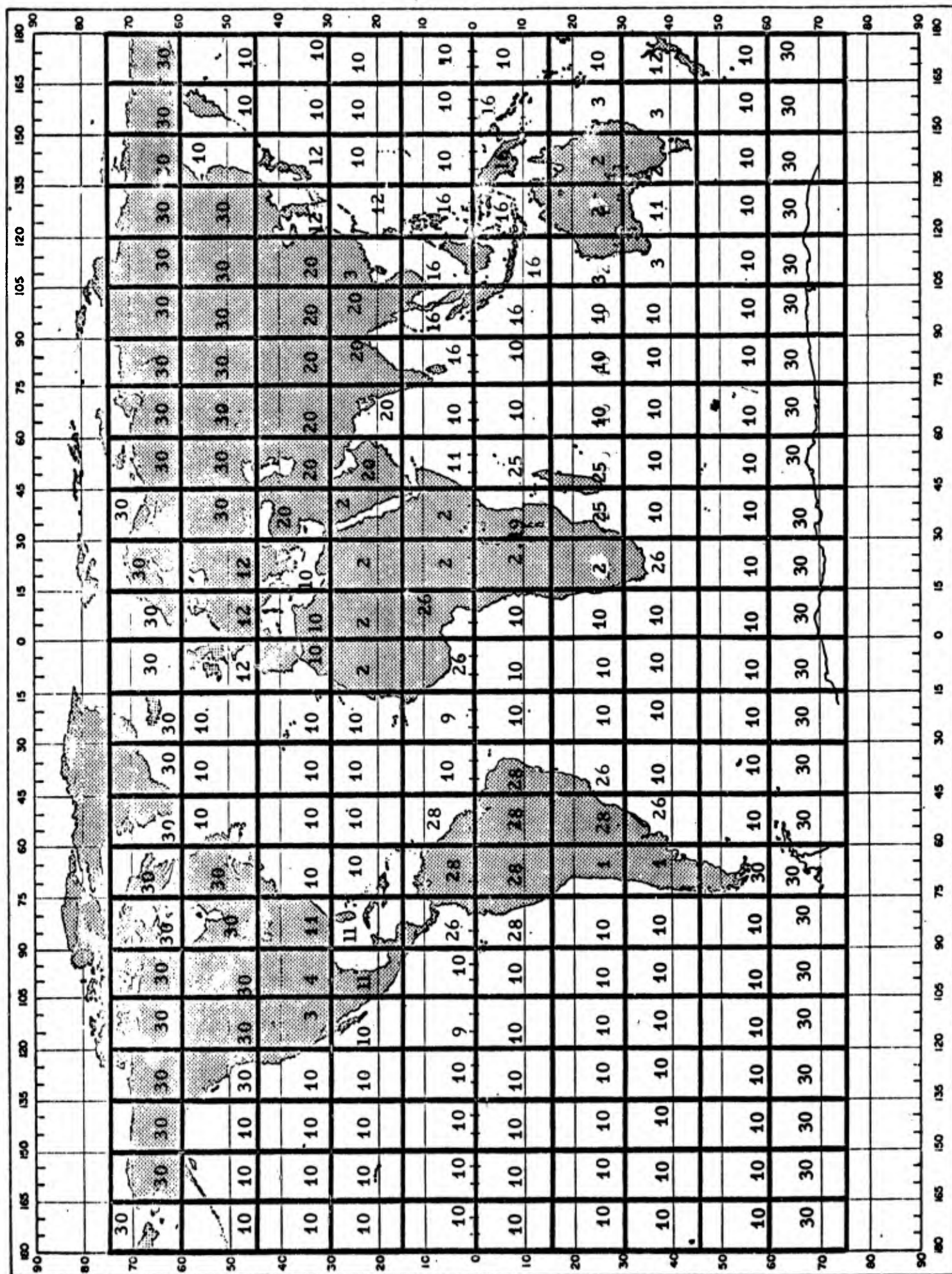
Table 6-1(a)

DIURNAL POWER MODIFIERS (LOCAL TIME)

MOD NO.	0100	0200	0300	0400	0500	0600	0700	0800	0900	1000	1100	1200
1	.026	.025	.024	.023	.022	.021	.020	.020	.020	.022	.024	.029
2	.023	.020	.018	.014	.010	.007	.005	.004	.003	.007	.013	.025
3	.027	.026	.025	.024	.023	.022	.021	.019	.016	.014	.015	.019
4	.039	.037	.035	.033	.031	.029	.026	.025	.023	.020	.020	.027
5	.015	.014	.013	.012	.011	.010	.010	.009	.009	.008	.012	.020
6	.030	.030	.030	.029	.028	.027	.026	.025	.022	.020	.021	.030
7	.035	.041	.062	.084	.085	.098	.095	.078	.062	.039	.024	.016
8	.021	.024	.030	.042	.050	.053	.052	.043	.034	.025	.017	.016
9	.083	.096	.100	.093	.082	.069	.054	.040	.026	.018	.013	.011
10	.064	.072	.075	.074	.068	.060	.050	.042	.036	.031	.027	.025
11	.041	.045	.051	.056	.055	.051	.043	.034	.026	.022	.019	.018
12	.047	.045	.043	.041	.040	.038	.036	.034	.031	.027	.025	.025
13	.020	.019	.018	.017	.017	.018	.020	.023	.032	.045	.068	.097
14	.014	.015	.012	.011	.009	.007	.006	.005	.003	.003	.007	.010
15	.016	.015	.014	.012	.010	.008	.007	.009	.020	.031	.046	.066
16	.050	.052	.054	.054	.050	.043	.030	.020	.014	.014	.016	.020
17	.027	.027	.031	.043	.050	.051	.049	.039	.023	.014	.014	.023
18	.048	.066	.090	.088	.065	.036	.020	.014	.010	.009	.009	.012
19	.034	.026	.018	.010	.006	.005	.005	.004	.003	.007	.013	.025
20	.030	.027	.026	.025	.024	.023	.022	.021	.019	.016	.014	.015
21	.051	.056	.055	.051	.043	.034	.026	.022	.019	.018	.018	.021
22	.023	.021	.020	.019	.018	.017	.017	.018	.020	.023	.032	.045
23	.040	.050	.060	.060	.050	.032	.020	.014	.011	.012	.014	.023
24	.060	.060	.059	.056	.050	.040	.032	.023	.016	.013	.012	.013
25	.060	.060	.059	.056	.050	.040	.032	.023	.016	.013	.012	.013
26	.042	.050	.053	.050	.040	.032	.024	.017	.015	.015	.020	.036
27	.042	.050	.053	.050	.040	.032	.024	.017	.015	.015	.020	.036
28	.030	.028	.024	.022	.020	.015	.012	.010	.008	.010	.015	.030
29	-.000	-.000	-.000	-.000	-.000	-.000	-.000	-.000	-.000	-.000	-.000	-.000
30	.041	.041	.041	.041	.041	.041	.041	.041	.041	.041	.041	.041

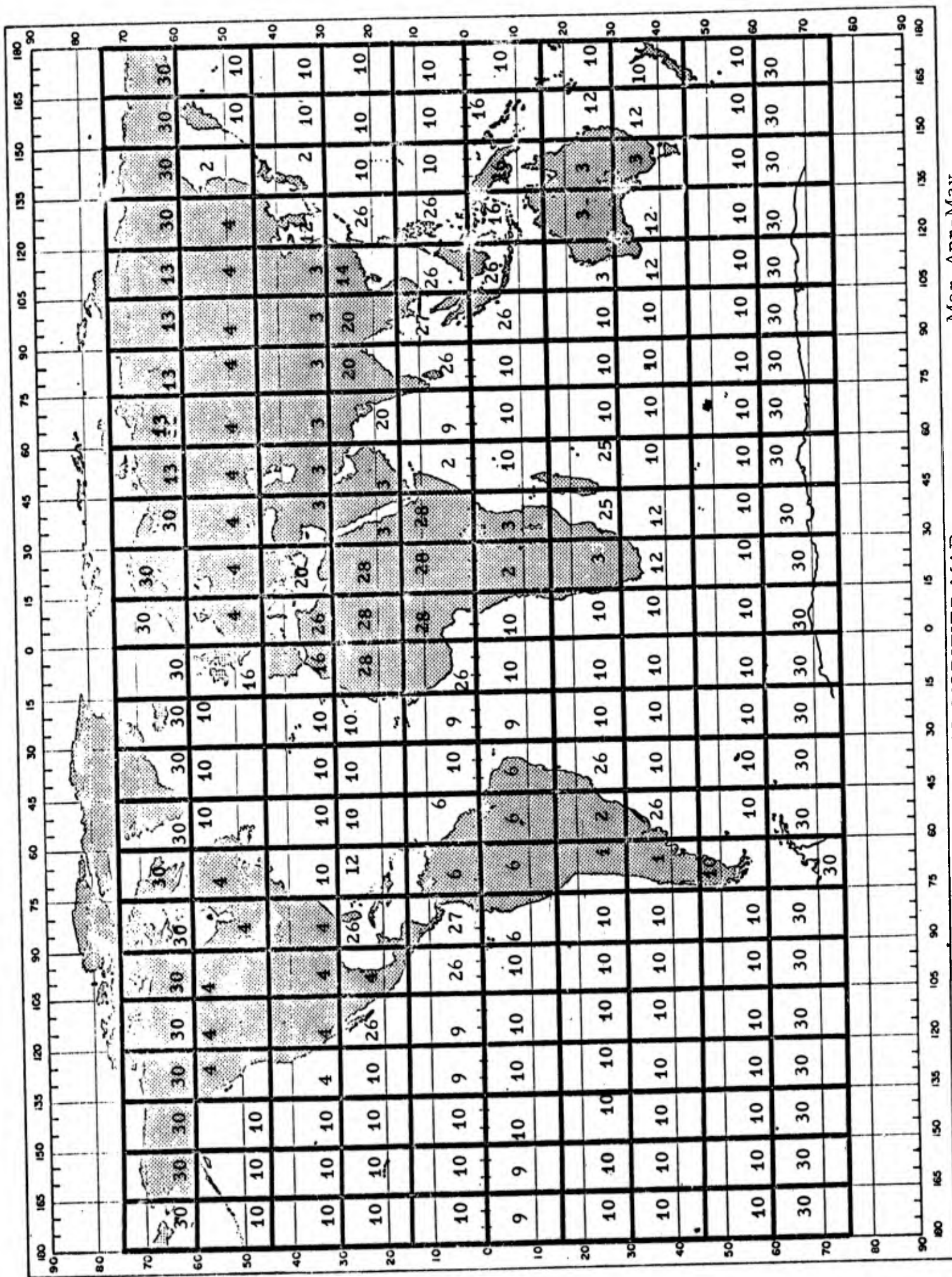
Table 6-1(b)
DIURNAL POWER MODIFIERS (LOCAL TIME)

MOD NO.	TIME											
	1300	1400	1500	1600	1700	1800	1900	2000	2100	2200	2300	2400
1	.036	.050	.067	.087	.105	.099	.080	.062	.046	.036	.029	.027
2	.055	.105	.117	.115	.103	.083	.067	.062	.052	.040	.030	.026
3	.030	.050	.070	.086	.093	.090	.080	.070	.060	.050	.040	.030
4	.039	.057	.063	.064	.064	.062	.060	.057	.054	.050	.044	.041
5	.040	.080	.113	.132	.132	.112	.080	.057	.042	.030	.022	.017
6	.055	.085	.098	.100	.090	.060	.044	.034	.029	.028	.029	.030
7	.014	.014	.014	.015	.017	.022	.026	.027	.029	.030	.031	.032
8	.032	.052	.073	.090	.089	.075	.052	.034	.027	.025	.023	.021
9	.010	.009	.009	.010	.011	.016	.021	.025	.033	.043	.055	.072
10	.023	.021	.020	.020	.021	.023	.026	.031	.037	.044	.052	.058
11	.018	.021	.026	.035	.048	.063	.070	.065	.058	.051	.044	.040
12	.027	.031	.037	.045	.052	.057	.060	.057	.054	.052	.049	.047
13	.103	.092	.088	.065	.053	.044	.039	.033	.029	.026	.023	.021
14	.023	.050	.075	.090	.102	.110	.113	.110	.096	.070	.040	.021
15	.081	.090	.094	.094	.090	.080	.066	.050	.036	.026	.022	.018
16	.034	.050	.056	.055	.051	.048	.046	.046	.047	.049	.050	.050
17	.039	.050	.060	.068	.070	.068	.062	.052	.043	.036	.032	.029
18	.014	.016	.020	.030	.048	.066	.072	.072	.060	.050	.044	.040
19	.055	.089	.098	.097	.090	.081	.074	.066	.060	.050	.044	.040
20	.019	.030	.050	.070	.086	.093	.090	.080	.070	.060	.050	.040
21	.026	.035	.048	.063	.070	.065	.058	.051	.044	.040	.041	.045
22	.068	.097	.103	.092	.088	.065	.053	.044	.039	.033	.029	.026
23	.039	.050	.060	.068	.070	.068	.062	.052	.043	.036	.032	.034
24	.017	.023	.030	.038	.046	.053	.057	.060	.061	.061	.060	.060
25	.017	.023	.030	.038	.046	.053	.057	.060	.061	.061	.060	.060
26	.060	.078	.088	.086	.073	.056	.040	.028	.023	.021	.023	.030
27	.060	.078	.088	.086	.073	.056	.040	.028	.023	.021	.023	.030
28	.062	.105	.117	.115	.095	.070	.050	.040	.034	.032	.030	.030
29	-0.000	-0.000	-0.000	-0.000	-0.000	-0.000	-0.000	-0.000	-0.000	-0.000	-0.000	-0.000
30	.042	.042	.042	.042	.042	.042	.043	.043	.043	.043	.042	.042



Dec-Jan-Feb

Figure 6-2 DIURNAL MODIFIER MAP



Mar-Apr-May

Figure 6-3 DIURNAL MODIFIER MAP

SEASON 3

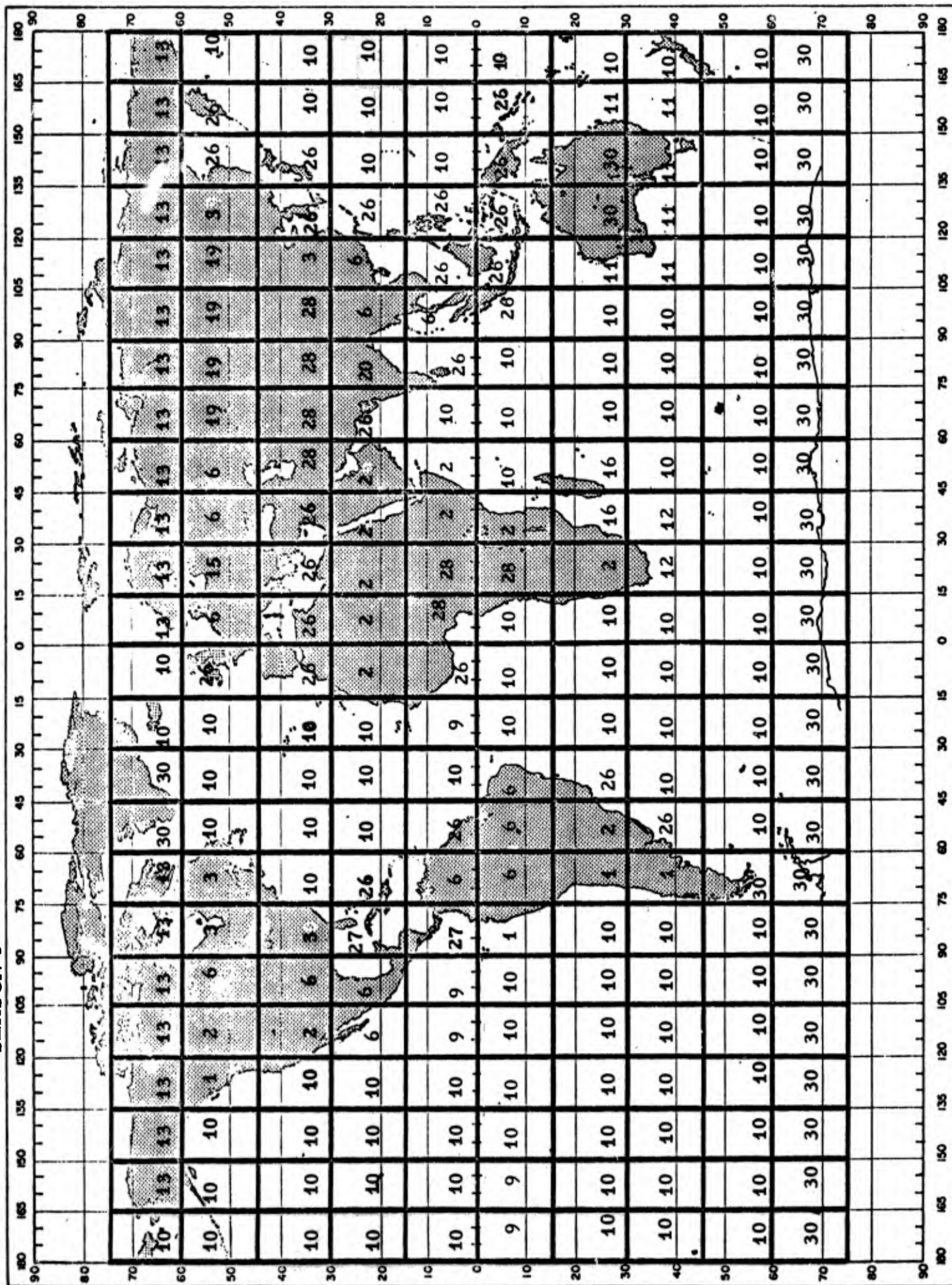
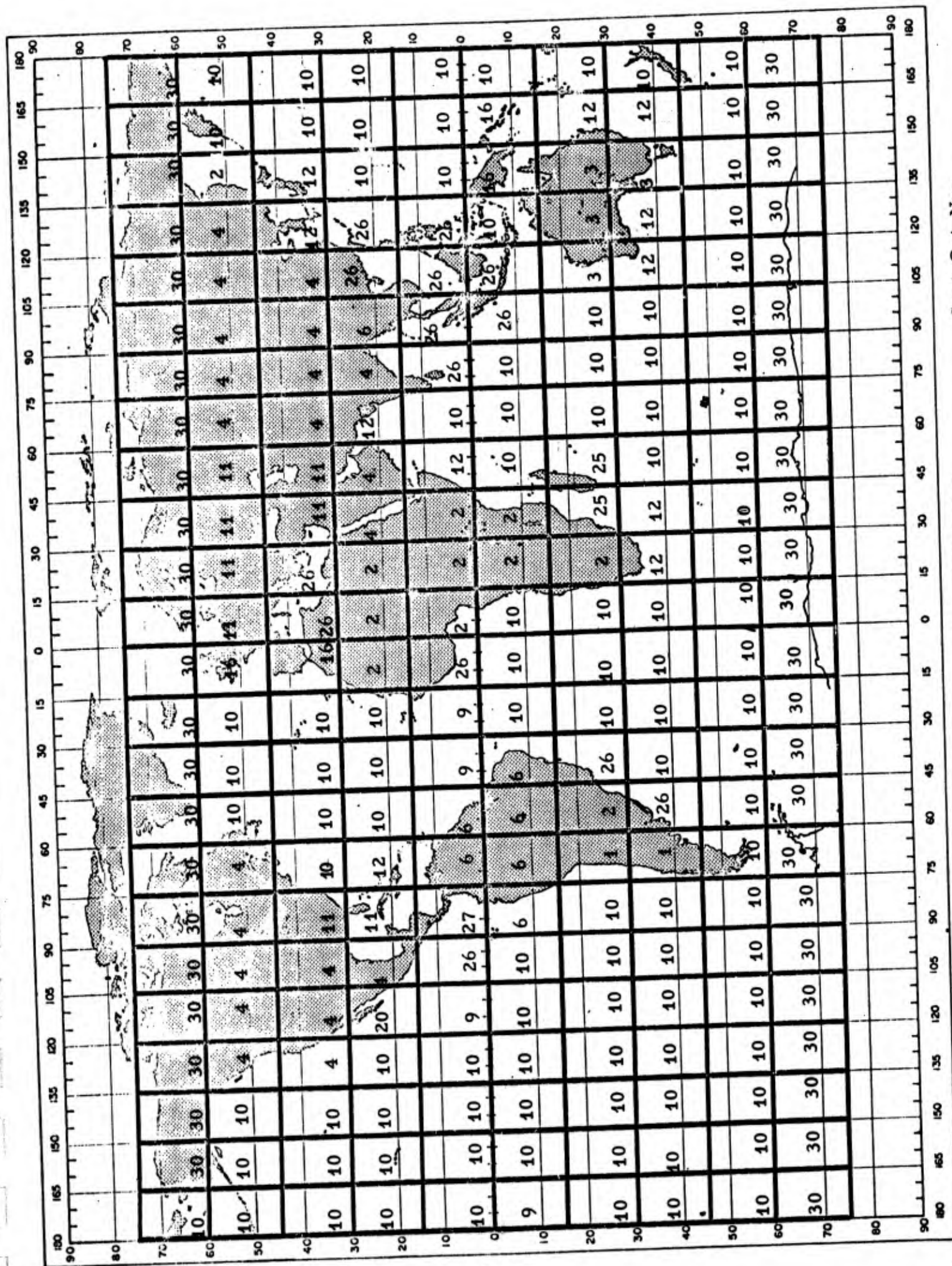


Figure 6-4 DIURNAL MODIFIER MAP

June-July-Aug



Sept-Oct-Nov

Figure 6-5 DIURNAL MODIFIER MAP

STEP VI

The power of most transmitters located in large ocean areas is lowered by 4 dB from that computed in step I. This is done because the altitude of cloud bases over the oceans are generally reported as being higher than those over land, and the number of cloud-to-ground lightning discharges at sea are reported as being very few. These two observations would indicate fewer cloud-to-ground discharges for storms over the oceans than storms over the land, thereby lowering the power radiated for the same number of total discharges compared to an equivalent land area. Exceptions to this have been made for transmitters located very close to the equator where equation (3-5) has already reduced the number of ground discharges to a very low value.

Also, the power of transmitters having a mixture of land and sea areas are lowered by 2 dB. This is based on the same reasoning presented above, except that only a part of the storms now occur over the oceans. Transmitters for which the thunderstorm day maps show most of the activity being over the land area within its region are not lowered at all.

This step is part of the computer program NOISLAN, Stone [1970].

STEP VII

Read in the coordinates of a receiver and compute the co-latitude and co-longitude of the receiver.

This step is also part of NOISLAN.

STEP VIII

Select the major transmitters which will be used for computing the field intensity for this receiver and determine which, if any, of the major transmitters should be replaced by the minor transmitters from which it was formed.

Both of these selections are based on the distance between each transmitter and the receiver and the power of the transmitter. Many transmitters are so low power that unless they are very close to the receiver for which fields are being computed they will have a negligible effect upon the total field intensity. As a matter of economy, it was desirable to select only those transmitters which will have a significant effect on the fields for the computations. This selection is accomplished as follows: the ratio expressed by the equation (6-1), below, is computed for each transmitter.

$$P_{RAT} = \frac{P_r}{10^{\alpha/10} \left(\sin \frac{d}{a} \right)} \quad (6-1)$$

where:

- α is attenuation coefficient and equals 1 dB/megameter,
- d is distance in meters between transmitter and receiver,
- a is earth radius in meters.
- P_r is power radiated in watts.

This computation very roughly approximates the effects of attenuation and distance using a very low attenuation coefficient to insure that no transmitter of any significance will be eliminated. The transmitters are then ordered according to the magnitude of P_{RAT} . Finally, those transmitters whose ratio, P_{RAT} , fall within 2 percent of the maximum P_{RAT} are selected for use in the actual field computations.

Computations have shown that addition of all other transmitters beyond those selected in this manner increases the field intensity by only a few tenths of a dB. A maximum on the number of transmitters to be used was set at 70.

This step is part of NOISLAN.

STEP IX

When a receiver is very close to a major transmitter, the minor transmitters making up the major are used for field computations. This provides a much more accurate field computation, since distance and direction of propagation become very critical for sources very close to the receiver. The nine minor transmitters more closely approximate the real world (at close range) than does one major transmitter. The criteria for using minor transmitters in place of the majors are based upon distance and power. If the major transmitter is more than 3 megameters from the receiver, it will not be broken up regardless of its power. If the major transmitter power is less than 200 milliwatts, it will not be broken up regardless of how close it is to the receiver. Transmitters which fall within the 3 megameters and 200 milliwatts limit are broken up if:

$$\frac{P_r}{d/10^6} < 0.4. \quad (6-2)$$

Finally, the minor transmitters are used in the calculations only if their power is greater than or equal to 2 percent of the major transmitter of which they are a part. These criteria are empirical based on test calculations, which showed little change in fields when more minor transmitters were used.

Both Steps VIII and IX are factors of economy and accuracy. We have undoubtedly sacrificed some economy in an attempt to eliminate any significant sacrifice of accuracy.

Step IX is also part of NOISLAN.

STEP X

In preparation for the computation of the actual field intensity for a given receiver and transmitter, the following parameters are computed:

1) the bearing from the receiver to the transmitter, 2) the lengths of path segments, within various conductivity areas between the receiver and transmitter, 3) modified power of the transmitter according to the diurnal modifier table and the equation:

$$P_{rm} = 24 D_m P_r \quad (6-3)$$

where:

D_m is the proportion (%/100) of the thunderstorms occurring for the particular hour at the transmitter (local standard time).

4) changes in ionospheric attenuation due to directional and latitude effects for each 4 megameter path segment between the receiver and transmitter, 5) lengths of day and night portions of the path between the transmitter and receiver, and 6) total path attenuation due to the ground and the ionosphere.

Computation of these parameters are accomplished in the following subroutines which are part of NOISLAN: BEARS, LAND, ATTION, POWER, SUNNY, and ATTEN. Refer to Stone [1970]^v for more details on these subroutines.

STEP XI

The square of the field intensity at the receiver location produced by each transmitter is computed using the square of equation (4-2). The final value for vertical electric field intensity for a given receiver is computed from the equation:

$$E_v = \left(\sum_{i=1}^n E_{v_i}^2 \right)^{1/2} \quad (6-4)$$

where:

E_{v_i} is the field from the i^{th} transmitter. This is based on the non-coherence of the equivalent noise transmitters.

It should be noted that the distance between transmitters and receivers is limited to a minimum of 500 kilometers. Smaller distances than this are not justified because of the spatial distribution of the actual source of noise, the individual thunderstorm.

More details on the actual computation of the field intensities can be obtained from section 4.0 of this report and from Stone [1970].

STEP XII

For the preparation of isofield contours for world-wide noise prediction maps, field intensities are computed on a 10° Long. by 10° Lat. grid or matrix. This matrix of field intensities is then fed into a program for plotting the isofield contours Stone [1970]. The plot program did not produce contours as smooth as might be desired but they accurately represent the computed values. The actual plotting was done on a CDC 280 microfilm system. This is an analog system which also caused some difficulty in maintaining quality plots for reproduction.

A program to annotate the contours during the computer plotting operation eliminated the opportunity for human error. We believe the accurate contours and error free annotations adequately compensate for their somewhat rough appearance.

STEP XIII

Season-time block values are computed by the equation

$$E_{vS-TB} = \frac{1}{12} \sum_{M=1}^3 \sum_{H=1}^4 E_{vM-H} \quad (6-5)$$

where:

E_{vM-H} are the month-hour values previously computed and

E_{vS-TB} are season - 4 hour time block values.

Use of the 12 monthly-hourly values to compute seasonal-time block values is much more accurate than computing them directly with seasonal thunderstorm day maps and mid-season computations of the sun's zenith angle.

THIS COMPLETES THIS ALGORITHM

The execution of the algorithm described above produced 288 month-hour and 24 season-time block sets of contours. These are presented in a VLF Noise Prediction Manual prepared under this contract for publication by the U.S. Government.

6.2 Description of the Computer Program

The major flow chart shown on Figure 6-6 is actually a flow chart for the entire noise prediction model. As such, it contains parts of the model pertaining to the calculation of standard deviation, voltage deviation (v_d or form factor) and direction of arrival plots. It is presented here because it should serve to clarify the flow of information and procedures described in the previous section. Although it is a greatly abbreviated description of the entire noise prediction model, the major steps and computer programs are included. Those parts of the flow chart dealing with standard deviation, etc. will become understandable upon reading later sections of this report.

Since a separate report has been written, Stone [1970], describing the computer programs in some detail, no information other than that contained in Figure 6-6 will be presented in this report.

6.3 Comparison of Calculated and Measured Values

During the International Geophysical Year 1957, the Central Radio Propagation Laboratory of the National Bureau of Standards established a worldwide network of noise measurement stations. This network was taken over by the Environmental Science Services Administration (ESSA) at the time that organization was established. Most of the stations made measurements at frequencies from 13 kHz to 10 MHz. Those stations for which data was obtained at 13 kHz include Balboa, Canal Zone; Boulder, Colorado; Cook, Australia; Enkoping, Sweden; Kekaha, Hawaii; New Delhi, India; Ohira, Japan; Pretoria, South Africa; Rabat, Morocco; and Singapore, Malaya. These stations operated for about 10 years before this program was discontinued. For various reasons, all of the stations did not have 10 years of data at 13 kHz, but 5 or more years of data were available at all stations.

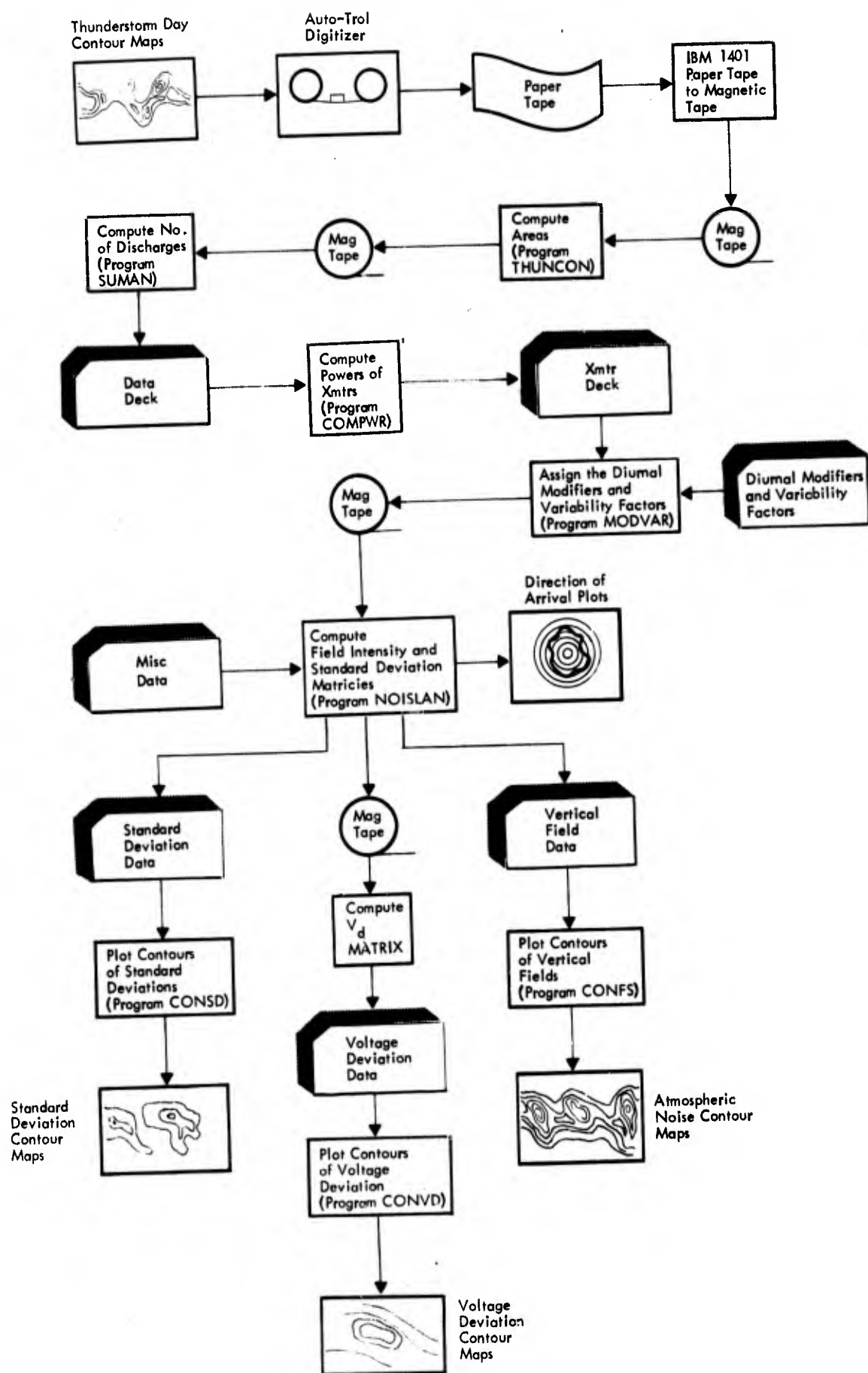


Figure 6-6 VLF Atmospheric Noise Prediction Flow Chart

All of the 13 kHz data available was digitized for use on this program. The last few years of data were available in digital form from ESSA, the earlier data were manually punched onto computer cards.

Average values of noise field intensity for each hour of the day, for each month and for each three month season, were computed for comparison with the calculations. Computer programs were written to compare measured and predicted values and automatically plot the difference between the two. This capability was extremely valuable and was used to verify attenuation coefficients, diurnal modifiers, transmitter powers, etc. It proved particularly valuable identifying small errors in the computer programs which might have gone undetected had not such detailed comparisons been possible. These comparisons were the only means for selecting diurnal modifiers for those regions of the world from which no data were available relative to the diurnal distribution of thunderstorms.

The comparison plots shown here, figures 6-7 to 6-14, were made after all adjustments and corrections had been made. It was extremely encouraging to find that little modification of the model developed for computing energy radiated from thunderstorm day and lightning discharge data was required. The only exception to this is the lowering of the power for storms at sea as was discussed in Section 6.1, STEP VI. All other computed powers for the noise transmitters were used without modification for all months and all locations. The only change made in the model during the course of these investigations was related to the number of pulses which should be included in each intra-cloud lightning discharge.

Although this would seem to indicate that our model is nearly perfect, we must caution against such an assumption. For instance, an error in the number of discharges may be compensated for by the power computed

BOULDER, COLORADO

(DEC., JAN., FEB.)

FINCH

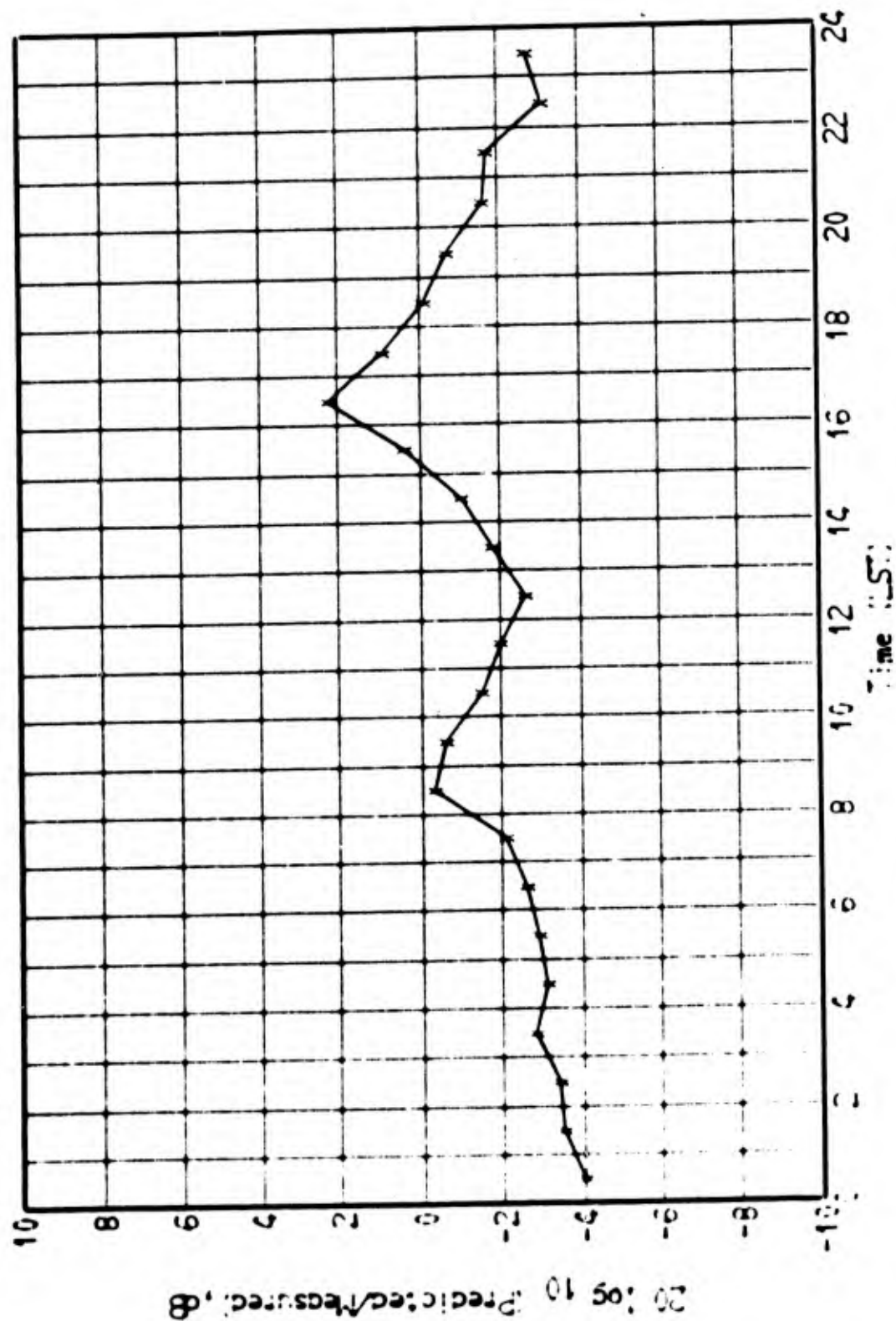


Figure 6-7 Finch: Comparison of Predicted and Measured Field Intensities

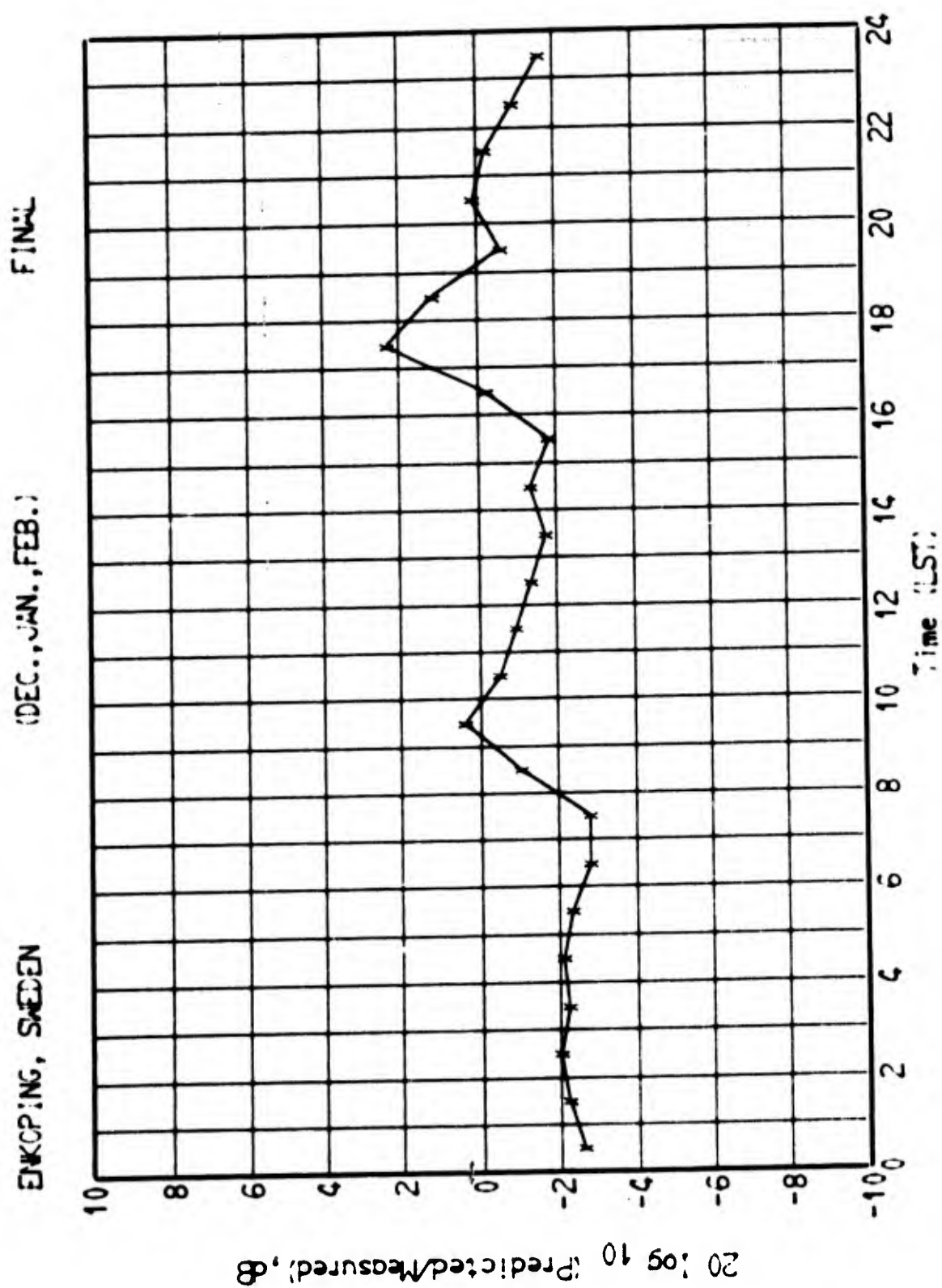
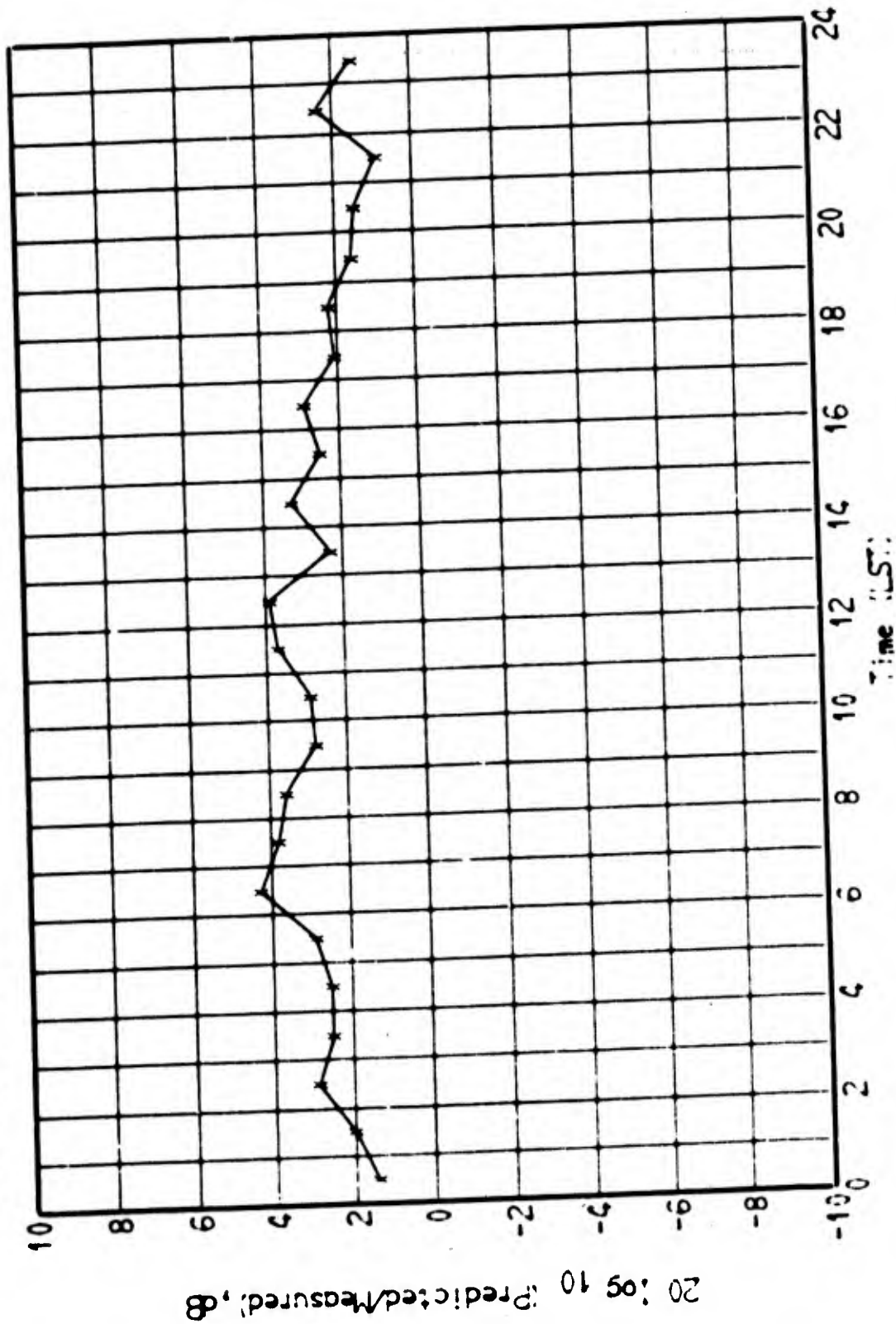


Figure 6-8 Final Comparison of Predicted and Measured Field Intensities

FINAL

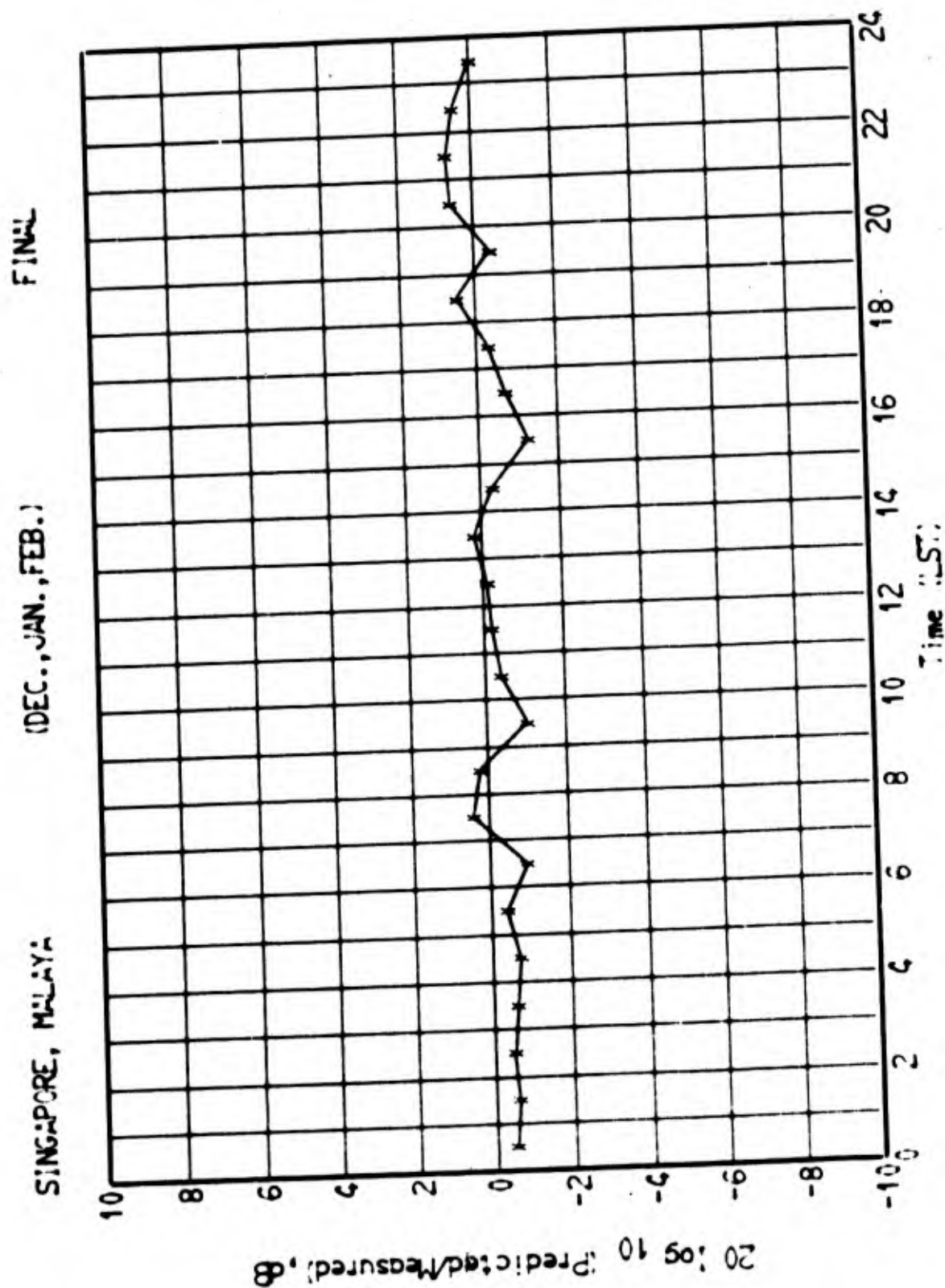
(DEC., JAN., FEB.)

PRETORIA, S. AFR.



Final Comparison of Predicted and Measured Field Intensities

Figure 6-9



6-22

Figure 6-10 Final Comparison of Predicted and Measured Field Intensities

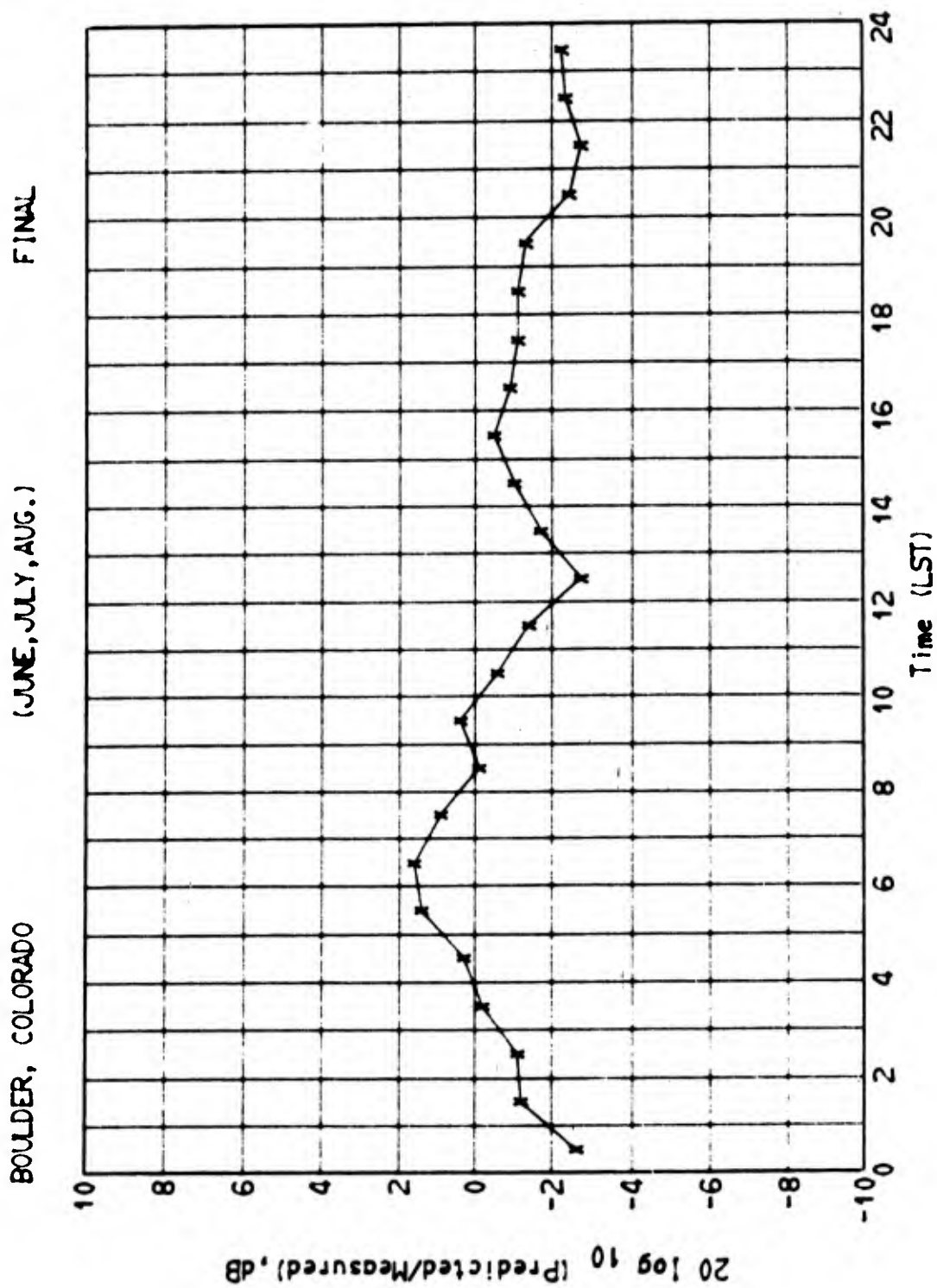


Figure 6-11 Final Comparison of Predicted and Measured Field Intensities

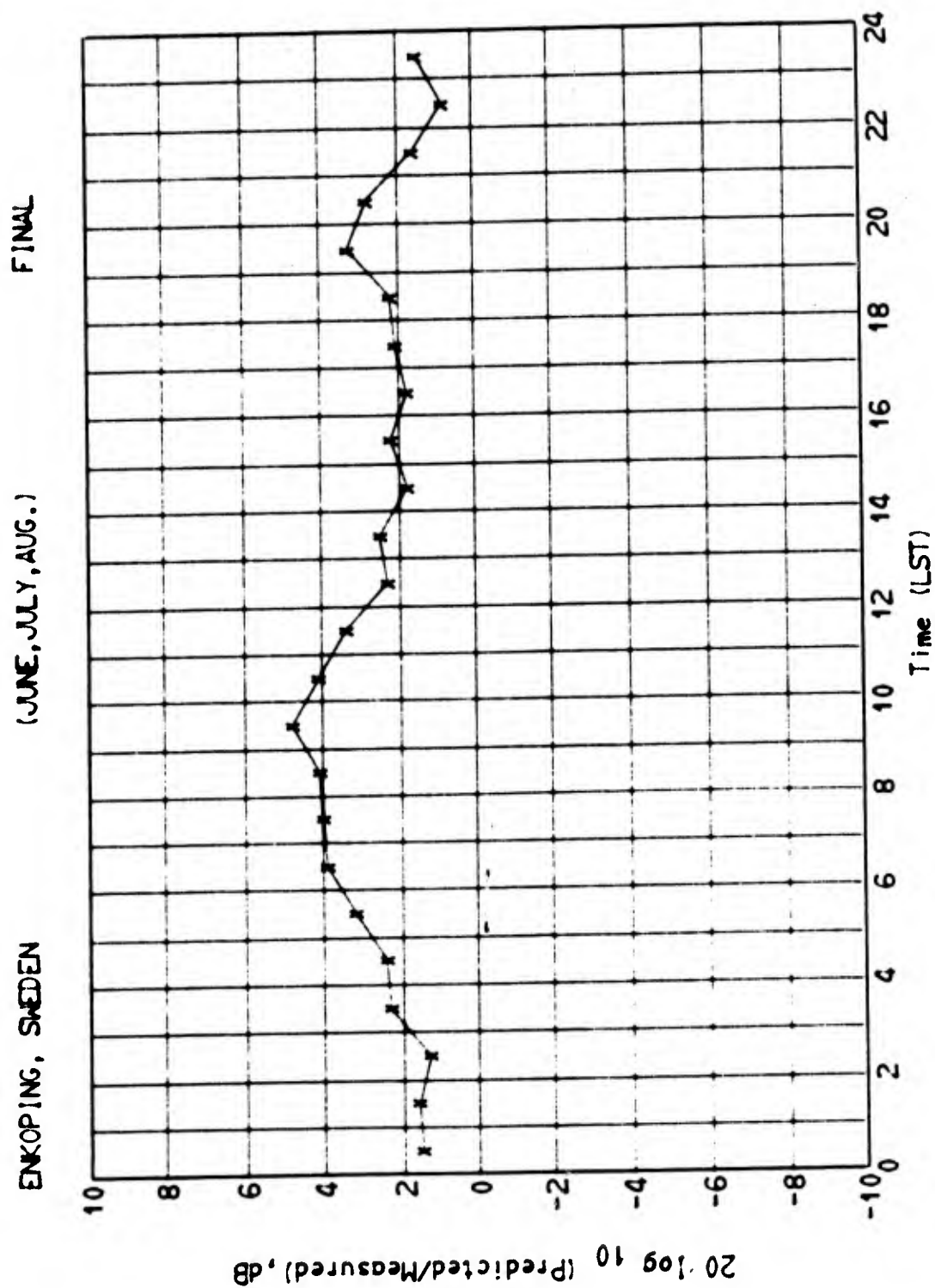


Figure 6-12 Final Comparison of Predicted and Measured Field Intensities

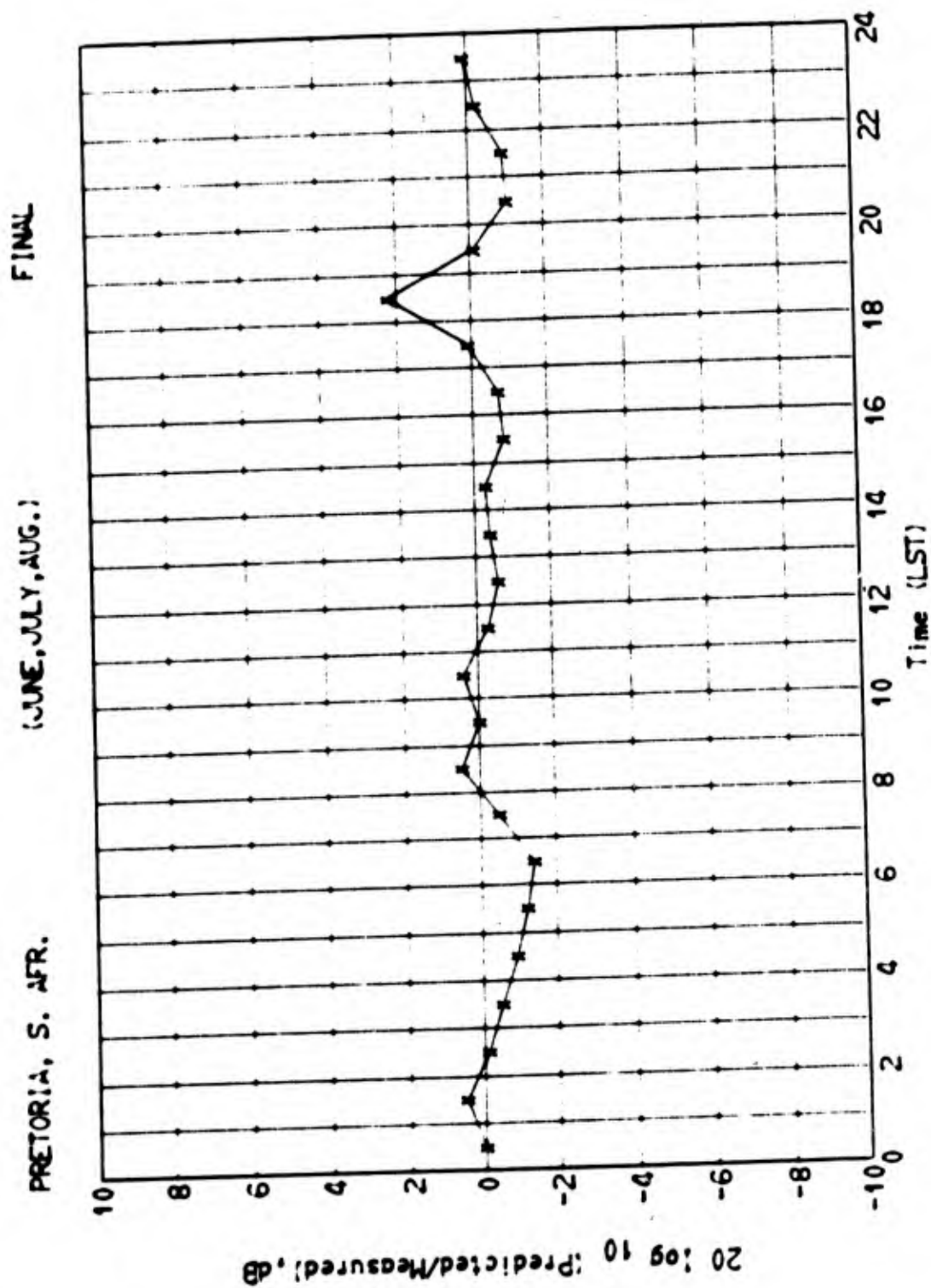


Figure 6-13 Final Comparison of Predicted and Measured Field Intensities

SINGAPORE, MALAYA

(JUNE, JULY, AUG.)

FINAL

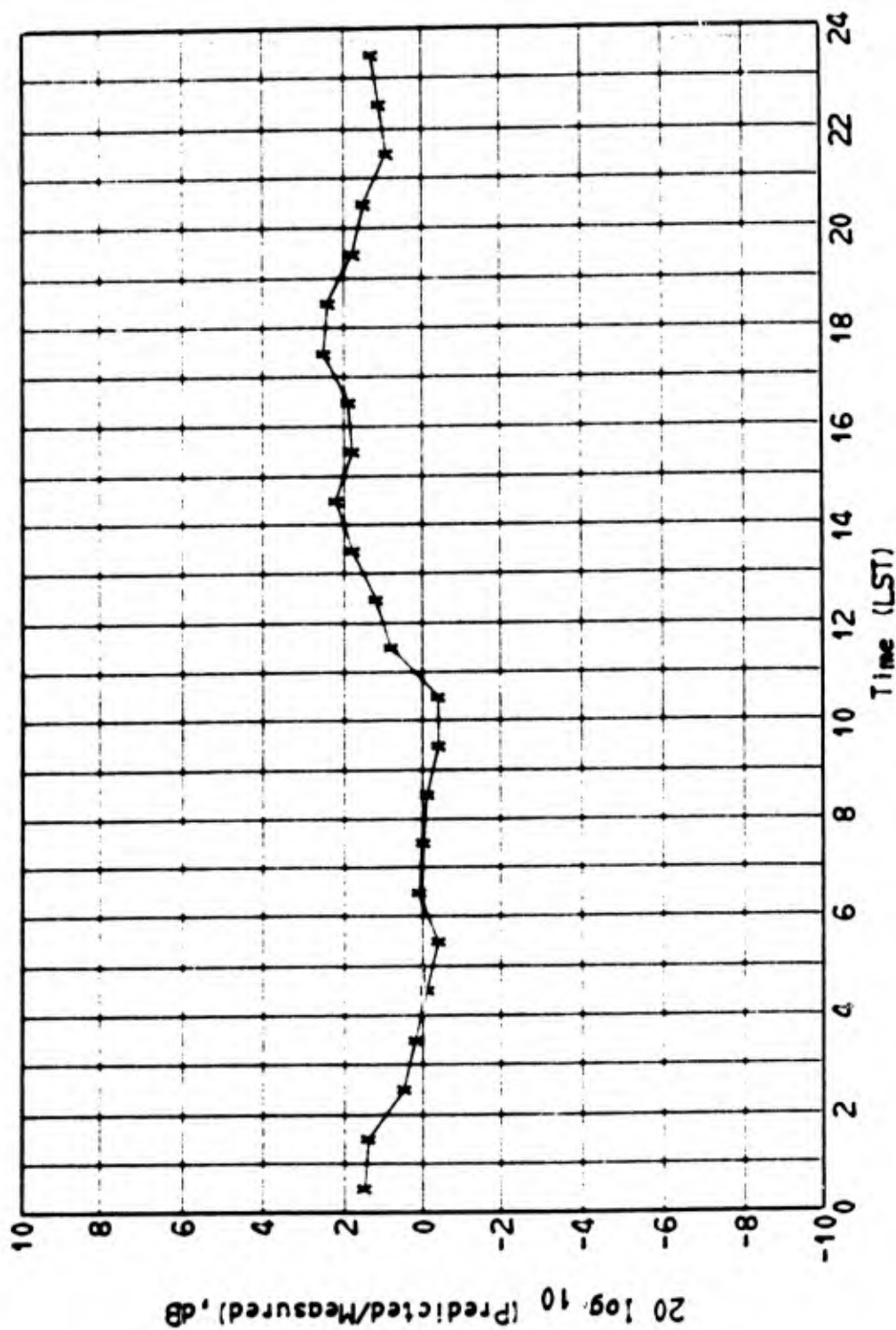


Figure 6-14 Final Comparison of Predicted and Measured Field Intensities

per discharge. Many other possibilities for compensating errors exist. We are of course very pleased with the results from this model and believe it to be a close approximation to reality. Of more significance, however, is the ability to relate this model to the individual events and parameters of the real world, since this offers the opportunity to improve the model as additional data become available.

The comparisons shown were made for three month averages of both computed and measured values. This helped in reducing a certain amount of scatter in the measured data and reduced the number of figures required to present the final comparisons. We were striving to maintain the difference between measured and calculated values within plus or minus 3 dB for all hours and all months. We did not quite accomplish this, although the results generally fall within these limits and for some stations are much better than this. The final comparison plots for Boulder, Colorado; Enkoping, Sweden; Pretoria, South Africa; and Singapore, Malaya are shown for the December-January-February and June-July-August seasons in Figures 6-7 through 6-14. These are a very representative sampling of the comparisons for all ten ESSA noise stations.

A plot of the field intensities for Boulder and Pretoria for these two seasons are shown in Figures 6-15 through 6-18. The accuracy with which the predicted values are able to follow the large diurnal changes in field intensity is further indication of the validity and value of the entire model. Comparisons were made for all seasons for all stations and no differences larger than those shown in these figures were found with the exception of Rabat, Morocco. At this station a difference of 6 dB was noted for two hours for the June-July-August season. The data for Rabat, however, show extremely large variations from month-to-month which cannot be explained from any known climatological change. It is our opinion, therefore, that the Rabat measured data is of questionable accuracy. For the

FINAL

(DEC., JAN., FEB.)

BOULDER, COLORADO

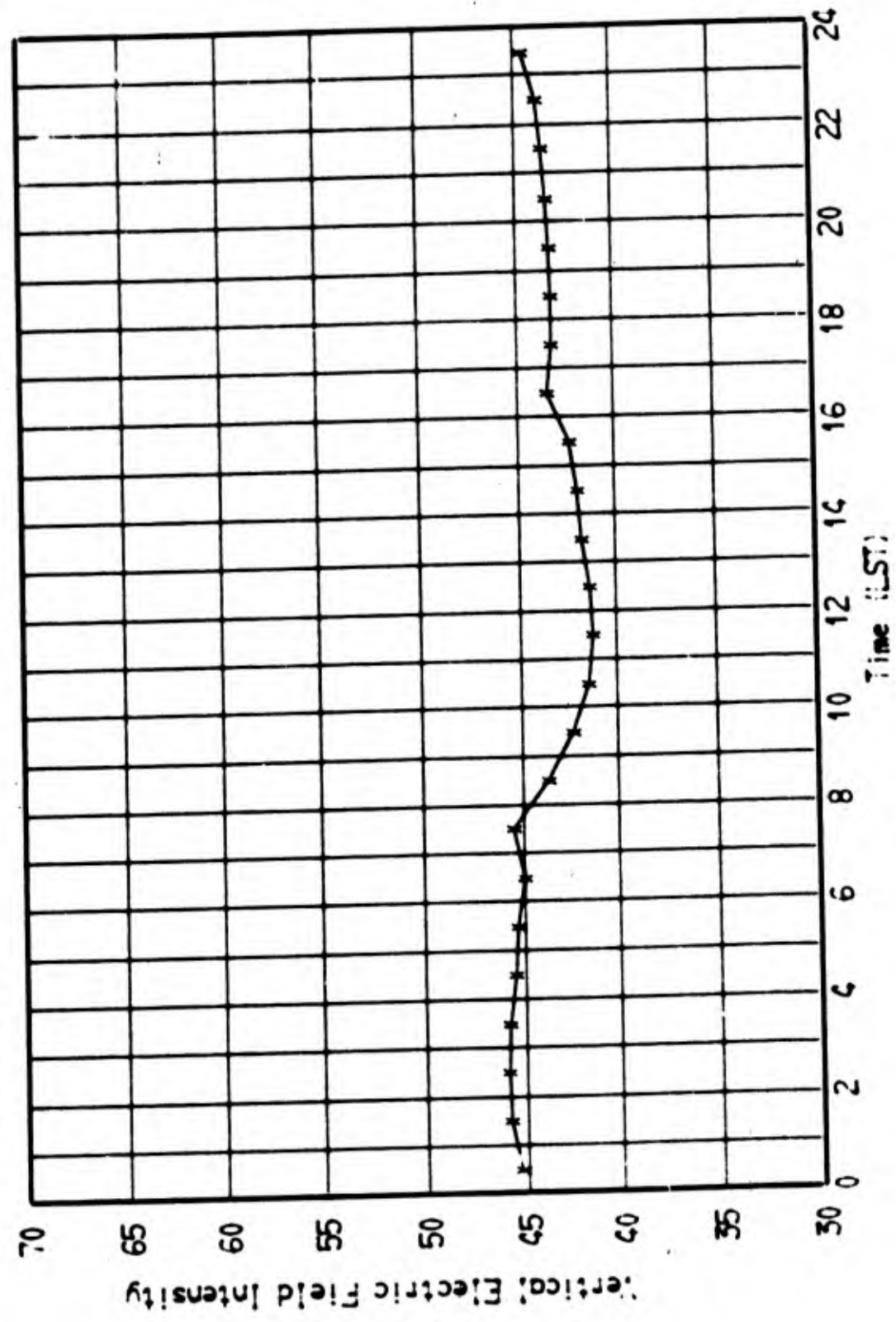


Figure 6-15 Vertical Electric Field Intensity at 15 kHz in dB rel to 1 $\mu\text{V}/\text{m}$ in a 1 kHz B.W.

FINAL

(DEC., JAN., FEB.)

PRETORIA, S. AFR.

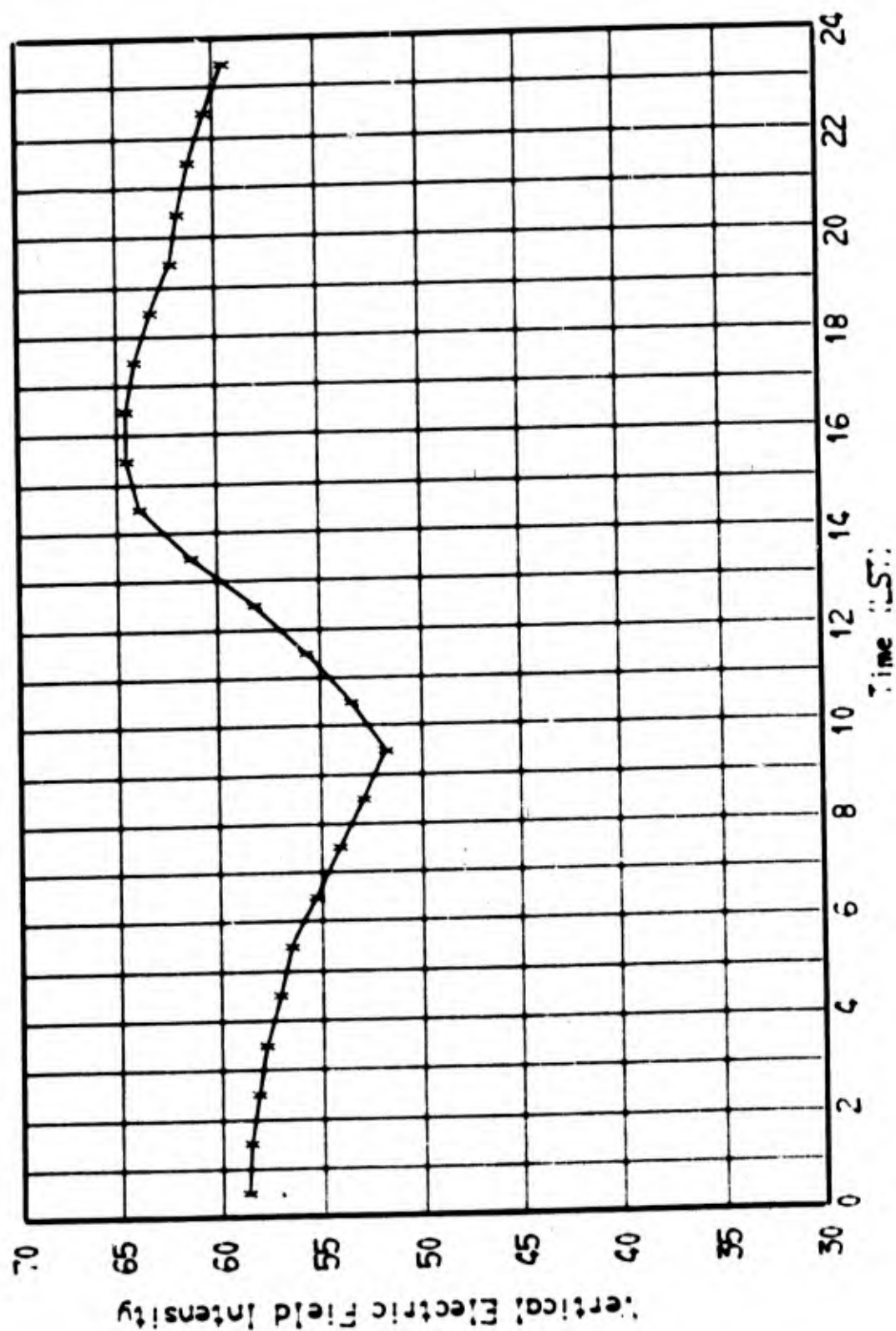


Figure 6-16 Vertical Electric Field Intensity at 15 kHz in dB rel to 1 $\mu\text{V/m}$ in a 1 kHz B.W.

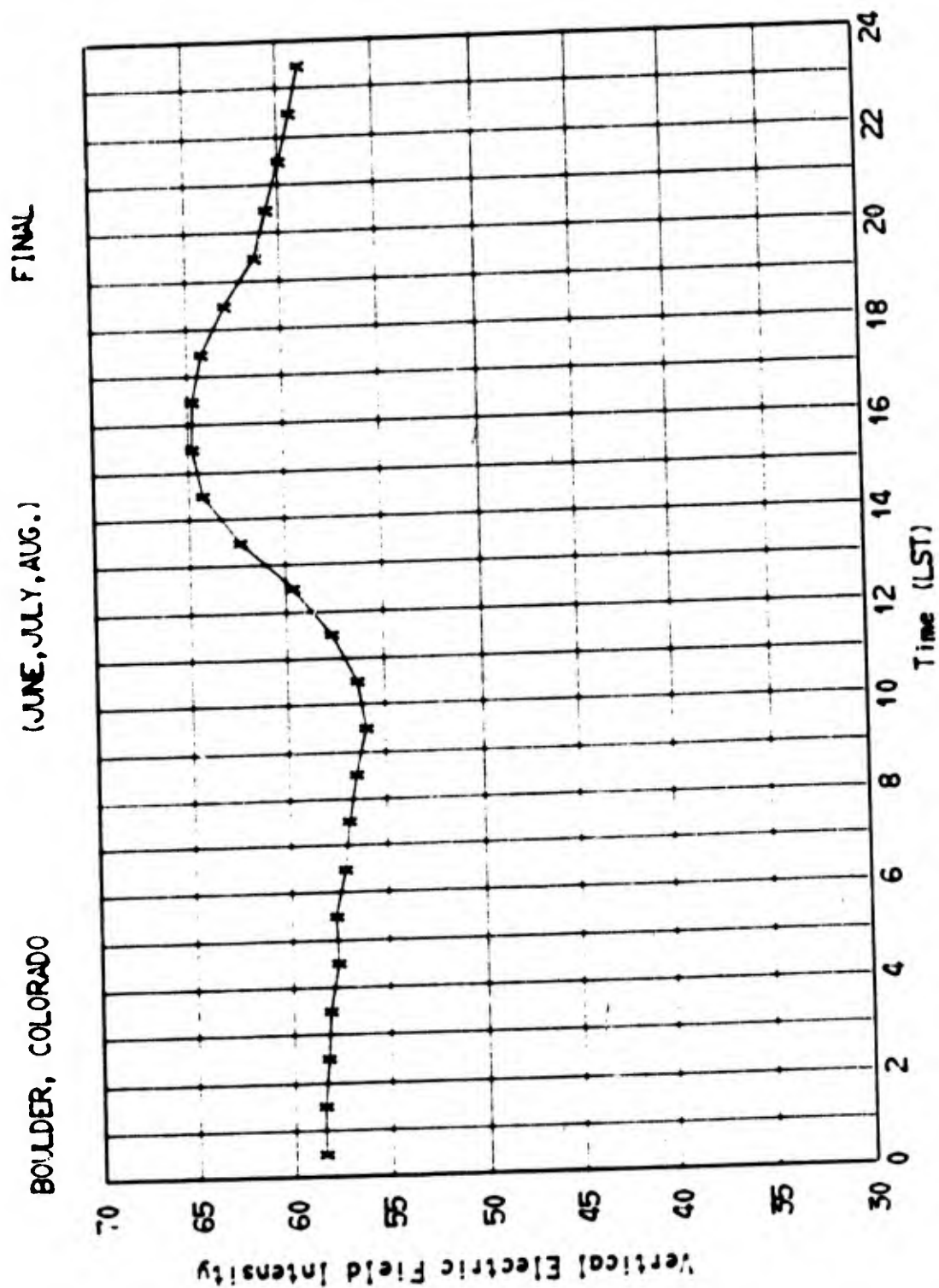


Figure 6-17 Vertical Electric Field Intensity at 15 kHz
in dB rel to 1 $\mu\text{V}/\text{m}$ in a 1 kHz B.W.

PRETORIA, S. AFR.

(JUNE, JULY, AUG.)

FINAL

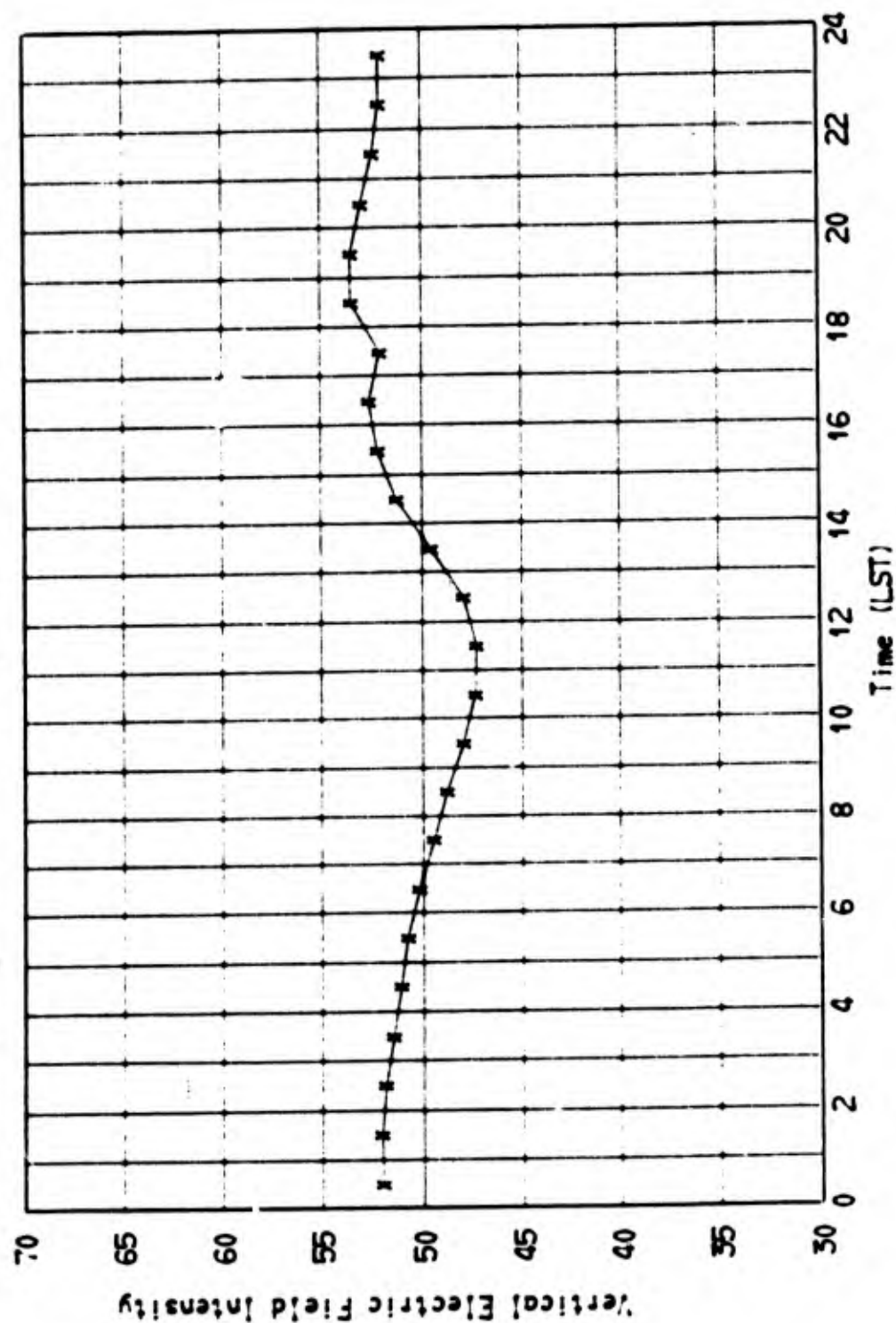


Figure 6-18 Vertical Electric Field Intensity at 15 kHz
in dB rel to 1 $\mu\text{V}/\text{m}$ in a 1 kHz B.W.

September-October-November season, for instance, only twelve of the 216 comparisons for the other stations (9 stations, all 24 hours) showed a difference greater than 3 dB. The maximum difference for these 9 stations was 3.8 dB for New Delhi at 08:30 local standard time. On the other hand, 14 of the 24 hourly comparisons for Rabat showed a difference greater than 3 dB with a maximum of 5.6. There appears to be good reason for suspecting the Rabat measured data.

Appendix A contains tables of the calculated and measured (ESSA) values and the difference, for all 10 ESSA locations,

6.4 Computation of Frequency Modifiers

One of the primary difficulties in using previous predictions of atmospheric noise, has been the lack of provision for source location and propagation effects on the spectrum of the noise. This shortcoming was alleviated by the direct computation of field intensities for each of the locations shown on Figure 6-19, for the frequencies 10, 13, 20, 25, and 30 kHz. A computer program was written to compute and plot the difference between 20 kHz and each of the other frequencies for all hours of the day; plots were made for six hours. The results for two locations on the Equator and the North and South Pole are shown on Figures 6-20 through 6-23 for the December-January-February season. The use of the proper frequency interpolation figure for each region outlined on Figure 6-19 (the regions are approximately equal in area) should produce good results.

Frequency interpolation calculations were made only for the middle month of each season and presented as being representative for each month of the season. If more accuracy is desired, some further interpolation could be done for in-between locations, at in-between months for in-between hours. For most purposes, interpolation should not be required.

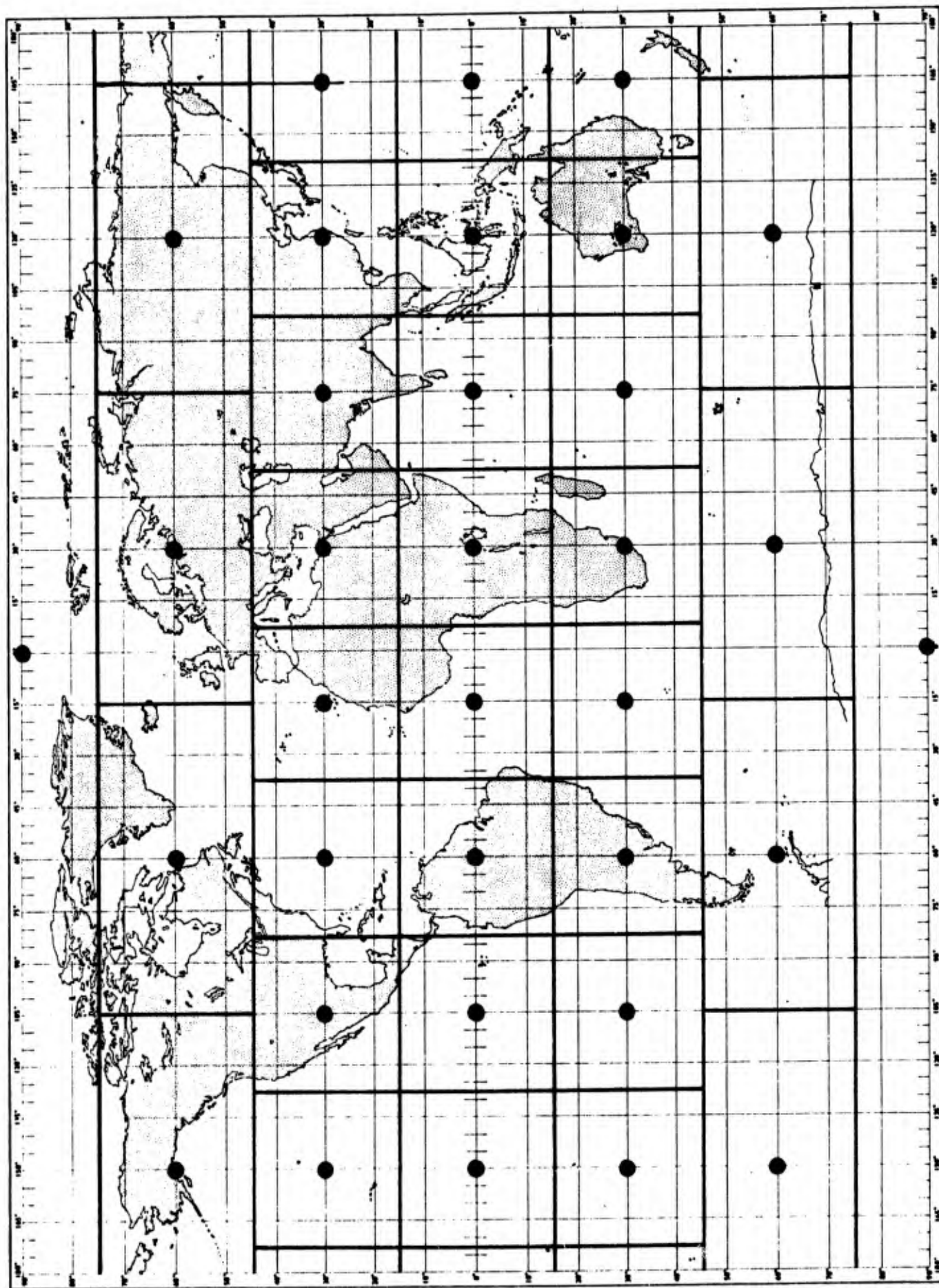
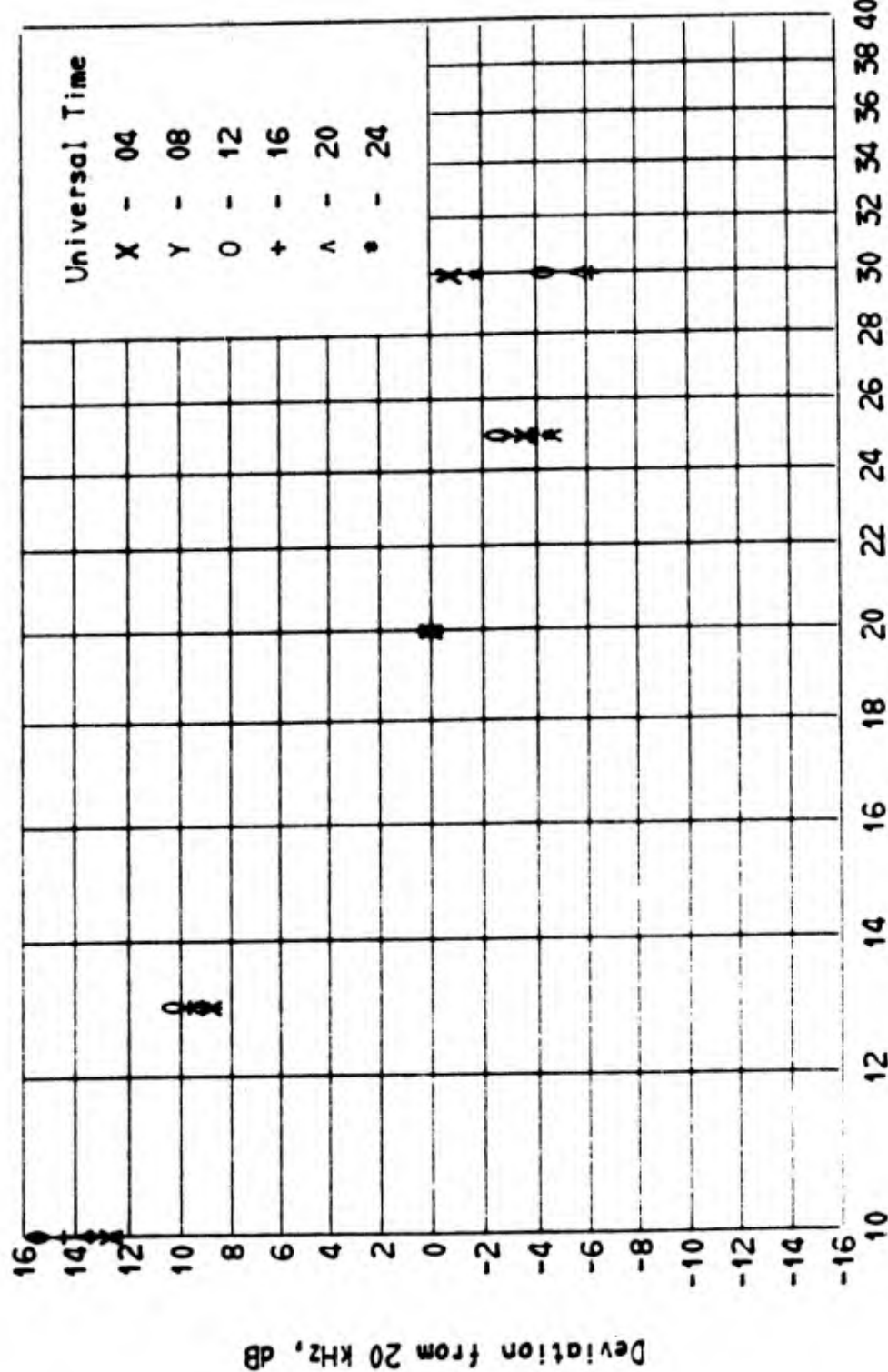


Figure 6-19 Locations for computation of frequency interpolations

0 E 90 N

DEC., JAN., FEB.



6-34

Figure 6-20 Frequency Interpolation of Vertical Electric Field Intensity

0 E 90 S

DEC., JAN., FEB.

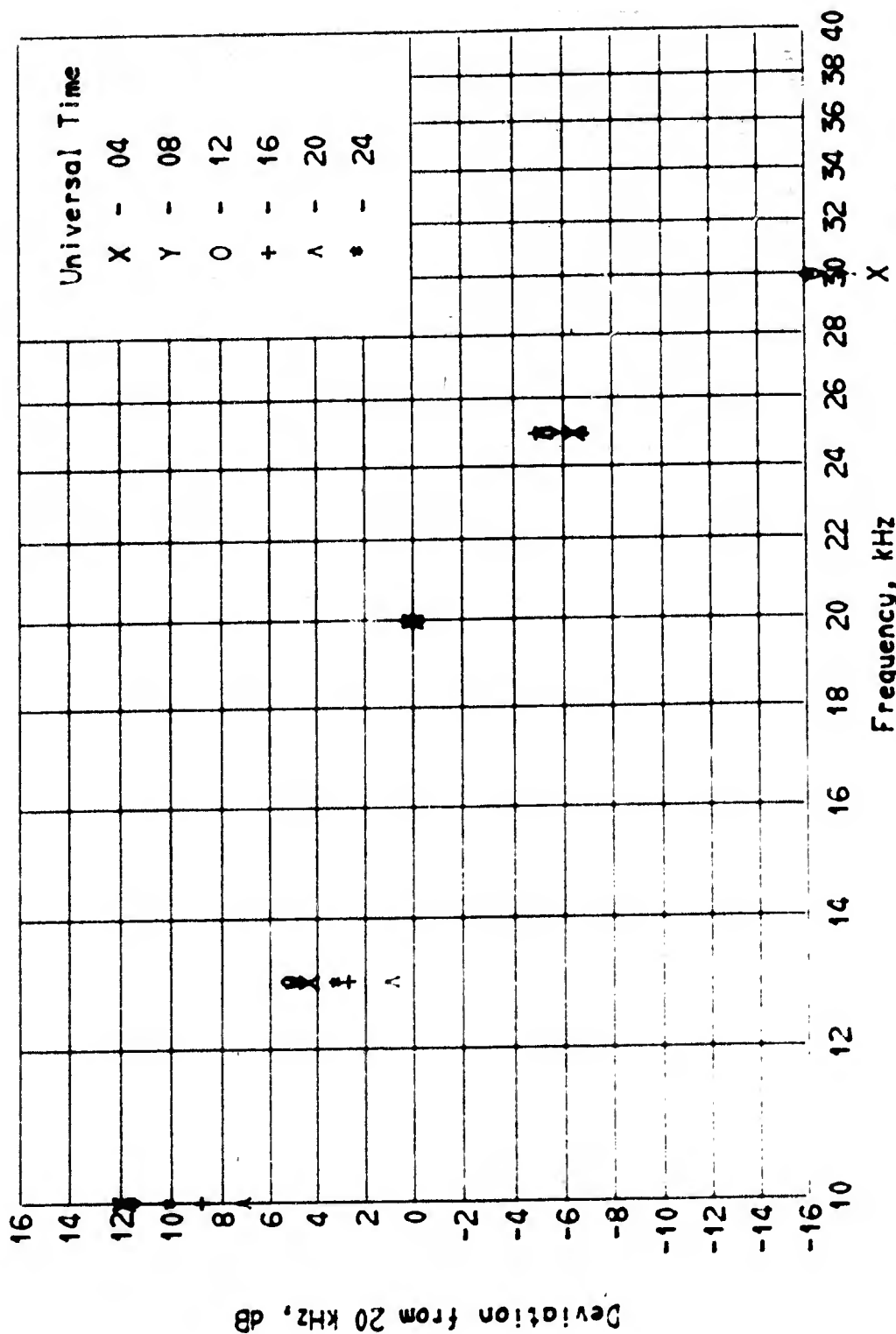


Figure 6-21 Frequency Interpolation of Vertical Electric Field Intensity

30 E 0 N

DEC., JAN., FEB.

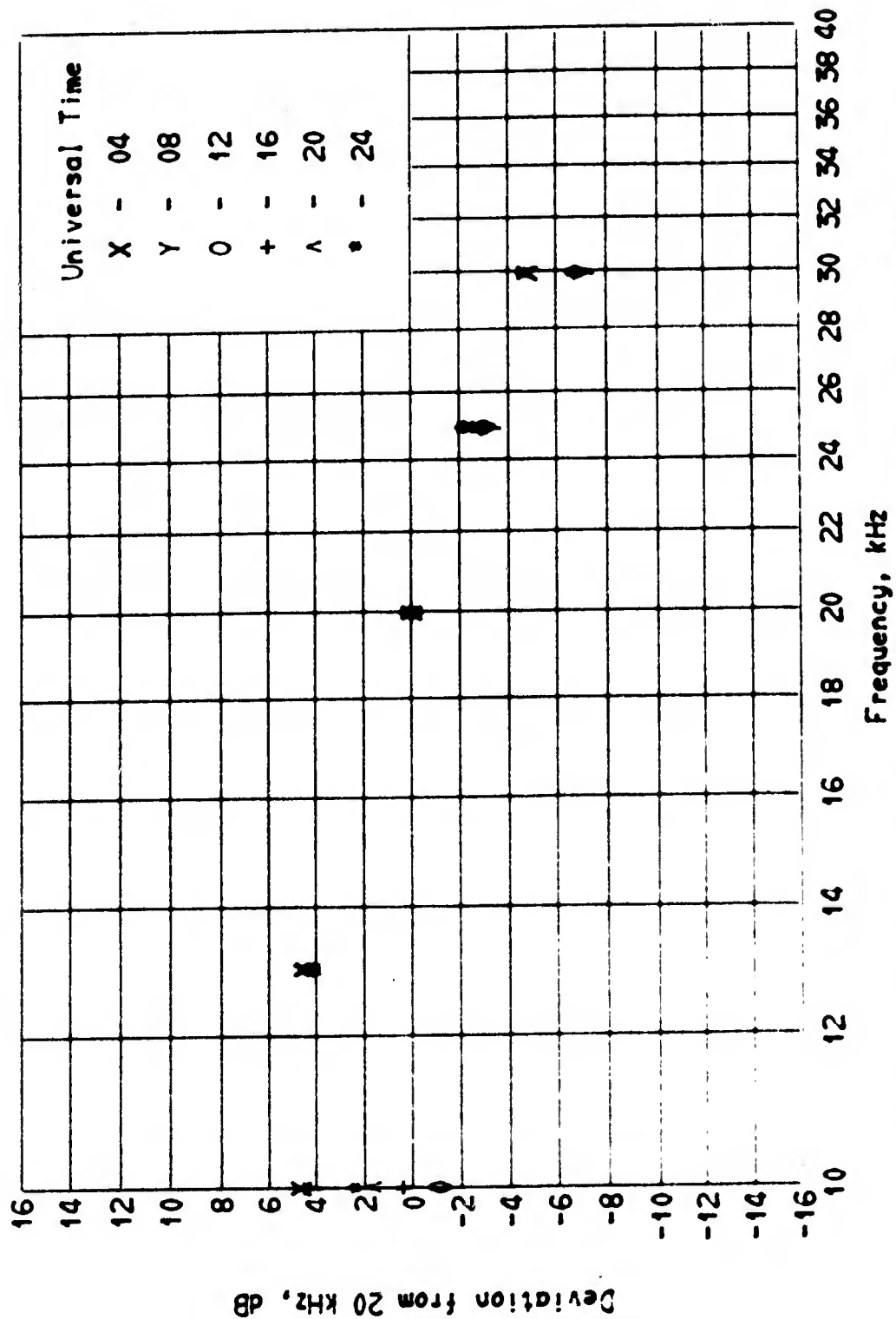


Figure 6-22 Frequency Interpolation of Vertical Electric Field Intensity

75 E 0 N

DEC., JAN., FEB.

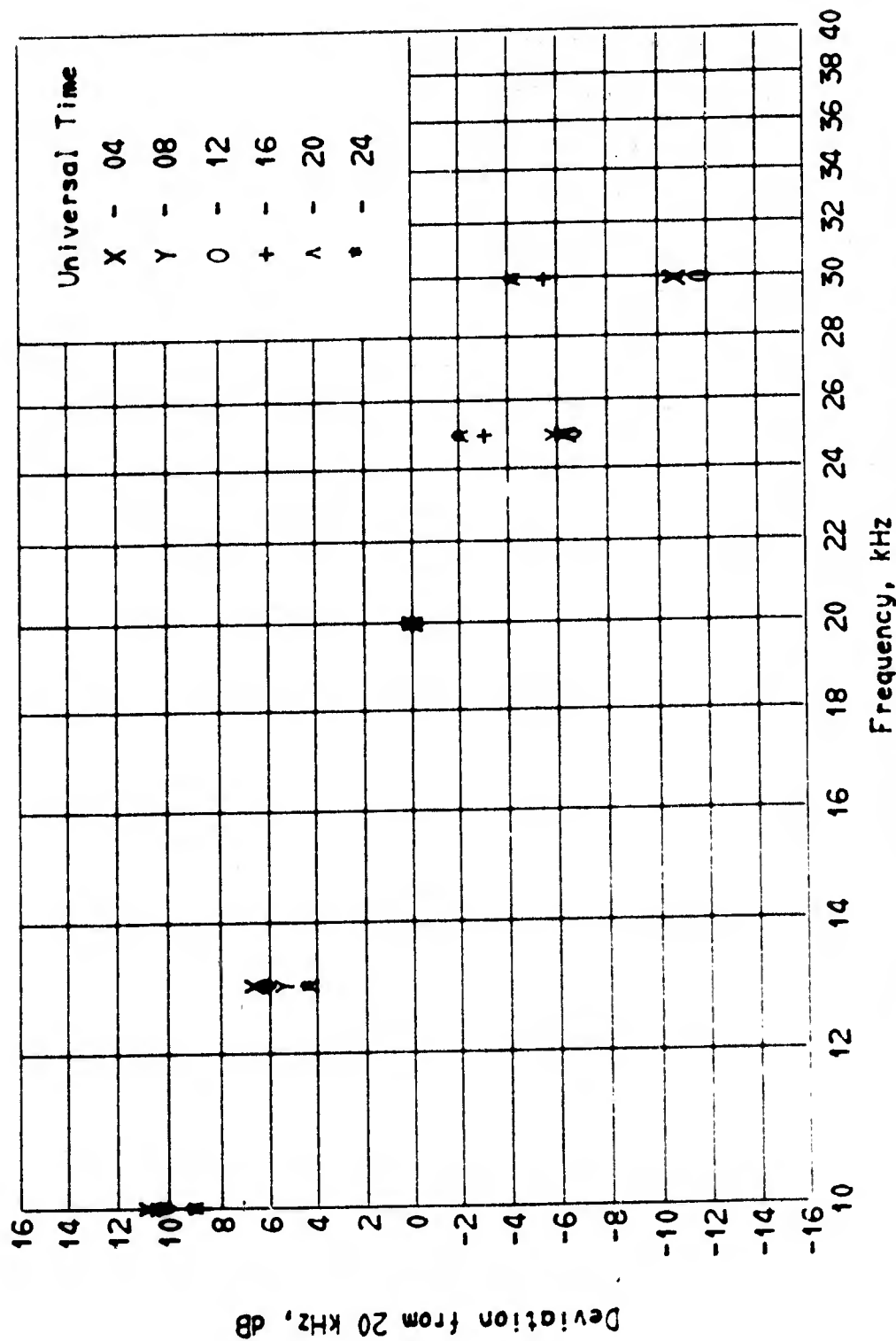


Figure 6-23 Frequency Interpolation of Vertical Electric Field Intensity

We are not aware of measured noise data obtained over a sufficiently long period of time, at a fixed station, for which comparisons could be made to check the accuracy of these frequency interpolation figures. The results seem reasonable, however, when compared with the general trends shown in CCIR report 322 and when compared with short term measurements such as those of Maxwell [1967].

The results for the four seasons for all 34 locations, shown in Figure 6-19, are presented in the VLF atmospheric Noise Manual mentioned previously.

7.0 CALCULATION OF STANDARD DEVIATION

The defining equation for the standard deviation of any collection of observations or values for a variable is

$$\sigma = \left[\frac{1}{n} \sum_{i=1}^n (X_i - \bar{X})^2 \right]^{1/2} \quad (7-1)$$

where

\bar{X} is the mean of the sample,

n is the number of values or observations in the sample,

X_i is one of the values which make up the sample.

Each individual value or observation in this case is the mean value of the vertical electric field intensity of atmospheric noise as measured during a given hour of a given day. The 30 values measured during each day of a month constitute a sample of monthly data. For a normal or log normal distribution the standard deviation corresponds to the difference between the mean and the 16 percent or 84 percent exceedance value. Upper and lower decile values are often used (see CCIR Report 322 and the ESSA Quarterly Noise Reports) instead of standard deviation. This is often done when the sample of data is small or when the data does not fit a normal or log normal distribution. For a given month, the sample of 30 values is too small to obtain an accurate computation of standard deviation. The ESSA Quarterly Noise Reports, which contain the data from their worldwide noise measuring stations, reports upper and lower decile values. CCIR Report 322 also contains estimates of upper and lower decile values instead of standard deviation. It will be noted, however, that the upper and lower decile values within the 10 to 30 kHz frequency range are almost identical.

On the assumption that the distribution of hourly data collected over a period of five to ten years will be log normal, the mean of the upper decile values for all of the ESSA data available at 13 kHz was used to calculate the standard deviation of hourly means according to the equation

$$\sigma_H = 0.78 D_U \quad (7-2)$$

where

D_U is the upper decile value in dB, and

σ_H is standard deviation in dB of hourly values obtained for one month.

In addition to the variation of hourly noise field intensity values from day-to-day there is also a year-to-year variation of the mean of the 30 values collected per month. In CCIR Report 322 this is given as $\sigma_{F_{am}}$ or the standard deviation of values of F_{am} .

Measured values for the standard deviation of monthly means was obtained by computing the standard deviation of the monthly mean field intensities available for approximately ten years of data in the ESSA Quarterly Noise Reports. The total observed or measured standard deviation of atmospheric noise was then designated

$$\sigma_N = \left[\sigma_H^2 + \sigma_M^2 \right]^{1/2} \quad (7-3)$$

where

σ_M is the standard deviation of monthly means.

This was the value we wished to predict.

7.1 Development of the Algorithm

It is interesting to note that the standard deviation of the number of thunderstorm days per month corresponds closely to the standard deviation of monthly means of atmospheric noise. They are quite closely related since the year-to-year variation of atmospheric noise is undoubtedly due to year-to-year variations in the weather. Likewise, the standard deviation of timeblock and daily totals of lightning discharges will be closely related to the day-to-day variation and hourly means of atmospheric noise. The hour-to-hour and day-to-day variation of atmospheric noise will also be related to variations in the propagation parameters. Our model required an algorithm for taking standard deviation of thunderstorm and lightning discharges and computing the standard deviation of atmospheric noise.

Since the power radiated from the equivalent noise transmitters is directly related to the number of lightning discharges, the standard deviation of the number of lightning discharges can be used directly to compute the standard deviation of the power radiated. The use of the standard deviation of thunderstorm days was not so straight forward. After studying the problem extensively it was finally decided that the known relationships between thunderstorms and lightning discharges were not adequate to rigorously compute the statistics of one from the other. In other words, the expression relating thunderstorm days to lightning discharges

$$N_{ld} = 0.06 N_{TD}^{1.5} \quad (7-4)$$

represents an empirical expression valid for data averaged over several years. This is not a rigorous expression by which a day when thunder is heard can be directly related to the number of lightning discharges which would be counted on that day at that location. Lacking such an expression

we then proceeded to establish empirical relationships based upon reasonable assumptions and normal statistical procedures. Fortunately, lightning counter data and thunderstorm day observations obtained during the same period of time were available for two active thunderstorm regions. These are Tororo, Uganda and Singapore, Malaya.

We therefore had the opportunity to check the computation of the standard deviation of lightning discharges based upon thunderstorm day data, with the standard deviation of the lightning counter data itself. As will be shown, a good agreement was obtained.

It had been decided that the computation of the standard deviation of atmospheric noise could best be accomplished by computing the standard deviation of the number of lightning discharges for each 5° by 5° region, from which the standard deviation of the power radiated from that region could be directly computed, on the same basis as mean power radiated. The standard deviation of field intensity due to variability of the propagation medium would be added to the standard deviation of the power

It seems logical that if the mean number of lightning discharges per square kilometer is related to $N_{TD}^{1.5}$, that the standard deviation of the individual observations of the number of thunderstorm days raised to the 1.5 power, could be substituted into equation (7-4) for direct computation of the standard deviation of the number of lightning discharges. This equation is

$$\sigma_{N_{ld_1}} = 0.06 \sigma_{N_{TD}^{1.5}} \quad (7-5)$$

where

$\sigma_{N_{ld_1}}$ is the standard deviation of the number of lightning discharges due to the variation of thunderstorm days.

The climatological data discussed in Section 5.1 was used to compute values for $\sigma_{N_{TD}^{1.5}}$. A scatter plot of these values vs. the number of thunderstorm days per month shown in Figure 7-1. The equation for the line drawn through this data

$$\sigma_{N_{TD}^{1.5}} = 1.65 N_{TD} \quad (7-6)$$

was used in the final algorithm.

The equation for the line on Figure 5-28

$$\sigma_{N_{ld_2}} = 4.7 N_{ld_2}^{0.835} \quad (7-7)$$

which computes the standard deviation of time block and daily lightning counts, is also required for the calculation of standard deviation of noise. Equations (7-5), (7-6), and (7-7) along with the relationships governing the distribution of a sum of identically distributed terms provide the basis for the calculation of the standard deviation of the noise.

Beckman [1968] and others have shown that the distribution of the sum of many independent random variables, each having the same distribution, asymptotically approaches the normal distribution, regardless of the distribution of the individual terms. Furthermore from Burrington and May [1958] we obtain the following expressions. Given that

$$U = C_1 X_1 + C_2 X_2 + \dots + C_m X_m \quad (7-8)$$

where the C's are constants and the X's are arbitrary random variables then let \bar{X}_i and σ_i^2 be the mean and variance, respectively of the

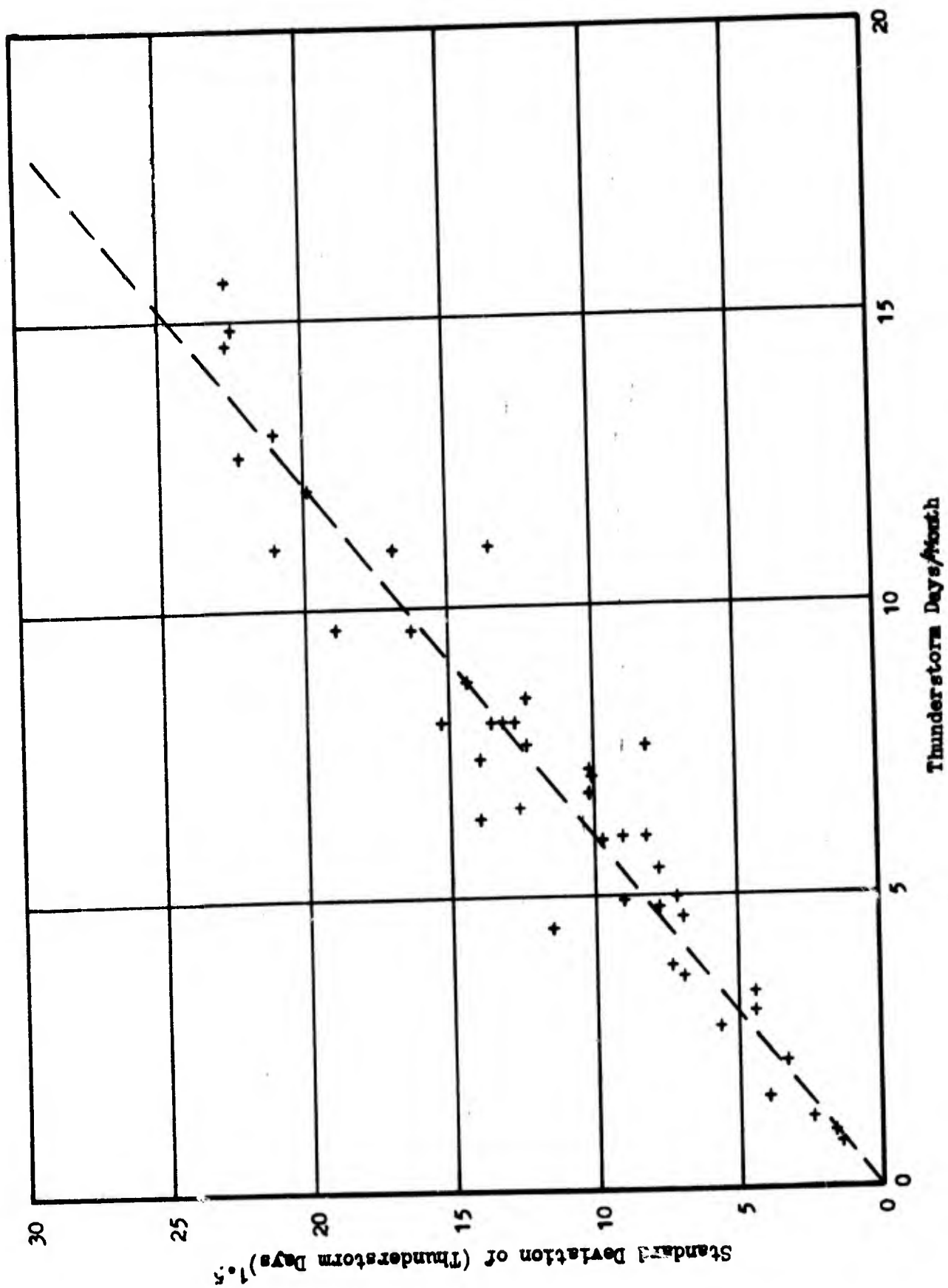


Figure 7-1 Scatter Plot of the Standard Deviation of (Thunderstorm Days)^{1.5} vs Thunderstorm Days.

distribution of the variable X_i .

Therefore,

$$\bar{U} = C_1 \bar{X}_1 + C_2 \bar{X}_2 + \dots + C_m \bar{X}_m \quad (7-9)$$

and variance σ_U^2 of the variable U is

$$\sigma_U^2 = \sum_{i=1}^m C_i^2 \sigma_i^2 + \sum_{\substack{i \neq j \\ i, j=1}}^m C_i C_j \rho_{ij} \sigma_i \sigma_j \quad (7-10)$$

where

ρ_{ij} is the correlation coefficient between the frequency distributions of X_i and X_j .

For the special conditions where constants are all equal to 1 and σ_i equals σ_j , i.e. all σ 's for each set of variables are equal, then

$$\sigma_U^2 = \left[m + (m^2 - m) \rho \right] \sigma_i^2 \quad (7-11)$$

Equation (7-8) can be used to accurately represent the method by which we determine the total number of lightning discharges in a 5° by 5° area. In other words, if the data obtained by each meteorological station or lightning counter location represents a set of variables X_i for a certain area (km^2) then the total number of lightning discharges for a 5° by 5° region may be obtained by summing the results from the number of lightning counters or meteorological observers which would be required to uniformly cover the entire region. Similarly equation (7-11) may be used to compute the standard deviation of the number of lightning discharges for the 5° by 5° region based on the standard deviation of the set of variables from a single

observer or single lightning counter. The specific equations for this application will be developed below.

It has been estimated that a meteorological observer may be expected to hear most thunder within a 10 kilometer radius. The area represented, therefore, by thunderstorm day data from any given station is approximately 300 square kilometers. From equations (7-5) and (7-6) we can now write

$$\sigma_{N_{ld_1}} = 0.06 \left(1.65 N_{TD} \right) 300 \quad (7-12)$$

where

$\sigma_{N_{ld_1}}$ is the standard deviation of the number of lightning discharges per month, for a 300 km² area.

Since this is determined from thunderstorm days per month data, this represents a yearly variation. Substituting this into equation (7-11) we obtain (σ_i (7-11) replaced by (7-2)),

$$\sigma_{N_{ld_1}}^2 = \left[m_1 + (m_1^2 - m_1) \rho_1 \right] \left[30 N_{TD} \right]^2 \quad (7-13)$$

where

$m_1 = \frac{A_{5^\circ}}{300}$, the area of a 5° by 5° region divided by the area covered by a single observer.

ρ , is the average correlation coefficient between thunder storm day samples taken in the 5° by 5° region, and

$\sigma_{N_{ld_1}}$ now represents the standard deviation for a 5° by 5° region.

Near the Equator M_1 is approximately 1000. Since the distribution of thunderstorm days for a single observer was not too far from a normal distribution, it would seem that the distribution for a combination of 1000 sets of data for a 5° by 5° region should be normal. The correlation coefficient, ρ , can be estimated from Figures 5-21, 5-22, and 5-23. Assuming an average separation between observers of 2° the correlation coefficient could be set at any value from 0.4 to 0.6. In the final analysis the best results were obtained with a correlation coefficient of 0.6.

Substituting equation (7-7) for σ_i in (7-11) we obtain

$$\sigma_{N_{ld_2}}^2 = \left[m_2 + (m_2^2 - m_2) \rho_2 \right] \left[4.7 N_{ld}^{0.835} A_2 \right]^2 \quad (7-14)$$

The area covered by the two lightning counters from which data was obtained are 1200 square kilometers and 5000 square kilometers. Using an average value of approximately 3000 square kilometers for A_2 , then M_2 equals approximately 100. Finally then, the total standard deviation of the number of lightning discharges for a 5° by 5° region is equal to

$$\sigma_{N_{ld_T}} = \left[\sigma_{N_{ld_1}}^2 + \sigma_{N_{ld_2}}^2 \right]^{1/2} \quad (7-15)$$

This is based on the assumption that both sets of combined variables can be represented by a normal distribution. This should be a reasonable assumption since we are combining sets of a large number of values in both cases.

The standard deviation of lightning discharges is converted to the standard deviation of power radiated from a 5° by 5° region by the expression

$$\sigma_{P_r} = P_r \left(\frac{\sigma_{N_{ld_T}}}{N_{ld_T}} \right) \quad (7-16)$$

where

N_{ld_T} is the number of lightning discharges from which P_r (power radiated) was computed.

In addition to the standard deviation of power radiated, the standard deviation of atmospheric noise is in part due to variations in propagation conditions and variations in the positions of the actual thunderstorms. From Watt [1967], Figure 7.2.2, we obtain the following approximate expressions for the standard deviation of a coherent signal (carrier),

$$\sigma_{C_D} = 0.6 d^{0.64} \quad (7-17)$$

$$\sigma_{C_N} = 1.8 d^{0.25} \quad (7-18)$$

where

d is the distance between the receiver,

σ_{C_D} is the standard deviation of the carrier during daytime conditions, and

σ_{C_N} is the standard deviation of the carrier under nighttime conditions.

The initial tests using these equations yielded values too large for the standard deviation of noise fields. Considering the spatial distribution of the actual sources of noise, i. e. individual thunderstorms, it would be expected that propagation changes have a lesser effect on the

standard deviation of noise than on the standard deviation of a signal from a single transmitter. For the final computations therefore the following expressions were used

$$\sigma_{C_D} = 0.45 d^{0.4} \quad (7-19)$$

$$\sigma_{C_N} = 0.9 d^{0.25} \quad (7-20)$$

The variation of noise field intensities due to the change in position of thunderstorms from hour-to-hour and day-to-day is approximated by the expression

$$\sigma_{P_{rd}} = \frac{P_r}{d/10^6} + 0.26 P_r \quad (7-21)$$

where we are expressing the standard deviation of distance in terms of the effective change in the radiated power due to the change in distance (d is given in meters). The first part of this expression accounts for the approximate $\frac{1}{d}$ variation of field intensity. The second part of the expression accounts for the attenuation of energy due to losses in the ionosphere and the imperfectly conducting earth, on the assumption that the average attenuation rate is 1 dB per megameter and the standard deviation of distance is 1 megameter. We did not have any data relative to the standard deviation of distance from thunderstorms. The only justification for equation (7-21), therefore, is that it improved the agreement between predicted and measured standard deviations of noise for those receiver locations close to thunderstorm centers.

Nevertheless, it was noted that computed standard deviations for those locations near very active thunderstorm regions were always too low. The probable reason for this lies in the fact that the movement of cold fronts, major cyclonic weather circulations, and high and low pressure regions generally affect the weather fairly uniformly over a region of several hundred to several thousand square kilometers. For a location where most of the noise power is received from one active thunderstorm region, the high correlation of the thunderstorm activity over that region would tend to have a pronounced effect on the standard deviation of the noise levels. A location distantly removed from all thunderstorm centers, however, would not experience this effect. Since the minor transmitters are used only when a receiver location is quite close to a region of high thunderstorm activity, increasing the standard deviation of the minor transmitters by a factor of 2, provided a simple and effective method to provide for regional correlation.

Initial tests also revealed that some of the ESSA receiver locations, during certain seasons, had measured extremely high values of standard deviation. Examination of the measured data revealed that these extremely high values of standard deviation were caused for the most part by year-to-year variations in the noise levels. Several climatological books and papers were studied in an effort to determine if this high variability were real, or if it might have been caused by errors in the measured data at specific locations. No specific reference to an abnormally high variability of thunderstorms was found. It was noted, however, that without exception, these areas of abnormally high standard deviation were near regions of converging warm and cold ocean currents and/or converging wind currents; see Rumney [1968], his figures 4.2, 4.3, and 6.11. Abnormally high thunderstorm activity, compared to surrounding regions of similar climate, was also found to exist at these locations. To provide for these regions of convergence, the standard deviation for minor and major transmitters were multiplied by a

variance modifier, V_m . The variance modifier values assigned to each major transmitter location are shown on Figures (7-2) through (7-5).

It was further noted that the calculated standard deviations for Enkoping, Sweden during the months of June, July, and August were abnormally high. From Finch, et al [1957] it was noted that unusually stable weather conditions exist over most of Europe and Northern Asia, during this season. This is due to the weather being dominated by winds from the North Atlantic, which are relatively cold and dry. The thunderstorms for this region would therefore be generated primarily by convection and orographic processes. The conditions for these generation processes are relatively consistent compared to the conditions for the generation of frontal storms. Most other regions have some frontal activity and/or rapidly changing weather conditions leading to alternately favorable and unfavorable conditions for the occurrence of thunderstorms. To account for this condition a variance modifier of 0.5 was assigned to Europe and Northern Asia as shown on Figure 7-4. It is probable that a similar condition exists for Western United States and Central Canada for this season and a modifier of 0.5 was assigned.

For these reasons the standard deviation of power for the minor transmitters are modified according to equation

$$\sigma_{P_{rm}} = 2 \sigma_{P_r} V_m \quad (7-22)$$

and the standard deviation of power for the major transmitters are modified according to equation

$$\sigma_{P_{rm}} = \sigma_{P_r} V_m \quad (7-23)$$

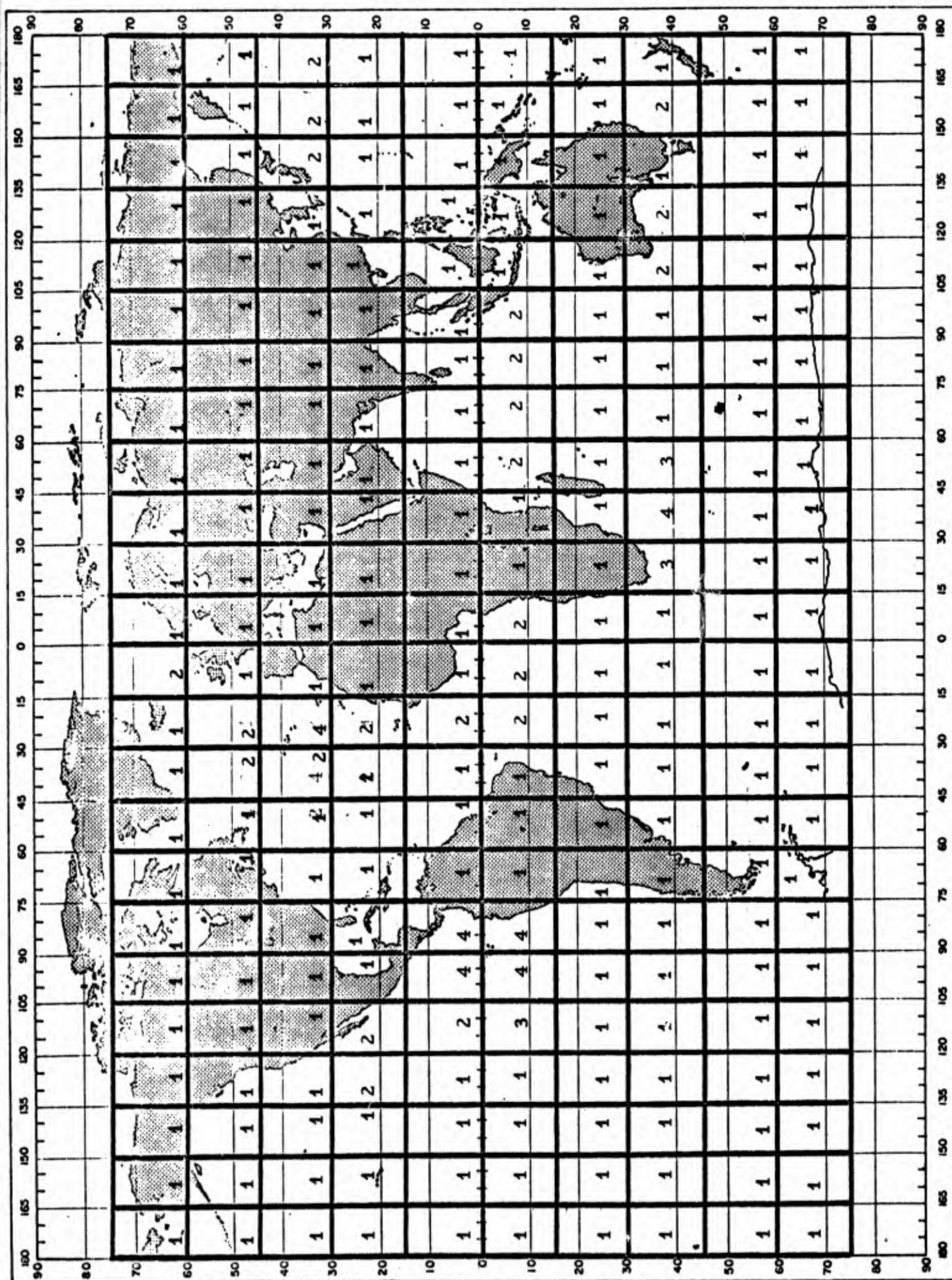


Figure 7-2 VARIANCE MODIFIER MAP Dec-Jan-Feb

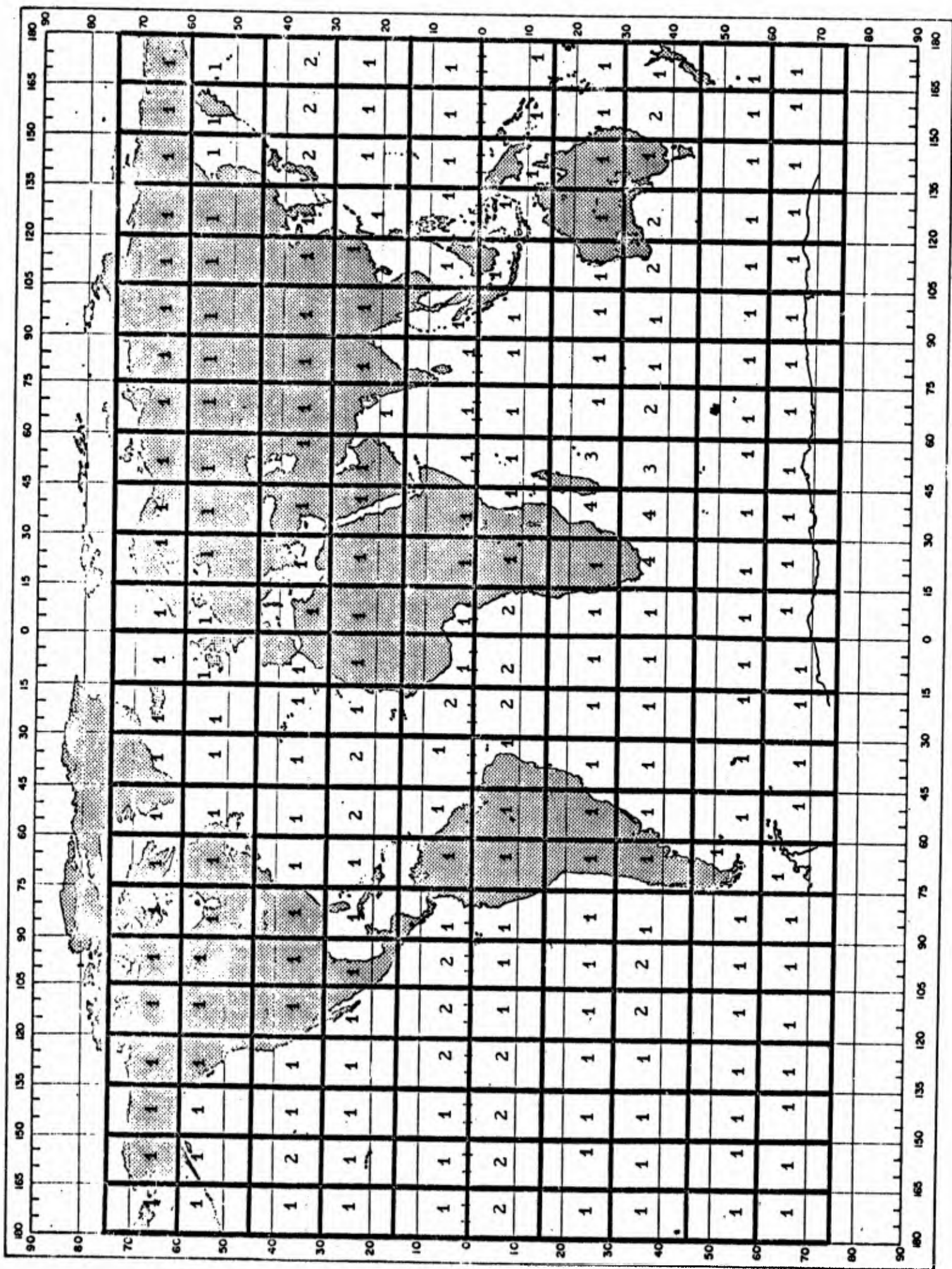
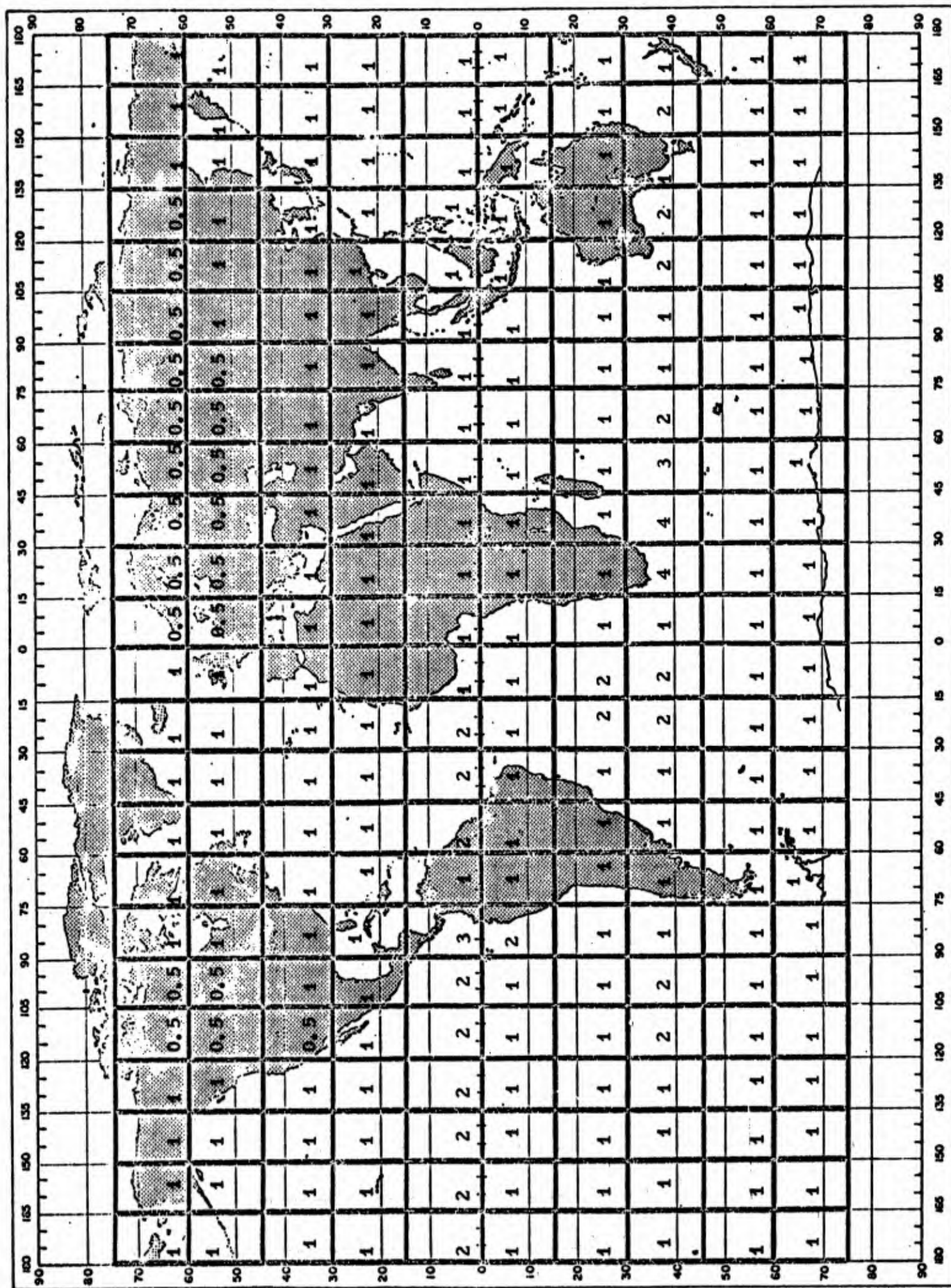


Figure 7-3 VARIANCE MODIFIER MAP

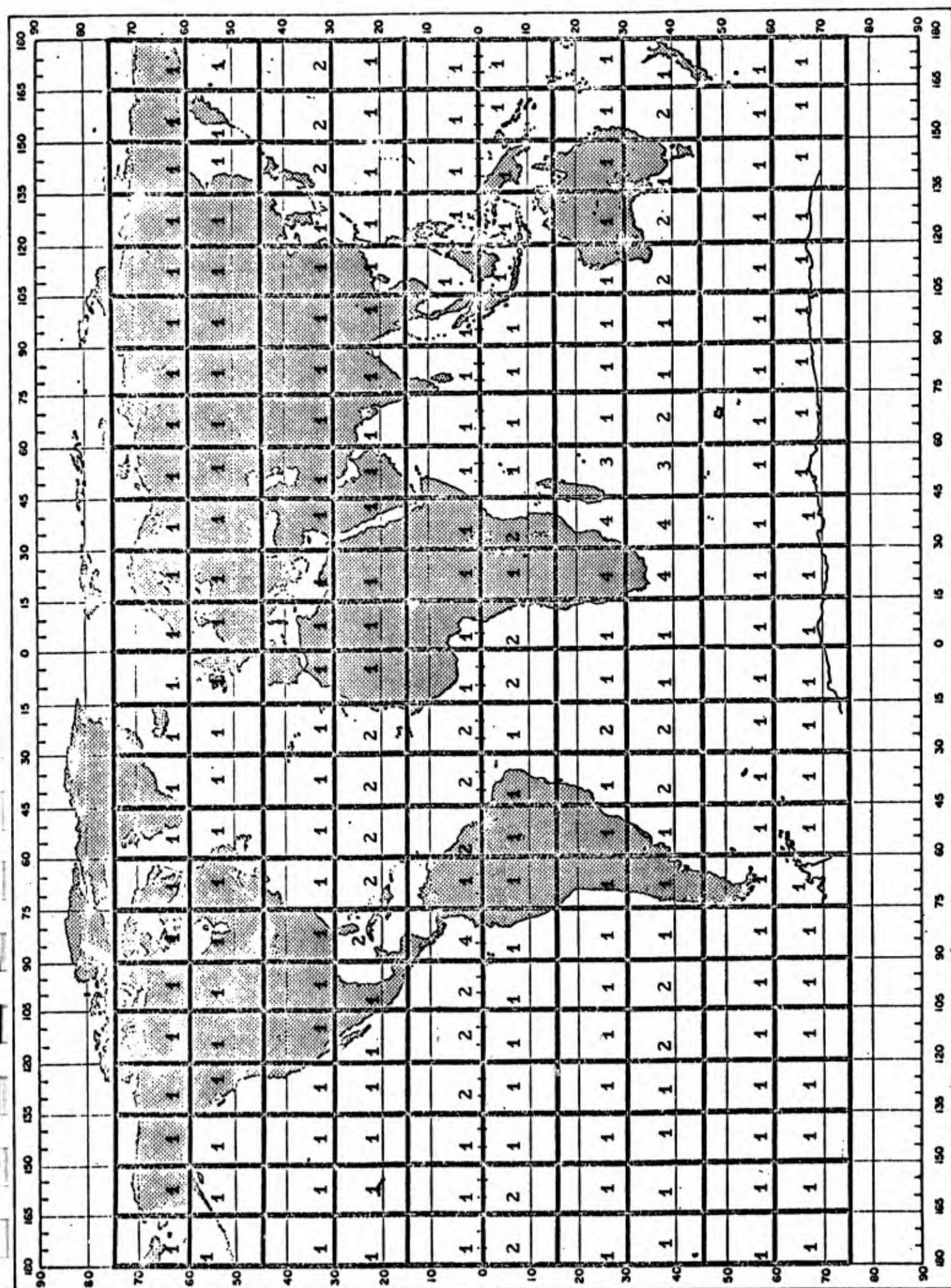
Mar. - Apr. - May



June-July-Aug

VARIANCE MODIFIER MAP

Figure 7-4



where

σ_{P_r} is computed from equation (7-16), and V_m is the variance modifier.

This completed the development of an algorithm for computing the standard deviation of noise.

7.2 Description of the Algorithm

This subsection will describe the step-by-step procedures used to calculate the standard deviation of atmospheric noise.

STEP I

The standard deviation of the number of lightning discharges occurring within each 5° by 5° region of the earth's surface is computed with equations (7-13) and (7-14). The number of thunderstorm days and the number of lightning discharges, input data required for equations (7-13) and (7-14), are those values determined for each minor transmitter by STEP I of the algorithm for the calculation of field intensities.

This step is accomplished in subroutine STDCOM Stone [1970].

STEP II

The standard deviation of power radiated for each minor and major noise transmitter is calculated using equations (7-15) and (7-16).

This step is accomplished in subroutine COMPWR Stone [1970].

STEP III

The proper variance modifier for each minor and major transmitter is identified for the month for which computations are being made (see Figure 7-2 through 7-5). Equations (7-22) and (7-23) are used to modify the

standard deviation of radiated power according to the variance modifier assigned.

This step is accomplished in programs COMPWR and NOISLAN.

STEP IV

The standard deviation of power for both minor and major transmitters at sea locations is reduced by 4 dB. The standard deviation of part land part sea transmitters are lowered by 2 dB. This is equivalent to STEP VI in the Field Intensity Algorithm and is done for the same reasons given there.

This step is part of the computer program NOISLAN.

STEP V

The effect of propagation variations and the change in position of thunderstorms are computed according to equations (7-19) through (7-21). These values become, in effect, an additional standard deviation of power radiated and are added to the actual standard deviation of power radiated to obtain the effective standard deviation of radiated power,

$$\sigma_{P_{\text{reff}}} = \left[\sigma_{P_{\text{rm}}}^2 + \sigma_{P_{\text{rd}}}^2 + \sigma_{P_{\text{ra}}}^2 \right]^{1/2} \quad (7-26)$$

where

$\sigma_{P_{\text{ra}}}$ is the effective standard deviation of power due to propagation variations.

STEP VI

The square of the standard deviation of field intensity, i. e. the variance of field intensity, is computed using the square of equation (4-2). The same procedures are used in computing the square of the standard deviation of field intensity as are used in computing the square of field intensity. STEPS VII through X of the Field Intensity Algorithm also apply to the computation of standard deviation.

The final value for the variance of the vertical field intensity for a given receiver is computed from the equation

$$\sigma_{E_v}^2 = \sum_{i=1}^n \sigma_{E_{v_i}}^2 \quad (7-24)$$

where

$\sigma_{E_{v_i}}$ is the standard deviation of field intensity for the i^{th} transmitter.

This value is converted to decibels by the equation

$$\sigma_{E_v} \text{ (dB)} = 10 \log_{10} \frac{\sigma_{E_v}^2 + E_v^2}{E_v^2} \quad (7-25)$$

This step is part of the main computer program NOISLAN.

STEP VII

Season-time block values are computed by averaging the appropriate 12 monthly hourly values to compute each seasonal-time block value in the same manner as was used in STEP XII for the Field Intensity Algorithm.

THIS COMPLETES THIS ALGORITHM

The execution of this algorithm produced 288 month-hour and 24 season-time block sets of contours.

7.3 Comparison of Calculated and Measured Values

The ESSA measurements of total standard deviation as defined by equation (7-3) were compared with the values calculated with the algorithm above. Our goal had been to obtain calculations accurate within plus or minus 1 dB of measured values. For the most part we met that goal, although differences as large as 2 or 3 dB exist for specific hours. As with field intensities, the comparisons were made for three month averages of predicted and measured values. Since no more than ten years of data was available for any one station, the sample for the computation of the standard deviation of monthly values is quite small. Thus, the measured values exhibit seemingly random variations of 1 to 3 dB from month-to-month, for specific hours. This is also apparent from Figures 7-6 through 7-9, where it will be noted that the computed values of standard deviation change very little from hour-to-hour, whereas the comparisons between predicted and measured values are quite erratic.

These comparisons for Balboa and Enkoping represent the extremes of highly variable and stable conditions. The computed values of standard deviation from location to location and month to month are quite similar so additional comparisons will not be shown here. More complete tables of comparisons are given in Appendix A.

Although the nature of the measured data makes a judgment rather uncertain, it would appear that the algorithm for predicting standard deviation of atmospheric noise is working quite well, even for those locations having anomalously high or low standard deviations.

BALBOA, CANAL ZONE (SEPT., OCT., NOV.) FINAL

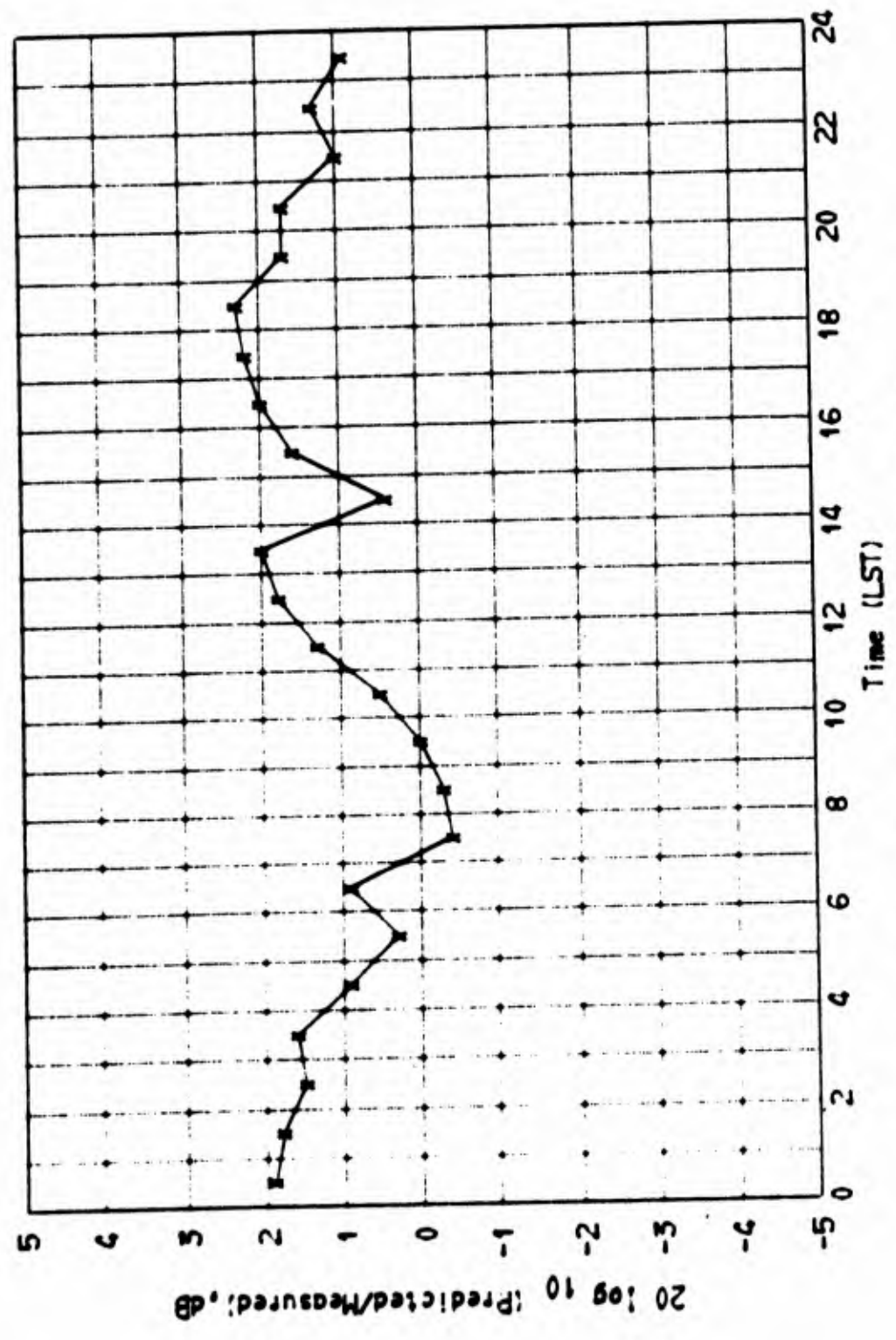


Figure 7-6 Final Comparison of Predicted and Measured Standard Deviation

BALBOA, CANAL ZONE (SEPT., OCT., NOV.) FINAL

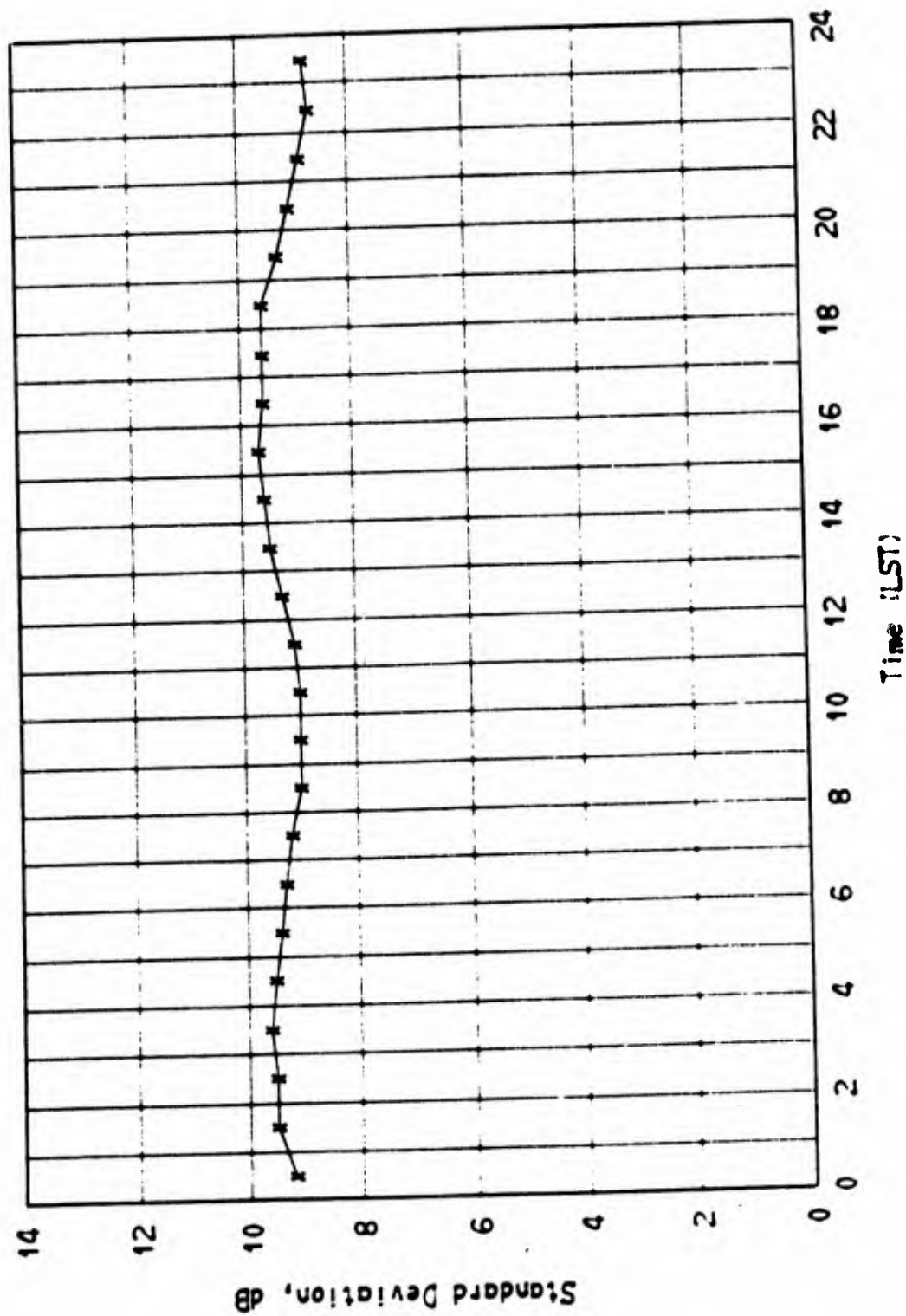


Figure 7-7 Estimated Standard Deviation of Atmospheric Noise at 13 kHz.

ENKOPING, SWEDEN

(JUNE, JULY, AUG.)

FINAL

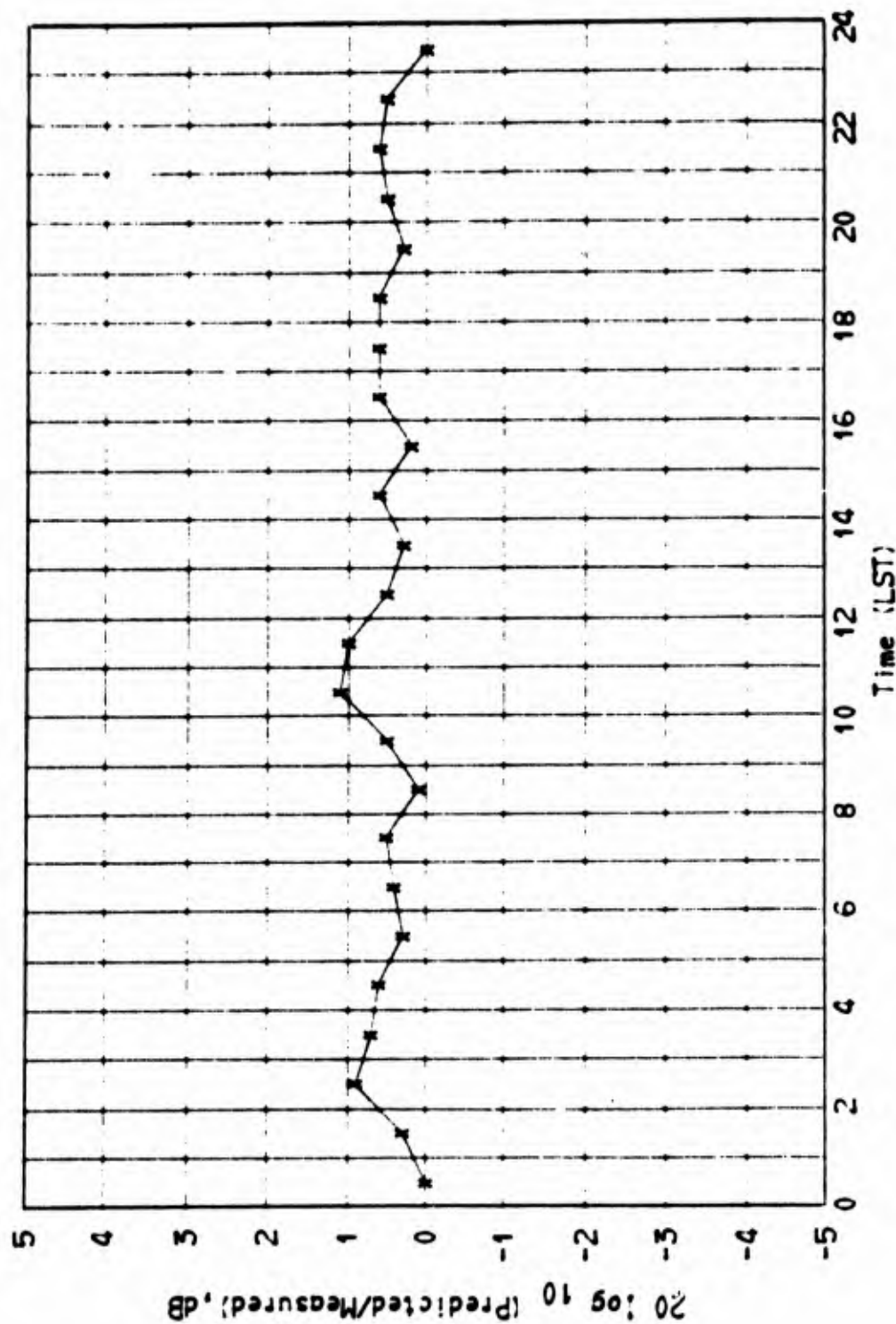


Figure 7-8 Final Comparison of Predicted and Measured Standard Deviation

FINAL

(JUNE, JULY, AUG.)

ENKOPING, SWEDEN

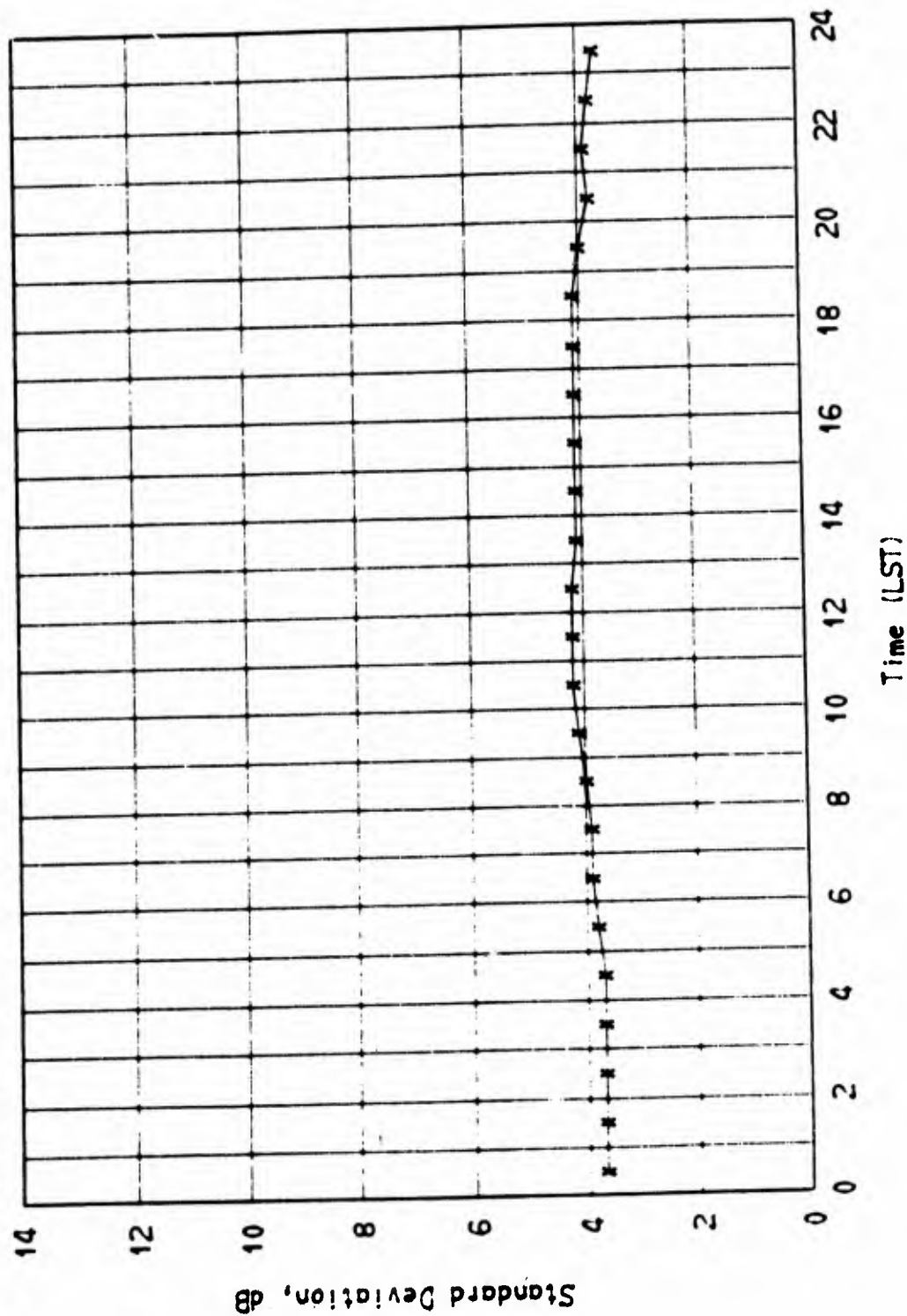


Figure 7-9 Estimated Standard Deviation of Atmospheric Noise at 13 kHz.

7.4 Variation With Frequency

The only significant variation in standard deviation with frequency should be due to variations in the propagation parameters. Almost no data is available on the variation of propagation parameters as a function of frequency. It was decided that an attempt to modify the expressions for standard deviation of a coherent signal (equations (7-17) and (7-18)) could not be justified. To do so would tend to indicate the availability of better data than actually exists.

Therefore, based in part upon the estimates given in CCIR report 322 and in part on results from Linfield [1965], we developed an empirical expression to estimate the variation of standard deviation with frequency. CCIR report 322 shows a positive correlation between the variation of field intensity with frequency and the variation of standard deviation with frequency. This correlation and data from Linfield were used to empirically establish equations (7-27) through (7-30)

$$\Delta \sigma_{10} = \Delta \sigma'_{10} - \left[\left(\Delta E_{v_{10}} - 6 \right) / 4 \right] \quad (7-27)$$

$$\Delta \sigma_{13} = \Delta \sigma'_{13} - \left[\left(\Delta E_{v_{13}} - 3.5 \right) / 4 \right] \quad (7-28)$$

$$\Delta \sigma_{25} = \Delta \sigma'_{25} - \left[\left(\Delta E_{v_{25}} + 2 \right) / 3 \right] \quad (7-29)$$

$$\Delta \sigma_{30} = \Delta \sigma'_{30} - \left[\left(\Delta E_{v_{30}} + 3.5 \right) / 3 \right] \quad (7-30)$$

where

$\Delta \sigma'_{(f)}$ is the difference between computed values at 20 kHz and the other frequencies ($f = 10, 13, 25$ and 30 kHz) using the algorithm described in Section 7.2, and

$\Delta E_{v(f)}$ is the difference between E_v values for 20 kHz and the other frequencies as computed for field intensity interpolations.

The term in brackets empirically provides for variations in the propagation parameters. All values are expressed in dB.

The locations for these frequency interpolation computations are the same as those shown on Figure 6-19. The presentation is also the same as that used for field intensities. No examples are shown here but all of the results are, of course, part of the VLF Noise Prediction Manual prepared under this contract for publication by the U. S. Government.

8.0 CALCULATION OF VOLTAGE DEVIATION (V_d)

The voltage deviation, or form factor of atmospheric noise or any noise, is defined by the expression

$$V_d = \frac{E_{rms}}{E_{avg}} \quad (8-1)$$

This ratio is directly related to the impulsiveness of the noise. The impulsiveness of the noise is, of course, related to the number of impulses which make up the total noise energy received and the range of amplitudes of the impulses. The impulsiveness of the noise is also a function of the bandwidth of the receiver or amplifier being used. Narrow bandwidths tend to spread out the energy in time, thereby increasing the overlap of energy from one pulse to the next and reducing the effective dynamic range.

The voltage deviation of atmospheric noise is therefore, directly related to number, amplitude, and distance of all the lightning discharges occurring around the world at any given time. The algorithm developed under this project to compute noise power radiated determines, as an intermediate step, the number of lightning discharges per square kilometer over the entire surface of the earth. It was apparent from the start of the program that this data might be used to directly compute V_d . This was tried by computing the distribution of the number of lightning discharges whose peak amplitudes fell within successive 3 dB intervals, or steps in field intensity. These results were quite promising but failed to show the diurnal variations of measured values for V_d . It became apparent that the successful use of the lightning discharge data would require a very extensive program, involving the individual impulses within each lightning discharge, and proper accounting for equipment bandwidth effects. This was clearly beyond the scope of this contract and this approach was put aside. It is hoped that it can be taken up again at a later date, since it offers the

opportunity for direct computation of short-term statistics of atmospheric noise.

8.1 The Algorithm for Estimating V_d

The calculation of V_d is accomplished in a computer subroutine separate from the main prediction program. During the computation of field intensity and standard deviation values, data for the ten most significant transmitters for each receiver location is printed out. This data includes the transmitter locations, their distance from the receiver, the P_{RAT} ratio defined by Equation (6-1) and the diurnal modifier index. This data, relative to the ten most significant transmitters for each receiver location, provides an indirect indication of the characteristics of the atmospheric noise. This can be best explained by a discussion of the single equation which forms the entire algorithm for computation of V_d .

The equation for the calculation of V_d is

$$V_d = 10 \left[\left(\frac{1/D_{\text{m avg}}}{2} \right)^{0.2} \right]^{(P_{\text{RAT}})^{0.25}} + \left[\left(\frac{1/D_{\text{m avg}}}{2} \right)^{0.25} \right]^{10 \frac{d_{\text{max}}}{d_{\text{min}}}}$$

(8-2)

where

$D_{\text{m avg}}$ is the average of the diurnal modifier values for the five most significant transmitters which are less than 10 megameters from the receiver,

P_{RAT} is defined by Equation (6-1),

d_{\max} and d_{\min}

are the maximum and minimum distances between the receiver and the five most significant transmitters, i. e., the five transmitters with the largest P_{RAT} for this receiver location.

V_d

is voltage deviation in a 200 Hz bandwidth. For a 1000 Hz bandwidth 7 dB is added (see CCIR report 322).

The diurnal variation of these measured V_d values is for most locations the exact inverse of the diurnal distribution of thunderstorm days. This is the basis, of course, for using the inverse of an average of diurnal modifier. It was apparent that neither the largest nor the closest transmitters controlled the diurnal variation of V_d . The best results were obtained by using the five most significant transmitters (based on P_{RAT}) which were not more than 10 megameters from the receiver. The different local time at the transmitters was considered when calculating average diurnal modifier values.

A large P_{RAT} ratio indicates a large noise transmitter close to the receiver location. Since this offers the opportunity for very near lightning discharges and the resultant increase in the impulsiveness of the noise, it would be expected that V_d would be larger for locations close to active thunderstorm centers. The use of P_{RAT} in Equation (8-2) will provide this effect.

Justification for using the ratio of the maximum and minimum distances between the first 5 transmitters and the receiver is more obscure. If this ratio is high, it is indicative that one or more relatively small noise transmitters are so close to the receiver location that they are equal in significance to a very powerful distant noise transmitter. Under these conditions, there is likely to be a few large noise impulses from

infrequent local thunderstorm activity, superimposed upon a nearly Gaussian noise background from many distant thunderstorms. This will result in very high maximum V_d values, without having much effect upon the lower or average V_d values. This was in agreement with measured data.

THIS IS THE ALGORITHM FOR COMPUTING V_d . It is accomplished with the computer program VSUBD as described by Stone [1970].

8.2 Comparison of Calculated and Measured Values

The comparisons were much better than might have been expected considering the nature of the algorithm. Differences between the diurnal variation of predicted and measured values seem to be the primary difficulty as evidenced by the comparisons and estimated V_d values shown in Figures 8-1 through 8-4. This problem undoubtedly relates to factors, other than the diurnal variation of thunderstorm occurrence, which are not provided for in this simple model. The ability to estimate geographical variations for these values is a significant advantage, even though the estimates may be appreciably in error during certain hours of the day. Be reminded that all comparisons in this report are with ESSA measured values at 13 kHz. Some tabulated comparisons are given in Appendix A. The comparisons for Boulder and Enkoping represent the worst and best of the results.

8.3 Variation of V_d with Frequency

CCIR Report 322 shows very little variation of V_d values with frequency from 10 to 30 kHz. This is in complete agreement with our knowledge of the lightning events which are significant to the generation of energy over this frequency range. No attempt was made, therefore, to estimate variations in V_d with frequency.

8.4 The Output

Because of the lesser significance of these estimates of V_d compared to the estimates of field intensity and standard deviation, it was mutually agreed between Westinghouse and the Navy that V_d contour plots would be prepared on a seasonal hourly basis. This resulted in 96 contour maps to be presented in the VLF Atmospheric Noise Manual.

BOULDER, COLORADO

(DEC., JAN., FEB.)

FINAL

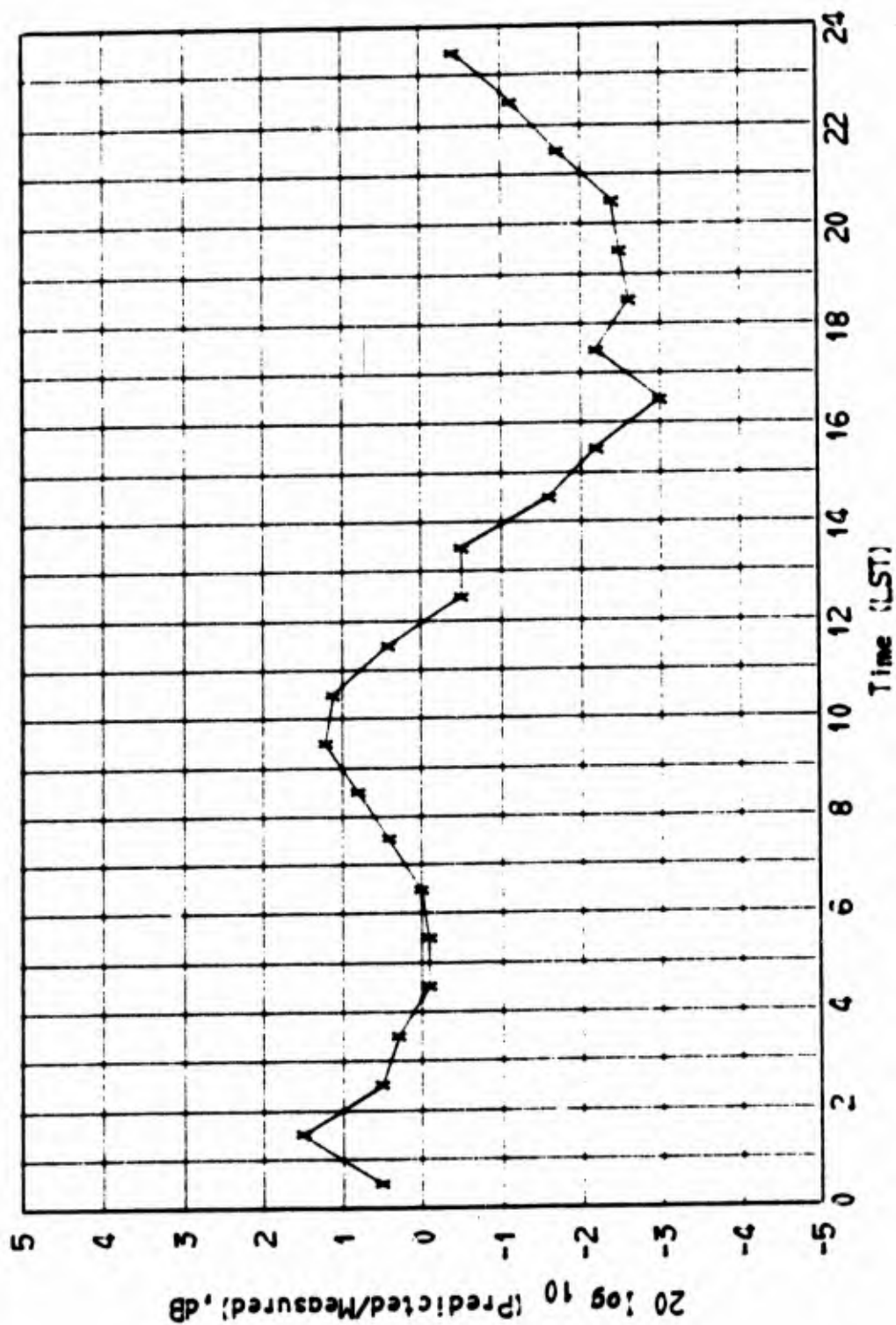


Figure 8-1 Final Comparison of Predicted and Measured Voltage Deviation

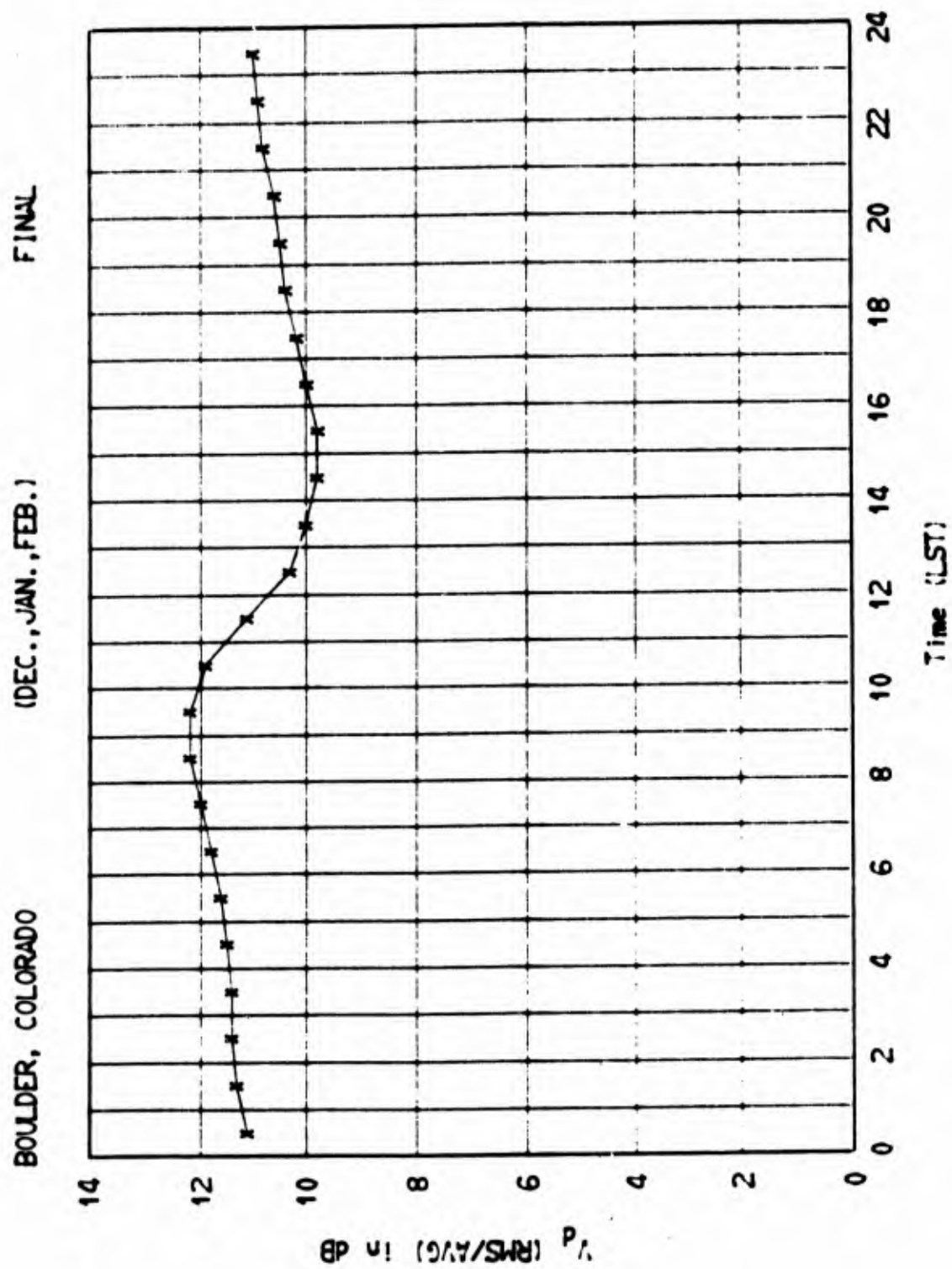


Figure 8-2 Estimated Values of Voltage Deviation for VLF
Atmospheric Noise - Bandwidth is 1 kHz.

FINAL

(DEC., JAN., FEB.)

ENKOPING, SWEDEN

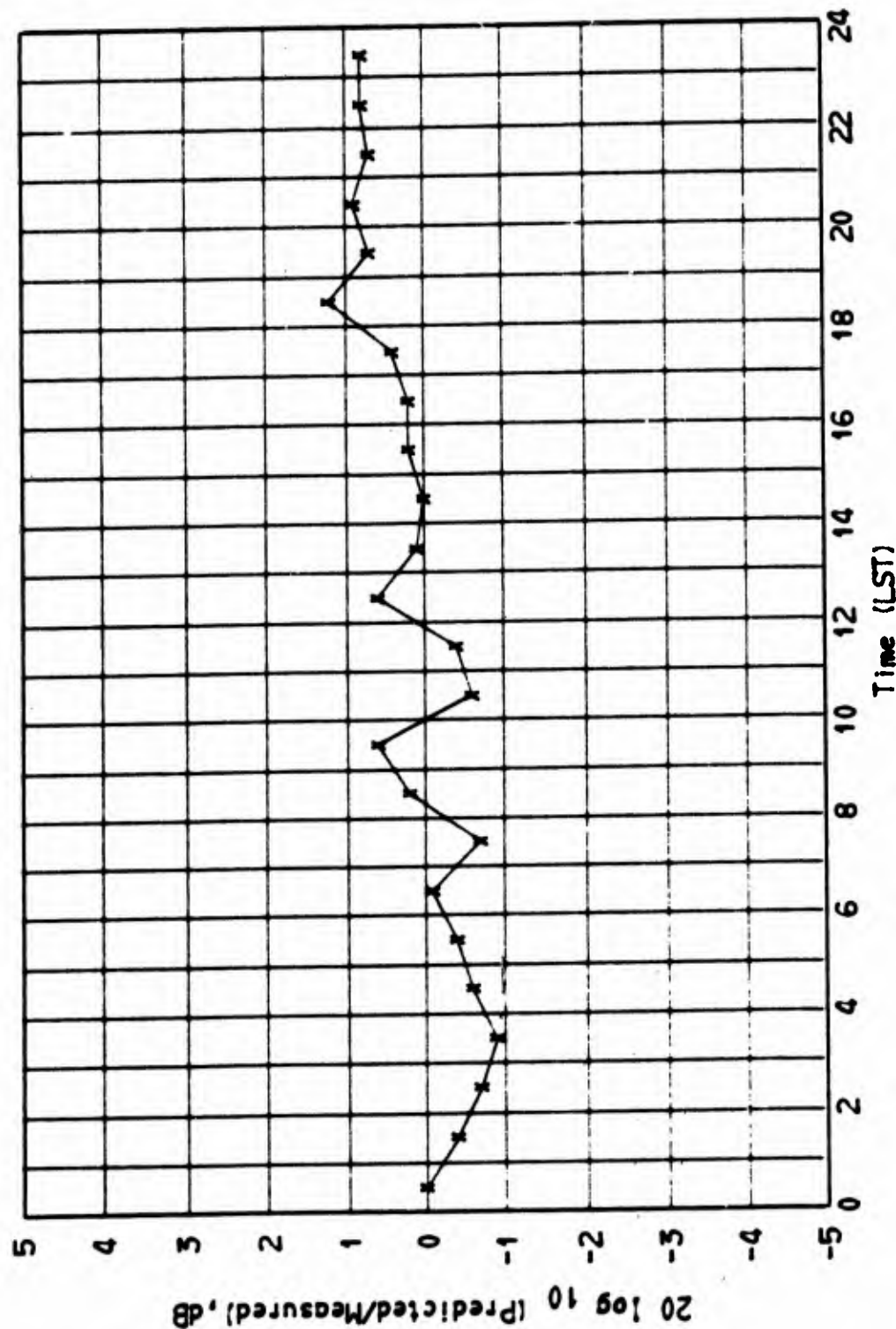


Figure 8-3 Final Comparison of Predicted and Measured Voltage Deviation

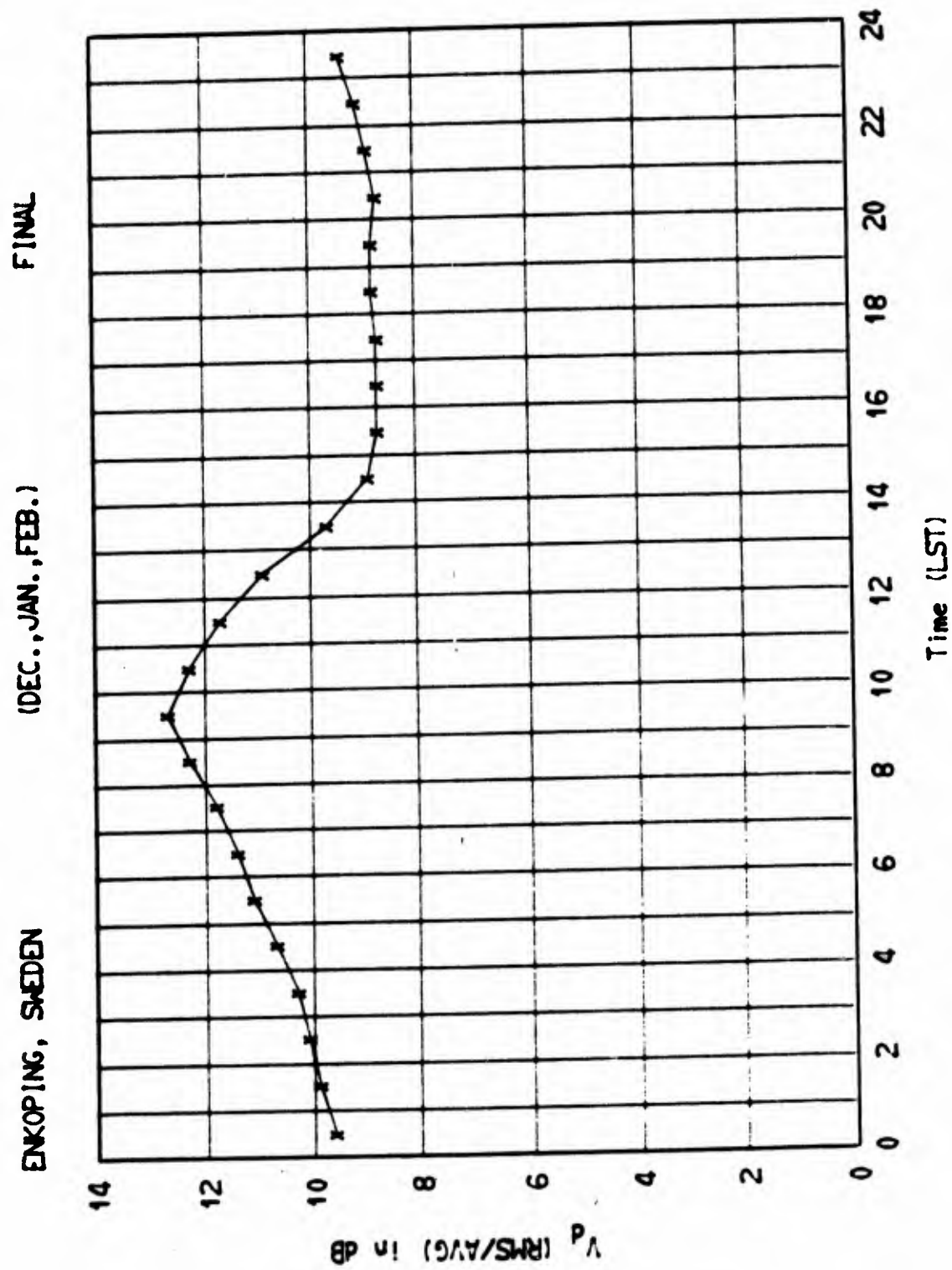


Figure 8-4 Estimated Values of Voltage Deviation for VLF Atmospheric Noise - Bandwidth is 1 kHz.

9.0 CALCULATION OF THE DIRECTION OF ARRIVAL OF ATMOSPHERIC NOISE

It is desirable to know the direction from which the atmospheric noise arrives at the receiving location so that directional antennas may be used to reduce the effective noise energy. Since the bearing from the receiver to the noise transmitter is computed in STEP X of the Field Intensity Algorithm, it was a relatively easy task to develop a computer program to establish the direction of arrival of the noise energy.

To accomplish this, the energy arriving in each 10° azimuthal sector was determined by summing the values for each individual noise transmitter whose bearing from the receiver lies within the sector. In effect, equation (6-4) was used to compute the effective field intensity for each 10° sector. The units for the field intensity in each sector are dB relative to 1 micro-volt per meter in a 1 kHz bandwidth. In other words, if a receiving antenna has unity gain over the 10° sector and 0 gain in all other directions, the field intensity computed for that sector would be observed.

A computer program was written to make a polar plot of the field intensities for each 10° sector. Figures 9-1 through 9-6 show the results of these plots at Point Barrow, Alaska for the month of October and the local time as indicated on each figure. This location was chosen because measured values were available for comparison at that location.

The measured rates of occurrence of atmospherics, plotted relative to their direction of arrival, for Point Barrow are shown in Figure 9-7 from Watt [1967]. This data was obtained during a four-day period in October, 1954. As such it represents a very small sample of data which would not be expected to correspond exactly with our computed direction of arrival (DOA) noise fields. During any four-day period some storm

centers will be quiet, others abnormally active. Also, a plot of the number of atmospherics exceeding background noise level cannot be closely related to atmospheric noise field intensity expressed in decibels. Considering these two problems, the general agreement between Figures 9-1 through 9-6 and Figure 9-6 is very reasonable.

Similar comparisons were made with the measurements reported by Martin and Hildebrand [1965]. The comparison with their measurements for the Southern California location were of the same general quality as these shown for Point Barrow.

The following criteria are used in determining the minor transmitters which should be used for the DOA computations. Any major transmitter within 3 megameters of the receiver location is broken up into its equivalent 9 minor transmitters if its power is greater than 200 milliwatts. In other words the ratio expressed by equation (6-2) is not used for the DOA calculations. This resulted in the use of more minor transmitters for greater DOA accuracy.

It should be noted that the computer plot program draws a line to the center of each 10° sector to represent the field intensity in that sector. If the fields in adjacent sectors are less than 0 dB relative to a microvolt per meter, the line starts from and returns to the center of the plot, thereby producing a single line or spike. This actually represents the energy in a sector plus or minus 5° from the position of the spike. This method of plotting also results in each of the lobes being 10° narrower than they should be, i.e. 5° should be added on each side of each lobe.

Over 100 DOA plots were produced for the Navy on this program and were supplied to them as a supplemental output.

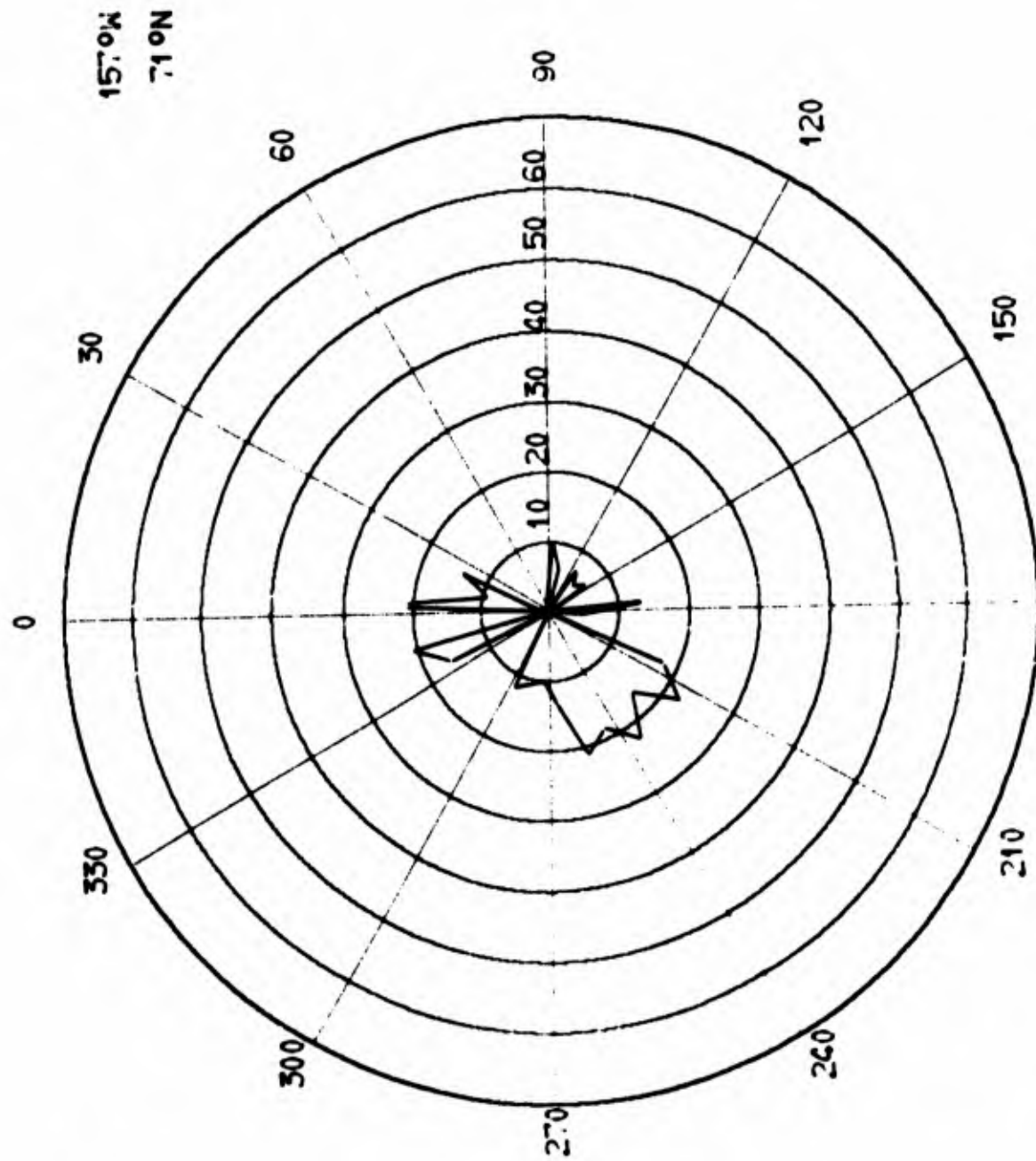
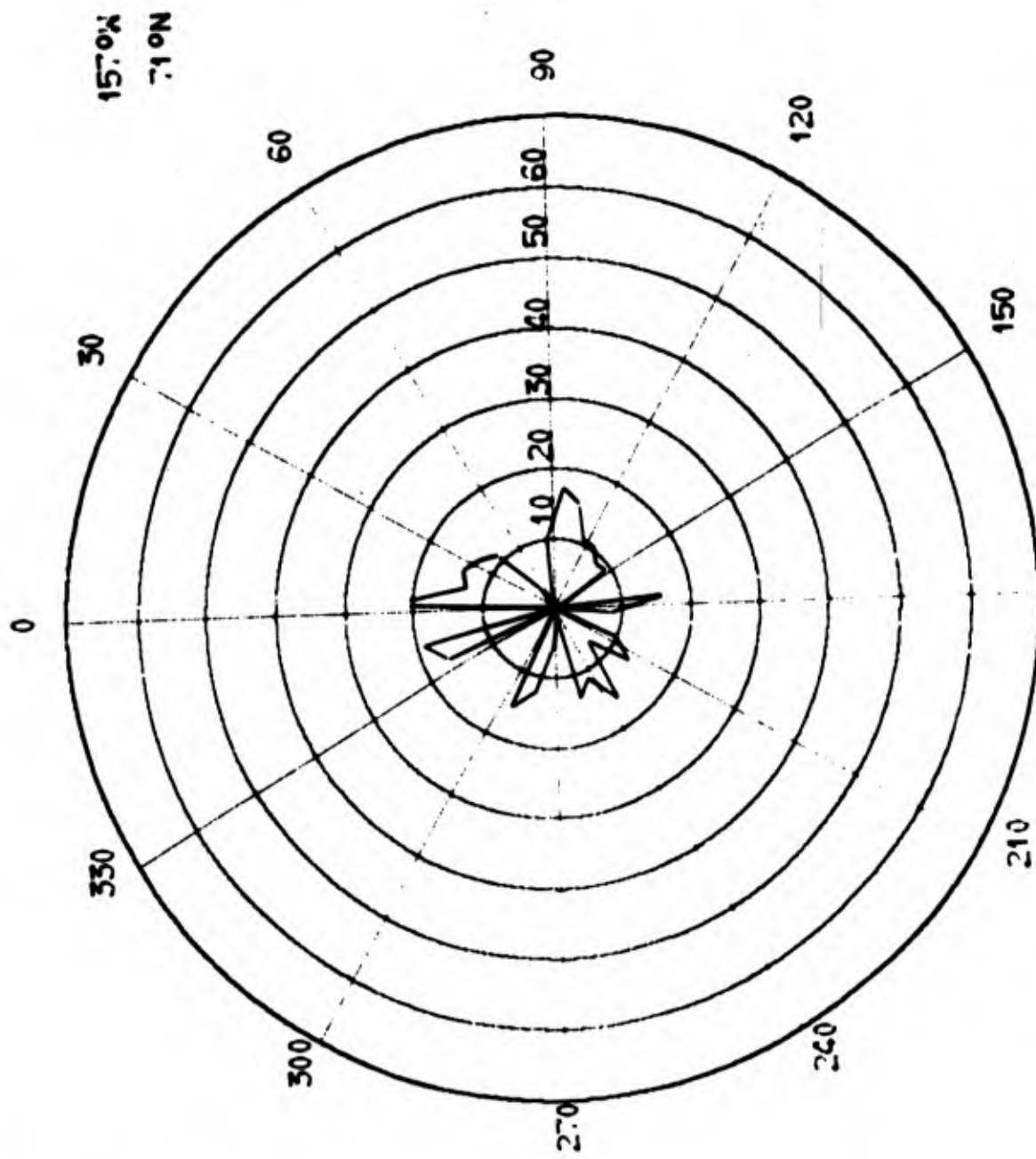


Figure 9-1 Expected Directional Variation of Atmospheric Noise- Effective Field intensity for 10° Sectors in dB re: 1 μ V/m in a 1 kHz bw



October
1200

Figure 9-2 Expected Directional Variation of Atmospheric Noise- Effective Field Intensity for 10° Sectors in dB re: 1 μ V/m in a 1 kHz bw

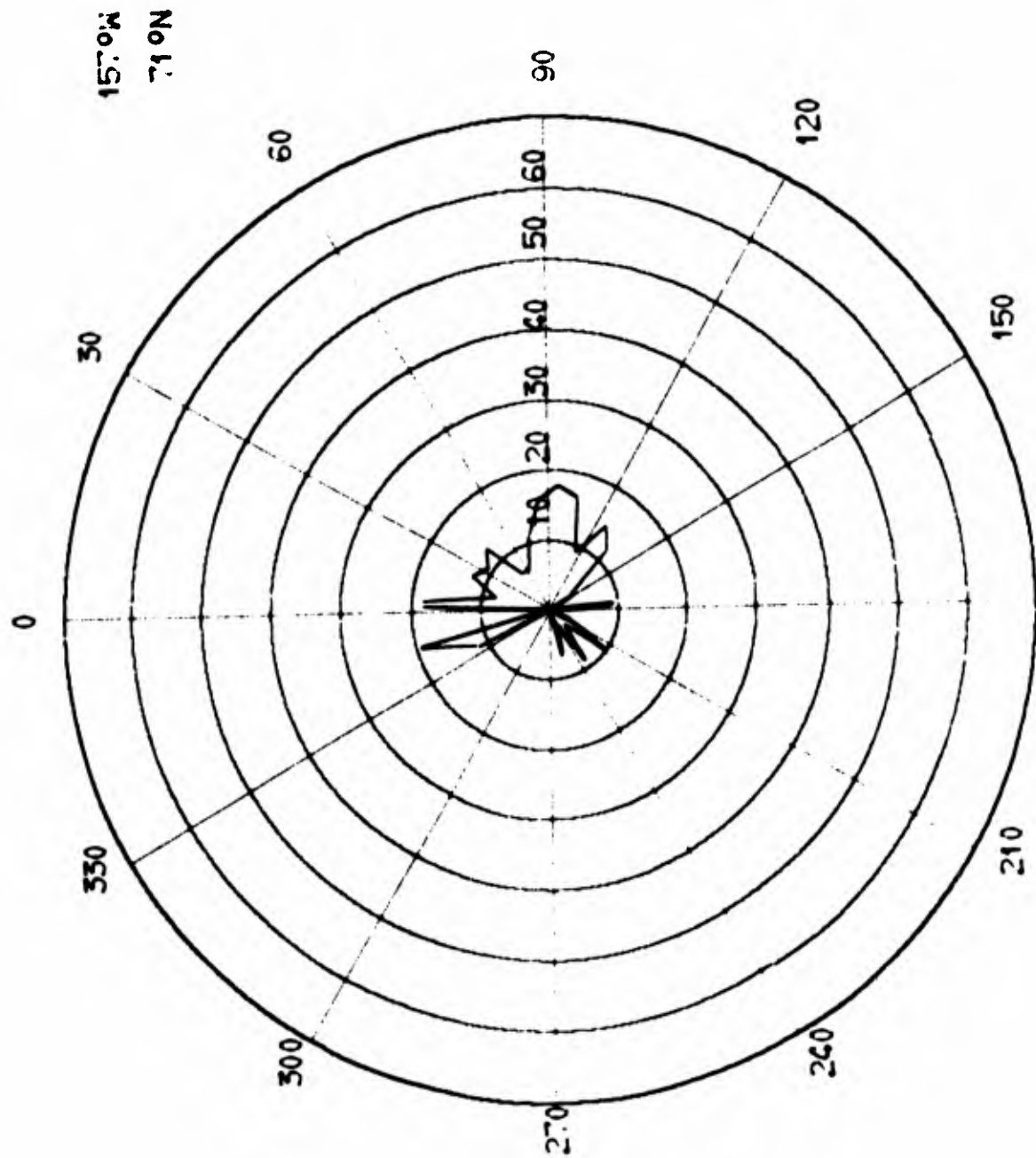


Figure 9-3 Expected Directional Variation of Atmospheric Noise- Effective Field Intensity for 10° Sectors in dB rel to 1 μ V/m in a 1 kHz bw

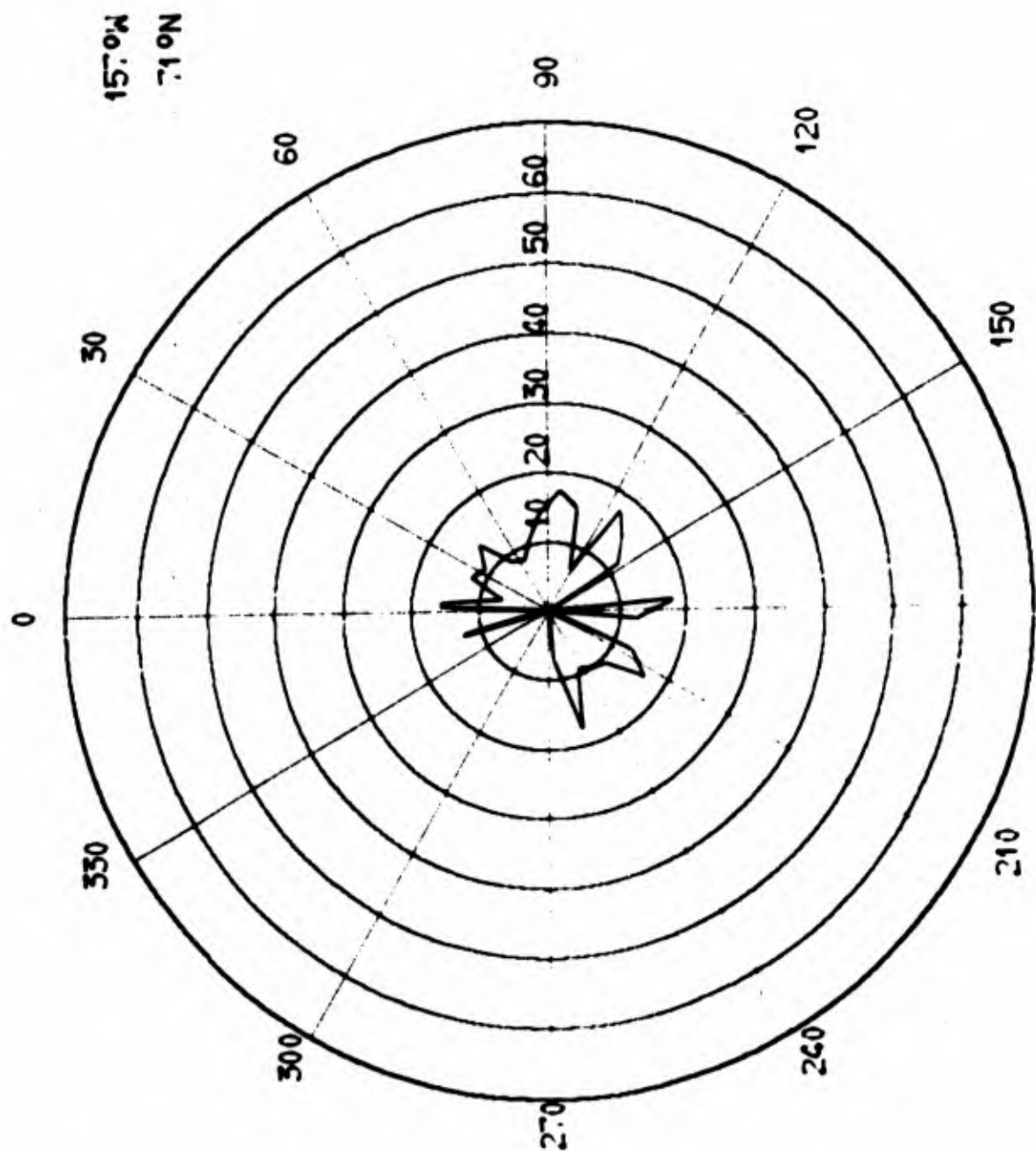


Figure 9-4 Expected Directional Variation of Atmospheric Noise- Effective Field Intensity for 10° Sectors in dB rel to 1μV/m in a 1 kHz bw

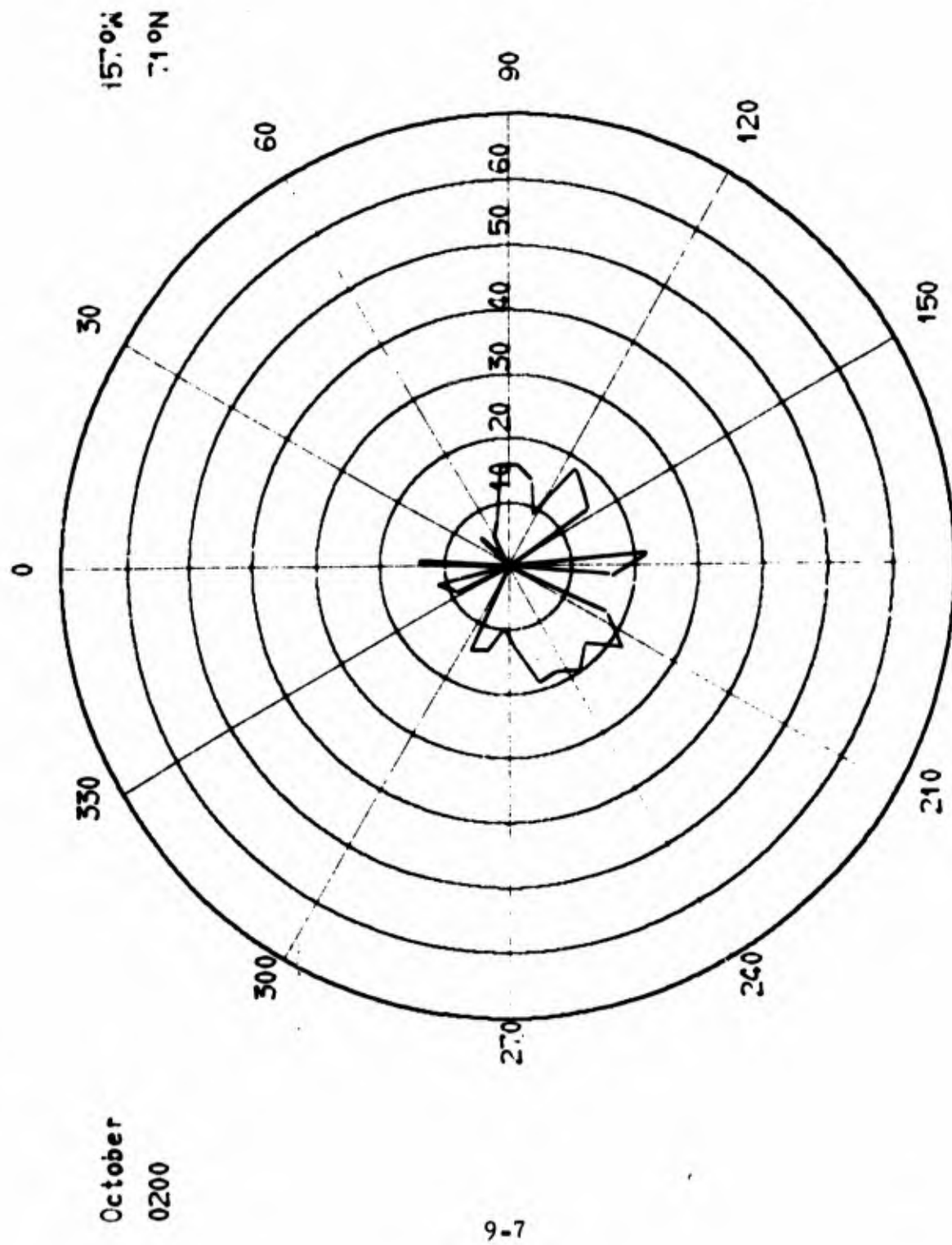


Figure 9-5 Expected Directional Variation of Atmospheric Noise- Effective Field Intensity for 10° Sectors in dB re: 1 μ V/m in a 1 kHz bw

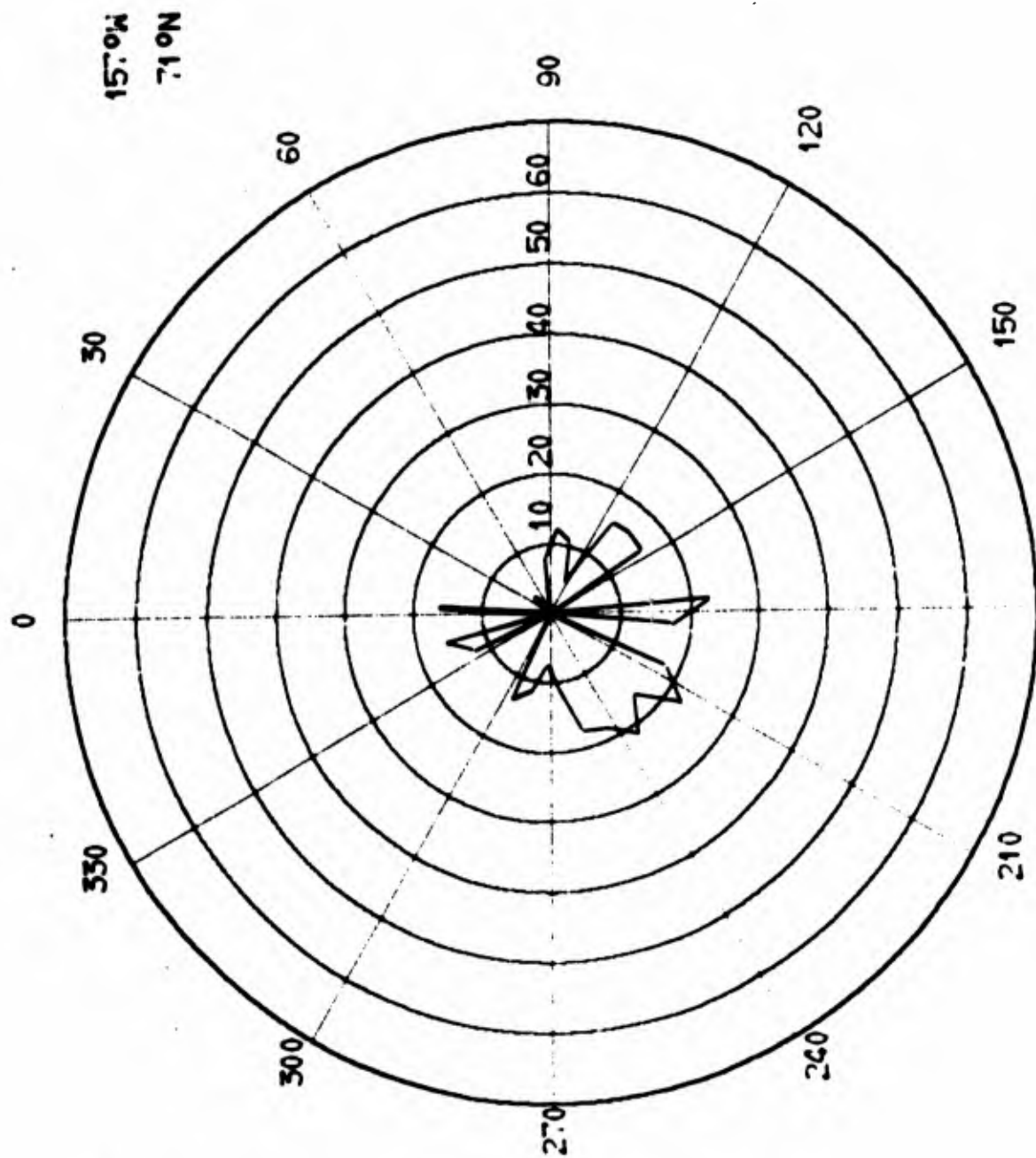


Figure 9-6 Expected Directional Variation of Atmospheric Noise- Effective Field intensity for 10° Sectors in dB rel to 1 μ V/m in a 1 kHz bw

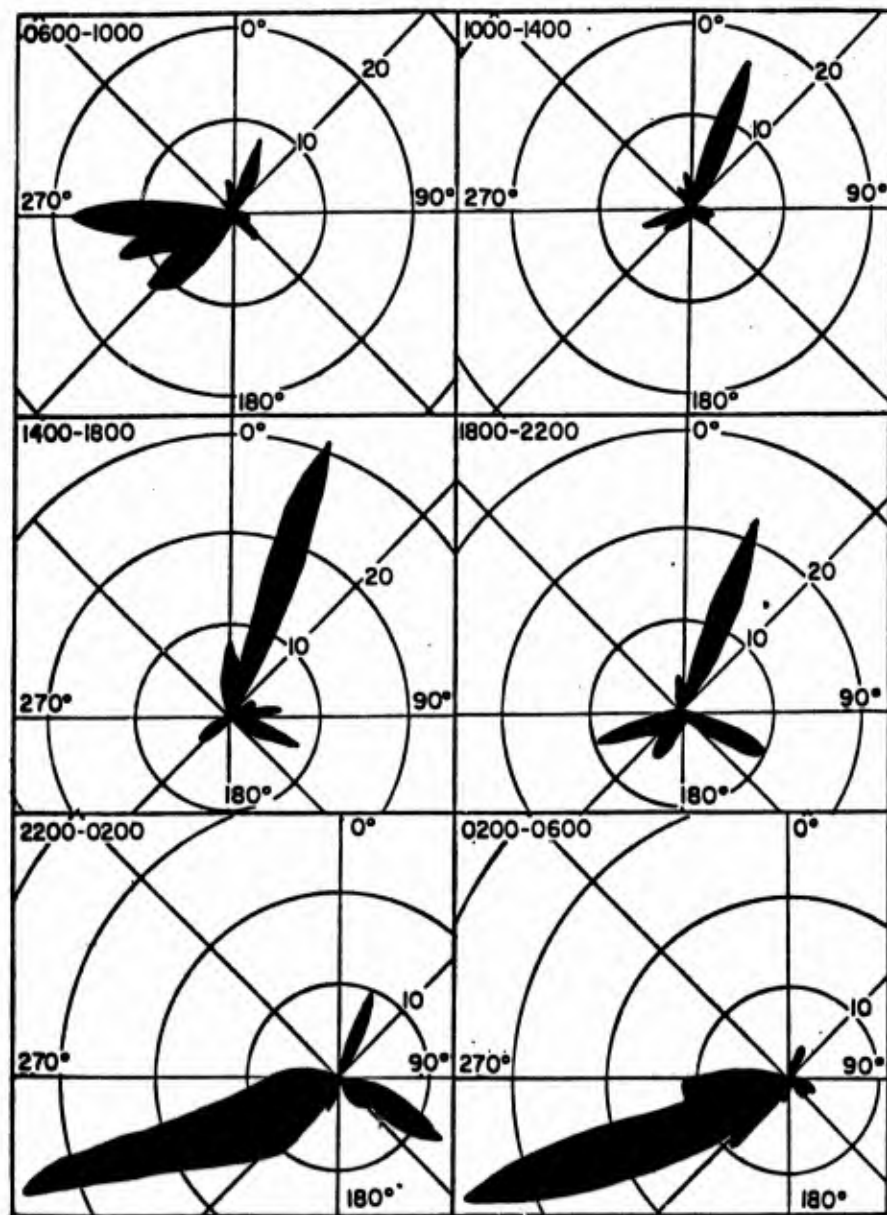


Figure 9-7 Average rates of occurrence of atmospherics over 4-hour intervals against their directions of arrival.

10.0 SUMMARY

Each of the nine desired improvements noted in the Introduction have been accomplished, with many of the results exceeding our expectations. The calculated values of all parameters have been shown to be reasonably accurate, by comparisons with measured ESSA data at 13 kHz. The digital computer model for predicting VLF atmospheric noise parameters is one of the most comprehensive ever developed. It is also one of the most realistic, in that data and equations representing the natural phenomena which produce atmospheric noise were used whenever possible. These include thunderstorm day data, cloud-to-ground and intra-cloud lightning discharges (including the individual events which make up each discharge), the electrical properties of the earth, diurnal and other statistical distributions of the various natural phenomena, and many more too numerous to mention here. Shortcomings and inaccuracies undoubtedly exist in this model. Because of its realism and comprehensiveness, however, it can easily and effectively be improved in the future, when more and better data become available.

The use of the model to prepare a VLF atmospheric noise prediction manual has resulted in the availability, for the first time, of noise prediction maps for the entire world for each hour and month, for field intensity and standard deviation values. Voltage deviation, V_d , prediction maps are available for each hour and each season. Frequency interpolation curves which are part of the manual prepared from this model, provide the ability to interpolate the 20 kHz values on the prediction maps to any frequency from 10 to 30 kHz, for each season and for 34 approximately equal area regions of the earth. Perhaps the most significant aspect of these results is the availability of standard deviation, V_d , and frequency interpolation data as a function of geographic location. Previously the estimates for these parameters had been average values supposedly valid for the entire world. It should be noted that all of the contour maps, frequency interpolation

plots, and direction of arrival plots were made by the computer, including the annotation of contours and labeling of abscissa and ordinate values. This virtually eliminated the opportunity for human error in the preparation of the atmospheric noise manual. The appearance of these computer plots are unfortunately not equivalent to their technical value. The plotting system is an analog device which produced some variability and roughness in appearance. That accuracy was given precedence over appearance is apparent and we trust justifiable.

The advances in the state-of-the-art made on this program have revealed many opportunities for further development. The most significant of these, which we believe should be considered for future efforts, are:

- 1) The opportunity to calculate directly the amplitude probability distribution of atmospheric noise. Since the present model computes the detailed characteristics of lightning discharges, as well as their number for every region of the world, it is very reasonable to consider that this data can be used to calculate amplitude probability distributions.
- 2) The manner in which the frequency interpolation calculations have been made offers the opportunity to computerize the results and their usage. It would be relatively straight forward to write a computer program which would identify receiver location within one of the 34 frequency interpolation regions, and then interpolate between the values for the specific frequencies already calculated, to any other frequency desired. This would be much cheaper than running the entire prediction model program and would probably produce acceptable results for many applications.
- 3) The computed values at each 10° longitude and 10° latitude for E_v , σ_N , and V_d have been presented to the Navy as one of the outputs from this program. These matrices of data for the 612 10° by 10° locations could be effectively used in communications system analysis, if signal values are computed for the same locations. Development of a computer capability to take advantage

of these noise data matrices is highly recommended. The computer program developed under this contract was delivered to the Navy for their use in making calculations for other frequencies and locations.

ACKNOWLEDGMENTS

This work could not have been accomplished without the data supplied by many individuals and organizations. We would like to recognize especially the National Weather Record Center (NWRC) which supplied most of the thunderstorm data. The personal interest shown by everyone at NWRC made the data collection there not only a success but a pleasure. The particular interest and assistance received from Mr. Dick Whiting deserves special recognition. The assistance received from the Naval Weather Service Environmental Detachment at NWRC is also acknowledged.

We are also indebted to those who supplied lightning counter data for this project. These include Dr. Fred Horner, Radio and Space Research Station, Slough, England; Professor S. A. Prentice, University of Queensland, Brisbane, Australia; Dr. R. H. Golde, Electrical Research Association, Leatherhead, England; The Bureau of Meteorology, Darwin, Australia; Mr. William Ahlbeck, Environmental Science Services Administration, Boulder, Colorado; and Dr. J. Keller-Jacobsen, Research Association of the Danish Electricity Supply Undertakings, Lyngby, Denmark. Without this data, supplied by these individuals and organizations, the atmospheric noise prediction model would not have been nearly so complete.

We acknowledge also the major assistance in computer programming and data analysis received from Mr. Allah C. Crail, Mrs. Carol Leyner, and Mr. John H. Swenson. Their interest and support throughout the program was most appreciated.

The preparation of over 1,000 figures and computer plots resulting from this project required a special effort from Mr. Robert L. Hill and Mr. Gary D. Uridil. Special thanks are extended to them for their efforts.

Finally we wish to acknowledge the helpful consultations held with Mr. William L. Taylor and Mr. Robert T. Disney, ESSA, and Dr. David Large and Mr. Charles Beach, WGL.

11.0 REFERENCES

1. Aiya, S. V. C. and B. S. Sonde [1963], Spring Thunderstorms over Bangalore, Proc. IEEE, Nov. 1963.
2. Atkinson, Gary D. [1967], Thunderstorms in Southeast Asia, Technical Study 11, Scientific Services, 1st Weather Wing, March 1967.
3. Batcha, J. P. and J. R. Reese [1964], Surface Determination and Automatic Contouring for Mineral Exploration, Extraction and Processing, Q. of the Colo. School of Mines, 59, No. 4, Oct. 1964.
4. Beckman, Petr [1968], Elements of Probability Theory, Harcourt, Brace and World, Inc., 1968, pp. 101-102.
5. Brook, M., N. Kitagawa and E. J. Workman [1962], Continuing Currents in Cloud to Ground Lightning Discharges, JGR, Vol. 67, No. 2, Feb. 1962.
6. Brook, M. and N. Kitagawa [1960], Some Aspects of Lightning Activity and Related Meteorological Conditions, JGR, Vol. 65, No. 4, April 1960, pp. 1189-1201.
7. Brooks, C. E. P. and N. Carruthers [1953], Handbook of Statistical Methods in Meteorology, London, Her Majesty's Stationery Office.
8. Burington, R. S. and G. C. May [1958], Handbook of Probability and Statistics with Tables, Handbook Publishers, Inc., 1958, p. 23.
9. Byers, Horace R. and Roscoe R. Braham [1949], The Thunderstorm, Supt. of Documents, Washington, D.C.
10. Byers, Horace Robert [1953], Thunderstorm Electricity, University of Chicago Press.
11. Chalmers, J. A., The Electricity of nimbo-stratus Clouds, Recent Advances in Atmospheric Electricity, Pergamon Press, N.Y., 1958, pp. 309-315.
12. Clarence, N. D. and D. J. Malan [1957], Preliminary discharge processes in lightning flashes to ground, Q. Jour. Roy. Met. Soc.
13. Finch, Toewartha, Robinson and Hammond [1957], Elements of Geography, McGraw-Hill, 1957.
14. Fuguay, D. M. [1962], Mountain Thunderstorms and Forest Fires, Weatherwise, Vol. 15, 11, pp. 149-152.
15. Hagenguth, J. H. [1947], Photographic study of lightning, A.I.E.E. Trans., 66, pp. 577-585.

16. Horner, F. [1961], Narrow-Band Atmospheric from Two Local Thunderstorms, J. Atmos. and Terrest. Phys., Vol. 27, pp. 13-25.
17. Horner, F. and P. A. Bradley [1964], The Spectra of Atmospheric from Near Lightning Discharges, Jour. of Atmos. and Terrest. Physics, Vol. 26.
18. Horner, F. [1964], Radio Noise From Thunderstorms, Advances in Radio Research, Vol. 2, edited by J. A. Saxton, Academic Press, London and New York.
19. Horner, F. [1967], Analysis of data from lightning-flash counters, Proc. IEE, Vol. 114, pp. 916-923.
20. Humphreys, W. J. [1964], Physics of the Air, Dover, New York, (original, 1920).
21. Isikawa, H. [1961], Nature of Lightning Discharges as Origins of Atmospheric, Proc. of the Res. Inst. of Atmospheric, Nagoya Univ., Japan, Vol. 8A, March 1961.
22. Kalakowsky, C. B. and E. A. Lewis, VLF Sferics of Very Large Virtual Source Strength, (source unknown).
23. Kendall, G. B. [1962], The application of the Poisson distribution to the frequencies of thunderstorm days in Canada, 2nd Conf. on Climatology, 209th Nat'l meeting of AMS, October 1962.
24. Kilson, E. and A. Thomson [1931], The Occurrence of Thunderstorms in New Zealand, New Zeal. Jour. of Sci. and Tech., Feb. 1931.
25. Kitagawa, N. and M. Brook [1960], A Comparison of Intracloud and cloud-to-ground Lightning Discharges, JGR, Vol. 65, No. 4, April 1960, pp. 1189-1201.
26. Ludlam, F. H. [1963], Severe local storms, A Review, Meteorological Monographs, Vol. 5, No. 27, Amer. Met. Soc.
27. Linfield, R. F. [1965], VLF System Design, Specification and Evaluation Processes, DECO Report 34-F, June 1965.
28. Mackerras, D. [1968], A Comparison of Discharge Processes in Cloud and Ground Lightning Flashes, JGR, Vol. 73, pp. 1175-1183.
29. Mackerras, D. [1963], Thunderstorm Observations Related to Lightning Counters I and II, Arkiv for Geofysik.
30. Malan, D. J. and B. F. J. Schonland [1953], Charge distribution and electrical processes deduced from lightning measurement, Thunderstorm Electricity, Univ. of Chicago Press.

31. Malan, D. J. [1958], Radiation from lightning discharges and its relation to the discharge process, Recent Advances in Atmospheric Electricity, Pergamon Press, N.Y.; pp. 557-563.
32. Malan, D. J. [1963], Physics of Lightning, The English Universities Press, Ltd., London.
33. Maxwell, E. L. and D. L. Stone [1966], VLF Atmospheric Noise Predictions, DECO Report 92-F-1, 15 April 1966.
34. Maxwell, E. L. [1967], Atmospheric Noise from 20 Hz to 30 kHz, Radio Science, Vol. 2, No. 6, June 1967.
35. Martin, F. N. and V. E. Hildebrand [1965], Statistical Evaluation of Sferics Distribution, NOLC Report 628, 16 August 1965.
36. Moore, C. B., B. Vonnegut and A. L. Bolka [1958], Results of an experiment to determine initial precedence of organized electrification and precipitation in thunderstorms, Recent Advances in Atmospheric Electricity, Pergamon Press, N.Y., pp. 333-360.
37. Morgan, R. R. [1968], World-Wide VLF Effective-Conductivity Map, Westinghouse Report 80133-F-1, 15 January 1968.
38. Muller-Hillebrand, D. [1963], 1963 Report on lightning counters, six years of lightning counting in Sweden, Uppsala Universitet Meddelanden Report.
39. Muller-Hillebrand, D. [1963b], Lightning Counters I and II, Arkiv for Geofysik.
40. Ogawa, Toshio and M. Brook [1964], The mechanism of the Intracloud lightning discharge, JGR, Vol. 69, No. 24, pp. 5147-5150, December 1964.
41. Norinder, H. [1954], The waveforms of the electric field in atmospherics recorded simultaneously by two distant stations, Arkiv for Geofysik, Band 2, No. 9, November 1954, pp. 161-195.
42. Pierce, E. T. [1955], Electrostatic Field-Charges due to Lightning Discharges, Q. Jour. Roy. Met. Soc., Vol. 81, pp. 211-228.
43. Pierce, E. T., H. R. Arnold and A. S. Dennis [1962], Very low frequency atmospherics due to lightning flashes, SRI Final Report, Contract AF33(657)7009.
44. Pierce, E. T. [1969], The Thunderstorm Area Source of Atmospheric Noise at Frequencies between 1 and 100 kHz, DASA Report 2299, June 1969.
45. Pierce, E. T. [1968], The Counting of Lightning Flashes, SRI Special Report 49, June 1968.

46. Prentice, S. A. and M. W. Robson [1968], Lightning Intensity Studies in the Darwin Area, Elect. Engr. Trans. of Inst. of Engineers, Australia, September 1968.
47. Rumney, George R. [1968], Climatology and The World's Climates, MacMillan, 1968.
48. Sartor, J. Doyne [1969], Electricity and Rain, Physics Today, Vol. 22, No. 8, August 1969.
49. Sartor, J. D. [1967], The role of particle interactions in the distribution of electricity in thunderstorms, Jour. of Atmos. Sci., Vol. 24, No. 6, November 1967.
50. Severe Local Storms [1963], Met. Monographs, Vol. 5, No. 27.
51. 6th Conference on Severe Local Storms [1969], Amer. Met. Soc.
52. 5th Conference on Severe Local Storms [1967], Amer. Met. Soc.
53. Stone, D. L. [1970], Computer Program Operational Manual for Atmospheric Noise Predictions, Westinghouse Report 70-1H2-VLFNO-R2, 30 June 1970.
54. Sullivan, A. W. and J. O. Wells [1957], A Lightning Stroke Counter, Bull. Amer. Meteorological Soc., Vol. 38, pp. 291-294.
55. Summers, Peter W. and Alec A. Paul, Some Climatological Characteristics of Hailfall in Central Alberta (source unknown).
56. Takagi, M. [1961], The mechanisms of Discharges in a Thundercloud, Proc. Res. Inst. Atmos., Nagoya Univ., Japan, Vol. 8B, pp.1-105.
57. Takagi, M. [1969], VHF radiation from ground discharges, Proc. of Res. Inst. Atmos., Nagoya Univ., Japan, Vol. 16, January 1969.
58. Takagi, M. and T. Takeuti [1963], Atmospheric radiation from lightning discharge, Proc. Res. Inst. Atmos., Nagoya Univ., Japan, Vol. 10, January 1963.
59. Taylor, W. L. [1969], Determining lightning stroke height from ionospheric components of atmospheric waveforms, Jour. of Atmos. and Terrest. Physics, Vol. 31, pp. 983-990.
60. Vonnegut, Bernard [1963], Some facts and speculations concerning the origin and role of thunderstorm electricity, Met. Monographs, Vol. 5, No. 27, 6.

61. Wang, C. P. [1963], Lightning discharges in the tropics, JGR, Vol. 68.
62. Watt, A. D. [1960], ELF electric fields from thunderstorms, Jour. of Research, NBS, Vol. 64D, No. 5, Sept.-Oct.
63. Watt, A. D. [1967], VLF Radio Engineering, Pergamon Press.
64. World Distribution of Thunderstorm Days, Part 2, WMO/OMM-No. 21, TP.21.

APPENDIX A

Tables of Comparisons between Measured and Predicted Noise Values

Atmospheric noise values were calculated at 13 kHz for vertical electric field intensity, E_v , standard deviation, σ_N , and voltage deviation, V_d , for each of the ESSA noise station locations at which 13 kHz data is available. The decibel values for the three months of each season were averaged for each hour for both calculated and observed (ESSA) data.

A difference or delta value was then obtained by subtracting observed from calculated values. Calculated, observed and delta values were tabulated for each hour and each season. Comparison plots were made for a few representative locations and seasons and are shown in the appropriate section of the report.

Complete tabulations for the December-January-February and June-July-August seasons are presented in this Appendix for E_v and σ_N . Tabulations for V_d are limited to the first 5 stations since Rabat and Pretoria had no V_d data and New Delhi V_d data does not seem reasonable.

The following notations are used:

EV(C)	---	Calculated vertical field intensity.
EV(O)	---	Observed vertical field intensity.
DELEV	---	EV(C) - EV(O).
STD	---	Calculated standard deviation.
SIGPRIM	---	Observed standard deviation.
DELSTD	---	STD - SIGPRIM
VD(C)	---	Calculated voltage deviation.
VD(O)	---	Observed voltage deviation.
DELVD	---	VD(C) - VD(O).

See Section 7.0, Equation (7.3) and note that SIGPRIM = σ_N .

TABLE A1 a

BALBOA, CANAL ZONE	(DEC., JAN., FEB.)											FINAL
HOUR (LST)	0030	0130	0230	0330	0430	0530	0630	0730	0830	0930	1030	1130
EV(C)	49.3	49.5	49.7	49.8	49.8	49.2	48.1	47.7	46.7	46.0	46.1	47.3
EV(O)	48.6	49.3	49.6	50.0	50.3	51.0	50.3	48.0	47.0	46.6	47.0	47.3
DELEV	.7	.2	.1	-.2	-.5	-1.8	-2.2	-.3	-.3	-.6	-.9	0.0

BOULDER, COLORADO	(DEC., JAN., FEB.)											FINAL
HOUR (LST)	0030	0130	0230	0330	0430	0530	0630	0730	0830	0930	1030	1130
EV(C)	45.3	45.8	45.9	45.8	45.5	45.4	45.0	45.5	43.7	42.4	41.5	41.3
EV(O)	49.3	49.3	49.3	48.6	48.6	48.3	47.6	47.6	44.0	43.0	43.0	43.3
DELEV	-4.0	-3.5	-3.4	-2.8	-3.1	-2.9	-2.6	-2.1	-.3	-.6	-1.5	-2.0

COOK, AUSTRALIA	(DEC., JAN., FEB.)											FINAL
HOUR (LST)	0030	0130	0230	0330	0430	0530	0630	0730	0830	0930	1030	1130
EV(C)	54.0	54.0	53.7	53.8	53.9	54.1	53.0	52.1	50.9	49.8	49.1	49.5
EV(O)	56.0	56.3	56.0	55.3	55.0	54.0	52.6	51.0	51.0	51.3	51.3	51.6
DELEV	-2.0	-2.3	-2.3	-1.5	-1.1	.1	.4	1.1	-.1	-1.5	-2.2	-2.1

ENKOPING, SWEDEN	(DEC., JAN., FEB.)											FINAL
HOUR (LST)	0030	0130	0230	0330	0430	0530	0630	0730	0830	0930	1030	1130
EV(C)	45.4	45.1	45.0	44.8	44.5	44.3	43.8	43.8	42.9	41.4	39.5	38.7
EV(O)	48.0	47.3	47.0	47.0	46.6	46.6	46.6	46.6	43.9	41.0	40.0	39.6
DELEV	-2.6	-2.2	-2.0	-2.2	-2.1	-2.3	-2.8	-2.8	-1.0	.4	-.5	-.9

KEKAHA, HAWAII	(DEC., JAN., FEB.)											FINAL
HOUR (LST)	0030	0130	0230	0330	0430	0530	0630	0730	0830	0930	1030	1130
EV(C)	50.7	51.1	51.5	51.8	52.2	52.1	52.4	51.1	49.7	48.5	47.6	46.8
EV(O)	50.6	50.6	50.0	50.3	51.0	51.0	51.3	52.0	47.3	46.0	46.6	46.3
DELEV	.1	.5	1.5	1.5	1.2	1.1	1.1	-.9	2.4	2.5	1.0	.5

TABLE A1 b

1230	1330	1430	1530	1630	1730	1830	1930	2030	2130	2230	2330
49.5	51.6	53.0	53.3	53.1	52.5	51.5	50.6	49.8	49.2	48.8	48.6
49.0	51.3	52.3	52.6	52.6	50.6	48.3	48.0	47.6	47.3	47.3	47.3
.5	.3	.7	.7	.5	1.9	3.2	2.6	2.2	1.9	1.5	1.3

1230	1330	1430	1530	1630	1730	1830	1930	2030	2130	2230	2330
41.4	41.8	42.0	42.4	43.5	43.2	43.2	43.3	43.4	43.6	43.9	44.6
44.0	43.6	43.0	42.0	41.3	42.3	43.3	44.0	45.0	45.3	47.0	47.3
-2.6	-1.8	-1.0	.4	2.2	.9	-.1	-.7	-1.6	-1.7	-3.1	-2.7

1230	1330	1430	1530	1630	1730	1830	1930	2030	2130	2230	2330
50.7	52.4	54.0	55.2	55.6	55.7	55.5	55.3	54.9	54.6	54.3	53.9
52.3	54.3	55.6	57.0	58.3	58.3	57.3	56.3	58.3	57.3	57.3	57.0
-1.6	-1.9	-1.6	-1.8	-2.7	-2.6	-1.8	-1.0	-3.4	-2.7	-3.0	-3.1

1230	1330	1430	1530	1630	1730	1830	1930	2030	2130	2230	2330
38.7	39.3	39.7	39.2	40.4	44.6	44.7	45.0	45.4	45.8	46.4	46.0
40.0	41.0	41.0	41.0	40.6	42.3	43.6	45.6	45.3	46.0	47.3	47.6
-1.3	-1.7	-1.3	-1.8	-.2	2.3	1.1	-.6	.1	-.2	-.9	-1.6

1230	1330	1430	1530	1630	1730	1830	1930	2030	2130	2230	2330
46.1	45.5	45.0	44.9	45.3	45.2	46.6	47.9	49.2	49.9	50.4	50.5
47.0	46.3	46.3	45.0	45.0	45.0	44.6	46.0	47.6	48.6	49.6	50.0
-.9	-.8	-1.3	-.1	.3	.2	2.0	1.9	1.6	1.3	.8	.5

TABLE A1 c

NEW DELHI, INDIA	(DEC., JAN., FEB.)	FINAL
HOUR (LST)	0030 0130 0230 0330 0430 0530 0630 0730 0830 0930 1030 1130	
EV(C)	50.8 50.3 49.9 49.3 49.1 48.6 48.5 46.6 44.9 43.9 43.1 42.6	
EV(O)	50.6 50.3 50.3 50.3 50.6 50.6 50.3 48.0 45.6 44.6 45.3 46.0	
DELEV	.2 0.0 -.4 -1.0 -1.5 -2.0 -1.8 -1.4 -.7 -.7 -2.2 -3.4	

OHIRA, JAPAN	(DEC., JAN., FEB.)	FINAL
HOUR (LST)	0030 0130 0230 0330 0430 0530 0630 0730 0830 0930 1030 1130	
EV(C)	49.9 50.1 49.6 49.5 49.4 49.0 48.9 47.6 46.3 45.0 44.2 44.0	
EV(O)	48.0 49.0 48.6 49.0 49.0 49.6 48.3 45.3 45.6 45.6 45.3 45.6	
DELEV	1.9 1.1 1.0 .5 .4 -.6 .6 2.3 .7 -.6 -1.1 -1.6	

PRETORIA, S. AFR.	(DEC., JAN., FEB.)	FINAL
HOUR (LST)	0030 0130 0230 0330 0430 0530 0630 0730 0830 0930 1030 1130	
EV(C)	58.7 58.6 58.2 57.8 57.1 56.5 55.3 54.1 52.9 51.8 53.5 55.7	
EV(O)	57.3 56.6 55.3 55.3 54.6 53.6 51.0 50.3 49.3 49.0 50.6 52.0	
DELEV	1.4 2.0 2.9 2.5 2.5 2.9 4.3 3.8 3.6 2.8 2.9 3.7	

RABAT, MOROCCO	(DEC., JAN., FEB.)	FINAL
HOUR (LST)	0030 0130 0230 0330 0430 0530 0630 0730 0830 0930 1030 1130	
EV(C)	49.7 49.9 49.9 50.0 50.1 49.9 49.6 49.4 48.0 47.1 46.5 46.1	
EV(O)	49.0 48.6 48.3 47.6 48.6 48.6 48.6 46.6 44.6 43.6 45.0 45.0	
DELEV	.7 1.3 1.6 2.4 1.5 1.3 1.0 2.8 3.4 3.5 1.5 1.1	

SINGAPORE, MALAYA	(DEC., JAN., FEB.)	FINAL
HOUR (LST)	0030 0130 0230 0330 0430 0530 0630 0730 0830 0930 1030 1130	
EV(C)	55.8 55.7 55.8 55.7 55.6 55.2 54.7 53.4 51.5 50.3 50.2 50.8	
EV(O)	56.3 56.3 56.3 56.3 56.3 55.6 55.6 53.0 51.3 51.3 50.6 51.0	
DELEV	-.5 -.6 -.5 -.6 -.7 -.4 -.9 .4 .2 -1.0 -.4 -.2	

TABLE A1 d

1230	1330	1430	1530	1630	1730	1830	1930	2030	2130	2230	2330
42.6	43.6	45.0	46.8	48.9	49.6	50.6	51.5	52.7	52.7	51.7	51.4
46.0	45.6	46.6	48.3	48.3	48.0	49.0	50.3	51.3	51.6	51.6	51.0
-2.4	-2.0	-1.6	-1.5	.6	1.6	1.6	1.2	1.4	1.1	.1	.4

1230	1330	1430	1530	1630	1730	1830	1930	2030	2130	2230	2330
44.4	45.2	46.2	47.1	47.2	47.9	49.1	49.4	49.1	49.2	49.4	49.7
45.6	46.0	46.6	47.3	47.6	47.3	47.6	49.3	50.0	49.6	49.3	48.3
-1.2	-.8	-.4	-.2	-.4	.6	1.5	.1	-.9	-.4	.1	1.4

1230	1330	1430	1530	1630	1730	1830	1930	2030	2130	2230	2330
58.2	61.3	63.9	64.5	64.5	64.1	63.2	62.2	61.8	61.2	60.4	59.5
54.3	59.0	60.6	62.0	61.6	62.0	61.0	60.6	60.3	60.3	58.0	58.0
3.9	2.3	3.3	2.5	2.9	2.1	2.2	1.6	1.5	.9	2.4	1.5

1230	1330	1430	1530	1630	1730	1830	1930	2030	2130	2230	2330
45.9	45.9	45.9	46.1	46.5	47.5	48.3	48.9	49.8	50.3	50.0	49.6
46.3	45.3	46.3	45.6	45.0	45.0	45.6	46.6	48.3	48.6	48.6	49.0
-.4	.6	-.4	.5	1.5	2.5	2.7	2.3	1.5	1.7	1.4	.6

1230	1330	1430	1530	1630	1730	1830	1930	2030	2130	2230	2330
51.9	53.8	55.0	55.4	55.3	55.0	54.8	54.9	55.2	55.7	56.1	56.3
52.0	53.6	55.3	56.6	56.0	55.3	54.3	55.3	54.6	55.0	55.6	56.3
-.1	.2	-.3	-1.2	-.7	-.3	.5	-.4	.6	.7	.5	0.0

TABLE A2 a

BALBOA, CANAL ZONE	(JUNE, JULY, AUG.)												FINAL
HOUR (LST)	0030	0130	0230	0330	0430	0530	0630	0730	0830	0930	1030	1130	
EV(C)	59.7	60.8	61.1	61.6	61.6	61.2	60.6	59.9	58.7	57.8	57.4	57.9	
EV(O)	61.6	62.6	63.3	64.0	64.3	64.0	62.7	61.6	62.0	60.6	60.7	60.0	
DELEV	-1.9	-1.8	-2.2	-2.4	-2.7	-2.8	-1.7	-1.7	-3.3	-2.8	-2.9	-2.1	

BOULDER, COLORADO	(JUNE, JULY, AUG.)												FINAL
HOUR (LST)	0030	0130	0230	0330	0430	0530	0630	0730	0830	0930	1030	1130	
EV(C)	58.4	58.4	58.2	58.1	57.6	57.7	57.2	56.9	56.5	56.0	56.4	57.6	
EV(O)	61.0	59.6	59.3	58.3	57.3	56.3	55.6	56.0	56.6	55.6	57.0	59.0	
DELEV	-2.6	-1.2	-1.1	-.2	.3	1.4	1.6	.9	-.1	.4	-.6	-1.4	

COOK, AUSTRALIA	(JUNE, JULY, AUG.)												FINAL
HOUR (LST)	0030	0130	0230	0330	0430	0530	0630	0730	0830	0930	1030	1130	
EV(C)	51.3	51.5	51.4	51.2	51.0	50.9	50.4	49.9	48.3	47.5	46.5	45.8	
EV(O)	51.0	51.3	51.3	51.3	51.3	51.3	51.0	50.6	47.0	46.3	46.6	46.3	
DELEV	.3	.2	.1	-.1	-.3	-.4	-.6	-.7	1.3	1.2	-.1	-.5	

ENKOPING, SWEDEN	(JUNE, JULY, AUG.)												FINAL
HOUR (LST)	0030	0130	0230	0330	0430	0530	0630	0730	0830	0930	1030	1130	
EV(C)	52.5	52.6	52.3	52.6	52.4	51.8	51.5	51.6	52.4	53.4	54.7	56.0	
EV(O)	51.0	51.0	51.0	50.3	50.0	48.6	47.6	47.6	48.3	48.6	50.6	52.6	
DELEV	1.5	1.6	1.3	2.3	2.4	3.2	3.9	4.0	4.1	4.8	4.1	3.4	

KEKAHA, HAWAII	(JUNE, JULY, AUG.)												FINAL
HOUR (LST)	0030	0130	0230	0330	0430	0530	0630	0730	0830	0930	1030	1130	
EV(C)	49.6	48.8	48.3	47.9	47.7	48.0	46.5	45.2	44.5	44.9	45.3	45.4	
EV(O)	51.0	51.6	51.3	51.3	51.0	51.3	51.0	48.3	47.3	47.3	47.3	48.3	
DELEV	-1.4	-2.8	-3.0	-3.4	-3.3	-3.3	-4.5	-3.1	-2.8	-2.4	-2.0	-2.9	

TABLE A2 b

1230	1330	1430	1530	1630	1730	1830	1930	2030	2130	2230	2330
59.7	61.9	63.6	64.5	64.8	64.5	63.4	62.0	60.6	59.4	58.8	58.6
60.0	61.6	63.6	64.0	63.6	63.0	60.4	60.0	62.0	62.0	61.6	61.6
-.3	.3	0.0	.5	1.2	1.5	2.4	2.0	-1.4	-2.6	-2.8	-3.0

1230	1330	1430	1530	1630	1730	1830	1930	2030	2130	2230	2330
59.6	62.3	64.3	64.8	64.7	64.2	62.9	61.3	60.6	59.9	59.3	58.8
62.3	64.0	65.3	65.3	65.6	65.3	64.0	62.6	63.0	62.6	61.6	61.0
-2.7	-1.7	-1.0	-.5	-.9	-1.1	-1.7	-1.3	-2.4	-2.7	-2.3	-2.2

1230	1330	1430	1530	1630	1730	1830	1930	2030	2130	2230	2330
45.4	45.7	46.5	47.7	48.9	49.0	50.1	51.6	51.8	51.5	51.3	51.3
45.6	46.3	46.6	47.0	48.3	47.6	47.4	49.6	50.3	51.0	50.6	51.0
-.2	-.6	-.1	.7	.6	1.4	2.5	2.0	1.5	.5	.7	.3

1230	1330	1430	1530	1630	1730	1830	1930	2030	2130	2230	2330
56.9	57.5	57.8	57.8	57.4	56.7	55.4	54.9	54.4	53.2	52.8	52.5
54.6	55.0	56.0	55.6	55.6	54.6	53.4	51.6	51.6	51.6	52.0	51.0
2.3	2.5	1.8	2.2	1.8	2.1	2.5	3.3	2.8	1.6	.8	1.5

1230	1330	1430	1530	1630	1730	1830	1930	2030	2130	2230	2330
45.0	44.4	43.6	43.1	43.7	44.7	45.0	46.1	47.1	48.3	49.1	49.6
48.6	48.3	47.6	46.6	46.0	46.0	45.4	45.6	46.6	48.0	48.6	50.0
-3.6	-3.9	-4.0	-3.5	-2.3	-1.3	-.5	.5	.5	.3	.5	-.4

TABLE A2 c

NEW DELHI, INDIA		(JUNE, JULY, AUG.)										FINAL
HOUR (LST)	0030	0130	0230	0330	0430	0530	0630	0730	0830	0930	1030	1130
EV(C)	56.3	56.1	55.8	55.6	55.3	55.3	54.6	54.0	53.3	53.0	53.5	55.2
EV(O)	55.3	55.6	55.0	55.0	55.0	54.0	51.6	51.0	50.6	50.6	51.3	52.3
DELEV	1.0	.5	.8	.6	.3	1.3	3.0	3.0	2.7	2.4	2.2	2.9

OHIRA, JAPAN		(JUNE, JULY, AUG.)										FINAL
HOUR (LST)	0030	0130	0230	0330	0430	0530	0630	0730	0830	0930	1030	1130
EV(C)	55.3	55.3	55.4	55.5	55.7	55.0	54.0	53.1	52.3	51.8	51.5	51.7
EV(O)	55.0	54.3	54.3	54.0	54.0	52.3	51.0	52.3	52.0	52.3	51.3	52.0
DELEV	.3	1.0	1.1	1.5	1.7	2.7	3.0	.8	.3	-.5	.2	-.3

PRETORIA, S. AFR.		(JUNE, JULY, AUG.)										FINAL
HOUR (LST)	0030	0130	0230	0330	0430	0530	0630	0730	0830	0930	1030	1130
EV(C)	52.0	52.1	51.9	51.5	51.1	50.8	50.2	49.5	48.8	48.0	47.4	47.3
EV(O)	52.0	51.6	52.0	52.0	52.0	52.0	51.6	50.0	48.3	48.0	47.0	47.6
DELEV	0.0	.5	-.1	-.5	-.9	-1.2	-1.4	-.5	.5	0.0	.4	-.3

RABAT, MOROCCO		(JUNE, JULY, AUG.)										FINAL
HOUR (LST)	0030	0130	0230	0330	0430	0530	0630	0730	0830	0930	1030	1130
EV(C)	53.5	53.1	52.9	52.8	52.6	52.6	51.4	50.5	49.4	48.9	49.4	50.7
EV(O)	50.0	50.0	50.3	49.6	50.0	50.0	48.3	48.0	46.3	46.3	45.6	47.0
DELEV	3.5	3.1	2.6	3.2	2.6	2.6	3.1	2.5	3.1	2.6	3.8	3.7

SINGAPORE, MALAYA		(JUNE, JULY, AUG.)										FINAL
HOUR (LST)	0030	0130	0230	0330	0430	0530	0630	0730	0830	0930	1030	1130
EV(C)	57.1	57.0	57.1	57.2	56.9	56.6	56.4	56.0	55.5	54.9	54.6	55.1
EV(O)	55.6	55.6	56.6	57.0	57.0	57.0	56.3	56.0	55.6	55.3	55.0	54.3
DELEV	1.5	1.4	.5	.2	-.1	-.4	.1	0.0	-.1	-.4	-.4	.8

TABLE A2 d

1230	1330	1430	1530	1630	1730	1830	1930	2030	2130	2230	2330
57.4	59.4	60.5	61.0	61.0	60.6	59.4	58.8	58.3	58.0	57.4	56.8
54.6	56.0	58.3	58.3	59.0	58.6	57.7	55.0	55.0	55.6	55.6	55.3
2.8	3.4	2.2	2.7	2.0	2.0	2.4	3.8	3.3	2.4	1.8	1.5

1230	1330	1430	1530	1630	1730	1830	1930	2030	2130	2230	2330
53.1	54.8	56.2	57.4	58.1	58.2	57.5	56.9	56.9	56.1	55.5	55.0
52.3	53.3	55.0	56.6	57.0	56.6	55.7	54.0	55.0	55.6	55.6	55.0
.8	1.5	1.2	.8	1.1	1.6	2.4	2.9	1.9	.5	-.1	0.0

1230	1330	1430	1530	1630	1730	1830	1930	2030	2130	2230	2330
48.0	49.4	51.3	52.2	52.6	52.1	53.4	53.5	53.0	52.4	52.1	52.1
48.6	50.0	51.6	53.0	53.3	52.0	51.4	53.6	54.0	53.3	52.3	52.0
-.6	-.4	-.3	-.8	-.7	.1	2.2	-.1	-1.0	-.9	-.2	.1

1230	1330	1430	1530	1630	1730	1830	1930	2030	2130	2230	2330
52.6	54.6	55.9	56.1	55.9	55.3	54.4	54.0	53.4	53.4	53.4	53.4
47.6	49.4	50.0	51.3	51.6	51.3	50.0	48.0	48.3	48.6	50.0	50.3
5.0	5.0	5.9	4.8	4.3	4.0	4.4	6.0	5.1	4.8	3.4	3.1

1230	1330	1430	1530	1630	1730	1830	1930	2030	2130	2230	2330
56.8	59.1	60.8	61.4	61.5	61.1	59.4	58.4	57.5	56.9	56.7	56.9
55.6	57.3	58.6	59.6	59.6	58.6	57.0	56.6	56.0	56.0	55.6	55.6
1.2	1.8	2.2	1.8	1.9	2.5	2.4	1.8	1.5	.9	1.1	1.3

TABLE A3 a

BALBOA, CANAL ZONE	(DEC..JAN..FEB.)											FINAL
HOUR (LST)	0030	0130	0230	0330	0430	0530	0630	0730	0830	0930	1030	1130
STD	5.4	5.4	5.4	5.4	5.3	5.2	5.4	5.2	5.2	5.2	5.2	5.2
SIGPRIM	5.3	5.5	5.7	5.6	5.9	6.0	5.5	5.4	5.6	5.5	5.6	5.6
DELSTD	.1	-.1	-.2	-.2	-.6	-.8	-.1	-.2	-.4	-.3	-.4	-.4

BOULDER, COLORADO	(DEC..JAN..FEB.)											FINAL
HOUR (LST)	0030	0130	0230	0330	0430	0530	0630	0730	0830	0930	1030	1130
STD	4.0	3.9	3.0	3.5	3.4	3.9	3.8	3.8	4.0	4.0	4.1	4.2
SIGPRIM	4.2	4.7	4.0	4.0	4.1	4.1	4.4	3.6	4.3	4.1	4.3	4.1
DELSTD	-.2	-.7	-.9	-.2	-.2	-.2	-.6	.2	-.3	-.1	-.2	.1

COOK, AUSTRALIA	(DEC..JAN..FEB.)											FINAL
HOUR (LST)	0030	0130	0230	0330	0430	0530	0630	0730	0830	0930	1030	1130
STD	3.9	3.0	3.0	4.0	4.1	4.1	4.3	4.4	4.5	4.5	4.5	4.2
SIGPRIM	4.1	3.0	3.4	3.5	3.1	3.6	3.4	3.4	3.7	4.7	4.6	4.8
DELSTD	-.2	.2	.5	.5	1.0	.5	.9	1.0	.8	-.2	-.1	-.6

ENKOPING, SWEDEN	(DEC..JAN..FEB.)											FINAL
HOUR (LST)	0030	0130	0230	0330	0430	0530	0630	0730	0830	0930	1030	1130
STD	3.0	3.7	3.8	3.8	3.4	4.0	4.1	4.1	4.1	4.3	4.6	4.5
SIGPRIM	2.7	4.0	2.6	2.8	2.0	2.7	2.4	3.2	3.1	3.7	3.9	3.2
DELSTD	.9	1.2	1.2	1.0	1.3	1.3	1.7	.9	1.0	.6	.7	1.3

KEKAHA, HAWAII	(DEC..JAN..FEB.)											FINAL
HOUR (LST)	0030	0130	0230	0330	0430	0530	0630	0730	0830	0930	1030	1130
STD	3.9	4.0	4.0	4.0	3.9	3.8	3.8	4.0	4.1	4.1	4.1	4.1
SIGPRIM	3.0	2.9	2.8	2.9	2.8	2.7	2.5	2.5	3.1	3.8	3.4	3.7
DELSTD	.9	1.1	1.2	1.1	1.1	1.1	1.3	1.5	1.0	.3	.7	.4

TABLE A3 b

1230	1330	1430	1530	1630	1730	1830	1930	2030	2130	2230	2330
5.3	5.4	5.4	5.5	5.5	5.5	5.3	5.2	5.1	5.1	5.0	5.0
5.5	4.7	5.2	4.4	4.8	5.0	5.9	5.6	5.9	6.4	5.9	5.8
-.2	.7	.2	1.1	.7	.5	-.6	-.4	-.8	-1.3	-.9	-.8

1230	1330	1430	1530	1630	1730	1830	1930	2030	2130	2230	2330
4.3	4.4	4.5	4.5	4.3	4.4	4.4	4.4	4.3	4.3	4.2	4.1
4.5	5.2	4.7	5.3	5.3	5.3	5.5	5.4	5.1	5.0	5.4	4.7
-.2	-.8	-.2	-.8	-1.0	-.9	-1.1	-1.0	-.8	-.7	-1.2	-.6

1230	1330	1430	1530	1630	1730	1830	1930	2030	2130	2230	2330
4.0	3.8	3.7	3.7	3.7	3.9	4.1	4.2	4.2	4.2	4.1	4.1
4.8	4.3	4.7	4.5	3.7	4.0	4.1	4.5	3.5	4.3	4.2	4.4
-.8	-.5	-1.0	-.8	0.0	-.1	0.0	-.3	.7	-.1	-.1	-.3

1230	1330	1430	1530	1630	1730	1830	1930	2030	2130	2230	2330
4.3	4.0	3.9	4.1	4.1	3.4	3.5	3.5	3.5	3.5	3.5	3.5
3.6	3.4	3.2	3.3	3.5	3.2	3.3	3.3	3.2	3.3	2.6	2.6
.7	.6	.7	.8	.6	.2	.2	.2	.3	.2	.9	.9

1230	1330	1430	1530	1630	1730	1830	1930	2030	2130	2230	2330
4.2	4.2	4.2	4.2	4.1	4.2	4.0	4.0	3.9	3.8	3.8	3.9
3.7	3.5	4.1	3.8	3.6	3.3	4.1	4.0	3.5	3.5	3.3	3.1
.5	.7	.1	.4	.5	.9	-.1	0.0	.6	.3	.5	.8

TABLE A3 c

NEW DELHI, INDIA

(DEC..JAN..FEB.)

FINAL

HOUR (LST)	0030	0130	0230	0330	0430	0530	0630	0730	0830	0930	1030	1130
STD	3.7	3.8	3.8	3.9	3.9	4.0	4.0	4.6	4.9	4.9	4.9	4.9
SIGPRIM	4.5	4.5	4.2	4.5	4.5	4.1	4.6	4.3	5.1	5.0	5.2	4.7
DELSTD	-0.8	-0.7	-0.4	-0.6	-0.6	-0.1	-0.6	.3	-0.2	-0.1	-0.3	.2

OHIRA, JAPAN

(DEC..JAN..FEB.)

FINAL

HOUR (LST)	0030	0130	0230	0330	0430	0530	0630	0730	0830	0930	1030	1130
STD	3.7	3.8	3.6	3.6	3.6	3.6	3.8	4.1	4.3	4.4	4.5	4.5
SIGPRIM	4.0	4.0	4.1	4.1	4.3	4.1	4.4	4.1	4.3	4.7	4.7	5.0
DELSTD	-0.3	-0.4	-0.5	-0.5	-0.7	-0.5	-0.6	0.0	0.0	-0.3	-0.2	-0.5

PRETORIA, S. AFR.

(DEC..JAN..FEB.)

FINAL

HOUR (LST)	0030	0130	0230	0330	0430	0530	0630	0730	0830	0930	1030	1130
STD	5.7	5.7	5.7	5.7	5.7	5.7	5.8	5.8	5.8	5.7	5.7	5.7
SIGPRIM	6.4	6.2	5.9	6.1	5.8	6.3	5.3	6.4	6.7	7.5	7.9	6.7
DELSTD	-0.7	-0.5	-0.2	-0.4	-0.1	-0.6	.5	-1.0	-0.9	-1.8	-2.2	-1.0

RABAT, MOROCCO

(DEC..JAN..FEB.)

FINAL

HOUR (LST)	0030	0130	0230	0330	0430	0530	0630	0730	0830	0930	1030	1130
STD	4.4	4.5	4.6	4.6	4.7	4.7	4.8	4.7	5.0	5.1	5.0	4.9
SIGPRIM	3.9	4.9	3.8	4.3	3.6	4.0	3.9	3.7	3.0	4.2	3.4	3.9
DELSTD	.5	1.0	1.0	.3	1.1	.7	.9	1.0	2.0	.9	1.6	1.0

SINGAPORE, MALAYA

(DEC..JAN..FEB.)

FINAL

HOUR (LST)	0030	0130	0230	0330	0430	0530	0630	0730	0830	0930	1030	1130
STD	4.1	4.1	4.2	4.2	4.2	4.3	4.3	4.4	4.4	4.4	4.3	4.3
SIGPRIM	3.5	3.7	3.6	3.9	3.7	3.3	3.4	4.0	4.4	5.0	4.4	4.2
DELSTD	.0	.4	.6	.3	.5	1.0	.9	.4	0.0	-0.6	-0.1	.1

TABLE A3 d

1230	1330	1430	1530	1630	1730	1830	1930	2030	2130	2230	2330
4.8	4.9	5.0	5.0	4.9	5.1	4.9	4.7	4.2	4.0	4.0	4.0
5.1	4.9	5.0	5.1	5.1	5.0	5.0	4.9	4.2	4.1	4.5	4.3
-0.2	0.0	0.0	-0.1	-0.2	.1	-0.1	-0.2	0.0	-0.1	-0.5	-0.3

1230	1330	1430	1530	1630	1730	1830	1930	2030	2130	2230	2330
4.5	4.4	4.3	4.3	4.4	4.2	4.0	3.8	3.9	3.9	3.8	3.7
4.4	4.1	4.0	3.9	3.5	3.7	4.5	3.5	3.7	4.1	4.0	3.8
.1	.3	.3	.4	.9	.5	-0.5	.3	.2	-0.2	-0.2	-0.1

1230	1330	1430	1530	1630	1730	1830	1930	2030	2130	2230	2330
5.8	5.8	5.8	5.9	5.8	5.8	5.8	5.7	5.7	5.7	5.7	5.7
6.3	6.6	6.5	5.9	7.2	7.7	7.4	7.0	6.5	6.4	7.6	7.2
-0.5	-0.8	-0.7	-0.1	-1.4	-1.9	-1.6	-1.3	-0.8	-0.9	-1.9	-1.5

1230	1330	1430	1530	1630	1730	1830	1930	2030	2130	2230	2330
4.8	4.7	4.6	4.5	4.4	4.0	4.0	4.0	3.9	3.8	4.0	4.2
3.1	3.5	3.0	3.3	3.7	3.7	4.0	3.9	3.1	2.9	3.3	2.8
1.7	1.2	1.6	1.2	.7	.3	0.0	.1	.8	.9	.7	1.4

1230	1330	1430	1530	1630	1730	1830	1930	2030	2130	2230	2330
4.4	4.4	4.5	4.5	4.5	4.4	4.4	4.3	4.2	4.1	4.1	4.0
4.0	4.3	4.5	4.8	4.3	4.4	4.2	4.0	3.9	3.8	3.1	3.7
.4	.1	0.0	-0.3	.2	0.0	.2	.3	.3	.3	1.0	.3

TABLE A4 a

BALBOA, CANAL ZONE

(JUNE, JULY, AUG.)

FINAL

HOUR (LST)	0030	0130	0230	0330	0430	0530	0630	0730	0830	0930	1030	1130
STD	8.0	8.1	8.1	8.1	8.1	8.1	8.1	8.0	7.9	7.9	7.8	8.0
SIGPRIM	7.4	6.4	6.5	6.9	7.4	7.7	8.5	8.6	8.6	8.3	8.5	7.8
DELSTD	.6	1.7	1.6	1.2	.7	.4	-.4	-.6	-.7	-.4	-.7	.2

BOULDER, COLORADO

(JUNE, JULY, AUG.)

FINAL

HOUR (LST)	0030	0130	0230	0330	0430	0530	0630	0730	0830	0930	1030	1130
STD	5.6	5.6	5.6	5.6	5.7	5.8	5.8	5.8	5.9	5.9	5.7	5.6
SIGPRIM	4.1	4.2	4.2	4.2	4.2	4.5	4.3	4.4	4.3	4.7	4.4	4.9
DELSTD	1.5	1.4	1.4	1.4	1.5	1.3	1.5	1.4	1.6	1.2	1.3	.7

COOK, AUSTRALIA

(JUNE, JULY, AUG.)

FINAL

HOUR (LST)	0030	0130	0230	0330	0430	0530	0630	0730	0830	0930	1030	1130
STD	3.7	3.6	3.6	3.7	3.8	3.9	4.0	4.2	4.4	4.5	4.4	4.4
SIGPRIM	2.2	2.1	2.1	2.1	2.0	2.0	2.0	2.4	2.5	2.6	3.5	3.3
DELSTD	1.5	1.5	1.5	1.6	1.8	1.9	2.0	1.8	1.9	1.9	.9	1.1

ENKOPING, SWEDEN

(JUNE, JULY, AUG.)

FINAL

HOUR (LST)	0030	0130	0230	0330	0430	0530	0630	0730	0830	0930	1030	1130
STD	3.7	3.7	3.7	3.7	3.7	3.8	3.9	3.9	4.0	4.1	4.2	4.2
SIGPRIM	3.7	3.4	2.8	3.0	3.1	3.5	3.5	3.4	3.9	3.6	3.1	3.2
DELSTD	0.0	.3	.9	.7	.6	.3	.4	.5	.1	.5	1.1	1.0

KEKAHA, HAWAII

(JUNE, JULY, AUG.)

FINAL

HOUR (LST)	0030	0130	0230	0330	0430	0530	0630	0730	0830	0930	1030	1130
STD	3.0	3.1	3.2	3.2	3.2	3.3	3.4	3.4	3.3	3.1	3.0	2.9
SIGPRIM	2.2	2.0	2.1	2.4	2.8	2.5	2.6	3.0	2.9	2.6	2.7	2.2
DELSTD	.8	1.1	1.1	.8	.4	.8	.8	.4	.4	.5	.3	.7

TABLE A4 b

1230	1330	1430	1530	1630	1730	1830	1930	2030	2130	2230	2330
8.1	8.1	8.1	8.1	8.0	8.0	8.0	7.8	7.7	7.6	7.6	7.7
7.8	8.0	8.2	8.8	8.1	7.7	7.7	7.4	6.8	6.4	6.8	6.9
.3	.1	-.1	-.7	-.1	.3	.7	.4	.9	1.2	.8	.8

1230	1330	1430	1530	1630	1730	1830	1930	2030	2130	2230	2330
5.6	5.6	5.6	5.6	5.6	5.7	5.4	5.5	5.5	5.5	5.5	5.5
5.0	5.2	5.2	4.6	4.6	3.9	4.4	4.5	4.3	4.8	4.1	4.3
.6	.4	.4	1.0	1.0	1.8	1.2	1.0	1.2	.7	1.4	1.2

1230	1330	1430	1530	1630	1730	1830	1930	2030	2130	2230	2330
4.3	4.2	3.9	3.7	3.7	3.9	4.0	3.8	3.8	3.9	3.9	3.8
3.2	3.3	3.5	3.1	2.7	2.6	3.2	2.8	2.7	2.7	2.6	2.3
1.1	.9	.4	.6	1.0	1.3	.8	1.0	1.1	1.2	1.3	1.5

1230	1330	1430	1530	1630	1730	1830	1930	2030	2130	2230	2330
4.2	4.1	4.1	4.1	4.1	4.1	4.1	4.0	3.8	3.9	3.8	3.7
3.7	3.8	3.5	3.9	3.5	3.5	3.5	3.7	3.3	3.3	3.3	3.7
.5	.3	.6	.2	.6	.6	.4	.3	.5	.6	.5	0.0

1230	1330	1430	1530	1630	1730	1830	1930	2030	2130	2230	2330
2.9	2.9	3.0	3.1	3.1	3.0	3.1	3.2	3.2	3.2	3.1	3.1
2.3	2.0	1.7	2.2	2.2	1.9	2.2	1.8	2.1	2.1	2.0	2.0
.6	.9	1.3	.9	.9	1.1	.9	1.4	1.1	1.1	1.1	1.1

TABLE A4 c

NEW DELHI, INDIA

(JUNE, JULY, AUG.)

FINAL

HOUR (LST)	0030	0130	0230	0330	0430	0530	0630	0730	0830	0930	1030	1130
STD	5.4	5.4	5.4	5.5	5.5	5.6	5.7	5.7	5.8	5.8	5.7	5.6
SIGPRIM	5.7	5.7	5.8	5.5	6.1	5.8	6.1	6.2	6.3	6.4	5.3	5.9
DELSTD	-.3	-.3	-.4	0.0	-.6	-.2	-.4	-.5	-.5	-.6	.4	-.3

OHIRA, JAPAN

(JUNE, JULY, AUG.)

FINAL

HOUR (LST)	0030	0130	0230	0330	0430	0530	0630	0730	0830	0930	1030	1130
STD	4.0	4.0	4.1	4.1	4.1	4.1	4.1	4.1	3.9	3.9	3.9	4.1
SIGPRIM	4.3	4.3	4.4	4.0	3.8	3.8	4.1	4.0	4.0	4.5	4.4	4.7
DELSTD	-.3	-.3	-.3	.1	.3	.3	0.0	.1	-.1	-.6	-.5	-.6

PRETORIA, S. AFR.

(JUNE, JULY, AUG.)

FINAL

HOUR (LST)	0030	0130	0230	0330	0430	0530	0630	0730	0830	0930	1030	1130
STD	4.3	4.3	4.3	4.4	4.4	4.4	4.5	4.8	5.1	5.2	5.3	5.2
SIGPRIM	5.4	5.4	4.9	5.0	5.3	5.5	5.5	5.8	5.3	6.5	7.3	6.3
DELSTD	-1.1	-1.1	-.6	-.6	-.9	-1.1	-1.0	-1.0	-.2	-1.3	-2.0	-1.1

RABAT, MOROCCO

(JUNE, JULY, AUG.)

FINAL

HOUR (LST)	0030	0130	0230	0330	0430	0530	0630	0730	0830	0930	1030	1130
STD	3.5	3.5	3.6	3.6	3.7	3.6	3.6	3.6	3.6	3.5	3.4	3.4
SIGPRIM	5.2	5.4	5.5	5.3	5.1	4.8	5.1	5.3	5.0	5.1	5.2	4.7
DELSTD	-1.7	-1.9	-1.9	-1.7	-1.4	-1.2	-1.5	-1.7	-1.4	-1.6	-1.8	-1.3

SINGAPORE, MALAYA

(JUNE, JULY, AUG.)

FINAL

HOUR (LST)	0030	0130	0230	0330	0430	0530	0630	0730	0830	0930	1030	1130
STD	5.0	5.1	5.1	5.1	5.1	5.2	5.3	5.3	5.4	5.5	5.4	5.4
SIGPRIM	4.7	4.7	4.7	4.3	5.0	4.7	4.3	4.8	4.7	4.4	5.7	5.4
DELSTD	.3	.4	.4	.8	.1	.5	1.0	.5	.7	1.1	-.3	0.0

TABLE A4 d

1230	1330	1430	1530	1630	1730	1830	1930	2030	2130	2230	2330
5.6	5.7	5.7	5.8	5.8	5.8	5.9	5.7	5.6	5.5	5.5	5.4
6.1	5.7	5.7	5.8	5.5	5.4	5.2	5.3	5.5	4.9	4.9	5.0
-.5	.6	0.0	0.0	.3	.4	.4	.4	.1	.6	.6	.4

1230	1330	1430	1530	1630	1730	1830	1930	2030	2130	2230	2330
4.4	4.5	4.5	4.3	4.2	4.0	4.0	3.9	3.8	3.7	3.8	3.8
4.8	4.8	4.9	4.7	4.4	4.0	4.2	4.7	4.0	4.1	3.9	4.2
-.4	-.3	-.4	-.4	-.2	0.0	-.2	-.8	-.2	-.4	-.1	-.4

1230	1330	1430	1530	1630	1730	1830	1930	2030	2130	2230	2330
5.0	4.7	4.4	4.3	4.3	4.6	4.2	4.1	4.2	4.4	4.4	4.4
6.6	6.7	6.0	5.6	5.1	5.5	6.4	5.8	5.7	5.5	5.8	5.8
-1.6	-2.0	-1.6	-1.3	-.8	-.9	-2.2	-1.7	-1.5	-1.1	-1.4	-1.4

1230	1330	1430	1530	1630	1730	1830	1930	2030	2130	2230	2330
3.5	3.6	3.8	3.8	3.9	3.9	3.9	3.7	3.7	3.6	3.5	3.4
5.0	6.1	5.1	6.0	5.7	5.7	4.7	5.8	5.4	5.6	5.6	5.0
-1.5	-2.5	-1.3	-2.2	-1.8	-1.8	-.0	-2.1	-1.7	-2.0	-2.1	-1.6

1230	1330	1430	1530	1630	1730	1830	1930	2030	2130	2230	2330
5.4	5.4	5.5	5.5	5.5	5.5	5.4	5.1	5.0	4.9	4.9	4.9
5.9	4.9	5.3	4.7	4.2	4.0	4.4	4.1	4.4	4.1	4.2	4.4
-.5	.5	.2	.8	1.3	1.5	1.0	1.0	.6	.8	.7	.5

TABLE A5 a

BALBOA, CANAL ZONE	(DEC., JAN., FEB.)											FINAL
HOUR (LST)	0030	0130	0230	0330	0430	0530	0630	0730	0830	0930	1030	1130
VD(C)	11.2	11.2	11.1	11.1	11.2	11.6	12.1	12.7	13.4	13.9	13.4	12.3
VD(O)	12.6	12.5	11.9	12.3	12.0	11.5	11.8	11.8	11.5	11.6	11.9	11.3
DELVD	-1.4	-1.3	-.8	-1.2	-.8	.1	.3	.9	1.9	2.3	1.7	1.0

BOULDER, COLORADO	(DEC., JAN., FEB.)											FINAL
HOUR (LST)	0030	0130	0230	0330	0430	0530	0630	0730	0830	0930	1030	1130
VD(C)	11.1	11.3	11.4	11.4	11.5	11.6	11.8	12.0	12.2	12.2	11.9	11.1
VD(O)	10.6	9.8	10.9	11.1	11.6	11.7	11.8	11.4	11.4	11.0	10.8	10.7
DELVD	.5	1.5	.5	.3	-.1	-.1	0.0	.4	.8	1.2	1.1	.4

COOK, AUSTRALIA	(DEC., JAN., FEB.)											FINAL
HOUR (LST)	0030	0130	0230	0330	0430	0530	0630	0730	0830	0930	1030	1130
VD(C)	10.1	10.2	10.3	10.3	10.3	10.4	10.7	11.1	11.9	12.6	12.9	12.3
VD(O)	9.7	9.4	9.2	9.6	10.1	10.7	10.5	11.5	12.7	12.9	13.5	13.4
DELVD	.4	.8	1.1	.7	.2	-.3	.2	-.4	-.8	-.3	-.6	-1.1

ENKOPING, SWEDEN	(DEC., JAN., FEB.)											FINAL
HOUR (LST)	0030	0130	0230	0330	0430	0530	0630	0730	0830	0930	1030	1130
VD(C)	9.6	9.9	10.1	10.3	10.7	11.1	11.4	11.8	12.3	12.7	12.3	11.7
VD(O)	9.6	10.3	10.8	11.2	11.3	11.5	11.5	12.5	12.1	12.1	12.9	12.1
DELVD	0.0	-.4	-.7	-.9	-.6	-.4	-.1	-.7	.2	.6	-.6	-.4

KEKAHA, HAWAII	(DEC., JAN., FEB.)											FINAL
HOUR (LST)	0030	0130	0230	0330	0430	0530	0630	0730	0830	0930	1030	1130
VD(C)	13.4	13.1	12.9	12.7	12.5	12.5	12.5	12.7	12.9	13.2	13.6	13.9
VD(O)	10.1	10.3	10.6	10.5	10.5	10.4	10.8	10.8	11.5	12.0	12.3	12.9
DELVD	3.3	2.8	2.3	2.2	2.0	1.9	1.7	1.9	1.4	1.2	1.3	1.0

TABLE A 5 b

1230	1330	1430	1530	1630	1730	1830	1930	2030	2130	2230	2330
10.7	9.4	8.7	8.4	8.4	8.7	9.7	9.7	10.3	10.8	11.1	11.2
11.0	10.8	10.5	10.6	11.0	11.5	12.5	12.7	13.4	13.0	13.1	12.6
-.3	-1.4	-1.8	-2.2	-2.6	-2.8	-3.4	-3.0	-3.1	-2.2	-2.0	-1.4

1230	1330	1430	1530	1630	1730	1830	1930	2030	2130	2230	2330
10.3	10.6	9.8	9.8	10.0	10.2	10.4	10.5	10.6	10.8	10.9	11.0
10.8	10.5	11.4	12.0	13.0	12.4	13.6	13.0	13.0	12.5	12.0	11.4
-.5	-.5	-1.6	-2.2	-3.0	-2.2	-2.4	-2.5	-2.4	-1.7	-1.1	-.4

1230	1330	1430	1530	1630	1730	1830	1930	2030	2130	2230	2330
11.1	9.9	9.2	8.6	8.5	8.6	8.7	8.9	9.2	9.4	9.6	9.9
12.5	11.6	9.4	8.0	7.8	7.8	8.6	8.8	9.7	10.2	10.3	10.1
-1.4	-1.7	-.2	.6	.7	.8	.7	.1	-.5	-.8	-.7	-.2

1230	1330	1430	1530	1630	1730	1830	1930	2030	2130	2230	2330
10.9	9.7	8.9	8.7	8.7	8.7	8.8	8.8	8.7	8.9	9.1	9.4
10.3	9.6	8.9	8.5	8.5	8.3	7.4	8.1	7.8	8.2	8.3	8.6
.6	.1	0.0	.2	.2	.4	1.2	.7	.9	.7	.8	.8

1230	1330	1430	1530	1630	1730	1830	1930	2030	2130	2230	2330
14.3	14.7	15.0	15.4	15.7	15.8	15.5	15.3	14.8	14.4	14.0	13.7
13.1	14.5	14.8	15.1	14.8	14.3	12.8	11.8	10.3	10.1	10.1	10.1
1.2	.2	.2	.3	.9	1.5	2.7	3.5	4.5	4.3	3.9	3.6

TABLE A6 a

BALBOA, CANAL ZONE	(JUNE, JULY, AUG.)												FINAL
HOUR (LST)	0030	0130	0230	0330	0430	0530	0630	0730	0830	0930	1030	1130	
VD(C)	11.1	10.9	10.4	9.9	9.6	9.7	10.0	10.7	11.3	12.2	13.1	13.4	
VD(O)	11.2	11.9	11.6	12.1	13.0	13.1	13.0	13.4	14.2	13.6	13.5	13.0	
DELVD	-.1	-1.0	-1.2	-2.2	-3.4	-3.4	-3.0	-2.7	-2.9	-1.4	-.4	.4	
BOULDER, COLORADO	(JUNE, JULY, AUG.)												FINAL
HOUR (LST)	0030	0130	0230	0330	0430	0530	0630	0730	0830	0930	1030	1130	
VD(C)	10.3	10.6	10.6	10.7	10.8	11.2	11.5	12.0	12.5	12.9	13.2	13.6	
VD(O)	9.7	10.4	10.4	10.7	11.4	11.6	12.0	12.5	13.1	12.4	11.4	10.5	
DELVD	.6	.2	.2	0.0	-.6	-.4	-.5	-.5	-.6	.5	1.8	3.1	
COOK, AUSTRALIA	(JUNE, JULY, AUG.)												FINAL
HOUR (LST)	0030	0130	0230	0330	0430	0530	0630	0730	0830	0930	1030	1130	
VD(C)	10.4	10.4	10.3	10.3	10.2	10.2	10.4	10.5	10.7	10.9	11.1	11.3	
VD(O)	7.3	7.0	7.3	7.6	7.8	7.8	7.6	7.8	8.3	9.3	10.6	11.1	
DELVD	3.1	3.4	3.0	2.7	2.4	2.4	2.8	2.7	2.4	1.6	.5	.2	
ENKOPING, SWEDEN	(JUNE, JULY, AUG.)												FINAL
HOUR (LST)	0030	0130	0230	0330	0430	0530	0630	0730	0830	0930	1030	1130	
VD(C)	11.0	11.0	11.1	11.2	11.4	11.5	11.7	12.0	12.2	12.1	11.7	10.9	
VD(O)	9.2	9.5	9.7	10.1	10.3	11.0	11.4	11.5	11.2	11.4	11.0	10.8	
DELVD	1.8	1.5	1.4	1.1	1.1	.5	.3	.5	1.0	.7	.7	.1	
KEKAHA, HAWAII	(JUNE, JULY, AUG.)												FINAL
HOUR (LST)	0030	0130	0230	0330	0430	0530	0630	0730	0830	0930	1030	1130	
VD(C)	9.9	10.1	10.3	10.5	10.8	11.0	11.2	11.3	10.9	10.3	9.8	9.1	
VD(O)	8.1	8.4	9.2	10.2	11.0	11.6	12.0	11.6	10.8	9.8	9.3	8.8	
DELVD	1.8	1.7	1.1	.3	-.2	-.6	-.8	-.3	.1	.5	.5	.3	

TABLE A6 b

1230	1330	1430	1530	1630	1730	1830	1930	2030	2130	2230	2330
12.9	10.9	9.0	7.9	7.3	7.2	7.4	8.0	8.8	9.7	10.5	11.0
11.9	11.5	10.5	10.0	9.3	8.6	8.8	9.4	10.0	9.5	10.1	10.4
1.0	-.6	-1.5	-2.1	-2.0	-1.4	-1.4	-1.4	-1.2	.2	.4	.6

1230	1330	1430	1530	1630	1730	1830	1930	2030	2130	2230	2330
12.9	11.7	10.2	8.5	7.4	7.1	7.2	7.5	8.2	8.9	9.3	9.8
9.7	8.6	7.8	7.3	7.5	7.5	7.5	7.6	8.4	9.1	9.3	9.5
3.2	3.1	2.4	1.2	-.1	-.4	-.3	-.1	-.2	-.2	0.0	.3

1230	1330	1430	1530	1630	1730	1830	1930	2030	2130	2230	2330
11.4	11.3	10.8	10.0	9.4	9.2	9.2	9.2	9.6	9.9	10.2	10.4
11.8	11.9	10.6	9.5	8.7	8.5	8.1	8.0	8.5	8.0	7.6	7.5
-.4	-.6	.2	.5	.7	.7	1.1	1.2	1.1	1.9	2.6	2.9

1230	1330	1430	1530	1630	1730	1830	1930	2030	2130	2230	2330
9.9	9.1	8.6	8.2	8.3	8.5	8.8	9.4	10.0	10.5	10.8	10.9
9.9	9.5	9.2	9.1	8.9	9.0	9.2	9.1	8.9	8.4	9.1	9.4
0.0	-.4	-.6	-.9	-.6	-.5	-.4	.3	1.1	2.1	1.7	1.5

1230	1330	1430	1530	1630	1730	1830	1930	2030	2130	2230	2330
8.7	8.6	8.7	8.9	9.3	9.6	9.9	10.0	10.2	10.1	10.0	9.9
8.5	8.1	8.5	9.5	10.2	10.4	9.9	8.6	7.9	7.8	8.0	7.8
.2	.5	.2	-.6	-.9	-.8	0.0	1.4	2.3	2.3	2.0	2.1

APPENDIX B

FOURIER TRANSFORMS AND SPECTRAL ANALYSIS

The well known Fourier integrals relating a time function $f(t)$ and its corresponding frequency function $g(\omega)$ are

$$f(t) = \frac{1}{2\pi} \int_{-\infty}^{\infty} g(\omega) e^{i\omega t} dt \quad (B-1)$$

$$g(\omega) = \int_{-\infty}^{\infty} f(t) e^{-i\omega t} dt \quad (B-2)$$

Since there are simple relationships between the radiated frequency spectrum and the spectrum of the current length moment, we will reconsider spectrum of moment pulses since these are usually simpler in shape and correspond to readily available transformations. The simplest pulse shape is the rectangular pulse shown in the upper right hand portion of Figure B-1 where the amplitude of the pulse is k and the pulse length is δ . Applying the transform equation (B-2) we obtain

$$g(\omega) = k e^{-i\omega t} \Big|_{-\delta/2}^{\delta/2} \quad (B-3)$$

$$= k \left(\frac{e^{-i\omega \delta/2} - e^{i\omega \delta/2}}{-i\omega} \right) \quad (B-4)$$

$$= k \delta \frac{\sin \omega \delta/2}{\omega \delta/2} \quad (B-5)$$

$$= k \delta \frac{\sin \pi \delta f}{\pi \delta f} \quad (B-6)$$

It is interesting to note the resulting Fourier transform has an amplitude which is equal to the pulse area, i. e. $k \delta \times \sin x/x$ variation with frequency. This function is shown in Figure B-1 where the amplitude is normalized to 1 at 0 frequency and the frequency is normalized in terms of the $f \delta$ product. Another simple time function shown in this figure is that of the symmetrical triangular pulse. The Fourier transform for this pulse is

$$g(\omega) = \int_{-\delta}^0 \left(\frac{kt}{\delta} + k \right) e^{-i\omega t} dt + \int_0^{\delta} \left(-\frac{kt}{\delta} + k \right) e^{-i\omega t} dt \quad (B-7)$$

$$= \frac{-2k}{\delta \omega^2} \frac{e^{i\omega \delta} + e^{-i\omega \delta}}{2} - 1 \quad (B-8)$$

$$= \frac{4k}{\delta \omega^2} \sin^2 \omega \delta / 2 \quad (B-9)$$

$$= k \delta \frac{\sin^2 (\pi \delta f)}{(\pi \delta f)^2} \quad (B-10)$$

It is interesting to observe that again we have an amplitude proportional to the pulse area but now with a frequency variation of $\sin^2 x/x^2$.

Numerous typical pulse shapes are shown in the upper right hand portion of Figure B-1 and all are chosen to have the same area, i. e. $k \delta$. The normalized frequency spectrum are found to be rather similar in the low frequency portion and also are seen to have a rather low value in the frequency region where $f \delta = 1$. If the pulse amplitude has the units of amperes-meters, the spectral density function has the units of amperes-meters-second.

It is important to note that the frequency function from equation B-2 extends from $-\infty$ to $+\infty$ and that we have only plotted the right hand portion in Figure B-1. The negative frequency concept is well known and + and - frequencies correspond to counter-rotating exponential functions. Any physically observable spectrum can only have positive frequencies and as a result if it is desired to obtain a frequency spectrum which corresponds to the envelope voltage of a unity gain receiver with an effective bandwidth of 1 cycle per second, the $g(\omega)$ function must be multiplied by 2 to obtain $g(f)$. The value so obtained is a peak value corresponding to the peak of the cosine function at the center frequency to which the spectrum analyzer is tuned. This becomes readily apparent when one considers that the addition of 2 counter rotating exponentials yields a cosine wave whose peak amplitude is equal to twice that of the individual exponential functions. When it is necessary to obtain spectral energy, it is required to use the rms value which will be equal to the peak value divided by the $\sqrt{2}$. As a result, we can write the relationships for transforming a 2-sided frequency spectrum $g(\omega)$ to a one sided frequency spectrum $g(f)$.

$$g(f)_{\text{peak}} = 2 g(\omega) \quad (\text{B-11})$$

$$g(f)_{\text{rms}} = \sqrt{2} g(\omega) \quad (\text{B-12})$$

An interesting check on the validity of these relationships can be made by means of the rectangular pulse. The energy in a simple rectangular pulse assuming that the impedance characteristics remain constant for both the time and frequency function is simply proportional to the amplitude squared times the time.

$$U_t = k^2 \delta \quad (\text{B-13})$$

The rms frequency function from equation (B-12) for the rectangular pulse should be

$$g(f)_{\text{rms}} = \sqrt{2} \, k \, \delta \, \frac{\sin \pi \delta f}{\pi \delta f} \quad (\text{B-14})$$

The energy of the frequency function is now obtained by squaring the amplitude of the individual components and integrating over the frequency spectrum. The result is

$$U_f = 2 \, k^2 \, \delta^2 \int_0^{\infty} \frac{\sin^2 \pi \delta f}{(\pi \delta f)^2} \quad (\text{B-15})$$

$$= 2 \, k^2 \, \delta^2 \cdot \frac{1}{2} \delta \quad (\text{B-16})$$

$$= k^2 \, \delta \quad (\text{B-17})$$

where it is seen that the energy obtained is the same as that for the time function.

There are several well known characteristics of the time to frequency transformations which should be mentioned. First that when there are discontinuities for the time function such as for the rectangular pulse the frequency function approaches an asymptotic $1/f$ relationship. When the discontinuity is in the first derivative, such as for the triangular pulse, the frequency spectrum approaches a $1/f^2$ relation. The generalized relationship is that if the time function has a discontinuity in its n^{th} derivative, the frequency function approaches a $f^{-(n+1)}$. Other useful observation can be made from this figure. It is seen that the amplitude of $g(\omega)$ is equal to the pulse area, $k\delta$, at frequencies which are small compared to the reciprocal of the pulse length. Skewing of the pulse such as the dotted saw-toothed wave compared to the solid triangular wave produces very little change in the lower frequency region.

The amplitude in the region $f \delta \approx 0.2$ to 0.6 is somewhat below the symmetrical waveform. For normalized frequencies $f \delta > 1$, the skewing produces spectral amplitudes greater than that of the symmetrical pulse.

Figure B-2 gives a normalized frequency spectrum, $G(\omega)$, which has been adjusted to represent the skewed, rounded pulse shapes of typical lightning events. For the eventual computer application of lightning model, it was easier, and just as accurate, to take numbers from Figure B-2 or to use equations to represent the pulse shape and its frequency spectrum. Actually, a log-log plot of Figure B-2 was used to obtain the accuracy required for small values of $G(\omega)$ and large values of $f \delta$.

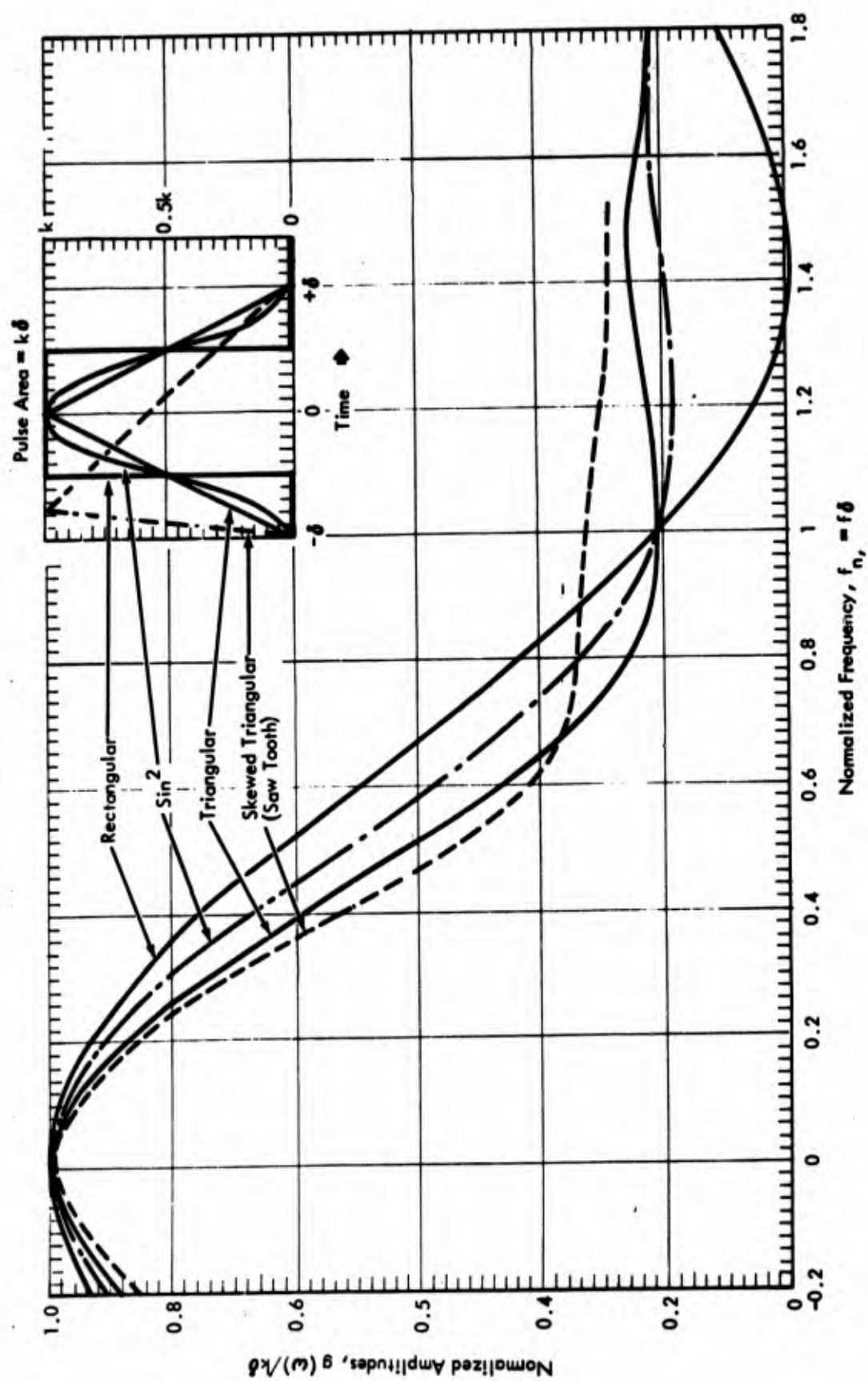


Figure B-1 Frequency Spectra of Several Pulse Shapes

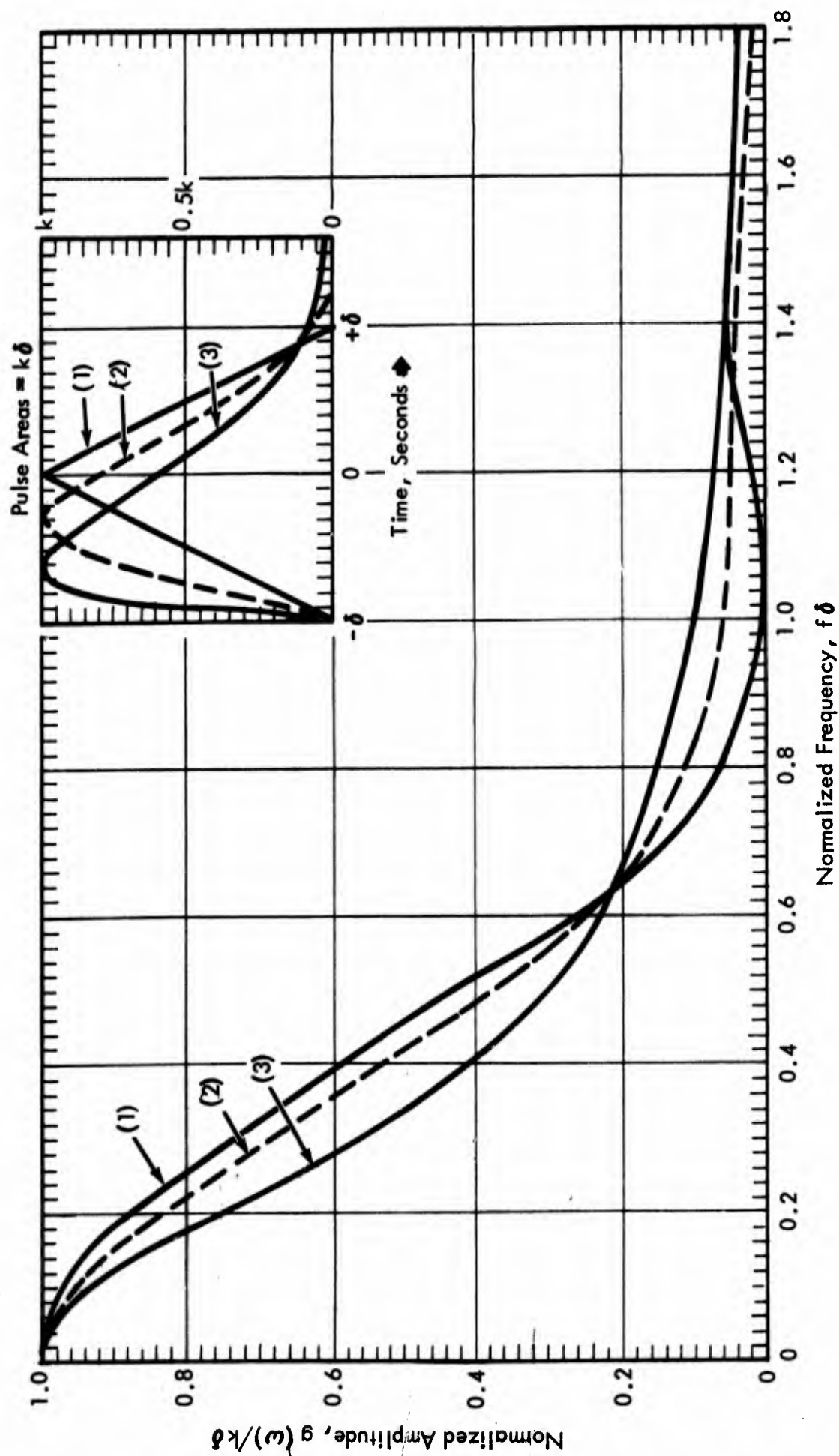


Figure B-2 Normalized Frequency Spectra of Triangular Like Shaped Pulses

Security Classification

DOCUMENT CONTROL DATA - R&D		
(Security classification of title, body of abstract and indexing annotation must be entered when the overall report is classified)		
1. ORIGINATING ACTIVITY (Corporate author)		2a. REPORT SECURITY CLASSIFICATION
Westinghouse Electric Corporation 8401 Baseline Road Boulder, Colorado 80303		Unclassified
		2b. GROUP
		NA
3. REPORT TITLE		
Development of a VLF Atmospheric Noise Prediction Model		
4. DESCRIPTIVE NOTES (Type of report and inclusive dates)		
Final		
5. AUTHOR(S) (Last name, first name, initial)		
Maxwell, Eugene L., Croghan, Roland D., Ball, Lawrence; Stone, Donald L., Watt, Arthur D.		
6. REPORT DATE	7a. TOTAL NO. OF PAGES	7b. NO. OF REFS
30 June 1970	243	64
8a. CONTRACT OR GRANT NO.	8b. ORIGINATOR'S REPORT NUMBER(S)	
N00014-69-C-0150	70-1H2-VLFNO-R1	
a. PROJECT NO.	9a. OTHER REPORT NO(S) (Any other numbers that may be assigned this report)	
c. NRL Reqn. 00173-9-005189/ 11-25-68	None	
d.		
10. AVAILABILITY/LIMITATION NOTICES		
Reproduction in whole or in part is permitted for any purpose by the United States Government.		
11. SUPPLEMENTARY NOTES	12. SPONSORING MILITARY ACTIVITY	
None	Office of Naval Research Department of the Navy Washington, D. C. 20360	
13. ABSTRACT		
<p>This report describes the development of a digital computer model for predicting the characteristics of VLF atmospheric noise. Five algorithms which form the basis for the model are: (I) An algorithm for computing electromagnetic power radiated from every region of the earth. (II) An algorithm for computing the standard deviation of power radiated for every region of the earth. (III) An algorithm for the propagation of energy within the earth-ionosphere waveguide. (IV) An algorithm which uses the results of I, II and III to compute noise field intensities (E_v), standard deviations (σ_N), V_d's and direction of arrival values for any location on the earth's surface, for any hour, any month and at any frequency from 10 to 30 kHz. (V) An algorithm to take the output of IV and prepare contour plots, polar plots, diurnal plots, frequency interpolation plots and data inputs to computer programs for communications system analysis.</p> <p>The prediction model was used to compute E_v, σ_N and V_d at 20 kHz, in a 1 kHz bandwidth, for every 10° longitude and every 10° latitude (from 80°S to 80°N). These were computed for each hour and month and were used in the preparation of contours for noise prediction maps. The calculations, contour plots, etc. were used in the preparation of a VLF atmospheric noise prediction manual to be published by the United States Government.</p> <p>Calculated values from the prediction model were compared with measured values of E_v generally agree within ± 3 dB; σ_N within ± 1 dB; and V_d within ± 2 dB.</p>		

DD FORM 1473
1 JAN 64Unclassified
Security Classification

14.

KEY WORDS

Atmospheric Noise
 Very Low Frequency (VLF)
 Noise Prediction Model
 Propagation - VLF
 Lightning
 Thunderstorms
 VLF Communications
 Noise Statistics
 Thunderstorm Statistics

LINK A

ROLE

WT

LINK B

ROLE

WT

LINK C

ROLE

WT

INSTRUCTIONS

1. **ORIGINATING ACTIVITY:** Enter the name and address of the contractor, subcontractor, grantee, Department of Defense activity or other organization (*corporate author*) issuing the report.

2a. **REPORT SECURITY CLASSIFICATION:** Enter the overall security classification of the report. Indicate whether "Restricted Data" is included. Marking is to be in accordance with appropriate security regulations.

2b. **GROUP:** Automatic downgrading is specified in DoD Directive 5200.10 and Armed Forces Industrial Manual. Enter the group number. Also, when applicable, show that optional markings have been used for Group 3 and Group 4 as authorized.

3. **REPORT TITLE:** Enter the complete report title in all capital letters. Titles in all cases should be unclassified. If a meaningful title cannot be selected without classification, show title classification in all capitals in parentheses immediately following the title.

4. **DESCRIPTIVE NOTES:** If appropriate, enter the type of report, e.g., interim, progress, summary, annual, or final. Give the inclusive dates when a specific reporting period is covered.

5. **AUTHOR(S):** Enter the name(s) of author(s) as shown on or in the report. Enter last name, first name, middle initial. If military, show rank and branch of service. The name of the principal author is an absolute minimum requirement.

6. **REPORT DATE:** Enter the date of the report as day, month, year; or month, year. If more than one date appears on the report, use date of publication.

7a. **TOTAL NUMBER OF PAGES:** The total page count should follow normal pagination procedures, i.e., enter the number of pages containing information.

7b. **NUMBER OF REFERENCES:** Enter the total number of references cited in the report.

8a. **CONTRACT OR GRANT NUMBER:** If appropriate, enter the applicable number of the contract or grant under which the report was written.

8b, 8c, & 8d. **PROJECT NUMBER:** Enter the appropriate military department identification, such as project number, subproject number, system number, task number, etc.

9a. **ORIGINATOR'S REPORT NUMBER(S):** Enter the official report number by which the document will be identified and controlled by the originating activity. This number must be unique to this report.

9b. **OTHER REPORT NUMBER(S):** If the report has been assigned any other report numbers (either by the originator or by the sponsor), also enter this number(s).

10. **AVAILABILITY/LIMITATION NOTICES:** Enter any limitations on further dissemination of the report, other than those imposed by security classification, using standard statements such as:

- (1) "Qualified requesters may obtain copies of this report from DDC."
- (2) "Foreign announcement and dissemination of this report by DDC is not authorized."
- (3) "U. S. Government agencies may obtain copies of this report directly from DDC. Other qualified DDC users shall request through _____."
- (4) "U. S. military agencies may obtain copies of this report directly from DDC. Other qualified users shall request through _____."
- (5) "All distribution of this report is controlled. Qualified DDC users shall request through _____."

If the report has been furnished to the Office of Technical Services, Department of Commerce, for sale to the public, indicate this fact and enter the price, if known.

11. **SUPPLEMENTARY NOTES:** Use for additional explanatory notes.

12. **SPONSORING MILITARY ACTIVITY:** Enter the name of the departmental project office or laboratory sponsoring (paying for) the research and development. Include address.

13. **ABSTRACT:** Enter an abstract giving a brief and factual summary of the document indicative of the report, even though it may also appear elsewhere in the body of the technical report. If additional space is required, a continuation sheet shall be attached.

It is highly desirable that the abstract of classified reports be unclassified. Each paragraph of the abstract shall end with an indication of the military security classification of the information in the paragraph, represented as (TS), (S), (C), or (U).

There is no limitation on the length of the abstract. However, the suggested length is from 150 to 225 words.

14. **KEY WORDS:** Key words are technically meaningful terms or short phrases that characterize a report and may be used as index entries for cataloging the report. Key words must be selected so that no security classification is required. Identifiers, such as equipment model designation, trade name, military project code name, geographic location, may be used as key words but will be followed by an indication of technical context. The assignment of links, rules, and weights is optional.

Unclassified

Security Classification